

# Vortex Dynamics in Bose-Einstein Condensates

Benjamin Michael Caradoc-Davies

A thesis submitted for the degree of  
Doctor of Philosophy  
at the University of Otago, Dunedin,  
New Zealand.



July 2000

Copyright © 2000 Benjamin Michael Caradoc-Davies

Permission is granted to make and distribute verbatim copies of this thesis in any medium. All other rights reserved.

Amended version, October 2000.

An electronic version of this thesis may be obtained by searching the Web, or from `<http://www.physics.otago.ac.nz/bec2/bmcd/phdthesis/>`.

The two papers included in Appendix F are used with permission.

Reference [19]:

Copyright © 1999 The American Physical Society

Reference [17]:

Copyright © 2000 The American Physical Society

# Abstract

We investigate in the mean field limit the dynamics of vortices in trapped Bose-Einstein condensates, using numerical simulations of the Gross-Pitaevskii equation in two and three dimensions. Vortices are found to be readily generated by a variety of mechanisms, including collisions between condensates or with an aperture, or by mechanically disturbing the condensate with a perturber. In particular, we study the rotational stirring of a condensate with a repulsive Gaussian potential, representing a far-blue-detuned laser. We find that for a condensate rotationally stirred just below a critical angular frequency, given by the energy difference between the ground and vortex eigenstates, a single vortex cycles into the centre of the condensate and then out. We analyse this behaviour in terms of a two state model, and show that it can be understood as nonlinear Rabi cycling between the ground and vortex states of the condensate. The single vortex cycling regime occurs both in two dimensions, and in three dimensions for a range of trap geometries. We show how this dynamical behaviour can be used to prepare a central vortex state in a parameter regime accessible to current experiments. We also show (in two and three dimensions) that a singly quantised central vortex is dynamically stable to a perturbation, while a doubly quantised central vortex immediately dissociates into two unit vortices upon perturbation. We give a simple geometrical explanation for this instability. We find that a central vortex remains in the condensate if a perturber is inserted and left in place: the condensate exhibits persistent flow past the obstruction, as is characteristic of a superfluid. Rotationally stirring a condensate in a spherically symmetric trap can form vortex lines which collide and exchange sections, an example of the rich dynamical behaviour of these structures.



# Acknowledgements

It has been a pleasure to work with Assoc. Prof. Rob Ballagh, and I thank him for his unfailing encouragement and guidance. No student could ask for a more diligent supervisor. I would also like to thank Dr. Don Warrington, my secondary supervisor, particularly for his careful proofreading. I have enjoyed collaborating with Prof. Keith Burnett, and I thank him for sharing his ideas with me. My many interesting discussions with Prof. Crispin Gardiner have influenced this work. I am particularly grateful to Blair Blakie, whose expertise and effort in producing eigenstates by optimisation methods have been essential. Thanks also to Terence Scott for his invaluable scholarly insights into the finer points of the Gross-Pitaevskii equation, and for being tall and pretty just when I needed it.

Thanks to Max Krüger, for teaching me how to write CDs, and for proving by example that I'm not a Free Software extremist; to Andreas Penckwitt for sharing his knowledge of field theory and the excruciating details of English grammar; and to Adam Norrie, for challenging my preconceptions. Thanks also to Sam Morgan and Matthew Davis for interesting discussions. I enjoyed working with Dr. Andrea Eschmann, who was brave enough to extend my Matlab code to deal with two-component condensates.

One of the great benefits of working in the Department of Physics has been the presence of an excellent experimental team, whose insights into the practical problems of BEC have been most valuable. In particular, I appreciate the many discussions I have had with Dr. Andrew Wilson, Dr. Jos Martin, Callum McKenzie, Nick Thomas, and also with Dr. Christopher Foot during his visit.

Thanks to Malcolm Fraser for all his assistance with our Linux machines,

and for answering my many questions. To the other staff and students of the Department of Physics, you have together created a warm and collegial atmosphere, and made my time here so rewarding.

I would like to thank my parents Gill and Tudor, and the other members of my family, who have been a constant source of encouragement. Most deeply, I am grateful to my dear wife Cheryl, not least for patiently proofreading this thesis. Your love makes everything worthwhile.

*This work was supported by the Marsden Fund of New Zealand under contracts PVT603 and PVT902.*

# Contents

<b>1</b>	<b>Introduction</b>	<b>1</b>
1.1	Bose-Einstein condensation . . . . .	1
1.1.1	Bose-Einstein statistics . . . . .	3
1.1.2	Superfluid helium . . . . .	4
1.1.3	Mean field . . . . .	5
1.2	Vortices . . . . .	6
1.2.1	Normal fluids . . . . .	6
1.2.2	Vortices in He II . . . . .	7
1.3	Motivation for this work . . . . .	8
1.4	Contemporary theoretical studies . . . . .	9
1.4.1	Properties of vortices . . . . .	9
1.4.2	Stability of central vortex states . . . . .	10
1.4.3	Vortices in rotating systems . . . . .	10
1.4.4	Schemes for coherent vortex formation . . . . .	11
1.4.5	Schemes for vortex detection . . . . .	13
1.4.6	Perturber moving in a straight line . . . . .	13
1.5	Experimental observations of vortices . . . . .	14
1.5.1	Two-component condensate . . . . .	14
1.5.2	Single component condensate . . . . .	15
1.6	This work . . . . .	15
1.6.1	Overview . . . . .	16
1.6.2	Peer-reviewed publications . . . . .	17
<b>2</b>	<b>Theory</b>	<b>19</b>
2.1	Introduction . . . . .	19

2.2	Gross-Pitaevskii equation . . . . .	19
2.2.1	Second quantised Hamiltonian . . . . .	20
2.2.2	Gross-Pitaevskii equation . . . . .	22
2.2.3	Axisymmetric harmonic trapping potential . . . . .	24
2.3	Dimensionless formalism . . . . .	24
2.3.1	Time-dependent Gross-Pitaevskii equation . . . . .	26
2.3.2	Time-independent Gross-Pitaevskii equation . . . . .	27
2.3.3	Thomas-Fermi limit . . . . .	28
2.3.4	Speed of sound and healing length . . . . .	29
2.4	Vortices . . . . .	30
2.4.1	Phase . . . . .	30
2.4.2	Vortices . . . . .	31
2.4.3	Properties of the circulation . . . . .	31
2.4.4	Example: central vortex eigenstate . . . . .	33
2.4.5	Vortices in the linear regime . . . . .	34
2.5	Light shift . . . . .	35
<b>3</b>	<b>Numerical techniques</b>	<b>39</b>
3.1	Introduction . . . . .	39
3.2	Discretisation of the mean field . . . . .	40
3.2.1	Presentation of data . . . . .	40
3.3	Solution of the Gross-Pitaevskii equation . . . . .	41
3.3.1	The RK4IP algorithm . . . . .	41
3.3.2	Runge-Kutta in the interaction picture . . . . .	42
3.3.3	Fast Fourier Transform . . . . .	44
3.3.4	Optimised implementation in Python . . . . .	45
3.3.5	Implementation performance . . . . .	46
3.3.6	Data storage . . . . .	47
3.3.7	MPEG-1 movies . . . . .	48
3.4	Validity of numerical solutions . . . . .	48
3.4.1	Time-reversal of simulations . . . . .	50
3.4.2	The Nyquist limit . . . . .	51
3.5	Eigenstates . . . . .	53



---

3.6	Vortex detection . . . . .	54
3.6.1	Phase unwrapping . . . . .	55
3.6.2	Phase jump counting . . . . .	56
3.6.3	Density curvature threshold for vortex detection . . . . .	58
3.6.4	Presentation of detected vortices . . . . .	59
3.6.5	Vortex lines . . . . .	60
<b>4</b>	<b>Vortex dynamics in two-dimensional condensates</b>	<b>63</b>
4.1	Introduction . . . . .	63
4.2	Collisions . . . . .	64
4.2.1	Linear regime . . . . .	64
4.2.2	Nonlinear regime . . . . .	66
4.3	Off-centre collisions . . . . .	68
4.4	Collision with an aperture . . . . .	68
4.5	Constant velocity perturber . . . . .	70
4.5.1	On-centre perturber . . . . .	71
4.5.2	Off-centre perturber . . . . .	72
4.5.3	Angular momentum . . . . .	72
<b>5</b>	<b>Rotational stirring of two-dimensional condensates</b>	<b>77</b>
5.1	Introduction . . . . .	77
5.2	Two-dimensional model . . . . .	79
5.3	Multiple vortex regime . . . . .	80
5.3.1	Interaction of vortices . . . . .	80
5.4	Single vortex cycling regime . . . . .	83
5.4.1	Dependence on parameters . . . . .	83
5.5	Speed of sound . . . . .	87
5.6	Summary . . . . .	89
<b>6</b>	<b>Nonlinear two state model</b>	<b>91</b>
6.1	Introduction . . . . .	91
6.2	Two state ansatz . . . . .	92
6.3	Coupled basis wavefunctions . . . . .	93
6.4	Nonlinear Rabi equations . . . . .	95

6.4.1	Linear Rabi cycling . . . . .	97
6.4.2	Numerical method . . . . .	97
6.4.3	Numerical solution . . . . .	99
6.5	Energy in the rotating frame . . . . .	102
6.5.1	Critical angular frequency of rotational stirring . . . . .	103
6.5.2	Energy barrier . . . . .	105
6.5.3	Other characteristics . . . . .	106
6.6	Regime of validity . . . . .	107
6.6.1	Linear regime . . . . .	108
<b>7</b>	<b>Rotational stirring of three-dimensional condensates</b>	<b>109</b>
7.1	Introduction . . . . .	109
7.2	Three-dimensional model . . . . .	110
7.3	Single vortex cycling . . . . .	111
7.3.1	Generation of a central vortex state . . . . .	111
7.4	Two state model in three dimensions . . . . .	117
7.5	Role of trap geometry . . . . .	118
7.6	Role of stirrer symmetry . . . . .	123
7.7	Vortex line collisions . . . . .	124
<b>8</b>	<b>Vortex stability and persistent flow</b>	<b>127</b>
8.1	Introduction . . . . .	127
8.2	Vortex stability in two dimensions . . . . .	128
8.3	Vortex stability in three dimensions . . . . .	129
8.4	Persistent flow in a condensate . . . . .	134
8.5	Effect of a uniform perturbation . . . . .	136
<b>9</b>	<b>Conclusion</b>	<b>139</b>
9.1	Vortex dynamics in condensates . . . . .	139
9.2	Directions for future work . . . . .	141
	<b>References</b>	<b>143</b>
<b>A</b>	<b>Properties of the Gross-Pitaevskii equation</b>	<b>155</b>
A.1	Outline . . . . .	155

---

A.1.1	Time-dependent Gross-Pitaevskii equation . . . . .	156
A.1.2	Useful identities . . . . .	156
A.2	Probability . . . . .	157
A.3	Energy . . . . .	157
A.4	Position . . . . .	158
A.5	Momentum . . . . .	159
A.6	Angular momentum . . . . .	160
A.7	Energy in the rotating frame . . . . .	161
<b>B</b>	<b>Implementation of the RK4IP algorithm</b>	<b>163</b>
B.1	Fourth-order Runge-Kutta . . . . .	163
B.2	Matlab implementation . . . . .	166
B.3	Efficient implementation in Python . . . . .	166
<b>C</b>	<b>Fourier techniques</b>	<b>169</b>
C.1	Fourier transform . . . . .	169
C.2	Discrete Fourier transform . . . . .	170
<b>D</b>	<b>Derivation of the nonlinear two state model</b>	<b>173</b>
D.1	Preliminary results . . . . .	173
D.1.1	Orthogonality by phase circulation . . . . .	174
D.1.2	Expansion of the GP equation . . . . .	174
D.2	Coupled basis wavefunctions . . . . .	175
D.3	Nonlinear Rabi equations . . . . .	176
D.3.1	Effects of the stirrer . . . . .	177
D.3.2	Rotating frame . . . . .	177
<b>E</b>	<b>Colour plates</b>	<b>179</b>
<b>F</b>	<b>Selected papers</b>	<b>191</b>
Reference [19]	. . . . .	193
Reference [17]	. . . . .	197



# Chapter 1

## Introduction

### 1.1 Bose-Einstein condensation

The observation in 1995 of Bose-Einstein condensation (BEC) in dilute alkali gases [3, 25] marks an important advance in physics. Condensates bring the counterintuitive rules of quantum mechanics from the realm of microscopic atoms into the macroscopic (although not yet everyday) world; it is now possible to directly see an individual material quantum object. Anticipated uses of Bose-Einstein condensates include using the precise control over matter which condensates afford to make highly accurate measurements of time and spatial curvature, or to directly deposit nanostructures. Manipulation of condensates will allow new tests of fundamental physics as well as technological applications.

Bose-Einstein condensates of dilute alkali gases are currently produced at extremely low pressure in vacuum systems, the atoms being suspended in a magnetic trap and isolated in near complete darkness, with the entire apparatus assembled on vibration-damping optical tables. Examples of configurations for the magnetic trap include the time-orbiting potential (TOP) trap, which gives a condensate shaped like a pancake, and the Ioffe-Pritchard trap which yields a cigar-shaped condensate. A typical scheme for the production of a condensate is to cool and trap atoms (such as  $^{87}\text{Rb}$  or  $^{23}\text{Na}$ ) in a single hyperfine state in a magneto-optical trap (MOT), and then load the atoms into the much shallower magnetic trap. The crucial next step is evaporative cool-

ing, in which techniques such as applying a radio-frequency field are used to selectively allow atoms with higher than average kinetic energy to escape from the trap. As the atomic cloud equilibrates, the removal of the higher energy atoms is reflected in cooling of the cloud. Evaporative cooling continues until the atomic cloud is sufficiently cold and dense for a Bose-Einstein condensate to form. Collisions between atoms in the condensate ensure that some thermal cloud always remains. In current experiments, condensates typically survive for times on the order of ten seconds, eventually dissipating through processes such as three-body recombination. Condensates are imaged using laser light, either destructively with resonant absorption imaging, or nondestructively with far-detuned phase contrast imaging.

As an indication of the temperatures, number of atoms, and scales involved, the first observation of BEC in  $^{87}\text{Rb}$  [3] occurred at 170 nK, with about 2000 atoms in the condensate. Even in this early experiment, the temperature could be lowered to 20 nK by adiabatically decompressing the condensate. More recent experiments report, for example,  $^{87}\text{Rb}$  condensates in an expanded TOP trap with about  $10^6$  atoms [70], and in a Ioffe-Pritchard trap,  $^{23}\text{Na}$  condensates with over  $10^7$  atoms [81]. Depending on the strength of the trapping potential and the number of atoms they contain, these condensates range from tens to hundreds of micrometres in diameter, dimensions which for a large condensate are accurately predicted by the Thomas-Fermi approximation (see Section 2.3.3).

A Bose-Einstein condensate of atoms is different from a gas of thermal atoms in the same way that laser light is different from candlelight. In a gas of thermal atoms (or in candlelight), each particle has a different momentum, while in a condensate (or laser light), all the particles have the same momentum (to the maximum amount permitted by Heisenberg's uncertainty principle). Furthermore, in a condensate or laser light, if we think in terms of the individual probability wave representing each particle, then these waves are "aligned" or in phase, and this property allows us to use exactly the same wavefunction for every individual particle. Note that this picture neglects quantum fluctuations and, in the case of a condensate, interactions with thermal atoms. The fact that a single wavefunction can be used to describe the

particles is an expression of *coherence*, and gives condensates and laser light the pure wavelike character of a single particle, amplified by the number of the particles in the condensate or laser mode. The crucial difference between a condensate and a laser is that while photons can be readily created and annihilated, the matter particles of the condensate/thermal-cloud system are fixed in number and do not come into or out of existence (although particles can move between the condensate and the thermal cloud).

### 1.1.1 Bose-Einstein statistics

Particles in nature are divided into two classes: a *boson* is a particle of integral spin, as distinguished from a *fermion*, a particle of half-odd-integral spin. Examples of bosons are photons, and atoms of  $^1\text{H}$ ,  $^4\text{He}$ ,  $^7\text{Li}$ ,  $^{23}\text{Na}$ ,  $^{85}\text{Rb}$ , and  $^{87}\text{Rb}$ . Examples of fermions are electrons, protons, neutrons,  $^3\text{He}$  and  $^6\text{Li}$ . The quantum state of a system of indistinguishable bosons must be fully symmetric: the exchange of any two particles must leave the system in exactly the same state.

When a system of bosons is in thermodynamical equilibrium, the ensemble-average occupation number for a single-particle state  $s$  with energy  $\epsilon_s$  (that is, the expected number of particles in state  $s$ ) is given by the Bose-Einstein distribution [82],

$$\langle n_s \rangle = \frac{1}{e^{(\epsilon_s - \mu)/kT} - 1}, \quad (1.1)$$

where  $k$  is Boltzmann's constant,  $T$  is the temperature, and  $\mu < \epsilon_s$  is the chemical potential. The striking feature of the Bose-Einstein distribution (in contrast to the Fermi-Dirac distribution for fermions, or the Maxwell-Boltzmann distribution for distinguishable particles), is that it is possible for a state to be occupied by very large numbers of particles. Considering Equation (1.1) for the state with lowest energy  $\epsilon_0$ , if  $T$  decreases (for some constant  $\mu < \epsilon_0$ ), the exponential approaches one from above, the denominator approaches zero, and the occupation number of the ground state  $\langle n_0 \rangle$  becomes arbitrarily large (limited only by the total number of particles in the system). This effect is known as *Bose-Einstein condensation* (BEC).

What are the conditions for BEC to occur? For an ideal gas of bosons in a box (all in the same internal state), the temperature for which  $e^{(\epsilon_0 - \mu)/kT} = 1$  is given by [38],

$$T_c = \frac{2\pi\hbar^2}{mk} \left( \frac{\rho}{2.612} \right)^{\frac{2}{3}}, \quad (1.2)$$

where  $\rho = N/V$  is the mean density of particles in the box, and  $m$  the particle mass.  $T_c$  is known as the *critical temperature* for Bose-Einstein condensation, and describes the temperature at which (for a large number of atoms) all the atoms would occupy the ground state. For particles in an external confining potential, the critical temperature depends on the shape of the potential [6]. Roughly speaking, BEC occurs when the mean number of atoms per atomic de Broglie wavelength cubed is at least (the order of) one: in this regime, the atoms lose their individual particle-like nature and behave as a collective wave.

### 1.1.2 Superfluid helium

The earliest example of Bose-Einstein condensation<sup>1</sup> was superfluid  $^4\text{He}$  (the phase known as He II), which was reported in 1932 by McLennan, Smith, and Wilhelm, who noticed that liquid helium suddenly ceased boiling when cooled below 2.17 K. Further experiments reported in 1938, by Allen and Misener, and independently by Kapitza, demonstrated superfluidity in He II, although at that time the reason for this unusual behaviour was unknown. In 1938, London proposed that the superfluid component was a condensate of the type proposed by Einstein.

The unusual behaviour of He II has provided a glimpse into the impact on macroscopic objects of quantum effects, including such phenomena as superfluidity and persistent flow. The latter subject is of particular interest in this thesis. Unfortunately, the strongly interacting nature of He II (due to its high density) prevents more than about 8–10% of the liquid being in the superfluid fraction, and the masking effect of the normal fraction has prevented detailed study of the microscopic dynamics of the fluid.

---

<sup>1</sup>A detailed account is given in [45] of early studies of superfluidity in  $^4\text{He}$  and of the development of theories of Bose-Einstein condensation.



### 1.1.3 Mean field

The second-quantised formalism of field theory can exactly describe a system of interacting particles, but because of the combinatorial growth with number of possible interactions between particles, complexity forbids the calculation of exact solutions for a system with a large number of particles. One particular class of approximations, which has proven to be very accurate under specific circumstances, is where some characteristic of the system can be represented by a mean field. A well known example of this is the Weiss molecular field approximation which successfully described the major features of ferromagnetism by replacing the interactions between adjacent atoms with an “internal” magnetic field [82]. This example also provides an archetypal illustration of spontaneous symmetry breaking: even though the system Hamiltonian is completely isotropic (in the absence of an external magnetic field) the magnetisation of the ferromagnet points in a particular direction in space.

In a dilute Bose-Einstein condensate, a large number of atoms occupy one mode of the system, and we represent them by a single complex number field, which is commonly known as the *mean field*. The mean field concept has been of great importance in understanding the behaviour of dilute alkali condensates. Such a field has a measurable phase relationship between two different points in the condensate: in the language of field theory, it has “off-diagonal long-range order.” This correlation, which Penrose and Onsager specified as a criterion for Bose-Einstein condensation, was first demonstrated experimentally in an interference experiment in  $^{23}\text{Na}$  by the MIT group, in which two condensates, separated by a sheet of  $\text{Ar}^+$  laser light, were allowed to expand into each other [4].

In contrast to the Weiss molecular field, the mean field which we use to describe the condensate has an absolute phase which, for an isolated system, has no physical meaning. This arbitrary, symmetry breaking choice of phase has some unphysical consequences, such as the Goldstone mode (see discussion in [79]), but the reasonableness of this procedure can be justified by number conserving arguments [72]. Although we represent our mean field as having an arbitrary phase, we should instead think of it as an order parameter: it is only the phase *difference* between any two points in the condensate which can

have any physical significance.

## 1.2 Vortices

### 1.2.1 Normal fluids

A vortex in a fluid (liquid or gas) is a point about which the fluid rotates, with a speed inversely proportional to the radius. Such motion is an example of *irrotational* flow, in which the vorticity (the curl of the velocity) is zero. In real normal fluids, which cannot reach infinite velocities, the irrotational flow breaks down in a central region known as the vortex core, such as the eye of a hurricane or the centre of a tornado: here the flow becomes rotational. The canonical example of rotational flow is rigid body rotation.

In irrotational flow, if a fluid particle changes its radius about a vortex, it maintains its angular momentum, because its azimuthal speed multiplied by the radius is constant. Angular momentum is not dissipated (except at the boundary): the presence of vortices in some driven physical fluid systems allows flow which conserves angular momentum. In a tornado or hurricane, for example, circulating air can flow inwards at low altitudes and outwards at high altitudes (rising in the core), while conserving angular momentum. The change in kinetic energy required for this particle motion is reflected in a pressure gradient.

If a fluid circulating in a cylindrical container contains a vortex (irrotational flow), then there is a rigid body motion of the fluid (rotational flow) with lower energy and the same angular momentum. This is because in rigid body motion, a particle can be moved to a larger radius and contribute the same angular momentum for a smaller speed (and kinetic energy). In the absence of a driving force, a vortex in a normal fluid will eventually decay into rotational motion. This dissipation occurs because, in irrotational flow, an element of the fluid becomes deformed over time and loses energy through viscous damping [90]. In rigid body motion (rotational flow), an element of the fluid retains its shape and viscous damping does not occur (except at the boundary).

In contrast to normal fluids, the Bose-Einstein condensates we consider are

described by a mean field, and one of the strict mathematical requirements on such a field is that of perfect irrotationality (where its density is nonzero). Because rotational flow is forbidden to it, a condensate behaves as a perfectly inviscid fluid, known as a *superfluid*.

### 1.2.2 Vortices in He II

In a famous piece of work, Landau showed that He II can be described by a two-component model in which the superfluid fraction is represented by a mean field wavefunction [94]. In He II (and in dilute alkali condensates), the complex wavefunction  $\psi$  describes both the density and velocity of the superfluid, with the density being proportional to  $|\psi|^2$  and the velocity proportional to the gradient of the phase of  $\psi$ . A notable feature of both the superfluid component of He II and of dilute alkali condensates is that they can only sustain irrotational flow: this is because the velocity is the gradient of the phase (a scalar), and so the vorticity (the curl of the velocity) is identically equal to zero wherever the phase of  $\psi$  is defined. This means that if the phase of the fluid is well defined over its extent, the fluid cannot support circulating flow.

How then do superfluids respond to rotational stirring? The answer, and the topic of this thesis, is through the formation of *vortices*. If the wavefunction  $\psi$  goes to zero at some point, then the phase of  $\psi$  may change by a multiple of  $2\pi$  when following a closed path about that point, around which the fluid is said to have a *circulation* of that amount. The quantum of circulation is  $2\pi$ .

Vortices are the mechanism by which superfluids support circulating flow. Experiments in He II have shown that if a rotating container of He I (ordinary  $^4\text{He}$ ) is cooled below the critical temperature (forming He II), depending on the angular speed of rotation one or more vortices may form in the fluid. This is because above a critical angular frequency of rotation, the presence of a vortex reduces the free energy of the fluid in the frame rotating with the container. If the rotation of the container is halted, the superfluid continues to circulate (although it can be stopped by a small vibration). If the container is toroidal, the circulation is stable against vibration, and continues even if the container had been packed with porous material. This phenomenon is known as *persistent flow*, and has been the subject of much attention in studies of

He II. Irrotational flow in a superfluid cannot slowly decay into rotational flow, as in a normal fluid, because rotational flow is forbidden to the mean field.

In He II, the density of the fluid is (mostly) homogeneous, and the angular momentum per particle of the fluid is quantised. By contrast, condensates in dilute trapped alkali gases have an inhomogeneous density, and the angular momentum associated with a vortex depends on its position.

In a classic experiment, Packard and Sanders [77] measured the quantisation of vortices in a thin rotating tube of He II. This work investigated the low rotational speed limit, and by counting the charge trapped on vortex lines, was the first to conclusively show the formation of vortex lines in jumps for increasing rotational speed. Later studies (see [94]) used photographic techniques to image the charge distribution and show vortex lattices.

Numerical investigations continue into the properties of vortices in He II. For example, Nore *et al.* [76, 75] used a mean field treatment to investigate the scaling of turbulence in a superfluid flow. One finding was that vortex line reconnection events are an important feature.

### 1.3 Motivation for this work

The observation of Bose-Einstein condensation in dilute alkali gases has opened a new field of possibilities in the understanding and exploitation of quantum effects on a macroscopic scale. The condensates achieved are much more weakly interacting than He II, allowing high purity (condensed fraction  $>90\%$ ) to be achieved. Unlike He II, trapped alkalis are readily manipulated and imaged by optical means. For these reasons, condensates in dilute alkali gases offer excellent opportunities to study the microscopic dynamical behaviour of condensed systems, both theoretically and experimentally. The techniques developed for alkalis may be applied in the future to other bosonic species. The property of remaining liquid when cooled arbitrarily close to absolute zero which was essential to the discovery of He II is not required for dilute (weakly interacting) gases in a magnetic or optical trap.

Theories analogous to those for He II have been employed to describe the

properties of vortices in condensates at thermodynamical equilibrium. The time taken for a dilute condensate to reach thermodynamical equilibrium is longer than for a higher density condensed system (such as He II), and may exceed the lifetime of the condensate. For this reason, dynamical processes are important in understanding the behaviour of condensates. When we commenced this work, the dynamical behaviour of vortices in condensates was not yet well characterised, and our aim was to remedy this situation. Among the results of the present work, we have achieved a quantitative understanding of the underlying dynamics of vortex formation in a rotationally stirred condensate, and of the stability of persistent flow past an obstruction, situations analogous to the rotating container experiments in He II.

## 1.4 Contemporary theoretical studies

During the course of our investigation, the formation and properties of vortices in dilute alkali condensates has attracted intense interest. In this section we summarise the main results of our predecessors and contemporaries. Comprehensive reviews of the history, theory, and experiments of Bose-Einstein condensation can be found in [46, 49].

### 1.4.1 Properties of vortices

Numerous investigators have studied the steady state properties of vortices in condensates. Edwards *et al.* [30] calculated vortex and ground eigenstates of a trap, and showed that the gap between the vortex and ground state energies decreases as the number of atoms in the condensate increases. Dalfovo and Stringari [24] have made extensive numerical investigations of the shape characteristics of condensates. Fetter [34] estimated the coherence length and critical velocities of condensates, and by analogy with He II, gave a prediction for a critical angular frequency of rotation for vortex thermodynamical stability.

Lundh *et al.* [62] made additional corrections to the Thomas-Fermi approximation to characterise the properties of condensates, including a prediction for

the critical angular velocity for vortex stability in a cigar-shaped condensate (for a vortex line running down the long axis).

Lundh *et al.* [63] studied the expansion of a condensate containing a vortex, both analytically and numerically, describing the changing relative sizes of the vortex core and cloud. Their conclusion was that vortices would be most easily observed with small numbers of atoms in shallow traps, where the effect of the vortex on the properties of the condensate is relatively larger.

### 1.4.2 Stability of central vortex states

The stability of vortices in condensates has been a contentious issue. Rokhsar [83] argued that central vortex states are all thermodynamically unstable, although in that work he does not make the distinction, as we do, between thermodynamical and dynamical stability. In Rokhsar's analytical investigation, a central vortex, which is displaced, circles about the centre of the condensate, and he asserts that drag interactions with the thermal cloud would cause the vortex to spiral out of the condensate. This work has often been misinterpreted to mean that a singly quantised central vortex state is dynamically unstable, but, as we show in Chapter 8, this is not the case.

Fetter [35] investigated the stability of vortices, and found that excitations could cause the vortex to move about the condensate. This result is consistent with our findings (see Chapter 8) in which a perturbed central vortex undergoes a small-amplitude oscillation, remaining near the centre of the condensate.

Pu *et al.* [80] investigated the “intrinsic” stability of central vortex eigenstates. Amongst their findings, they show that the singly quantised central vortex state (for repulsive atomic interactions) is stable. They conclude that their results are consistent with our findings (see Chapter 8).

### 1.4.3 Vortices in rotating systems

Key to the understanding of vortices in He II has been the study of rotating systems, and the effect of the presence of vortices. Similarly, many investigators have considered rotating dilute alkali condensates. Butts and Rokhsar [16] used numerical techniques to find, in three dimensions, the lowest energy

rotating states of a condensate as a function of angular momentum. Their striking results showed, as the angular momentum was increased, the formation of at first one vortex (moving into the condensate), and then lattices of vortices. This investigation suggests no mechanism, however, by which the angular momentum might be transferred to the cloud, or the rates of transfer, describing the condensate as reaching equilibrium with a thermal cloud.

Feder *et al.* [32, 33] have found the eigenstates of rotating completely anisotropic traps numerically by using propagation of the GP equation in imaginary time. The use of imaginary-time propagation to find the lowest energy states in a rotating trap effectively mimics a damping process. In contrast to the work of Butts and Rokhsar [16], these traps do not have symmetry about the axis of rotation, and so such a rotating trap can impart angular momentum to the condensate, the thermal cloud acting only to drain energy from the condensate. We remark, though, that this work only finds the eigenstates of the system. In [33], high frequency excitations of the condensate are needed to allow time-dependent simulations to produce vortices in the manner suggested by the eigenstates, which the authors claim shows a need for vortex “nucleation”. In contrast, we show in Section 7.6 that a symmetric distortion (as used in [32, 33]) cannot produce the coherent formation of a single vortex because such a transition is forbidden by symmetry. We interpret the need for excitations in the time-dependent results of [33] as a means of breaking this symmetry and permitting vortex formation.

#### 1.4.4 Schemes for coherent vortex formation

In the present work (and in [17]), we detail a straightforward scheme (which we proposed in [19]) for the coherent formation of a central vortex in a condensate. A number of other approaches have been suggested. Marzlin *et al.* [69] proposed a scheme in which copropagating Gauss-Laguerre laser beams (with opposite circular polarisations) interact with the condensate atoms via a Raman transition, transferring the atoms to another internal state, and so imparting mean field angular momentum to the condensate, leaving it in a vortex state. Dum *et al.* [28] proposed using a Raman transition to achieve an adiabatic transfer of a condensate from an initial mean-field ground state

in one internal state to a mean-field excited state in a second internal state, the excited state being either a dark soliton or vortex eigenstate. In this procedure, the adiabatic parameter is the two-photon Raman detuning, and the end-points of the process are chosen to counteract the changing interaction energy of the condensate.

Marzlin and Zhang [68] showed that, in a noninteracting (that is, linear) condensate, a rotating anharmonic potential (as described in [67]) could be employed to drive a condensate into a vortex state. The rotation of the potential is provided by four far-detuned laser beams, and precise requirements on the phases and frequencies of these beams are given in [67]. If interactions were added, however, very carefully tailored modulation of the frequency of rotation over time was required to overcome the effects of the nonlinearity of the system: they presented numerical results for this in two dimensions. Of particular note is their finding that, in the linear case, a rotating harmonic trap creates multiple vortices, an effect they showed was due to the equal spacing of the energy levels in the harmonic trap.

Marshall *et al.* [65] used a mean field representation to simulate (in two dimensions) the evaporative cooling of a condensate. Their approach was to model the thermal atoms by starting with a superposition of simple harmonic oscillator eigenstates, populated according to the Bose-Einstein distribution, with random phase between the states. Their initial state was generated by slowly turning on the nonlinearity, and represents an interacting thermal cloud. The evaporative cooling process was modelled by absorbing at the edge of the computational grid over time, which removed the high frequency excitations. They found that it was possible for a vortex to be trapped in the condensate by this process.

Williams and Holland [98] proposed a scheme for transferring a ground state condensate in one hyperfine state into a topological vortex composed of two superposed hyperfine states, in which the vector order parameter is twisted about the condensate. In this procedure, a relative motion of the trapping potentials for the two components is combined with a population transfer mechanism (such as a radio-frequency or microwave field) between the hyperfine states. This scheme was successfully implemented by the JILA



group (see Section 1.5.1).

### 1.4.5 Schemes for vortex detection

The detection of vortices poses an experimental problem. The size of a vortex, which is given approximately by the healing length, reduces as the number of atoms in a condensate increases. Because an increased number of atoms is desirable for effective imaging of a condensate, the direct detection of vortices in trapped condensates is very difficult. Furthermore, a scheme for the conclusive detection of vortices should also detect the phase circulation. A variety of schemes have been proposed for the direct or indirect detection of vortices.

As an example of an indirect means of vortex detection, the presence of a vortex has been predicted by Dodd *et al.* [26] to significantly change the excitation frequencies of a condensate. Those authors have proposed that such effects allow the detection of vortices in condensates.

A type of experiment yet to be achieved is the detection of vortices by interferometric means. This has been suggested by Bolda and Walls [14], who simulated the collision of two condensates, one of which contained a vortex, and separately by Tempere and Devreese [93] who calculated the fringe pattern of two overlapping condensates (neglecting atomic interactions). Given that the first interference experiment [4] was performed by allowing a separated condensate to freely expand, a practical vortex detection method may be a combination of these two types of techniques.

Detecting the Doppler shift of a Raman transition due to the vortex circulation has been proposed as a vortex detection method by Marzlin *et al.* [69]. The authors do not, however, address the small size of such a shift compared to even a narrow Raman laser linewidth.

### 1.4.6 Perturber moving in a straight line

The Durham group have made extensive investigations of vortex formation in condensates. Jackson *et al.* [51] simulated in two dimensions the effect of a Gaussian perturber moving in a straight line, passing through the centre of a condensate. Vortices were found to be formed, and this process was interpreted

in term of phase slip accumulation. These simulations are like some of our (contemporaneous) simulations, which we describe in Chapter 4, although our work differs by also studying the effect of off-centre perturber motion.

Jackson *et al.* [52] studied the effect on a condensate of dragging a smaller, more tightly confined condensate through the first. Their three-dimensional simulations showed a mutual drag, and the reduction of this drag when a vortex ring was formed. Winiecki *et al.* [99, 100] have found such ring formation in numerical studies of flowing extended quantum fluids.

To study the experiment of Raman *et al.* [81], Jackson *et al.* [53] simulated an oscillating Gaussian potential in a condensate, and found enhanced heating above a critical velocity, in agreement with the experiment. This additional heating was caused by the generation of vortices.

## 1.5 Experimental observations of vortices

### 1.5.1 Two-component condensate

A notable achievement has been the observation of a topological vortex in a two-component system by the JILA team [70]. This experiment was based on theoretical and numerical work by Williams and Holland [98]. In this experiment, the  $|F = 1, m_F = -1\rangle$  hyperfine state of a trapped  $^{87}\text{Rb}$  condensate is transferred to the  $|F = 2, m_F = +1\rangle$  hyperfine state by a two-photon microwave transition. A focussed laser beam rotates around the edge of the condensate, moving the position of strongest coupling, and leading to the formation of a circulation in either component (selected by varying the experimental parameters). These structures are then imaged by interfering the components by coupling them into the same state. Strictly speaking, the vortex formed in this experiment may not be a “true” single component vortex, but can only be confirmed to be a topological vortex. However, it seems reasonable that the system may be a single component vortex in (say) the  $|F = 1, m_F = -1\rangle$  hyperfine state, pinned by the remainder of the condensate in the  $|F = 2, m_F = +1\rangle$  state.

Very recent work by this group, in which the pinning nonvortex compo-

nent was removed, convincingly demonstrates that the remaining component is indeed in a vortex state [2].

### 1.5.2 Single component condensate

In a recent development, Madison *et al.* [64] have made the first observation of a vortex (and indeed, multiple vortices) in a single component condensate. The condensate is formed in a Ioffe-Pritchard trap in which (in effect) two red-detuned beams stir the cloud about the long axis of the trap. For stirring above a critical angular frequency, a single vortex is observed as a deep hole in an absorption image, taken after the condensate is allowed to expand freely for a time. For higher speeds of stirring, up to four vortices are seen. They note a discrepancy between the observed critical angular frequency of stirring and the value calculated by the theory of Lundh *et al.* [62].

In a report just to hand, García-Ripoll and Pérez-García [41] find excellent agreement with the Madison *et al.* [64] experiment, with the shift in critical angular frequency shown to be due to bending of the vortex line.

## 1.6 This work

In this work we investigate the formation and dynamics of vortices in Bose-Einstein condensates. We consider the mean field limit, in which the Gross-Pitaevskii equation is an accurate representation of the dynamics of the condensate. In this regime, thermal atoms are neglected and the system is assumed to be entirely represented by the mean field wavefunction, an approximation which is valid when the system is highly condensed.

The Gross-Pitaevskii equation is a partial differential equation, and contains a nonlinear term reflecting collisional interactions. This nonlinearity couples the modes of the condensate, making the system analytically intractable. To explore the dynamics of the system, we must solve the GP equation numerically.

### 1.6.1 Overview

In Chapter 2 we give the theoretical background for this work, including a brief derivation of the Gross-Pitaevskii equation, and a description of the notation and dimensionless quantities we use. We also survey the properties of the phase circulation that characterises vortices.

The numerical solution of the time-dependent Gross-Pitaevskii equation is intrinsically difficult for the same reason that it is analytically intractable: the nonlinearity couples excitations at different frequencies and in different directions. Because of this, highly accurate numerical techniques are required for successful solution. Furthermore, the number of computational grid points required to study the system is large in two dimensions, and in three dimensions makes solution almost unfeasible on commodity PC hardware. We have developed, tested, and applied efficient implementations of a numerical method to allow us to perform these computationally intensive tasks.

In Chapter 3 we describe in detail the key techniques which we have developed in the course of our investigation. The evolution of the mean field is calculated using a fourth-order spectral method, and in this chapter we describe an efficient implementation of the algorithm which permits the study of the system in two and three dimensions. A simple and robust algorithm which detects vortices in the wavefunction is also described.

In Chapter 4 we perform a variety of simulation of condensates in two dimensions. We find that vortices can be formed in collisions of condensates, either with other condensates or with an aperture. We also describe the dynamics of vortices in condensates perturbed by a Gaussian potential moving in a straight line, and the transfer of angular momentum as the perturber passes through the condensate off-centre.

We have conducted an extensive investigation of rotational stirring of a condensate in two dimensions, described in Chapter 5. Vortices are readily formed in the condensate, and we describe intricate vortex dynamics including pair creation and annihilation. We also find a single vortex cycling regime, a coherent process in which a single vortex penetrates the condensate deeply and then falls out. This cycling occurs when the stirrer moves below a critical angular frequency. We find that vortices can be generated in the condensate with

a stirrer which moves substantially below the speed of sound, and we conclude that the single vortex cycling regime is not a speed of sound phenomenon.

In Chapter 6, we derive an analytical nonlinear two state model to describe the single vortex cycling behaviour, in which the presence of the stirring potential induces Rabi cycling from the ground to the vortex state. We show that this model makes quantitatively accurate predictions for most of the phenomenology of the cycling behaviour, including the critical angular frequency of rotational stirring.

Two-dimensional simulations are not easily related to real experimental scenarios. In Chapter 7, we extend our study of rotationally stirred condensates into three dimensions. This is a major computational undertaking, and yet, using a completely reimplemented numerical method, we are able to perform our calculations on commodity PC hardware. We show that the single vortex cycling behaviour is also present for a range of trap geometries. We relate our simulation parameters to an easily accessible experimental scenario for  $^{87}\text{Rb}$  in a TOP trap, and show that the single vortex cycling behaviour can be used to generate a central vortex state. We also demonstrate dynamical features in three dimensions which have no analogue in two dimensions: for a rotationally stirred condensate in a spherical trap, vortex lines can undergo collisions in which sections are exchanged.

We show in Chapter 8 that singly quantised central vortices are stable, while doubly quantised central vortices are unstable, both in two dimensions and in three dimensions for a range of trap geometries. We interpret these features using our nonlinear two state model and also a simple geometrical argument. We also predict that even in the presence of a fixed obstruction, the condensate exhibits persistent flow, a result much like that observed in He II.

### 1.6.2 Peer-reviewed publications

Much of the work presented in this thesis has been published in peer-reviewed journals. Our initial report of the single vortex cycling regime in two dimensions (Chapter 5) and the nonlinear two state model (Chapter 6), including its application to vortex stability (Chapter 8), has been published in *Phys-*

*ical Review Letters* [19] (included in Appendix F). Further two-dimensional simulations, an explanation of the energy surface deformation, and our initial report into finding the single vortex cycling regime in three dimensions are to appear in a memorial volume of *Lecture Notes in Physics* [9].

The report of our three-dimensional simulations (from Chapter 7), including the single vortex cycling regime in three dimensions for a range of trap geometries, experimental parameters to generate a central vortex state, and the stability of vortices (from Chapter 8), has been published in *Physical Review A* [17] (included in Appendix F).

The numerical method in two dimensions, described in Chapter 3 and Appendix B, has been extended to a condensate with two hyperfine components coupled by electromagnetic fields. This method has been used to investigate Ramsey fringes, with the results reported in the *Journal of Optics B: Quantum and Semiclassical Optics* [31].

# Chapter 2

## Theory

### 2.1 Introduction

In this chapter, we describe the theoretical basis for our study of Bose-condensed alkali gases, and present the notation that we will use throughout the remainder of this thesis. The fundamental questions of superfluidity in which we are interested are in essence questions of phase. The whole understanding of superfluidity in He II is based on the mean field representing the superfluid component, and we use the same formalism in our treatment of condensates.

The starting point for our investigation is the second quantised Hamiltonian for a gas of interacting bosons. We do not dwell on this exact but intractable description, but instead briefly outline how, in the limit of an  $s$ -wave approximation to the binary atomic collisions at low temperatures, the system can be approximated by a classical wave equation, the well-known Gross-Pitaevskii (GP) equation.

### 2.2 Gross-Pitaevskii equation

We give here a simplistic derivation of the GP equation to illustrate the basic ideas involved. In a more comprehensive derivation, Gardiner [42] has shown that the Bogoliubov approximation is a valid expansion if and only if the wavefunction  $\psi$  satisfies the time-dependent GP equation, and also demonstrates that the time-independent GP equation can be found by minimising the second

quantised Hamiltonian, and that the chemical potential arises as a Lagrange multiplier for the constraint of fixed normalisation. This analysis shows that the classical wave we use to describe the condensate should be interpreted as a mode function.

### 2.2.1 Second quantised Hamiltonian

A gas of interacting particles can be described exactly by a second quantised field operator<sup>1</sup>  $\hat{\Psi}(\tilde{\mathbf{r}}, \tilde{t})$ . This full representation is the starting point for all investigations of Bose condensates: various authors have studied finite temperature effects with approximations derived from the full field operator (for example [48, 79, 72]). We, however, study only the limit in which all the particles are condensed into the same single-particle state. For notational compactness, in this section we denote the particular spatial variable over which a quantity is defined with the same number of primes as that variable, so  $\hat{\Psi} \equiv \hat{\Psi}(\tilde{\mathbf{r}}, \tilde{t})$ ,  $\hat{\Psi}' \equiv \hat{\Psi}(\tilde{\mathbf{r}}', \tilde{t})$ , and  $\hat{\Psi}'' \equiv \hat{\Psi}(\tilde{\mathbf{r}}'', \tilde{t})$ , and similarly for  $\tilde{\nabla}^2$  and  $\tilde{V}$ . The second quantised Hamiltonian for a gas of bosons (all in the same internal state) interacting by binary collisions and contained by an external trapping potential is [37, 12, 79]

$$\begin{aligned} \hat{H} = & \int \hat{\Psi}'^\dagger \left[ -\frac{\hbar^2}{2m} \tilde{\nabla}'^2 + \tilde{V}' \right] \hat{\Psi}' d\tilde{\mathbf{r}}' \\ & + \frac{1}{2} \iint \hat{\Psi}'^\dagger \hat{\Psi}''^\dagger \tilde{V}_I(|\tilde{\mathbf{r}}' - \tilde{\mathbf{r}}''|) \hat{\Psi}'' \hat{\Psi}' d\tilde{\mathbf{r}}'' d\tilde{\mathbf{r}}', \end{aligned} \quad (2.1)$$

where  $\tilde{V} = \tilde{V}(\tilde{\mathbf{r}}, \tilde{t})$  is the external potential and  $\tilde{V}_I(\tilde{r})$  is the full interatomic potential between two particles separated by a distance  $\tilde{r}$ . Note that we do not consider inelastic (internal state changing) collisions, which would require a tensor form for the interatomic potential.

For the cold, dilute alkali gases that we consider, the atomic de Broglie wavelength is much greater than the distance over which interatomic interactions can occur, and collisions are dominated by elastic *s*-wave scattering [97].

---

<sup>1</sup>All quantities with hats or tildes are in dimensional units. The unadorned forms of these symbols are reserved for the final set of dimensionless quantities that we obtain in Section 2.3 and use in the rest of this thesis.



Under these circumstances, we can make a pseudopotential approximation, in which we replace the full interatomic potential with a delta function

$$\tilde{V}_I(\tilde{r}) = \frac{4\pi\hbar^2 a}{m} \delta(\tilde{r}), \quad (2.2)$$

where  $a$  is the  $s$ -wave scattering length and  $m$  is the particle mass. In cold alkali gases, this approximation has been found to be very accurate.

Scattering lengths have been obtained experimentally and theoretically for various species of alkali gases. The scattering length is not necessarily a positive quantity; for example, for  $^{133}\text{Cs}$ , the scattering length of atoms in the  $|F = 4, m_F = 4\rangle$  hyperfine state is negative, representing attractive cold collisions. Under these conditions, a very small condensate is possible (in a trapping potential) but collapses above a critical number of atoms. By comparison, in  $^{87}\text{Rb}$  the  $|F = 2, m_F = 2\rangle$  hyperfine state has a positive scattering length (repulsive collisions), with  $a \approx 100 a_0$  [97], and a large condensate can form.

Conceptually, we can picture the pseudopotential approximation as treating collisions between atoms as being collisions between hard spheres whose radius is determined by the scattering length. The problems with this approximation are discussed by Proukakis [79] and by Morgan [72], and we merely mention them here. In making our pseudopotential approximation, in which we use only a single pseudopotential, we have neglected the higher (such as  $d$ -wave) scattering terms which are included in a two-body  $T$ -matrix approach. The pseudopotential we use is essentially an approximation of the low energy terms of the two-body  $T$ -matrix, and becomes inaccurate for higher particle momenta. The effect of the condensate on the collisions between particles is also not considered; a many-body  $T$ -matrix approach can be used to remedy this. Morgan [72] has shown that, to avoid divergences in the theory, the pseudopotential approximation should be made for the  $T$ -matrix rather than for  $V_I$ .

The pseudopotential approximation reduces the double integral in the second term of Equation (2.1) into a single integral, so that we can write

$$\hat{H} = \int \hat{\Psi}'^\dagger \left[ -\frac{\hbar^2}{2m} \tilde{\nabla}'^2 + \tilde{V}' \right] \hat{\Psi}' d\tilde{\mathbf{r}}' + \frac{\tilde{U}_0}{2} \int \hat{\Psi}'^\dagger \hat{\Psi}'^\dagger \hat{\Psi}' \hat{\Psi}' d\tilde{\mathbf{r}}', \quad (2.3)$$

where

$$\tilde{U}_0 = \frac{4\pi\hbar^2 a}{m}. \quad (2.4)$$

We now use this form of the Hamiltonian to derive the time evolution of  $\hat{\Psi}(\mathbf{r}, t)$ . The Heisenberg equations of motion of  $\hat{\Psi}$  are given by

$$i\hbar \frac{\partial \hat{\Psi}}{\partial t} = [\hat{\Psi}, \hat{H}], \quad (2.5)$$

and using the Bose commutation relations [37, 12]

$$[\hat{\Psi}, \hat{\Psi}'] = [\hat{\Psi}^\dagger, \hat{\Psi}'^\dagger] = 0, \quad [\hat{\Psi}, \hat{\Psi}'^\dagger] = \delta(\tilde{\mathbf{r}} - \tilde{\mathbf{r}}'), \quad (2.6)$$

we obtain

$$\begin{aligned} i\hbar \frac{\partial \hat{\Psi}}{\partial t} &= \hat{\Psi} \hat{H} - \int [\hat{\Psi} \hat{\Psi}'^\dagger - \delta(\tilde{\mathbf{r}} - \tilde{\mathbf{r}}')] \left[ -\frac{\hbar^2}{2m} \tilde{\nabla}'^2 + \tilde{V}' \right] \hat{\Psi}' d\tilde{\mathbf{r}}' \\ &\quad - \frac{\tilde{U}_0}{2} \int [\hat{\Psi} \hat{\Psi}'^\dagger - 2\delta(\tilde{\mathbf{r}} - \tilde{\mathbf{r}}')] \hat{\Psi}'^\dagger \hat{\Psi}' \hat{\Psi}' d\tilde{\mathbf{r}}' \\ &= \left[ -\frac{\hbar^2}{2m} \tilde{\nabla}^2 + \tilde{V} + \tilde{U}_0 \hat{\Psi}^\dagger \hat{\Psi} \right] \hat{\Psi}. \end{aligned} \quad (2.7)$$

Note that the nonlinear term in Equation (2.7) contains no reference to the number of particles  $N$ , but it is implicit that

$$\int \hat{\Psi}^\dagger \hat{\Psi} d\tilde{\mathbf{r}} = \hat{N}. \quad (2.8)$$

### 2.2.2 Gross-Pitaevskii equation

The fundamental approximation which gives us a classical wave equation from Equation (2.7) is that a single mode of the system is macroscopically occupied. Under these circumstances, we can replace the field operator with a classical wavefunction  $\psi(\mathbf{r}, t)$ . The formal procedure for this replacement is to decompose the field operator as [37, 36]

$$\hat{\Psi} = \sqrt{N} \tilde{\psi} + \hat{\delta}, \quad (2.9)$$

where  $N$  is the number of condensate atoms and  $\hat{\delta}$  is the fluctuation operator (which satisfies  $\langle \hat{\delta} \rangle = 0$ ). We may then write our classical wavefunction by taking the expectation value of Equation (2.9) to obtain

$$\tilde{\psi} = \frac{1}{\sqrt{N}} \langle \hat{\Psi} \rangle. \quad (2.10)$$

The Bogoliubov approximation which we now make is to replace  $\hat{\Psi}$  with  $\tilde{\psi}$  and neglect  $\hat{\delta}$ . Substituting Equation (2.9) into Equation (2.7), taking the expectation values of both sides, and neglecting all terms in  $\hat{\delta}$  yields the time-dependent Gross-Pitaevskii equation for the normalised wavefunction,

$$i\hbar \frac{\partial \tilde{\psi}(\tilde{\mathbf{r}}, \tilde{t})}{\partial \tilde{t}} = \left[ -\frac{\hbar^2}{2m} \tilde{\nabla}^2 + \tilde{V}(\tilde{\mathbf{r}}, \tilde{t}) + N\tilde{U}_0 |\tilde{\psi}(\tilde{\mathbf{r}}, \tilde{t})|^2 \right] \tilde{\psi}(\tilde{\mathbf{r}}, \tilde{t}). \quad (2.11)$$

Although the fluctuation operator satisfies  $\langle \hat{\delta} \rangle = 0$ , the expectation values of the higher products of  $\hat{\delta}$ , such as  $\langle \hat{\delta}^\dagger \hat{\delta} \rangle$ ,  $\langle \hat{\delta} \hat{\delta} \rangle$ , and  $\langle \hat{\delta}^\dagger \hat{\delta} \hat{\delta} \rangle$ , which are formed by the nonlinear term of Equation (2.7), are not in general zero. In particular,  $\langle \hat{\delta}^\dagger \hat{\delta} \rangle$  represents the depletion of the condensate by collisional interactions, and  $\langle \hat{\delta} \hat{\delta} \rangle$  represents the anomalous correlations between those atoms. The Bogoliubov approximation we make neglects all these terms. More general treatments (see [44], and discussions in [79, 72]) retain some of these higher-order averages, and allow the study of the system at finite temperatures. The form we use [Equation (2.11)] is not generally applicable at finite temperatures; nonetheless, Marshall *et al.* [65] have demonstrated a procedure in which this form may be used to represent the effect of thermal atoms. The Gross-Pitaevskii treatment discards all thermal effects, but has been experimentally verified as a very accurate representation of a weakly interacting condensate at low temperatures.

Note that because of the nonlinearity of Equation (2.11), it is essential to specify the normalisation of the wavefunction, since scaling the wavefunction by a factor  $\alpha$  changes the strength of the nonlinearity by a factor of  $\alpha^2$ . We normalise our wavefunction

$$\int |\tilde{\psi}(\tilde{\mathbf{r}}, \tilde{t})|^2 d\tilde{\mathbf{r}} = 1, \quad (2.12)$$

The number operator

$$\hat{N} = \int \hat{\Psi}^\dagger \hat{\Psi} d\tilde{\mathbf{r}}, \quad (2.13)$$

has expectation value  $N_{total} = \langle \hat{N} \rangle$ . Again making the Bogoliubov approximation [Equation (2.9)], we find that

$$N_{total} = N + \langle \hat{\delta}^\dagger \hat{\delta} \rangle, \quad (2.14)$$

where the second term represents the depletion of the condensate due to fluctuations, and although  $\langle \hat{\delta} \rangle = 0$ , the depletion is not zero. However, in a highly condensed system,  $N \approx N_{total}$ .

### 2.2.3 Axisymmetric harmonic trapping potential

Many experimental trapping configurations can be described as an axisymmetric harmonic trapping potential

$$\tilde{V}_0(\tilde{\mathbf{r}}) = \frac{1}{2}m[\omega_r^2(\tilde{x}^2 + \tilde{y}^2) + \omega_z^2\tilde{z}^2] \quad (2.15)$$

where  $\omega_r$  and  $\omega_z$  are the trap frequencies in the radial and axial directions respectively. We denote the trap anisotropy parameter by

$$\lambda = \frac{\omega_z}{\omega_r}. \quad (2.16)$$

The main reason for writing  $V_0$  in this form is mere notational convenience. We could easily describe the trapping potential using  $\omega_x$ ,  $\omega_y$ , and  $\omega_z$ , the trap frequencies in each direction. However, the experimental configurations we investigate in this work are all axisymmetric. A noticeable exception to the prevalent axisymmetric traps is the TOP trap variant used by the NIST group [55], in which  $\omega_x : \omega_y : \omega_z = 2 : \sqrt{2} : 1$ .

## 2.3 Dimensionless formalism

An appropriate choice of dimensionless quantities allows us to minimise the number of adjustable parameters in our simulations, and scales quantities

closer to unity for improved computational precision. We follow the choice of Ruprecht *et al.* [87, 85] and choose dimensionless quantities

$$\mathbf{r} = \left( \frac{\hbar}{2m\omega_r} \right)^{-\frac{1}{2}} \tilde{\mathbf{r}}, \quad (2.17)$$

$$t = \omega_r \tilde{t}, \quad (2.18)$$

that is, our length and time are in units of  $(\hbar/2m\omega_r)^{1/2}$  and  $\omega_r^{-1}$  respectively. We also define our dimensionless momentum operator as

$$\mathbf{P} = (2m\hbar\omega_r)^{-\frac{1}{2}} \tilde{\mathbf{P}} = -i\nabla, \quad (2.19)$$

where  $\tilde{\mathbf{P}}$  is the dimensional momentum operator. Our unit of momentum is thus  $(2m\hbar\omega_r)^{1/2}$ . In our dimensionless formalism, the angular momentum operator is given by

$$\mathbf{L} = \mathbf{r} \times \mathbf{P}, \quad (2.20)$$

and its  $z$  component (which in two dimensions is the *only* component) by

$$L_z = xP_y - yP_x = -i \left[ x \frac{\partial}{\partial y} - y \frac{\partial}{\partial x} \right]. \quad (2.21)$$

Our unit of angular momentum is  $\hbar$ . The dimensionless energy is given by

$$E = \int \left[ -\psi^* \nabla^2 \psi + V|\psi|^2 + \frac{1}{2}C|\psi|^4 \right] d\mathbf{r}, \quad (2.22)$$

where our unit of energy is  $\hbar\omega_r$ . The contribution to the energy from the first term of Equation (2.22) is the kinetic energy  $E_k$ , that from the second term is the potential energy  $E_p$ , and that from the third is the mean-field energy  $E_m$ . Our axisymmetric harmonic trapping potential is given by

$$V_0(\mathbf{r}) = \frac{x^2 + y^2 + \lambda^2 z^2}{4}, \quad (2.23)$$

and we note that  $\tilde{V}_0(\tilde{\mathbf{r}}) = \hbar\omega_r V_0(\mathbf{r})$ . For our two-dimensional simulations, we consider a symmetric trapping potential, which is equivalent to Equation (2.23) with  $z = 0$ .

### 2.3.1 Time-dependent Gross-Pitaevskii equation

Substituting Equation (2.17) and Equation (2.18) into Equation (2.11) yields the dimensionless time-dependent Gross-Pitaevskii (GP) equation,

$$i\frac{\partial\psi(\mathbf{r},t)}{\partial t} = [-\nabla^2 + V(\mathbf{r},t) + C|\psi(\mathbf{r},t)|^2] \psi(\mathbf{r},t), \quad (2.24)$$

where we also impose the normalisation condition

$$\int |\psi(\mathbf{r},t)|^2 d\mathbf{r} = 1. \quad (2.25)$$

The strength of the nonlinear part of the GP equation is characterised by the single parameter  $C$ , which for the full three-dimensional system is given by

$$C = N \frac{4\pi\hbar a}{m\omega} \left( \frac{\hbar}{2m\omega} \right)^{-\frac{3}{2}} = 8\pi a N \left( \frac{\hbar}{2m\omega} \right)^{-\frac{1}{2}}, \quad (2.26)$$

which we note is dimensionless.

We do not draw a direct comparison between our use of  $C$  in two dimensions and an experimental situation, but we note that various investigators [54, 50, 65] have shown that a tight constraint in one dimension reduces the effective dimensionality of the GP equation. In these treatments, a Thomas-Fermi or Gaussian approximation (as appropriate) is used to separate out the dynamics in the tightly confined dimension(s). In two dimensions, in a homogeneous system or a harmonic trap, Bose-Einstein condensation does not occur. However, local coherence (a “quasicondensate”) has been observed in a two-dimensional gas of spin-polarised H adsorbed on the surface of a  $^4\text{He}$  film [88]. We consider our two-dimensional simulations to be an approximation of pancake condensates (as can be produced in a TOP trap) which are tightly confined in the  $z$  direction. In Chapter 7 we use full three-dimensional calculations to compare to experiment.

In Equation (2.26), a subtle yet important transformation has been made. If we consider the dimensional requirements placed on the probability density  $|\tilde{\psi}(\tilde{\mathbf{r}},t)|^2$  by the normalisation condition of Equation (2.12), the density must have units of one over length cubed. In linear quantum mechanics, the units of the wavefunction are not of importance because the normalisation of the field

does not affect the equations of motion. In the nonlinear system, a change in units directly affects the coefficients of the nonlinear terms. Unfortunately, this factor has been omitted by a number of authors [8, 65]; however, this varies only the interpretation of their results.

In Appendix A, we prove a number of important properties of the time-dependent GP equation. For those quantities which are not conserved, we derive their rates of change. The time-dependent GP equation conserves normalisation, but energy is conserved only if the external potential  $V$  is constant. The expectation values of position and momentum evolve according to the Ehrenfest theorem, and are not conserved in general. Each component of the angular momentum expectation value is conserved only if  $V$  is symmetric about the axis in that direction. We derive a torque equation analogous to the Ehrenfest theorem result. The energy in a rotating frame is conserved if the external potential is constant in that rotating frame.

### 2.3.2 Time-independent Gross-Pitaevskii equation

We denote the eigenstates of the time-independent GP equation [for the case of a static potential  $V = V(\mathbf{r})$ ] as those states which satisfy

$$\frac{\partial \psi}{\partial t} = -i\mu\psi(\mathbf{r}), \quad (2.27)$$

for real  $\mu$ . The time evolution of an eigenstate  $\psi$  is simply a uniform rotation of the phase

$$\psi(\mathbf{r}, t) = e^{-i\mu t}\psi(\mathbf{r}), \quad (2.28)$$

where  $\psi(\mathbf{r})$  is  $\psi(\mathbf{r}, t)$  at time  $t = 0$ ; because the time evolution of  $\psi$  is known explicitly, we write  $\psi$  as a function of position only. Substituting Equation (2.27) into Equation (2.24) gives us the time-independent Gross-Pitaevskii equation

$$\mu\psi(\mathbf{r}) = [-\nabla^2 + V(\mathbf{r}) + C|\psi(\mathbf{r})|^2]\psi(\mathbf{r}), \quad (2.29)$$

where  $\psi(\mathbf{r})$  and  $\mu$  are the eigenfunction and eigenvalue respectively. The quantity  $\mu$  is commonly known as the chemical potential, although Morgan [72] has shown that this is the chemical potential of the condensate alone, not that of the larger system.

The lowest energy eigenstate, the ground state, has the same phase everywhere. Without loss of generality, we can write this eigenstate as being a real function. In an axially symmetric external potential ( $V = V_0$ ), the ground eigenstate is also axially symmetric. Condensates in axially symmetric potentials also have central vortex eigenstates with a phase circulation about the axis of symmetry (the  $z$  axis), which be written

$$\psi_v = \alpha e^{im\theta}, \quad (2.30)$$

where  $\theta$  is the usual azimuthal component of  $\mathbf{r}$  in the polar representation, and gives the angle around the axis of symmetry, and  $\alpha$  is independent of  $\theta$  and can be chosen to be real. These eigenstates have angular momentum of  $\langle L_z \rangle = m$  [20]. Due to the nonlinearity, it has so far proved impossible to find an analytical solution of Equation (2.29), and so we find these eigenstates numerically.

Dalfovo *et al.* [22] give a result, derived using the virial theorem, which relates  $E_k$ ,  $E_p$  and  $E_m$  [see Equation (2.22)] for any eigenstate of the time-independent GP equation. In two dimensions, this is given by

$$E_k - E_p + E_m = 0, \quad (2.31)$$

and in three dimensions by

$$2E_k - 2E_p + 3E_m = 0. \quad (2.32)$$

We make use of these identities to verify the accuracy of our numerical solutions of Equation (2.29), which we later use as starting points for our time-dependent simulations.

### 2.3.3 Thomas-Fermi limit

The Thomas-Fermi limit is an approximation where the term in Equation (2.29) containing  $\nabla^2$ , which represents the kinetic energy, is neglected. This approximation becomes increasingly accurate as the number of atoms in the condensate increases and the mean-field energy of the condensate dominates the kinetic energy. Under these circumstances, the time-independent GP equation can be solved analytically. This is a useful technique for estimating the



size and properties of all condensates in which the mean-field energy is large, and has been shown to be useful for a variety of calculations. Here we use it only to estimate the healing length and indicate the scaling properties of the speed of sound.

In the Thomas-Fermi limit, the probability density profile of the ground state of the condensate is given by

$$(|\psi(\mathbf{r})|^2)_{tf} = \frac{\mu_{tf} - V(\mathbf{r})}{C}. \quad (2.33)$$

In a harmonic trap ( $V = V_0$ ), the probability density is an (inverted) parabola in each dimension, the peak density is given by  $\mu_{tf}/C$ , the condensate has radius  $2\mu_{tf}^{1/2}$ , and in three dimensions has a half-width in the  $z$  direction of  $2\mu_{tf}^{1/2}/\lambda$ . For the harmonic traps we describe, the Thomas-Fermi chemical potential is given in two dimensions by

$$\mu_{tf} = \left( \frac{C}{2\pi} \right)^{\frac{1}{2}}, \quad (2.34)$$

and in three dimensions by [11]

$$\mu_{tf} = \left( \frac{15C\lambda}{64\pi} \right)^{\frac{2}{5}}. \quad (2.35)$$

Note that for both two and three dimensions,  $\mu_{tf}$  increases monotonically for increasing condensate number, as  $C \propto N$ .

### 2.3.4 Speed of sound and healing length

The speed of sound in a condensate can be obtained from the dispersion relation of the quasiparticle excitation spectrum (see for example [11, 34, 36]), and is

$$c_s = (2C|\psi|^2)^{\frac{1}{2}}. \quad (2.36)$$

For the centre of a Thomas-Fermi density profile, the speed of sound is given by  $(2\mu_{tf})^{1/2}$ , which increases with  $\mu_{tf}$ . For larger condensates, we thus expect a higher speed of sound at the centre. The healing length describes the distance over which a condensate, constrained to zero density at one point, recovers to

a homogeneous density (see for example [11, 24, 36, 22]). This length, a useful estimate of the size of a vortex, is given by

$$\eta = (C|\psi|^2)^{-\frac{1}{2}}. \quad (2.37)$$

As a rough guide, at near the centre of a Thomas-Fermi condensate, the healing length is given by  $\mu_{tf}^{-1/2}$ , and thus, for larger condensates, we expect shorter healing lengths.

## 2.4 Vortices

### 2.4.1 Phase

The crucial difference between a (mean field) condensate and a normal fluid is that the condensate has a well-defined phase (except where the density is zero). The phase of the complex mean field  $\psi$  is given by  $\arg \psi$ , and is many-valued, that is, the phase is only determined plus or minus a multiple of  $2\pi$ . When displaying our numerical results in figures, we always show the principal value of the phase  $\text{Arg } \psi \in (-\pi, \pi]$ , but it must always be held in mind that the true phase of the mean field is many-valued. It is from this feature of the complex mean field that the properties of vortices arise.

The phase circulation is the integral about a closed curve  $\sigma$  of the gradient of the phase of  $\psi$ . From the gradient theorem, taking account of the many-valued nature of  $\arg \psi$ , the phase circulation is

$$\int_{\sigma} (\nabla \arg \psi) \cdot d\mathbf{s} = 2\pi m, \quad (2.38)$$

where  $m$  is an integer. This means that tracing any closed path in the mean field, the phase will change by an integral multiple of  $2\pi$ . The velocity field of the condensate is given (for our choice of dimensionless quantities) by [91]

$$\mathbf{v} = 2\nabla \arg \psi. \quad (2.39)$$

The vorticity is [90]

$$\boldsymbol{\omega} = \nabla \times \mathbf{v} = \mathbf{0}, \quad (2.40)$$

and so the mean field is *irrotational*. A notable exception is where the density is zero; at these points the phase is undefined, as is the vorticity.

### 2.4.2 Vortices

In two dimensions, a vortex is a point about which the phase circulation is  $2m\pi$ ; as the path about the vortex core is reduced, the phase circulation remains the same, and so the gradient of the phase (to which the velocity is proportional) become large. Thus, to maintain a finite kinetic energy, the density at the centre of the vortex must be zero.

In three dimensions, vortices take the form of vortex lines (also known as vortex filaments), which are an extension of the two-dimensional phenomenon into three dimensions. If we consider any plane passing through a vortex line, then on that plane, the line behaves exactly as in two dimensions. The possible curvature and freedom of movement of a vortex line in three dimensions gives rise to additional dynamical behaviour, which we discuss in Chapter 7.

### 2.4.3 Properties of the circulation

Using Equation (2.40), Stokes' theorem, and the gradient theorem, any surface  $S$  (not necessarily simply connected) on which the phase is well-defined has a total phase circulation

$$\int_B (\nabla \arg \psi) \cdot d\mathbf{s} = \frac{1}{2} \int_S \boldsymbol{\omega} \cdot d\mathbf{A} = 0, \quad (2.41)$$

where  $B$  is the boundary of  $S$ . It is important to note that any vortices must be excluded from  $S$  for Equation (2.41) to hold.

We can understand the implications of Equation (2.41) by considering the two-dimensional case, where the total phase circulation about a region is given by the sum of the circulations of each of the vortices contained in the region. This is illustrated in Figure 2.1, in which we show some region of the field which contains three singly quantised vortices. In Figure 2.1(a), the surface  $S$  consists of the region with three small holes cut out, so  $S$  does *not* contain the vortices, and Equation (2.41) applies. Note that the line integrals over the inner parts of the boundary of  $S$  are made so as to keep  $S$  on the left-hand side of the direction of integration. We can thus deduce that the circulation of the whole region [as shown in Figure 2.1(b)] is simply the sum of the circulations of the enclosed vortices, in this case,  $2\pi[(+1) + (+1) + (-1)] = 2\pi$ .

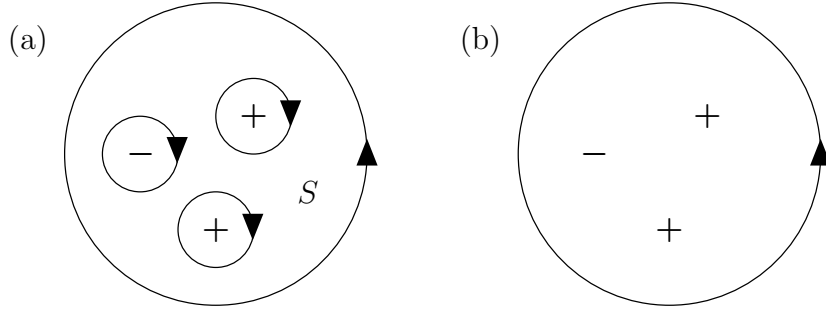


Figure 2.1: The circulation properties of a region of the mean field containing three singly quantised vortices. The outer circle bounds the region. In (a) the surface  $S$  of Equation (2.41) corresponds to the region *excluding* the three vortex containing holes, and the surface is multiply connected; the total circulation about the boundary (including the three inner edges) is zero. In (b) the circulation of the boundary is  $2\pi$ . Note that the paths we show here can be any simple closed paths; the circular shape we choose here is not significant.

An immediate and profound consequence of Equation (2.41) is that *a mean field containing no vortices has no circulation*. This is why a superfluid resists rotation; vortices must be formed before it can circulate. Similarly, a circulating superfluid will exhibit persistent flow until the vortices which permit the circulation are annihilated.

If we make the physically reasonable assumption that  $\psi(\mathbf{r}, t)$  is continuous in space and time, we expect that, if no vortices pass through the boundary of the region, the circulation about that region is conserved. This is because the circulation is quantised, and so any change in the circulation without a vortex passing through the boundary of the region would represent a discontinuous jump in the field. This does not, however, mean that the number of vortices in a region must remain fixed: two vortices of opposite circulation can be created or annihilated in pairs. For example, in Figure 2.1(b), one of the positive vortices could annihilate with the negative vortex, or a positive-negative pair could be created, all without changing the circulation of the region. We observe such dynamical behaviour in our simulations (see Chapter 5).

It is the requirement that the circulation around a region be preserved that gives vortices their curious robustness and particle-like behaviour: a single

vortex in a region cannot simply decay or otherwise disappear. Nothing in this analysis has removed the possibility of the region moving over time, so we can have a region follow a vortex like a spotlight, and without the entry of a vortex of the opposite sign into that region, the vortex will remain.

In three dimensions, we can choose a region on any plane (for example), and all of the properties we have described for two dimensions must hold in that region. An example of this is that two vortex lines which collide and annihilate must be antiparallel (parallel and of opposite circulation); a cross-section of such an event looks like vortices of opposite sign annihilating. We find in Chapter 7 that when two vortex lines collide, they become locally antiparallel.

#### 2.4.4 Example: central vortex eigenstate

As a concrete example of a vortex, we present in Figure 2.2 a central vortex state (in two dimensions), the  $m = +1$  eigenstate for that case. Of particular interest is Figure 2.2(b), in which the phase of the condensate is depicted. As we will show many of these phase images in this work, their interpretation is a matter of importance. Using the phase scale at the right (which runs from  $-\pi$  to  $\pi$ ), the phase circulation can clearly be seen. Lines of constant phase (not shown) would extend radially from the central vortex (at the origin). Starting at point A where the phase is 0 we follow a path of increasing phase to point B where the phase is  $\pi/2$ , and thence to point C where a phase discontinuity appears to occur. It must be remembered however, that the actual phase of the wavefunction is multivalued, and so the phase  $\pi$  near point C is actually equivalent to the adjacent phase  $-\pi$ .

Continuing along the path of increasing phase from point C, where the phase is equivalent to  $-\pi$ , to point D, where the phase is  $-\pi/2$ , and back to point A, we have completed a closed path with phase circulation of  $2\pi$ . This is the characteristic signature of a vortex. It can be seen that if we reduce the radius of the path about the origin, we eventually locate the vortex to a neighbourhood of the origin. In a similar manner, we can numerically detect vortices in a discretised representation by the examination of small closed paths. The symbol marked on Figure 2.2(a) is placed by such an algorithm, described in Section 3.6.

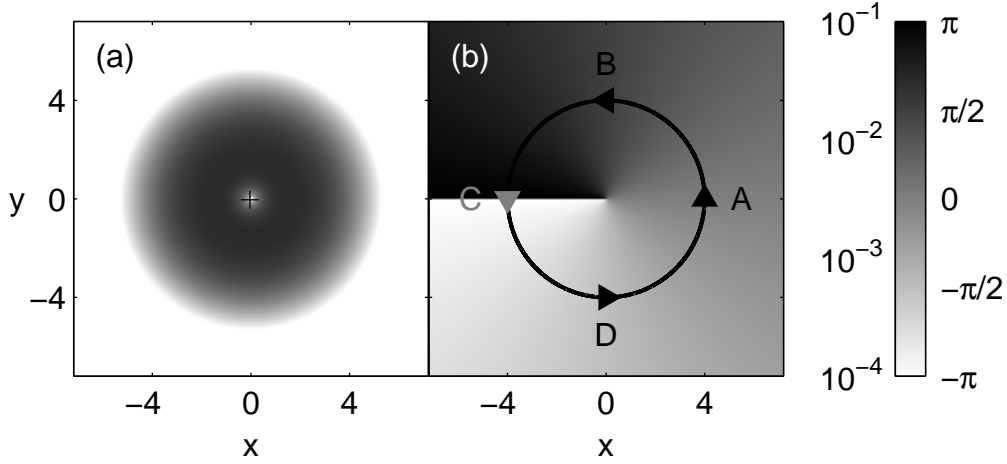


Figure 2.2: The  $m = +1$  central vortex eigenstate in two dimensions for  $C = 96.75$ , showing (a) probability density (left side of scale), and (b) phase (right side of scale).

It is worth noting that the apparent discontinuity of the phase at point C in Figure 2.2(b) is an artifact of the one-dimensionality of the greyscale. By comparison, a colour representation of phase which varies hue alone has no discontinuity [see for example Figure E.4(d)]. For ease of production of this thesis, and for the convenience of readers who cannot perceive colour, we present our results in greyscale in the body of this work. We provide alternative colour representations of selected figures in Appendix E.

#### 2.4.5 Vortices in the linear regime

There is a common misconception that vortices are a feature of only nonlinear systems, but this is incorrect. While nonlinear interaction may lead to the formation of vortices, and modify their shape by healing the condensate around the vortex core, a linear system is quite capable of supporting vortices. Vortices can readily be produced by interference, such as a travelling plane wave encountering a stationary Gaussian ground state (for an appropriate choice of parameters). Such effects are well known in linear optics.

We now give a concrete example of a vortex in a linear system. In the linear ( $C = 0$ ) limit, the GP equation reduces to the linear Schrödinger equa-

tion. We shall consider the two-dimensional symmetric harmonic trap, which is separable in the absence of a nonlinearity or asymmetric external potential to mix the two dimensions. That is, an eigenfunction  $\psi$  can be written as

$$\psi_{n_x, n_y}(\mathbf{r}) = A(n_x, n_y) \phi_{n_x}(x) \phi_{n_y}(y), \quad (2.42)$$

where  $\phi_{n_\alpha}$  is the eigenstate of the one-dimensional harmonic oscillator with quantum number  $n_\alpha \geq 0$ , and  $A(n_x, n_y)$  is a normalisation constant [20]. We can write an eigenstate with angular momentum expectation value  $\langle L_z \rangle = +1$  as a superposition of two eigenstates of the system,

$$\psi_v = \frac{1}{\sqrt{2}} (\psi_{10} + i\psi_{01}). \quad (2.43)$$

This is the central  $m = +1$  vortex eigenstate of the system, which we have produced by simply interfering two noncirculating eigenstates of the system. We note of course that the same solution can be obtained directly by separating the wavefunction in polar coordinates [20].

The energy of the each harmonic oscillator is given by  $E_\alpha = n_\alpha + 1/2$ , and so the total energy of the two-dimensional harmonic oscillator is  $E = n_x + n_y + 1$ . The difference in energy between the vortex eigenstate  $\psi_v$  and the ground ( $n_x = 0, n_y = 0$ ) eigenstate is one. We shall refer to this result in Section 6.6.1.

## 2.5 Light shift

Later in this thesis, we shall present simulations in which we manipulate a condensate with a Gaussian stirring potential. In this section, we show that an external potential  $W$  applied to the condensate (in addition to the harmonic trapping potential) can be produced by a far-detuned laser beam, and we quantitatively relate the potential to the beam intensity required. Such potentials have been used experimentally, for example, Andrews *et al.* [4] separated a  $^{23}\text{Na}$  condensate into two halves by using a sheet of far-blue detuned  $\text{Ar}^+$  laser light to insert a potential barrier in the middle of the condensate.

A fully stretched atomic transition behaves as a two level atom. An example of such a system is the 780 nm transition in  $^{87}\text{Rb}$  between the  $|5S_{1/2}, F = 2, m_F = 2\rangle$  and  $|5P_{3/2}, F = 3, m_F = 3\rangle$  hyperfine states, with the connecting

light field provided by a  $\sigma^+$  laser beam. This system was used in the first observation of Bose-Einstein condensation [3]. A two level atom in a resonant light field undergoes complete population cycling at a frequency known as the Rabi frequency; this quantity is a useful measure of the strength of effect the light has on an atom. The angular Rabi frequency  $\Omega_L$  of the stretched transition is [1, 21]

$$\Omega_L = -\frac{d}{\hbar}\mathcal{E}_L, \quad (2.44)$$

where  $d$  is the dipole matrix element for the stretched transition, and  $\mathcal{E}_L$  is the electric field amplitude of the light. The spontaneous decay rate  $\gamma$  of the upper state is given by [61, 95]

$$\gamma = \frac{\omega^3 d^2}{3\pi\epsilon_0\hbar c^3}, \quad (2.45)$$

where  $\omega$  is the natural (angular) frequency of the transition. This form allows us to eliminate  $d$ , and use instead the more convenient  $\gamma$ , which can be directly measured in an experiment. For the  $^{87}\text{Rb}$  case mentioned above,  $\gamma = 3.7 \times 10^7 \text{ s}^{-1}$  [47]. The intensity of the light is related to the electric field amplitude by [61]

$$I_L = \frac{1}{2}\epsilon_0 c \mathcal{E}_L^2, \quad (2.46)$$

and so, combining Equations (2.44)–(2.46), the Rabi frequency (squared) is

$$\Omega_L^2 = \frac{6\pi c^2 \gamma}{\hbar \omega^3} I_L. \quad (2.47)$$

The effect of a far-detuned field on a two level atom is to induce only extremely weak Rabi cycling [1], in effect shifting the energy of the ground state, while causing negligible population transfer. A far-detuned laser beam can thus be used to manipulate a condensate, because it does not scatter significantly or cause unwanted heating of the condensate. A resonant beam is instantly deadly to a condensate, and is used only in absorption imaging.

A convenient method for determining the energy shift of the ground level due to the presence of a far-detuned light field is to use the dressed state result (for example, see Cohen-Tannoudji *et al.* [21]). For a far-detuned light field, the



ground state can be considered to become the dressed state closest in energy to the ground state. The dressed states of a two level atom are separated in energy by

$$\hbar\Omega'_L = \hbar\sqrt{\Delta_L^2 + \Omega_L^2}, \quad (2.48)$$

where  $\Delta_L$  is the detuning (in angular units) of the light field from the atomic transition, and  $\Omega'_L$  is known as the effective Rabi frequency. Each dressed state is shifted the same amount from the unperturbed levels, which themselves are separated by  $\hbar\Delta_L$  in the dressed state picture. The effect of the far-detuned light field is to shift the ground state into the nearest dressed state, a change in energy given by

$$U_L = \hbar \frac{\sqrt{\Delta_L^2 + \Omega_L^2} - \Delta_L}{2} = \hbar \frac{\Delta_L}{2} \left( \sqrt{1 + \frac{\Omega_L^2}{\Delta_L^2}} - 1 \right). \quad (2.49)$$

For the case of large detuning,  $\Omega_L^2/\Delta_L^2 \ll 1$  and a Taylor series expansion (to first order) yields the shift in energy of the ground state of the atom, commonly known as the light shift,

$$U_L = \hbar \frac{\Omega_L^2}{4\Delta_L}. \quad (2.50)$$

Using Equation (2.47), we immediately obtain the light shift in terms of the intensity of the beam

$$U_L = \frac{3\pi c^2 \gamma}{2\omega^3} \frac{I_L}{\Delta_L}. \quad (2.51)$$

It is implicit that  $I_L$  may have a spatial dependence. Note that if the light field is far-blue detuned ( $\Delta_L > 0$ ), the light shift is positive and the condensate is repelled from the beam, while in the case of far-red detuning ( $\Delta_L < 0$ ), the light shift is negative and the condensate is attracted to the beam. The latter case has been exploited to make optical traps for condensates.

Given that our unit of energy is  $\hbar\omega_r$ , the effect of the light field on the dimensionless GP equation [Equation (2.24)] is given by an extra potential

$$W = \frac{3\pi c^2 \gamma}{2\hbar\omega_r\omega^3} \frac{I_L}{\Delta_L}, \quad (2.52)$$

which is included as part of the total external potential  $V$ . This expression allows us to relate the potential with which we perturb a condensate to the intensity of the laser beam, as we do in Chapter 7.



# Chapter 3

## Numerical techniques

### 3.1 Introduction

In this chapter, we describe the computational techniques which we have developed in the course of this work. These include efficient implementations of a numerical method to solve the time-dependent GP equation, both in two and three dimensions, and a robust algorithm for detecting vortices in the mean field wavefunction. Our algorithms are implemented in the Matlab, Python, and C programming languages.

The time-dependent GP equation is a type of nonlinear Schrödinger equation (NLSE), a nonlinear partial differential equation. The effect of the nonlinearity in the GP equation is to couple excitations at different frequencies [86] and in different modes [23]. There are, in general, no exact analytical solutions for this equation, and even the steady state [Equation (2.29)] requires numerical solution [29]. While some approximate analytical results have been found, such as the frequencies of collective excitations in the hydrodynamic regime [91], the full behaviour of the GP equation is revealed only by numerical solution. To explore the dynamics of vortices in condensates, we start with some initial condition (such an eigenstate of the condensate), and simulate an experiment (for example, stirring the condensate with a Gaussian laser beam) by numerically solving the GP equation.

The vortices that we find in our simulations can be readily identified by manually examining images of the phase of the condensate, but this is a la-

borious task. We enhance our ability to depict and interpret the mean field by automating the process of vortex detection. Instead of displaying both the probability density and phase of the condensate, we can show only the probability density, marked with the position and sign of the vortex cores.

In Chapter 6 we will introduce a nonlinear two state model to describe the dynamics of a rotationally stirred condensate, and we defer until then our description of the numerical methods we have developed to solve that model.

## 3.2 Discretisation of the mean field

Fundamental to our methods is a discretisation of the mean field wavefunction on an equispaced position basis. The wavefunction  $\psi(\mathbf{r}, t)$  is represented in two dimensions by  $\psi_{ij}$  corresponding to positions  $(x_i, y_j)$ , and in three dimensions by  $\psi_{ijk}$  on positions  $(x_i, y_j, z_k)$ . Each index  $i$ ,  $j$ , or  $k$  increases for increasing values of  $x$ ,  $y$ , or  $z$  respectively. We specify the form of the computational grid in each dimension as a range  $R_\alpha$  (also known as the spatial extent) and number of points  $N_\alpha$  for the  $\alpha$  direction. The position basis is centred on zero in each dimension and spans the range, for example,  $x_i$  runs from  $-R_x/2$  to  $R_x/2$  in steps of  $R_x/(N_x - 1)$ . We always choose each  $N_\alpha$  to be a power of two, so that we may employ efficient Fast Fourier Transform spectral techniques. We note that no point has any of  $x_i$ ,  $y_j$ , or  $z_k$  equal to zero; when we refer to a point as being on, say, the  $z = 0$  plane, we actually use the nearest plane of grid points parallel to that plane. This centring of the grid gives us convenient four-fold rotational symmetry about the  $z$  axis of the harmonic trap. We denote the difference in position between two grid points in the  $x$  direction by  $\Delta x$ , and likewise for the other dimensions.

### 3.2.1 Presentation of data

In two dimensions, we display the probability density of the wavefunction as an image using a logarithmic scale, which permits both the convenience and clarity of consistent limits, but also, by Beer's law, mimics the optical depth characteristics of absorption imaging (without saturation or Zeeman effects)

[66, 74]. We also display the principal phase (using a linear scale) to permit manual identification of vortices. Our images are produced in Matlab [71] using that package's various image and colour manipulation commands, such as `image` and `colormap`.

In three dimensions it is possible to visualise the condensate states with the same techniques as in two dimensions, but now applied to different cross-section planes of the condensate. However, to more readily capture the three-dimensional form of the condensate, we usually choose to show probability density isosurfaces and vortex lines. A probability density isosurface is a surface of constant probability density.

### 3.3 Solution of the Gross-Pitaevskii equation

#### 3.3.1 The RK4IP algorithm

The numerical method central to our investigations is that used to propagate the wavefunction  $\psi$  in time, according to the time-dependent Gross-Pitaevskii equation. We call this method the Fourth-Order Runge-Kutta in the Interaction Picture (RK4IP) algorithm. The basic algorithm has been developed by Ballagh [7] and by Fox *et al.* [39]. The method is essentially a close cousin of the symmetrised split-step method used in optics to solve the nonlinear Schrödinger equation (NLSE). Wall [96] makes comparisons between the RK4IP algorithm and other methods. Drummond [27] discussed some of the issues involved in using Fourier propagation methods, including the use of apodisation (filtering), which we do not use in this work. Krüger [56] makes a number of observations on the algorithm, generalises our two-dimensional implementation to a condensate in two hyperfine states, and implements apodisation to absorb the untrapped component which is outcoupled by a radio-frequency field.

The novel feature of the present work is that it uses a highly efficient implementation of the RK4IP algorithm, optimised to minimise memory usage and bandwidth, which has made possible the first use of this algorithm in three dimensions, and the first time-dependent full-three-dimensional propa-

gation of the GP equation on commodity PC computer hardware [18]. This general three-dimensional implementation does not rely on any symmetries of the system to reduce the computational dimensionality.

To perform our calculations, we have used commodity PC computers of the Intel x86 family, running under the GNU/Linux operating system. Our two-dimensional simulations were performed mainly on single-processor Pentium Pro 200 MHz machines with 96 MB of memory, while our three-dimensional simulations were performed on dual-processor Pentium III 450 MHz machines.

### 3.3.2 Runge-Kutta in the interaction picture

We transform the GP equation into an interaction picture to separate the effect of diffusion (which links spatial points) from the nondiffusive terms (which act only locally), allowing us to solve the equation as if it were an ordinary differential equation. The time-dependent GP equation can be written

$$\frac{\partial \psi}{\partial t} = -i[D + N]\psi, \quad (3.1)$$

where the operators

$$D = -\nabla^2, \quad (3.2a)$$

$$N(t) = V(t) + C|\alpha|^2, \quad (3.2b)$$

give the diffusive and nondiffusive parts respectively. In Equation (3.2b),  $\alpha$  is the wave upon which  $N$  operates; for example,  $\alpha = \psi$  in Equation (3.1). The operator  $D$  is a linear operator, while the operator  $N$  is in general nonlinear. The potential  $V$  will in general depend on both  $\mathbf{r}$  and  $t$ , but in our notation we neglect the spatial dependence of  $V$  for clarity. It is essential, however, to record the time dependence of  $V$  and  $N$ . We choose to write  $\psi$  in an interaction picture defined by

$$\psi_I = e^{+i(t-t')D}\psi, \quad (3.3)$$

where  $t'$  is the time the interaction picture separates from the normal picture. It is worth noting that as  $D$  is a linear operator, the operator exponential in

Equation (3.3) is also linear. The evolution of  $\psi_I$  is given by

$$\frac{\partial \psi_I}{\partial t} = -iN_I\psi_I, \quad (3.4)$$

where

$$N_I = e^{+i(t-t')D} N e^{-i(t-t')D}, \quad (3.5)$$

is the nondiffusion operator in the interaction picture. Equation (3.4) has the same form as a system of ordinary differential equations with time as the independent variable; all coupling between the spatial points is now contained in  $N_I$ . The system of equations can now be solved by a variety of methods, but we choose to implement a fourth-order Runge-Kutta, which is known to have a high performance for a given computational cost, and furthermore has midpoints which allow us to make half of the exponential transformations in Equation (3.3) vanish with an appropriate choice of  $t'$ . These optimisations, and the precise form of the numerical method, are detailed in Section B.1. We implement the numerical method for two dimensions in Matlab [71], and also a highly optimised implementation for two and three dimensions in Python [84] (although we have only used the latter in three dimensions).

The fourth-order Runge-Kutta (see for example [78]) is one of the early workhorses for the numerical solution of ordinary differential equations. This method is often, and rightly, replaced by more modern methods with adaptive step-size control, such as Runge-Kutta-Fehlberg methods. However, the fourth order method can be implemented to have very low memory consumption (as we show in Section B.3), which is an important feature because of the large storage requirements of the problem. Ease of implementation and the advantageous position of the midpoints erode any benefits of the Runge-Kutta-Fehlberg methods, but the lack of automatic step size adaptation means care is required to select a sufficiently small temporal step size. An advantage of using Runge-Kutta methods over multistep methods, which improve accuracy by “remembering” values of the solution at earlier times, is that we can make nonsmooth or even discontinuous changes to the external potential  $V$  at the beginning of any step and retain the accuracy of the method.

Our two-dimensional simulations are carried out on a  $512 \times 512$  point grid with range  $40 \times 40$ . Typically, our time step size is  $\pi/500$ , and this step size

$\lambda$	$N_x \times N_y \times N_z$	$R_x \times R_y \times R_z$
$\sqrt{8}$	$128 \times 128 \times 64$	$30 \times 30 \times 15$
1	$128 \times 128 \times 128$	$30 \times 30 \times 30$
1/3	$64 \times 64 \times 128$	$25 \times 25 \times 50$

Table 3.1: Computational grids used in our three-dimensional simulations, showing the number of points and the spatial extent of each grid.

is used for the simulation shown in Figure 5.1. However, for the  $C = 88.13$  single vortex cycling shown in Figure 5.4, a step size of  $\pi/250$  is satisfactory. By contrast, for the  $C = 200$  single vortex cycling [9], a step size of  $\pi/500$  is essential to maintain numerical stability to  $t = 24\pi$ . In three dimensions, we invariably use a temporal step size of  $\pi/500$ . The computational grid is chosen appropriately for the trap anisotropy, and is given in Table 3.1.

### 3.3.3 Fast Fourier Transform

A key component of our implementation is the use of the Fast Fourier Transform (FFT) [78] to efficiently calculate the diffusion exponential (detailed in Appendix C). To gain speed of computation, we have tried various strategies, including our own FFT implementations in C and in hand-optimised assembly language. For an extensive discussion of the various types of implementation of the Fast Fourier Transform, and the computational issues that arise, see van Loan [60]. We have found, however, that “The Fastest Fourier Transform in the West” (FFTW) by Frigo and Johnson [40] yields consistently better results than even our most highly optimised assembly language. This library, instead of having a single highly optimised algorithm, dynamically adapts itself to the computer hardware for each grid shape. Furthermore, this dynamic optimisation is based on actual timing and includes the effect of memory bandwidth limitations, which our hand-optimised implementations do not consider.

From within Python, the facilities of the FFTW library are accessed transparently using code written in C known as a “wrapper”; this code, originally written by others, is distributed with the FFTW library. We have extended



the existing wrapper to give access to the multithreading capabilities of the FFTW library from within Python. This allows an individual FFT calculation to be executed in parallel on both processors of our dual Pentium III systems. This is known as dual threaded operation of the algorithm, but we emphasise that only the FFT calculations use multithreaded operation in our current Python implementation.

In our Matlab implementation, the FFT operations consume (typically) 55% of the computational time, even though we use the slow FFT implementation supplied with Matlab. In Python, we use FFTW (which is roughly twice the speed even singly-threaded); we also reduce the cost of the other parts of the algorithm until the time spent performing FFT operations increases to 70% of the total computational time. These large proportions confirm the importance of an efficient FFT implementation in achieving good performance of our algorithm, and also why our careful choice of the interaction time  $t'$  to eliminate four calculations of the diffusion exponential is important.

### 3.3.4 Optimised implementation in Python

The speed at which a computer can perform calculations is limited not only by the performance of its processor, but also by the ability of its memory subsystem to feed the processor with requested data; this capability is known as *memory bandwidth*. Contemporary computers have been marked by an explosive growth in the speed of their processors, and the availability of computers with multiple central processing units (such as our dual Pentium III machines). The performance of memory subsystems has not matched the growth in processor power, and so calculations can become limited by the available memory bandwidth, rather than processor performance.

We find that the performance of our algorithm given by Equations (B.10) is limited by memory bandwidth, and in fact the time taken for each full step is easily predicted by totalling the temporary working space used. We roughly quadruple the performance of our algorithm by minimising the number of temporary variables that are used, and performing operations in-place and unrolled across the wavefunction, as we now describe. An in-place operation on a large array modifies the array directly, rather than placing the result of

the operation in a second array of the same size, and so in-place operations reduce the memory used and memory bandwidth consumed. As the semantics of the Matlab language prohibit in-place modification of an argument of a function, we implement our most efficient form of the algorithm in Python [84] using the Numerical Python package [5]. The Python language, in addition to being more expressive than Matlab, also permits an array passed to a function to be modified in that function without allocating extra storage. We detail the Python implementation in Section B.3. We also write a number of core operations in C to allow the unrolling of operations across vectors (the opposite of “vectorisation”) to further reduce memory bandwidth consumption; this C code is readily accessed from within Python.

A key performance optimisation is the minimisation of the number of temporary variables (those that are large arrays) to reduce the memory bandwidth consumed by the algorithm. A  $128 \times 128 \times 64$  computational grid stored in complex double precision (16 bytes per grid point) requires 16 MB of memory, while a  $256 \times 256 \times 128$  grid requires 128 MB. The three large arrays ( $\psi$ ,  $\psi_I$ , and  $\psi_K$ ) that our efficient Python implementation uses occupy a total of 48 MB or 384 MB memory for the two cases respectively. The less efficient Matlab implementation (if it were extended to three dimensions) would use roughly four times the memory of the Python implementation.

### 3.3.5 Implementation performance

Much of our computational work in two dimensions was performed on single-processor Pentium Pro 200 MHz systems with 96 MB of memory. On these systems, the  $512 \times 512$  grid can be advanced in 18 s per step. Our Python implementation is also capable of solving the two-dimensional problem, and is significantly more efficient than our best Matlab implementation. On our dual Pentium III 450 MHz machines, using a  $512 \times 512$  grid, the Matlab implementation takes 8.0 s per step and requires 60 MB, while the Python implementation achieves 2.3 s per step in 14 MB. If we use dual-threaded operation for FFTW in Python, this is further reduced to 1.9 s. We see that the faster hardware gives an improvement of (roughly) a factor of two, while our algorithmic optimisations yield another factor of four, for an eightfold

increase in the speed of the calculation. The Python implementation uses less than a quarter of the memory of the Matlab implementation.

In three dimensions, for a  $128 \times 128 \times 64$  grid, our Python implementation requires 11 s per step (7.8 s dual threaded) and performs the calculation in 50 MB of memory. For example, each curve of Figure 7.2 (propagation to  $32\pi$  in 16000 steps) requires 34 hours in dual threaded operation. With only a single thread, this increases to some 50 hours. The  $128 \times 128 \times 128$  grid used in the spherical trap ( $\lambda = 1$ ) simulations takes 22 s per step (single threaded) using 100 MB of memory, which corresponds to 50 hours to propagate to  $t = 16\pi$  (in 8000 steps). As we have performed many simulations to explore a wide range of parameters, the time required to complete the calculations is significant, representing many weeks of solid computation.

Our dual Pentium III machines have 512 MB of memory, and it is possible to perform a simulation on a  $256 \times 256 \times 128$  grid, which uses 390 MB of memory. This represents a doubling of the resolution in each dimension of our  $\lambda = \sqrt{8}$  grid. Such a simulation requires 68 s per step for dual threaded operation. We have not yet applied this high resolution capability to physical problems, but these benchmarks indicate that our implementation scales very well, taking a time approximately proportional to the number of points in the computational grid.

### 3.3.6 Data storage

While the RK4IP algorithm has been applied successfully in one dimension with a few thousand spatial grid points [8, 10], the storage demands of the two and three-dimensional problems place a large constraint on the investigation. For example, while 8192 points can be enough for a high fidelity one-dimensional simulation, a  $512 \times 512$  simulation in two dimension has 262,144 points, and a  $128 \times 128 \times 64$  simulation has 1,048,576 grid points. Given that a double precision complex number occupies 16 bytes of machine storage, storing 800 frames<sup>1</sup> for later analysis from a single  $128 \times 128 \times 64$  simulation would require 12.5 GB of storage. At the time that these simulations were performed,

---

<sup>1</sup>By analogy with a movie, we call a snapshot of the full wavefunction a frame.

this was approximately the entire capacity of a commodity hard disk drive.

To make data storage practical, we save only the central half of the grid points in each dimension, and so in two dimensions, our storage requirements are divided by four, and in three dimensions divided by eight. This is a suitable technique because in our simulations the condensate remains close to the centre of the trap. Furthermore, we store our data in single precision (8 bytes per complex number), halving our data storage requirements. This lower precision is satisfactory because the data is used only for analysis, not propagation.

### 3.3.7 MPEG-1 movies

As a compact, portable, and standardised means of presenting the time evolution of our simulations, we can render them as MPEG-1 format movies. We plot the frames of the simulation and save the plots as sequentially numbered high-quality JPEG images, and then use an external tool (`mpeg_encode` from the Berkeley MPEG Tools package) to convert this sequence into an MPEG-1 movie. It is worth noting that we pad the number of frames with title frames (we use at least ten to identify the movie) at the beginning so that we have  $3n + 1$  movie frames ( $n$  an integer) so that we may use the superior performance “IBBPBBPBBPBB” MPEG encoding pattern. For example, 300 MB of stored data in 601 frames (padded to 613 frames with title frames) can be converted into a 1.6 MB colour MPEG movie showing the probability density for the same situation as in Figures 5.1–5.3 from  $t = 0$  to  $t = 12\pi$ . In this way, we can represent our simulations in a format which can be readily downloaded and displayed using any viewer supporting this standard format. Our MPEG movies are an expressive means of conveying the dynamical features of our simulations.

## 3.4 Validity of numerical solutions

We ensure the validity of our numerical solutions by monitoring the conservation properties of the GP equation given in Appendix A, and also by ensuring that violations of the Nyquist limit do not occur in our spectral method. For

example, in the single vortex cycling regime presented in Figure 7.2, after the simulation has continued to  $t = 32\pi$ , the normalisation of the wavefunction has fallen from unity by only  $4.95 \times 10^{-6}$ . Once the stirrer has been fully inserted (at  $t = \pi$ ), the energy in the rotating frame  $E'$  (which we expect to be conserved) fluctuates (peak to peak) by  $4.02 \times 10^{-4}$  about a mean of 7.398, a relative fluctuation (peak to peak) of only  $5.43 \times 10^{-5}$ . We achieve this high degree of conservation even though we calculate this energy only on the stored grid, having discarded the other seven eighths of the full grid used for the computation.

Three parameters are important in determining the successful numerical propagation of the field. These are the temporal step size of the RK4IP algorithm, the spatial extent of the discretised computational grid, and the spacing between the spatial grid points (which is related to the spatial extent by the number of points in that dimension).

The temporal evolution of an eigenstate is a pure rotation of phase [see Equation (2.28)]. For an explicit numerical method (such as the fourth-order Runge-Kutta) to be able to follow such a rotation, the temporal step size  $\Delta t$  must be small enough that the angle through which the phase rotates per step is small. We can use the Thomas-Fermi chemical potential to estimate this for the ground state of the condensate, giving

$$\Delta t \ll \mu_{tf}^{-1}, \quad (3.6)$$

as a requirement for successful numerical solution.

The spatial extent and grid spacing are intrinsically connected. We use discrete Fourier techniques to evaluate spatial derivatives, and these are the only element of the GP equation connecting spatial points. We transform between a position and momentum representation of the field, and the spatial extent and grid spacing give us limits of the maximum width of the condensate that our model can represent. From the periodicity in space of the discrete Fourier transform, we really model an infinite array of identical condensates, and we must prevent them from interacting by using a sufficiently large spatial extent. We can estimate from the Thomas-Fermi profile the constraints on the

spatial extent needed to successfully propagate a ground state as

$$R_{x,y} \gg 2\sqrt{\mu_{tf}}, \quad (3.7a)$$

$$R_z \gg 2\sqrt{\mu_{tf}}/\lambda. \quad (3.7b)$$

However, it must be understood that the particular type of simulation can stretch these requirements considerably. For example, vigorous rotational stirring with a wide stirrer can throw large amounts of the condensate towards the edge of the computational grid. We store for later analysis the central half in each dimension of the spatial grid; if any nonnegligible amount of the condensate leaves this region, we consider the normalisation criterion to have been broken. This very conservative approach gives us a spatial buffer of one half of the extent in each dimension between the space we are interested in and its Fourier-periodicity image.

Similar considerations apply for the momentum representation. The grid spacing must be sufficiently small to properly represent sharp variations in the field, particularly vortices: this is the same as saying that our momentum representation must have a sufficiently large extent. The Nyquist limit [78] implies that a wave is fully represented by a discretised sampling if the sampling interval is less than half the wavelength of the shortest wavelength component of the wave. We can use the healing length (which gives us an approximation of the half-width of a sharp feature) to directly estimate the requirement on the grid spacing in the  $x$  direction as

$$\Delta x \ll \mu_{tf}^{-1/2}, \quad (3.8)$$

and the same requirement applies to  $\Delta y$  and  $\Delta z$  (this is why we choose these quantities approximately the same). We discuss the Nyquist limit in more detail in Section 3.4.2.

### 3.4.1 Time-reversal of simulations

As a robust test of the temporal step size, we start from the final state  $\psi_f$  of a simulation and run our simulation in reverse. We then compare the initial condition  $\psi_i$  to the reconstructed initial condition  $\psi_r$ , which for a perfect numerical method should be identical. Because the fourth-order Runge-Kutta

is not symmetric in the independent variable (time in our case), this reconstruction is not accurate if the step size is too large. As a test of the accuracy of the reconstruction  $\psi_r$ , we compare it against the initial condition  $\psi_i$  by calculating: (a) the normalisation error  $\int |\psi_r|^2 d\mathbf{r} - 1$ , (b) the integral of the density error magnitude  $\int |(|\psi_r|^2 - |\psi_i|^2)| d\mathbf{r}$ , and (c) the integral of the density weighted phase error magnitude  $\int |\psi_i|^2 |\text{Arg}(\psi_r/\psi_i)| d\mathbf{r}$ . For perfect reconstruction, these diagnostic quantities are all zero. In general, we find that the diagnostic quantities are very small for the simulations that we have reversed; in practice we have found that the normalisation of  $\psi_f$  (the *unreversed* normalisation) is a good predictor of our ability to reverse the simulation, and we typically monitor this quantity rather than reverse all of our simulations. We find that if the temporal step size is too large, the normalisation of the final wavefunction  $\psi_f$  is wrong (typically too small): we have not found a case where  $\psi_f$  had an accurate normalisation in a simulation that could not be successfully reversed. We note that violations of the Nyquist limit (caused by using too sparse a spatial grid) do not cause a loss of normalisation, and indeed are not necessarily detected by the time-reversal technique. Thus the Nyquist criteria must be monitored separately, as we now discuss.

### 3.4.2 The Nyquist limit

We use small temporal step sizes and large spatial extents to easily satisfy the requirements of our numerical method. The most difficult test of our method is given in Chapter 7, and in particular, the stirring of a  $C = 1000$  oblate ( $\lambda = \sqrt{8}$ ) condensate to generate single vortex cycling. This combination of  $C$  and  $\lambda$  gives a ground state of the trap with  $\mu = 8.95$ , which is one of the highest chemical potentials we have used, and so we expect the healing length to be one of the shortest of our investigations. In this case the grid spacing is 0.24, while the Thomas-Fermi estimate of the healing length is 0.34, and so although the grid spacing is less than the healing length, it is not very much less, so we apply numerical tests to verify our results. As a robust test of the Nyquist criterion, we repeat this simulation, halving the number of points in each dimension to  $64 \times 64 \times 32$ . We find that the solution is indistinguishable from the first (except for a very small divergence  $\langle L_z \rangle$  in at the very end of the

simulation). This is extremely strong numerical evidence that this simulation is within the Nyquist limit.

To investigate the effects of violating the Nyquist limit, we halve the number of points in each dimension again, to  $32 \times 32 \times 16$ , and this time the simulation diverges from the higher resolution simulations into a completely different type of dynamical behaviour, which is reflected in the evolution of  $\langle L_z \rangle$ . Instead of single vortex cycling, a vortex enters the condensate and orbits the centre. Despite this divergence, the normalisation is still well preserved, and the energy in the rotating frame  $E'$  (which should be conserved) increases only slightly, from 7.399 at  $t = \pi$  (when the stirrer is fully inserted) to 7.434 at  $t = 32\pi$  (an increase of 0.47%). Furthermore, the simulation can be run backwards to reconstruct its initial condition, with all of the reconstruction diagnostic quantities very much less than one; by far the largest is the phase diagnostic of 0.057, which is not unreasonable for such a long simulation. Halving or doubling the temporal step size has no effect on the outcome, and gives the same (but incorrect) evolution of  $\langle L_z \rangle$  with time. This finding demonstrates the insidious nature of violations of the Nyquist criterion: too small a grid spacing places a constraint on the system which subtly modifies the dynamics, cannot be easily detected by its effects on conserved quantities, and cannot be remedied by changing the step size (so adaptive step size Runge-Kutta methods give no advantage).

The only way to directly detect Nyquist limit violations is to monitor the high frequency components of  $\psi$ , and we do so after a simulation has run by analysing the saved portion of the grid (this has the effect of doubling the spacing of the grid points in momentum space). We examine the momentum representation of  $\psi$ , which we find using the discrete Fourier transform. We take the highest density at the Nyquist momentum, which is the highest density on any point on the edge of the grid in momentum space, and denote this density  $\mathcal{P}$ . A uniform momentum distribution with the same normalisation as the actual momentum distribution has a momentum density at each grid point that we denote  $\mathcal{P}_u$ . We write  $\mathcal{P}$  relative to  $\mathcal{P}_u$  as  $\mathcal{P}_r = \mathcal{P}/\mathcal{P}_u$ . This technique counters scaling effects which dilute  $\mathcal{P}$  for high spatial resolution computational grids. The relative density  $\mathcal{P}_r$  (for the largest density on the



edge of the momentum grid) is a valuable quantitative measure of the degree of violation of the Nyquist limit. When we compare the failed simulation above with the successful simulations (and our other simulations), we note a large jump in  $\mathcal{P}_r$  (two orders of magnitude) for the invalid simulation over the valid ones. This is the distinctive signature that the failed simulation has violated the Nyquist limit. In momentum space, the condensate has reached the edges of the momentum representation and is beginning to interfere with the other “virtual” condensates, which are present because of the periodicity of the discrete Fourier transform. The fact that our other simulations do not have this signature gives us confidence that they are not Nyquist limited.

### 3.5 Eigenstates

Eigenstates of the condensate are a natural choice of initial condition for many of our simulations. We find these eigenstates using efficient optimisation techniques, in which we specify a particular  $C$  and calculate  $\psi$  and  $\mu$  constrained by the normalisation condition<sup>2</sup>. In two dimensions with a symmetric trap (in the absence of a Gaussian stirrer), we find the ground and vortex eigenstates by the same method described in Section 6.4.2, but using  $n_v = 0$  or  $n_v = 1$  respectively.

High fidelity eigenstates have been calculated for us by P. B. Blakie, using efficient conjugate-gradient optimisation techniques [13]. These have included full two-dimensional ground eigenstates in the presence of a Gaussian stirrer (used as initial conditions in Chapter 5), and axially symmetric three-dimensional ground and vortex eigenstates of the harmonic trap (used as initial conditions in Chapter 7). We use interpolation techniques to transfer these eigenstates from cylindrical coordinates onto our Cartesian grid. The eigenstates are verified by independently calculating their chemical potential and normalisation, by propagating them, and by applying the virial theorem

---

<sup>2</sup>A few of our calculations of eigenstates were performed using numerical damping techniques or other types of optimisation; for those calculations, a target  $\mu$  was specified and  $C$  and  $\psi$  were calculated, so these eigenstates have values of  $C$  which are not whole numbers. We now exclusively use the more efficient optimisation methods we describe.

identity.

### 3.6 Vortex detection

Vortices in a complex wavefunction are characterised by a phase circulation about the vortex core, and also by a positive curvature of the probability density. In this section, we describe a numerical vortex detection algorithm which we have used to locate vortices in the mean field wavefunction  $\psi$ , and which is suited to an efficient implementation. The algorithm not only locates vortices, but also determines their sign and multiplicity.

The bulk of a trapped condensate lies in the centre of the trap where the probability density is high; this central mass is surrounded by regions of very low density. Where the density is very small, the wavefunction has little physical significance; it is as if the condensate was not there. Furthermore, the wavefunction in these very low density outlying areas is dominated by tiny high frequency excitations and so the phase in these low density regions fluctuates wildly; this has no physical implications, as phase without significant density is meaningless. However, because our vortex detection algorithm relies on phase, we must exclude the low density regions where the phase is uninteresting, or the algorithm will detect vast numbers of “noise” vortices. We do this by imposing an arbitrary density curvature threshold on the vortex detection algorithm, to exclude the low density “noise” in which we are not interested. We can see the condensate as being surrounded by an “Oort cloud” of low density vortices; unlike He II in which homogeneous density makes all vortices important, in trapped alkali condensates, vortices are only important if they are near regions of significant density.

In two dimensions, the algorithm examines the entire discretised wavefunction, but in three dimensions we only examine a single plane (parallel to the  $z = 0$  plane) at a time. All the points of the plane wavefunction are examined except for those on the edge. The operation of the algorithm is to take the wavefunction  $\psi$  and calculate a vortex detection array  $\mathcal{V}$ . If  $\mathcal{V}_{ij} = m$  is nonzero, that indicates that the algorithm has found a vortex of circulation  $2\pi m$  near  $(x_i, y_j)$ ; otherwise, no vortex was found.

We express the vortex detection algorithm conceptually in terms of phase unwrapping. However, in Section 3.6.2 we describe an elegant form of the algorithm which counts phase jumps and is formally equivalent to the phase unwrapping approach.

### 3.6.1 Phase unwrapping

When we calculate the principal phase of the wavefunction, we have lost information about how the phase at a grid point is related to the phase at adjacent points, because the mapping of the continuous phase  $\arg \psi$  onto  $(-\pi, \pi]$  in calculating the principal phase  $\text{Arg } \psi$  introduces discontinuous jumps in the phase. If, for example, we follow the circulation of phase around an  $m = +1$  vortex, the phase will jump at some point from just below  $\pi$  to just above  $-\pi$ . The process of reconstructing the phase circulation around a path is known as phase unwrapping.

The vortex detection algorithm considers a single grid point of the discretised wavefunction at  $(x_i, x_j)$  and determines the phase circulation about that point by examining the eight adjacent points, as shown in Figure 3.1. The algorithm starts and ends at point 1, following the direction indicated. First, the principal phase  $\phi_p = \text{Arg } \psi$  at every point  $p$  is calculated. Considering every sequential pair of points, the algorithm adjusts the phase of the second point by adding an integral multiple of  $2\pi$  to the phase so that the difference in phase between the two points is less than  $\pi$ . After making eight comparisons (for eight sequential pairs), the algorithm has returned to point one. The phase circulation is then given by the new phase at point 1 minus the original principal phase at point one  $\text{Arg } \psi_{(i-1)(j-1)}$ . We can then find  $\mathcal{V}_{ij} = m$  by dividing the phase circulation by  $2\pi$ .

Figure 3.2 gives two examples of the operation of the phase unwrapping procedure. For the case shown in Figure 3.2(a), a single phase jump is present at A, which when unwrapped, yields Figure 3.2(c) and the phase circulation is  $2\pi$ . In Figure 3.2(b) there are three jumps, at B, C, and D, and when these are removed we see in Figure 3.2(d) that the phase again has a circulation of  $2\pi$ . The vortex detection algorithm would thus assign  $\mathcal{V}_{ij} = +1$  to denote a positive vortex detected in the vicinity of  $(x_i, y_j)$ .

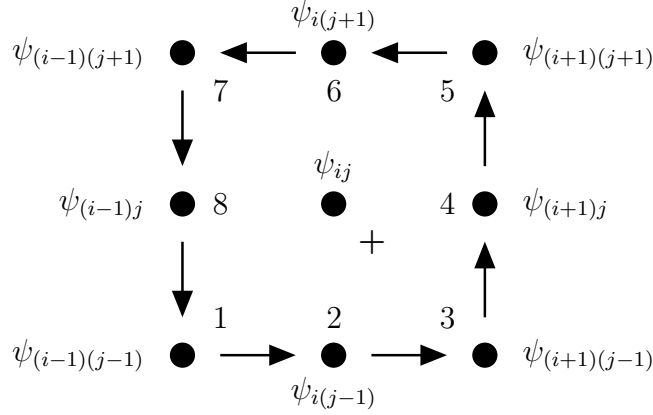


Figure 3.1: Grid points considered by the vortex detection algorithm. The central point (where the wavefunction is  $\psi_{ij}$ ) is the point under examination, and the phases of all adjacent points are considered. The numerals identify the eight outer points. The single + illustrates a hypothetical vortex core (for the continuous wavefunction).

The algorithm we describe examines the phase by considering eight phase changes. Because of the need to detect the sense of the circulation, each change in phase between two points considered must be smaller than  $\pi$  or it cannot be distinguished from a smaller phase change of the opposite sense. With eight intervals to consider, this gives  $8\pi = 4 \times 2\pi$  or the circulation of an  $m = \pm 4$  vortex as the unreachable upper bound. Changes of  $\pi/2$  between points are comfortably detected, and so we see that the  $4\pi = 2 \times 2\pi$  or the circulation of an  $m = \pm 2$  vortex is a more reasonable limit. There is no reason why the local eight-point circulation techniques cannot detect an  $m = \pm 3$  vortex.

### 3.6.2 Phase jump counting

The most elegant form of the vortex detection algorithm combines the generality of the phase unwrapping concept with simplicity and efficient implementation. This form of the algorithm merely counts the jumps in the principal phase for each step shown in Figure 3.1 and adds them according to their sign, counting +1 for every negative jump of magnitude larger than  $\pi$ , and -1 for every positive jump of magnitude larger than  $\pi$ . This algorithm is identical in effect to the phase unwrapping we have described: instead of adding multiples

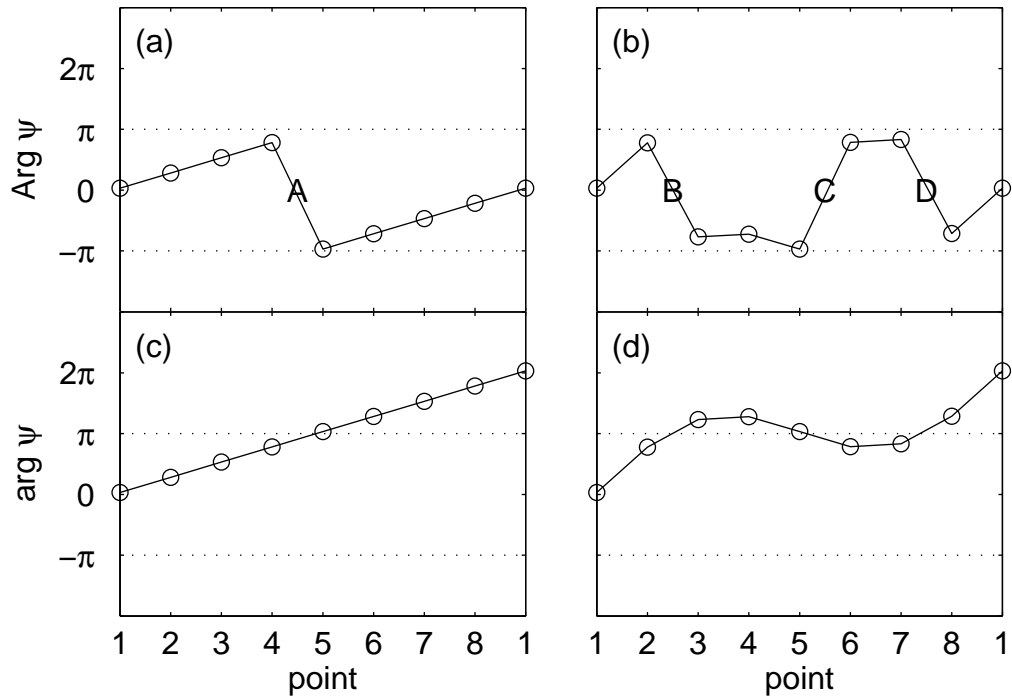


Figure 3.2: Two examples of the numerical reconstruction of the phase circulation, showing (a,b) the principal phase and (c,d) the unwrapped phase, where (c) is reconstructed from (a), and (d) is reconstructed from (b). In each case, the phase starts with  $\phi_1 = 0.1$  and ends with an unwrapped phase of  $2\pi + 0.1$ , and so the phase circulation is  $2\pi + 0.1 - \phi_1 = 2\pi$ .

of  $2\pi$ , subtracting the original phase, and later dividing by  $2\pi$  to obtain  $m$ , we simply count the number of  $2\pi$  jumps that would be corrected in phase unwrapping. Formally, the vortex detection array  $\mathcal{V}_{ij}$  is given by

$$\mathcal{V}_{ij} = \sum_{(\alpha, \beta) \in A_{ij}} \mathcal{U}(\alpha, \beta) \quad (3.9)$$

where  $A_{ij} = \{(\phi_1, \phi_2), (\phi_2, \phi_3), \dots, (\phi_7, \phi_8), (\phi_8, \phi_1)\}$ , and

$$\mathcal{U}(\alpha, \beta) = \begin{cases} -1 & \text{if } \beta - \alpha > \pi, \\ 0 & \text{if } -\pi \leq \beta - \alpha \leq \pi, \\ +1 & \text{if } \beta - \alpha < -\pi. \end{cases} \quad (3.10)$$

For example, applied to Figure 3.2(a), only jump **A** provides a nonzero contribution (+1), and  $\mathcal{V}_{ij} = +1$ . For Figure 3.2(b), jump **B** contributes +1, **C** contributes -1, and **D** contributes +1, and so  $\mathcal{V}_{ij} = (+1) + (-1) + (+1) = +1$ .

### 3.6.3 Density curvature threshold for vortex detection

As we have discussed, low density regions of our simulations are dominated by extremely weak high frequency excitations and may contain wild phase fluctuations which have no physical relevance. We are only interested in vortices in regions where the density is significant, and in order to restrict our vortex detection algorithm to these vortices, we impose an arbitrary density curvature threshold  $\kappa_v$  for the detection of vortices.

The density itself is not a useful measure of how interesting a vortex might be, because the mean field density must become zero at the centre of the vortex. However, the density curvature is a useful quantity to consider: a vortex must have zero density at its core, and in a homogeneous background we expect the density to heal back to the background density in a length given approximately by the healing length [Equation (2.37)]. As a consequence, if we move slightly away from the centre of a vortex in a region of significant density, we expect the density to increase, which indicates that a vortex is characterised by a positive density curvature. However, if the density near the vortex is very low, the density curvature will also be low.

The density curvature (in three dimensions, the component in the plane parallel to  $z = 0$ ) is given by a finite difference approximation as

$$\kappa = \frac{|\psi_{(i-1)j}|^2 + |\psi_{(i+1)j}|^2 - 2|\psi_{ij}|^2}{(\Delta x)^2} + \frac{|\psi_{i(j-1)}|^2 + |\psi_{i(j+1)}|^2 - 2|\psi_{ij}|^2}{(\Delta y)^2}, \quad (3.11)$$

and we neglect vortices where  $\kappa$  is less than the vortex detection threshold  $\kappa_v$ , since this indicates the vortex is in a very low density region of the condensate. Typically, we choose  $\kappa_v = 10^{-3}$ , although this can vary from  $10^{-2}$  to  $10^{-6}$  depending on the part of the condensate in which we are interested. We find that the phase circulation and density curvature threshold, used together as a criterion for the detection of a significant vortex, provide a flexible and highly robust vortex detection technique.

In the low density regions of the condensate, tiny fluctuations can cause vortices to be formed and annihilated, and yet because they are in regions of such low density, these have little physical significance. Our vortex detection threshold excludes such vortices from consideration. When, in our simulations, a vortex is drawn into the condensate from the outlying low density regions, it must be remembered that this vortex is not being created, but merely drawn from the “Oort cloud”, the reservoir of insignificant vortices in the low density regions.

The reason for using a finite difference approximation for the density curvature (rather than highly accurate Fourier methods) is that high accuracy is not needed. This approach also allows both the phase circulation and density curvature threshold calculations to be conveniently implemented in C with a single loop over the array storing  $\psi$ , reducing the computer memory bandwidth required.

### 3.6.4 Presentation of detected vortices

Our vortex detection algorithm typically detects a group of four adjacent points as being near a vortex (given a sufficiently large density curvature for each point). For example, in Figure 3.1, a single hypothetical  $m = +1$  vortex core is indicated by the  $+$  sign. For this vortex, the algorithm would find  $\mathcal{V}_{ij} = +1$  (for the central point). Repeating the detection algorithm for each of the

other points adjacent to the central point would yield  $\mathcal{V}_{i(j-1)} = +1$  (point 2),  $\mathcal{V}_{(i+1)(j-1)} = +1$  (point 3), and  $\mathcal{V}_{(i+1)j} = +1$  (point 4), and in the absence of other vortices, none of the other points in Figure 3.1 would be detected as being near a vortex.

In two dimensions, we present numerically detected vortices by marking them with a symbol on probability density figures, either  $+$  or  $-$  depending on the sense of the vortex. To eliminate duplicate symbols for a single vortex, we select one point of the (up to) four detected for the vortex. The vortex detection array is searched starting from the most negative  $x$  and  $y$ , and for each  $y$  searching in the direction of increasing  $x$ . When a nonzero element  $\mathcal{V}_{ij}$  is found, a symbolic vortex is drawn, and any nonzero elements  $\mathcal{V}_{(i+1)j}$ ,  $\mathcal{V}_{i(j+1)}$ , or  $\mathcal{V}_{(i+1)(j+1)}$  are set to zero to eliminate other elements detected for that vortex. Thus we arbitrarily draw the symbol at the lower left corner of the group. Because of the fine resolution of our grid, this does not move the symbolic vortex by an appreciable amount. We find that this technique works satisfactorily for the situations we present.

### 3.6.5 Vortex lines

In three dimensions, we construct the vortex detection array by using the vortex detection algorithm on each plane of constant  $z$ , and  $\mathcal{V}$  has the same shape at the computational grid for  $\psi$ . We visualise the spatial structure of the vortices by finding and plotting an isosurface of  $|\mathcal{V}|$  using Matlab's `isosurface`. Even though the elements of the vortex detection array are discretised (each  $|\mathcal{V}_{ij}|$  is typically 0 or 1), the `isosurface` function (using an arbitrary level of  $0 < 10^{-4} < 1$  for the surface) finds an acceptable approximate containing surface for the vortex line.

We describe the sense of circulation of the vortex line at a point by considering the vector  $\mathbf{u}$  tangent to the line, where the direction of  $\mathbf{u}$  is given from the phase circulation by the right-hand rule. Where  $\mathbf{u}$  has a positive  $z$  component, we say the vortex line has positive sense. This description is useful because our rotational stirring simulations tend to generate vortices roughly parallel with the axis of rotation (the  $z$  axis). We can deduce the sense of the circulation of the vortex line by a more detailed examination of  $\mathcal{V}$  which considers the



sign of its elements, and it is possible to represent this by mapping different colours onto the vortex line (as in Figure E.7), but in this work we typically just describe the sense.



# Chapter 4

## Vortex dynamics in two-dimensional condensates

### 4.1 Introduction

In this chapter, we explore the dynamics of vortices in condensates. Because the nonlinearity of the GP equation greatly complicates analytical treatments, the only accurate way that we may learn about the evolution over time of condensates and the vortices within them is to perform a broad range of numerical “experiments” and examine the resulting dynamics. We have simulated condensates extensively in two dimensions, and we find that vortices are readily formed in many different scenarios, including collisions between condensates or with an aperture, or by mechanically disturbing a condensate with a moving Gaussian probe. These simulations also demonstrate the range of applicability and robustness of our numerical techniques.

The situations showing vortex formation that we describe in this chapter do not easily admit quantitative analysis, but it is possible to interpret qualitatively some of the simple dynamics we observe in terms of Feynman’s picture of vortex formation by shearing [38]. By contrast, we have developed a quantitative understanding of vortex formation in rotationally stirred condensates; that behaviour is the topic of Chapters 5–7.

## 4.2 Collisions

The simplest type of experiment which can be performed to demonstrate the coherence of a condensate is an interference experiment, for example, the experiment reported in 1997 by the MIT group [4]. Interference phenomena in linear systems are well understood, since the fringes can be predicted by considering each constituent wave to propagate separately, and then calculating their superposition. The nonlinearity of the GP equation, however, makes the study of collisions of condensates analytically intractable, but we can study these phenomena by numerical simulation.

A condensate ground state displaced from the centre of a symmetric harmonic trap and allowed to evolve, undergoes a shape-preserving simple harmonic oscillation [91, 73] with period  $T = 2\pi$ , which we refer to as the dipole mode. We use this behaviour to study collisions of condensates by taking two copies of the  $C = 92.74$  ground eigenstate of the trap, one displaced in the  $+x$  direction and one in the  $-x$  direction by the same distance. Once the system is renormalised [see Equation (2.25)] the nonlinear parameter increases to  $C = 185.5$ , indicating the doubling of the total number of atoms. In the absence of the other condensate, each would follow simple harmonic motion and reach the bottom of the trap at  $t = \pi/2$ . As shown in Figure 4.1 (for two different initial separations), the condensates instead collide, forming interference fringes.

### 4.2.1 Linear regime

When the initial separation of the condensates is large (comparable to the diameter of each condensate), the peak kinetic energy of the condensates is large and dominates the nonlinearity. When the condensates collide, interference fringes are formed which are almost straight, as can be seen in Figure 4.1(a), exactly the fringes that would be expected when two waves in a linear system are superposed. The condensates pass through each other and reform (only slightly distorted), each moving to the other's original position at  $t = \pi$ , much like the dipole oscillation of a single condensate. Collisions of condensates in one dimension have been investigated by Scott *et al.* [89]: they also found that,

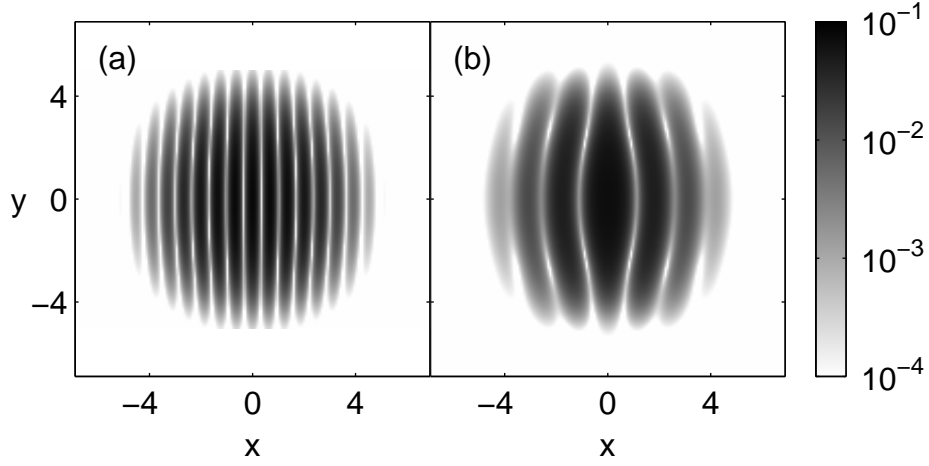


Figure 4.1: Probability density of two condensates colliding in a trap. The condensates each initially have the shape of the ground eigenstate of the trap (for  $C = 92.74$ ), but are displaced from the centre of the trap by the same amount, one in the  $+x$  direction and the other in the  $-x$  direction. The condensates are allowed to fall together from rest (with the phase  $\text{Arg } \psi = 0$  everywhere), and are shown at time  $t = \pi/2$  after their release, when a single condensate in a dipole oscillation would pass the centre of the trap. In (a) the initial separation of the condensate centres was 20.0, while in (b) the initial separation was 10.0. Vortex detection is not used for this figure. For the combined system,  $C = 185.5$ . See also Figure E.1.

for large initial separations, the condensates underwent linear interference and then reformed.

### 4.2.2 Nonlinear regime

When the initial separation is reduced, the kinetic energy is correspondingly smaller and the nonlinearity becomes more important. As we show in Figure 4.1(b), the effect is that the central fringe is broadened by the nonlinearity into a large lenticular shape. This result, which we presented in [10], is strikingly similar to the experimental observation of interference by Andrews *et al.* [4], in which a cigar-shaped  $^{23}\text{Na}$  condensate was separated by a far-blue-detuned argon ion laser and then allowed to recombine.

In Figure 4.2, we present a sequence showing the continued evolution of the case in Figure 4.1(b). The most obvious feature is that the condensates no longer pass cleanly through each other to reform into separated condensates at  $t = \pi$  (as in the linear regime). Instead, the nonlinearity mixes the motion in two dimensions, causing the two condensates to merge into one [Figure 4.2(a)]. This combined condensate undergoes contraction and expansion with a period of  $\pi$ , exhibiting intricate dynamical features, including vortex pair creation and annihilation events. As the expanded system begins to contract, two pairs of vortices are formed near the centre of the condensate, as shown in Figure 4.2(b). The vortices of each pair separate [Figure 4.2(c)], while the two pairs move closer together [Figure 4.2(d)], until each vortex annihilates with the vortex of opposite sign in the other pair, forming a soliton ring [Figure 4.2(e)]. The system continues to expand and contract, and near each contraction minimum the structure of the system becomes very complicated, containing numerous vortices, as shown in Figure 4.2(f). This simulation is symmetric<sup>1</sup> in  $\psi$  about both the  $x$  and  $y$  axes, due to the choice of initial conditions and symmetry of the trapping potential. We remark that, as reported by Scott *et al.* [89], condensate collisions in the nonlinear regime in one dimension lead to the formation of grey solitons.

---

<sup>1</sup>A vortex has the opposite sign of its mirror image.

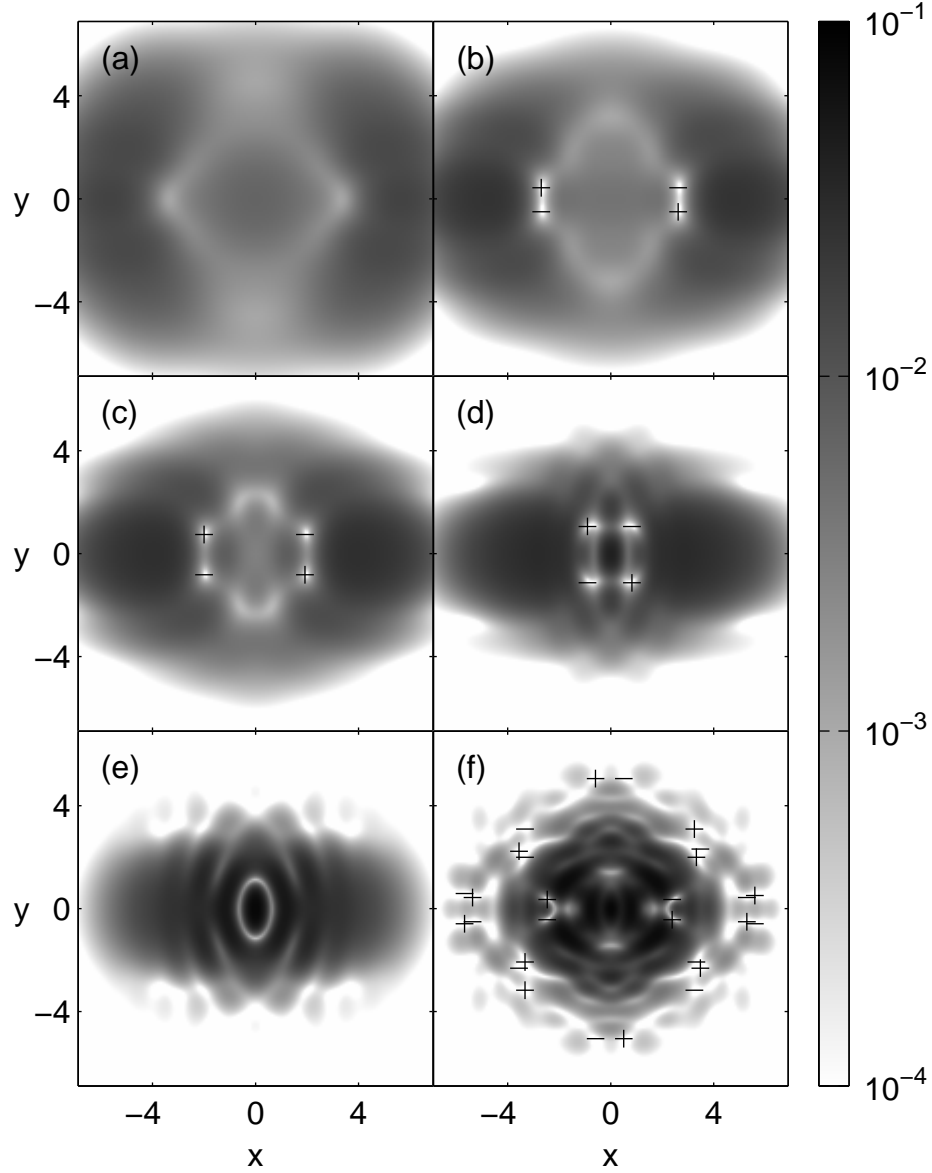


Figure 4.2: Sequence showing the probability density of two condensates colliding in a trap. This is the continuation of the simulation shown in Figure 4.1(b), at times (a)  $t = \pi$ , (b)  $t = 3.58$ , (c)  $t = 3.83$ , (d)  $t = 4.15$ , (e)  $t = 4.40$ , and (f)  $t = 10.93$ . The vortex detection threshold is  $\kappa_v = 10^{-2}$ , and other parameters are as for Figure 4.1(b).

### 4.3 Off-centre collisions

Feynman [38] gave a description of how lines of vortices could be produced by the shearing effect of two superfluids flowing past each other. The central idea is that because the velocity of a flow is proportional to the gradient of the phase, two adjacent flows of different velocities have points which are in and out of phase with each other. Feynman realised that a  $\pi$  phase difference between the flows would lead to a phase circulation of  $2\pi$  about a point on the boundary between the flows. These, he suggested, would heal into vortices to reduce the energy of the condensate.

We demonstrate how these lines of vortices can be formed in condensates by repeating our collision simulations, but offsetting the initial condensates so that their centres do not travel through the centre of the trap. This is achieved by giving the initial condensates each a small azimuthal velocity in opposite directions. As shown in Figure 4.3, the condensates fall together, meeting at the bottom of the trap, but the initial velocities cause the condensates to flow past each other, rather than collide square on as in Figure 4.1(a). A Feynman line of vortices forms between the two condensates as they join, required by the shearing of the two superfluid flows. Because the initial phases of the two condensates differ by  $\pi$ , symmetry requires that one of these vortices forms and remains at the centre of the condensate; a different choice of initial phase difference moves the position of the vortices along the line.

### 4.4 Collision with an aperture

Superfluid  $^4\text{He}$  flows through narrow apertures without friction [94], and here we conduct simulations to study the analogous effect in condensates. Obstacles in the path of the condensate can be simulated by modifying the trapping potential to include thin regions of very large potential. We illustrate this in Figure 4.4, which shows a condensate released from the left entering the centre of the trap and encountering an aperture placed along the line  $x = 0$ . A large portion of the condensate has passed through the aperture into the right-hand half of the figure, and a smaller fraction has tunnelled through



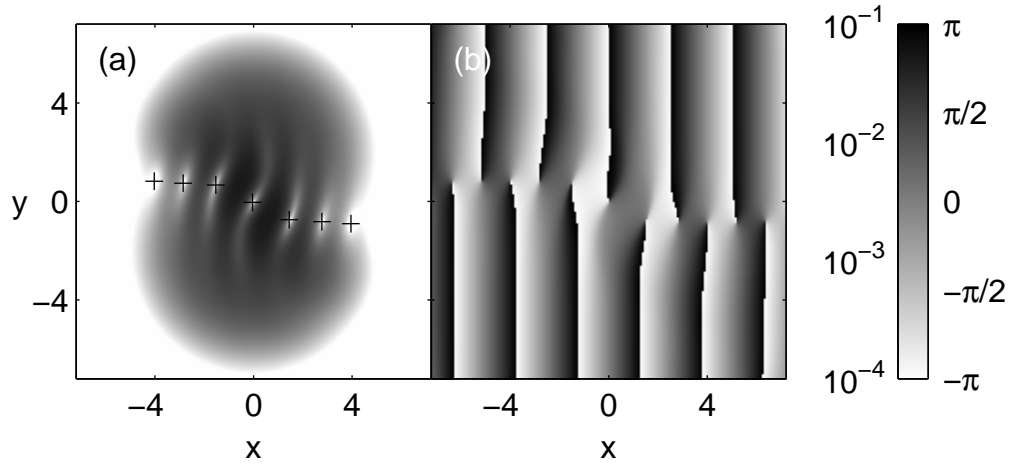


Figure 4.3: An off-centre collision of two condensates in a trap, showing (a) probability density and (b) phase, at time  $t = \pi/2$  after their release. The condensates centres are initially separated in the  $x$  direction by 10.0 [as in Figure 4.1(b)], and each condensate is given a uniform vertical phase gradient corresponding to a velocity of 2, in the  $+y$  direction for the right-hand condensate, and in the  $-y$  direction for the left-hand condensate. Initially, the centres of the condensates differ in phase by  $\pi$ . Parameters are as in Figure 4.1(b), and  $\kappa_v = 10^{-3}$ . See also Figure E.2.

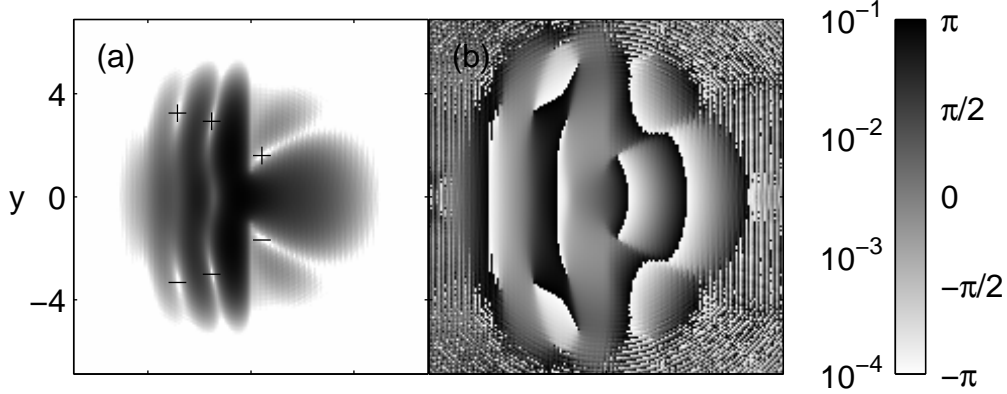


Figure 4.4: Condensate colliding with an aperture, showing (a) probability density and (b) phase, at  $t = \pi/2$ . The initial condensate is the ground state, with its centre displaced to  $\mathbf{r} = (-5.0, 0)$ , and at rest. In addition to the harmonic trapping potential, a narrow potential barrier of height 100 on the line  $x = 0$  blocks the path of the condensate. The barrier, which is 0.16 thick, has a gap 1.88 wide centred on the origin. Parameters are  $C = 92.74$  and  $\kappa_v = 10^{-2}$ .

the potential barrier above and below the aperture. The phase delay of this tunneling induces interference fringes and vortices between the faster moving central portion and the slower tunnelled lobes. The bulk of the condensate is reflected off the barrier, and undergoes self-interference. Vortices are also formed in the reflection interference pattern.

## 4.5 Constant velocity perturber

An important property of a superfluid, investigated experimentally in He II [94], is the movement of an object through the fluid without resistance. Recent experiments by Raman *et al.* [81] have investigated critical speed phenomena in a cigar-shaped  $^{23}\text{Na}$  condensate, by perturbing the condensate with a blue-detuned laser focussed to a narrow waist (a stirrer). In these experiments, the stirrer moves at a constant speed along the length of the condensate (in an oscillating motion). Those authors related heating of the condensate above a critical speed to the speed of sound, and the shedding of vortices from the

stirrer was proposed as an explanation for this effect.

We have investigated the response of a condensate to a perturber moving in a straight line at a constant speed through the condensate. In our simulations, the condensate is initially in the ground state (stationary in the centre of the trap). We perturb the condensate with a narrow Gaussian potential (the stirrer) given by

$$W(\mathbf{r}, t) = W_s \exp \left[ - \left( \frac{|\mathbf{r} - \mathbf{r}_s(t)|}{w_s/2} \right)^2 \right], \quad (4.1)$$

where  $W_s$  is the height,  $w_s$  is the width, and  $\mathbf{r}_s = x_s \hat{\mathbf{x}} + y_s \hat{\mathbf{y}}$  is the position of the stirrer. The  $y$  component of the position  $y_s$  is constant, and the speed of the stirrer is given by  $v_s = dx_s/dt$ . The stirring potential is included in the GP equation as part of the total potential  $V = V_0 + W$ . The stirrer starts at the left ( $x = -10$ ) of the condensate, and moves right with a constant speed along the line  $y = y_s$ .

#### 4.5.1 On-centre perturber

For  $y_s = 0$ , as shown in Figure 4.5, the perturber passes through the centre of the condensate, and no angular momentum can be transferred to the condensate by the stirrer. We find that for a slow stirrer velocity  $v_s = 0.75$ , a weak dipole oscillation is excited but no vortices are formed. Unlike the He II case in which the superfluid is not excited by a slowly moving object, we find that, even for this very low stirrer velocity, momentum is imparted to the condensate. As the perturber speed  $v_s$  is increased, complicated excitations are also generated, and numerous vortices form in the condensate. In Figure 4.5, we show a sequence in which the perturber speed exceeds the speed of sound near the centre of the condensate. In Figure 4.5(a), the perturber enters the condensate, and as it approaches the centre, in Figure 4.5(b), a shock wave forms on the far side of the condensate. As the stirrer leaves the condensate [Figure 4.5(c)], two pairs of vortices are formed on the  $y = 0$  line behind the stirrer, and separate, while two more vortices enter from above and below. In Figure 4.5(d), the rightmost pair of vortices separate (and later fall out of the condensate), while the adjacent pair created in the condensate separate and

are each attracted to a vortex of opposite sign drawn in from outside (with which they later annihilate). Figure 4.5(e) shows the creation of another pair of vortices, which persist for a short time and then annihilate, leaving the condensate briefly free of vortices [Figure 4.5(f)]. The type of simulation we have described here was also independently investigated by Jackson *et al.* [51] in a different parameter regime; they described the formation of the vortices they found in terms of accumulated phase slip, and related these effects to the speed of sound.

### 4.5.2 Off-centre perturber

If we change the path of the perturber so that  $y_s > 0$ , angular momentum is imparted to the condensate even for very low stirrer velocities, and higher stirrer speeds impart more angular momentum. This is very interesting in the context of the formation of vortices, because we know that central vortex states have angular momentum, and vortices allow lower energy configurations of the condensate to exist for a given angular momentum. These findings lead us naturally to consider the rotational stirring of condensates, which is the subject of Chapters 5–7.

The sequence in Figure 4.6 shows the effect of an off-centre perturber passing through the condensate. In Figure 4.6(a), the stirrer enters the condensate, and by Figure 4.6(b) a single vortex is drawn into the condensate. That vortex rapidly moves around the condensate in a clockwise direction and falls out, and, as shown in Figure 4.6(c) a second vortex is drawn into the condensate behind the stirrer, and moves deeply into the condensate [Figure 4.6(d)]. This vortex also falls out of the condensate [Figure 4.6(e)], and yet another vortex enters [Figure 4.6(f)]. Because the stirrer moves through the condensate off-centre, an odd number of vortices can be present in the condensate.

### 4.5.3 Angular momentum

We have investigated the final angular momentum transferred to the condensate for various choices of  $y_s > 0$  and  $v_s$ , and these are plotted in Figure 4.7. We see in Figure 4.7(a) that, regardless of the stirrer speed, the offset  $y_s = 2$

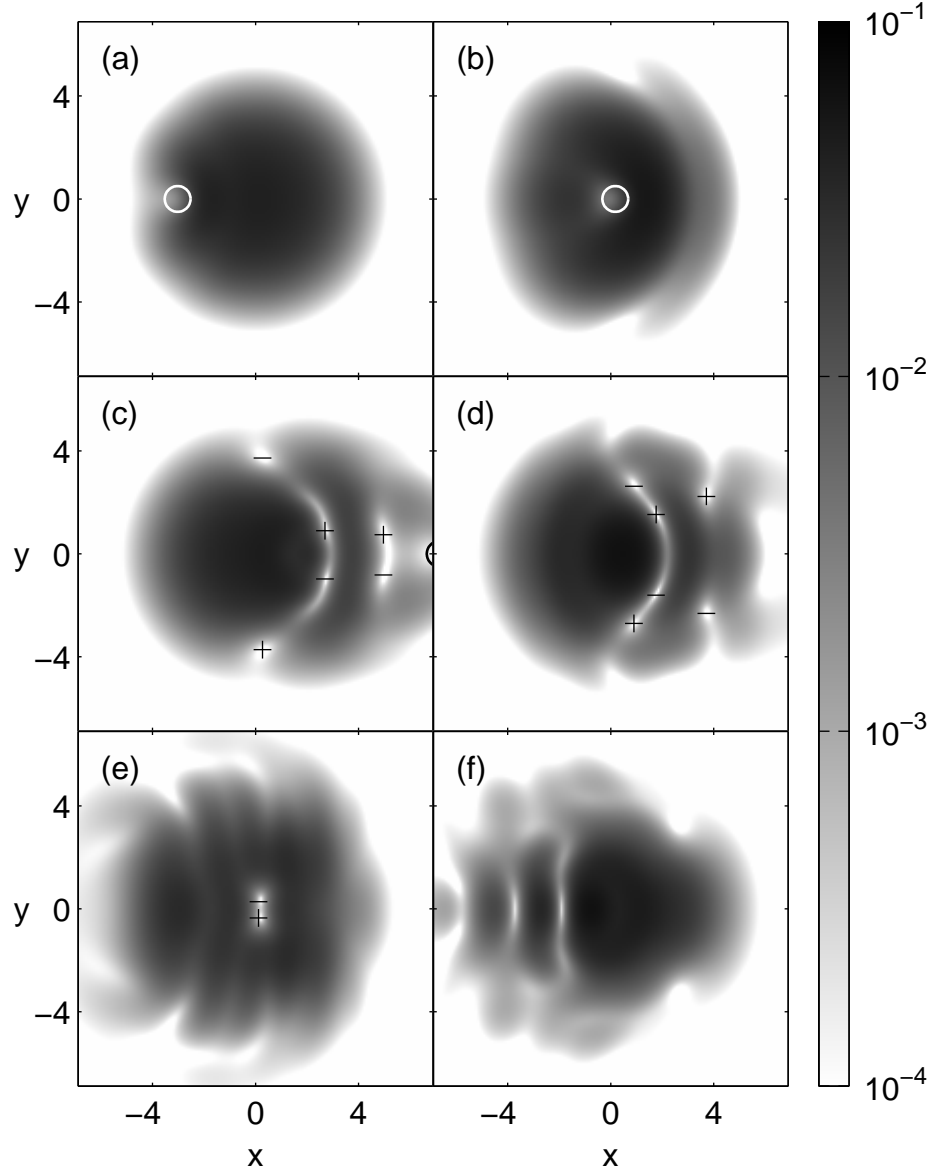


Figure 4.5: Sequence showing probability density for a constant velocity perturber moving through the centre of a condensate. The condensate is initially in the ground state, and the stirrer (marked with a circle) comes from the left. Times are (a)  $t = 2.32$ , (b)  $t = 3.39$ , (c)  $t = 5.72$ , (d)  $t = 6.28$ , (e)  $t = 7.73$ , and (f)  $t = 9.49$ . Parameters are  $C = 92.74$ ,  $W_s = 10$ ,  $w_s = 1$ ,  $y_s = 0$ ,  $v_s = 3$ , and  $\kappa_v = 10^{-2}$ . Initially,  $x_s = -10$ .

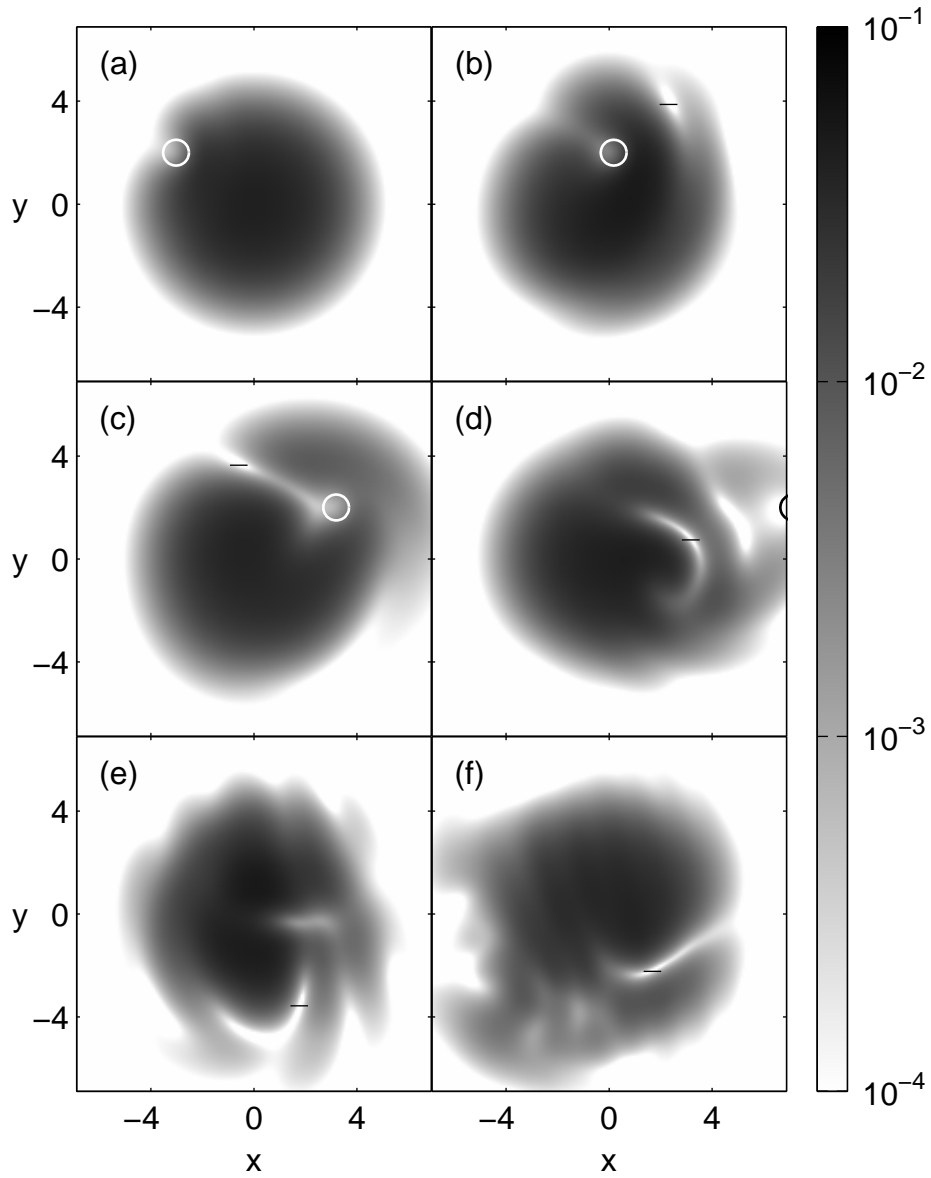


Figure 4.6: Sequence showing probability density for a constant velocity off-centre perturber moving through a condensate. The stirrer is marked with a circle. Times are (a)  $t = 2.32$ , (b)  $t = 3.39$ , (c)  $t = 4.40$ , (d)  $t = 5.72$ , (e)  $t = 6.72$ , and (f)  $t = 7.98$ . Parameters are as in Figure 4.5, except that  $y_s = 2$ .

provides optimal angular momentum transfer to the condensate; in Chapter 5 we likewise find an optimal radius for rotational stirring.

The magnitude of the angular momentum transferred to the condensate increases with increasing  $v_s$  for all  $y_s$  [as shown in Figure 4.7(b)]. We note that for the  $v_s = 0.75$  simulations, we observe no vortices drawn into the bulk of the condensate, and little angular momentum is transferred to the condensate for any  $y_s$ . This strongly suggests that the ability of the stirrer to impart angular momentum is related to the formation of vortices in the condensate, and that this is a critical phenomenon related to the speed of the stirrer. For each  $y_s$  we have investigated, a greater angular momentum is transferred for a faster stirrer.

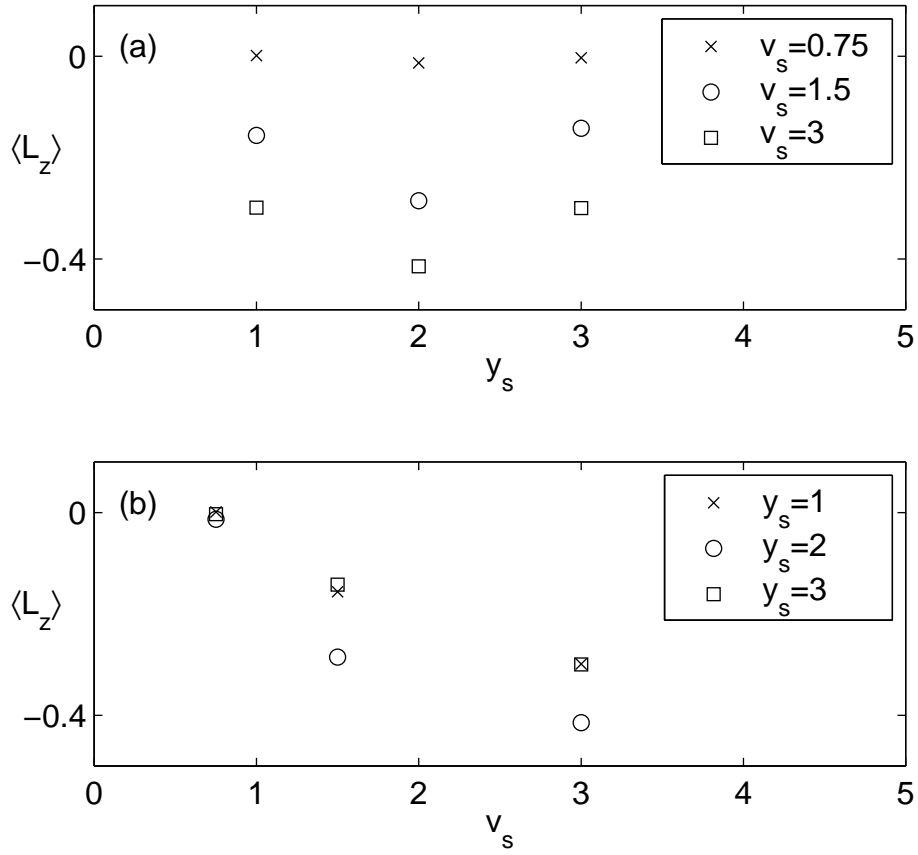


Figure 4.7: Angular momentum expectation value after a constant velocity stirrer has passed through the condensate, with (a) and (b) providing different representations of the same data. Parameters for each simulation are as in Figure 4.5, except that  $y_s$  and  $v_s$  vary as given above.



# Chapter 5

## Rotational stirring of two-dimensional condensates

### 5.1 Introduction

In the previous chapter, we described different scenarios in which vortices could be formed in condensates. Because of the many possible configurations of these simulations, it is difficult to quantify the reasons for the formation of vortices in each case. In this chapter, we make an extensive numerical study of the rotational stirring of condensates in two dimensions, a type of simulation which provides us with a small number of adjustable parameters. We have found a simple regime of behaviour in which the formation of a single vortex in a rotationally stirred condensate can be quantitatively predicted from calculable properties of the condensate eigenstates.

Prior to the experimental observation of Bose-Einstein condensation in dilute alkali gases, the only available condensate was He II, in which the study of vortices was a central issue [77, 94]. Vortices were observed when  $^4\text{He}$  was cooled below the critical point in a rotating container, but only if the angular frequency of rotation of the container exceeded a critical value. This critical angular frequency is found from a thermodynamical equilibrium argument to be proportional to the difference in the free energy between the vortex and ground states [57, 59]. The reason for this is that, in the rotating frame at the critical frequency, the free energy in these two states is the same, and above

this frequency, the vortex state is thermodynamically preferred.

We simulate rotational stirring of a condensate by using a Gaussian laser beam which plays a role analogous to surface roughness in the He II experiment. In contrast to the He II situation, we find that the formation of vortices in the condensate is a dynamical process which does not depend on the system reaching thermal equilibrium. Nevertheless, we show that the conditions for vortex formation are very similar to those for thermodynamical stability of a central vortex in He II.

Stirring the condensate with a perturber is a conceptually simple situation. A key feature, for our purposes, is that the parameters of this situation, such as the radius and speed of stirring, are well defined. There is also the advantage that there is no upper limit on the time that the process can continue, in contrast to a perturber moving with a constant velocity (see Section 4.5 and also Jackson *et al.* [51]).

We find that vortices are readily produced by rotational stirring of the condensate if the stirring is sufficiently fast. Our most striking result is the discovery of a single vortex cycling behaviour. If the condensate is rotationally stirred just below a critical angular frequency  $\omega_c$ , a single vortex enters the condensate, moves close to the centre of the condensate, and then falls back out again. We can understand all the features of this behaviour by describing it in terms of nonlinear Rabi cycling between the ground and vortex states, and we give a detailed description of this simple two state model in Chapter 6.

The use of a narrow stirrer also allowed us to test the importance of local quantities, especially the speed of sound. Various investigators have suggested that the speed of sound and vortex formation play a crucial role in damping and dissipation of flow in He II; the speed of sound determines the low frequency slope of the He II excitation spectrum proposed by Landau [94]. For dilute alkali condensates, Raman *et al.* [81] have conducted an experiment in which a stirrer oscillating in a straight line caused heating above a critical velocity. Simulations of that experiment by Jackson *et al.* [53] implicate vortex formation as a mechanism for increased heating of the condensate, for a stirrer moving faster than a critical velocity (related to the speed of sound). However, we find that the speed of sound is unimportant in the rotational stirring we

study. Even in the linear ( $C = 0$ ) limit, in which the speed of sound is zero (and so the stirrer is always supersonic), there is a range of stirring speeds for which no vortices are formed.

## 5.2 Two-dimensional model

Far-blue and far-red detuned laser beams have been used in a number of experiments to manipulate condensates [81]. We simulate stirring the condensate with a far-blue detuned Gaussian laser beam by including a Gaussian potential

$$W(\mathbf{r}, t) = W_s(t) \exp \left[ - \left( \frac{|\mathbf{r} - \mathbf{r}_s(t)|}{w_s/2} \right)^2 \right], \quad (5.1)$$

as a component of the total external potential  $V$  in the GP equation [Equation (2.24)]. The Gaussian width  $w_s$  is a Full Width 1/e Maximum (FW1/eM) of the potential. The stirrer moves anticlockwise on a circular path with radius  $r_s$  about the origin. We choose a beam waist that is somewhat narrower than the condensate, and this permits us to investigate the effect of varying the radius of the stirrer's motion and also to localise the effect of the stirrer so that we can compare its speed with the speed of sound.

In the majority of our stirring simulations ( $C = 0$ ,  $C = 30$ ,  $C = 88.13$ ), the stirrer height  $W_s(t) = W_0$  is constant and we begin the stirring simulation with the ground eigenstate of the trap with the stirrer present. Transient effects are kept to a minimum by linearly increasing the stirrer speed until  $t = \pi$ , when it reaches its final angular speed  $\omega_f$ . In the  $C = 200$  stirring simulations, we instead start with the ground eigenstate with the stirrer absent, and linearly introduce the stirrer (which has constant angular speed  $\omega_f$ ) starting at  $t = 0$ , until  $t = \pi$  when  $W_s(t)$  reaches its final value of  $W_0$ . We find that both are satisfactory techniques for reducing transient effects at the start of stirring, but the latter is more convenient, because it allows a wide range of stirrer parameters to be used with the same initial state, avoiding the need for recalculating the initial eigenstate. For this reason, we use the second technique when we rotationally stir condensates in three dimensions (see Chapter 7).

### 5.3 Multiple vortex regime

A condensate stirred well above the critical angular frequency  $\omega_c$  exhibits complex behaviour, including the prolific formation of vortices, as shown in Figure 5.1. Most of the vortices in this case are of positive sign, reflecting the positive angular momentum imparted to the condensate by the stirrer. If we continue to stir the condensate, the angular momentum expectation value quickly increases until  $\langle L_z \rangle > 11$ . However, in order to show that the vortices have a rich dynamical behaviour even in the absence of the stirrer, for this case (and this case alone), we linearly remove the stirrer between  $t = 4\pi$  and  $t = 5\pi$  and subsequently allow the condensate to freely evolve, constrained only by the symmetric trapping potential. We find that, after the stirring potential has been withdrawn, the condensate has constant angular momentum expectation value  $\langle L_z \rangle = 1.66$ ; this is expected as angular momentum is conserved for an axially symmetric total potential  $V$  (see Section A.6). Nevertheless, vortices continue to move in and out of the condensate, and intricate dynamical features are observed. As time progresses, vortices of positive and negative circulation form, move relative to each other, and annihilate when a positive and negative pair collide.

The early part of the stirring process is illustrated in Figure 5.2, in which the stirrer, moving faster than the local speed of sound (ahead of the stirrer) carves out a depression in the condensate. In Figures 5.2(c–f) a single positive vortex can be seen at the edge of the condensate, riding the “bow wave” of the distortion caused by the stirrer. The sequence shows that at first a single vortex is drawn deeply into the condensate, and then a second vortex. The low density regions “outside” the condensate can be viewed as a reservoir of vortices, because in these regions, vortices contribute negligible energy or angular momentum to the condensate. The motion of the stirrer distorts the condensate and draws these vortices deeply into the condensate.

#### 5.3.1 Interaction of vortices

The evolution of the condensate after the stirrer has been withdrawn, shown in Figure 5.3, demonstrates the complicated dynamical behaviour of vortices

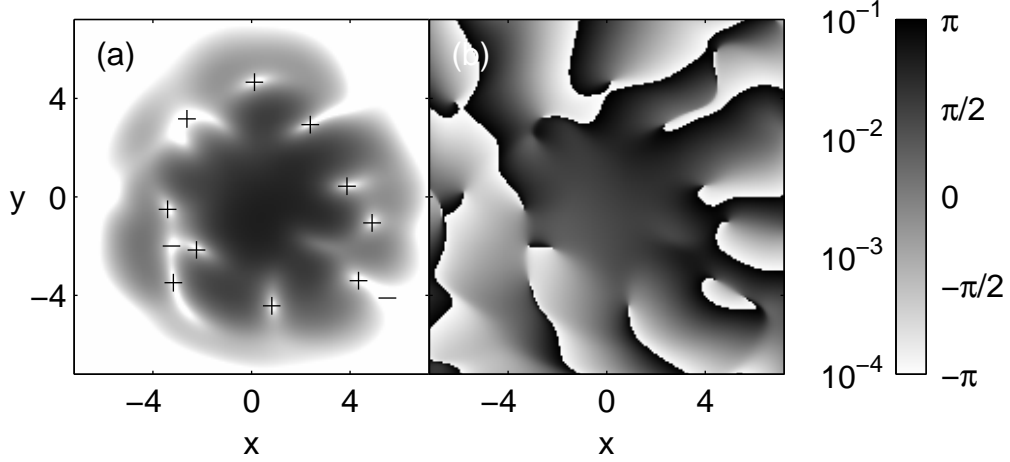


Figure 5.1: Probability density (a) and phase (b) at time  $t = 12\pi$  for a condensate which has been rotationally stirred, where the stirrer was gradually withdrawn between  $t = 4\pi$  and  $t = 5\pi$ . Parameters are  $C = 88.13$ ,  $W_0 = 10$ ,  $w_s = 1$ ,  $r_s = 3$ ,  $\omega_f = 1$ , and  $\kappa_v = 10^{-3}$ . See also Figure E.3.

which can occur even though the system is now undriven and so energy and angular momentum are conserved. The condensate contains a large number of vortices, mostly positive, which circulate about the condensate in a generally anticlockwise direction. The vortices continue to interact, and pair creation and annihilation events occur. The sequence shown in Figure 5.3 follows the evolution of such an event, and marks the three vortices involved as thicker symbols than the others in the condensate. In Figure 5.3(a), the vortex in which we are interested is moving to the left (an anticlockwise path through the condensate). To the left of the vortex, a deep depression (marked with an arrow) has formed, which contains no vortices. In Figure 5.3(b) a pair of opposite vortices have formed in the depression, and in Figures 5.3(c,d) the negative vortex moves closer to the original vortex (while the structure of the condensate as a whole rotates in the anticlockwise direction). In Figure 5.3(e) the negative vortex is about to collide with the original positive vortex, and in Figure 5.3(f) the annihilation of these two vortices has taken place. To an observer unaware of the vortex creation and annihilation, it would appear that the original vortex [in Figure 5.3(a)] has advanced by a jump, moving faster

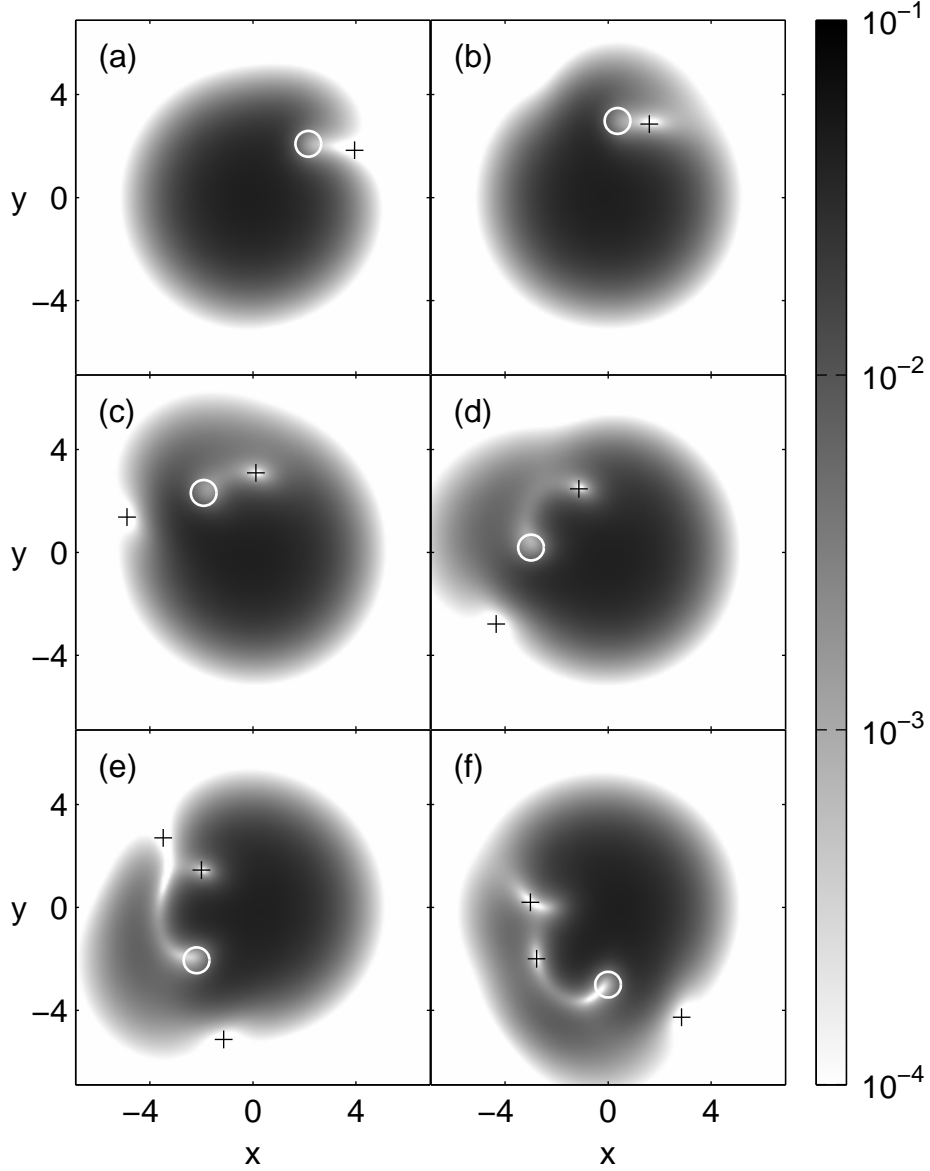


Figure 5.2: Sequence showing the probability density for a rotationally stirred condensate. This is the early evolution of the condensate for the same simulation as in Figure 5.1. In this sequence, times are equally spaced; (a)  $t = 2.20$ , (b)  $t = 3.02$ , (c)  $t = 3.83$ , (d)  $t = 4.65$ , (e)  $t = 5.47$ , and (f)  $t = 2\pi$ . The stirrer is marked with a circle. Parameters are as in Figure 5.1.

than the other vortices in the condensate.

## 5.4 Single vortex cycling regime

Amidst the complexity of possible behaviours, an important and simply characterised behaviour emerges, namely the formation and dynamics of a single vortex. This single vortex cycling occurs when the stirrer angular frequency  $\omega_f$  is just below a critical angular frequency, which we denote  $\omega_c$ . An example which illustrates the main features is given in Figure 5.4, where sequential sub-figures show the evolution of the condensate as the stirrer revolves. A single vortex enters at the edge of the visible region of the condensate, then cycles to the centre of the condensate, and back to the edge. This cycle repeats regularly, as can be seen in Figure 5.5, where the thick line shows the angular momentum expectation value  $\langle L_z \rangle$  plotted as a function of time for this case. Because  $\langle L_z \rangle = 0$  for the ground state and  $\langle L_z \rangle = 1$  for the  $m = +1$  central vortex eigenstate, the peak value of  $\langle L_z \rangle$  provides a quantitative measure of the strength of single vortex cycling.

At lower stirring speeds, similar vortex cycling occurs, but with progressively smaller amplitudes as  $\omega_f$  decreases, so that the vortex oscillates only near the condensate edge and  $\langle L_z \rangle$  remains much less than one (as shown by the lower thin line of Figure 5.5). We have found that the condensate gains angular momentum even for very small values of  $\omega_f$ . As  $\omega_f$  increases, the amplitude of the cycling becomes larger until, for  $\omega_f$  only slightly below  $\omega_c$ , the single vortex reaches the centre of the condensate, and at its peak,  $\langle L_z \rangle$  approaches one from below (the thick line in Figure 5.5). If  $\omega_f$  is increased above  $\omega_c$  (as in the upper thin curve of Figure 5.5), multiple vortices penetrate the condensate and  $\langle L_z \rangle$  exceeds one.

### 5.4.1 Dependence on parameters

We have studied the single vortex cycling regime for a range of values of the nonlinearity parameter  $C$ , and find that it is present for all the nonzero values of  $C$  we have investigated. We find that the critical angular frequency of

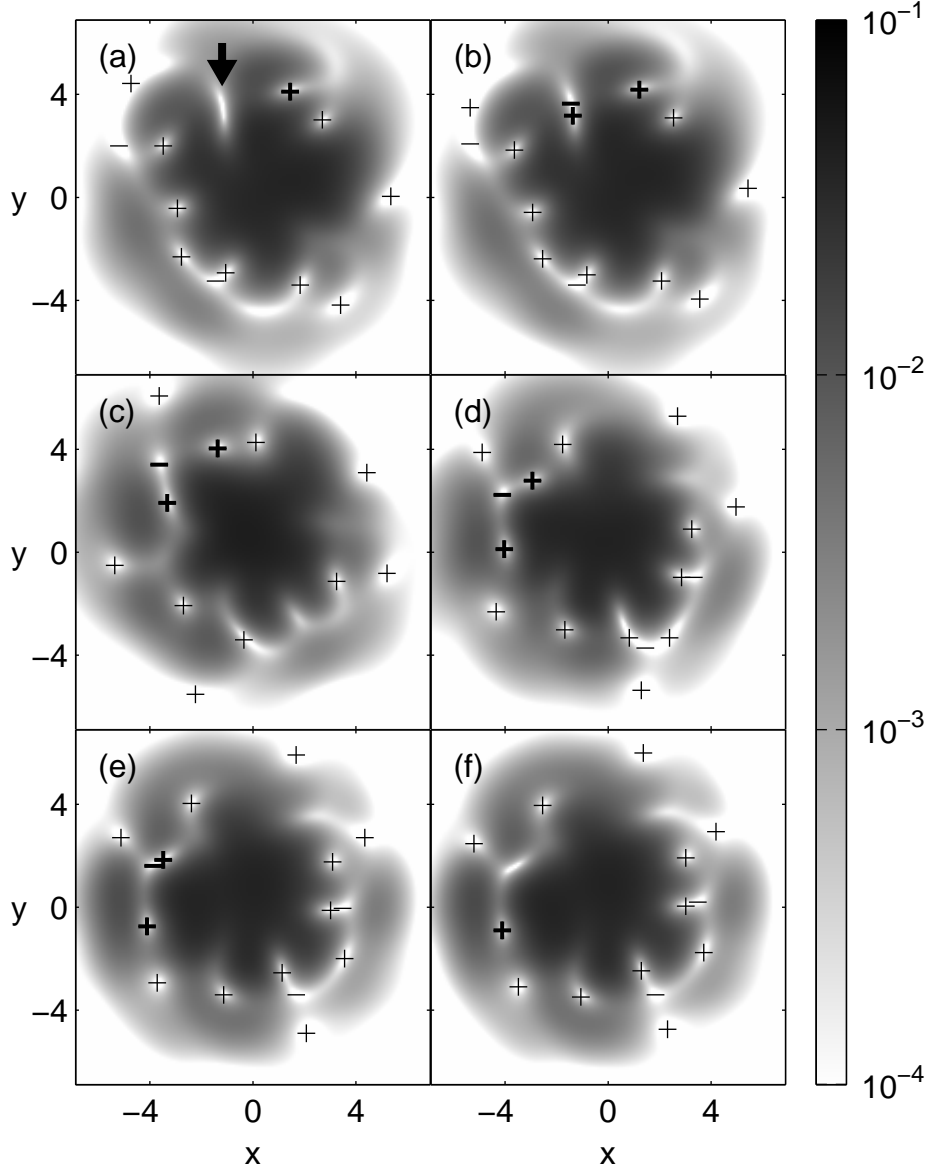


Figure 5.3: Sequence showing the probability density of a condensate which has been rotationally stirred, exhibiting the dynamics of vortex pair creation and annihilation. The condensate is evolving freely after the stirrer has been withdrawn, for the same simulation as in Figures 5.1 and 5.2. The vortices involved in the pair creation and annihilation events are marked with thicker symbols. Times are (a)  $t = 26.83$ , (b)  $t = 26.89$ , (c)  $t = 27.65$ , (d)  $t = 28.21$ , (e)  $t = 28.46$ , and (f)  $t = 28.53$ . Parameters as in Figure 5.1.



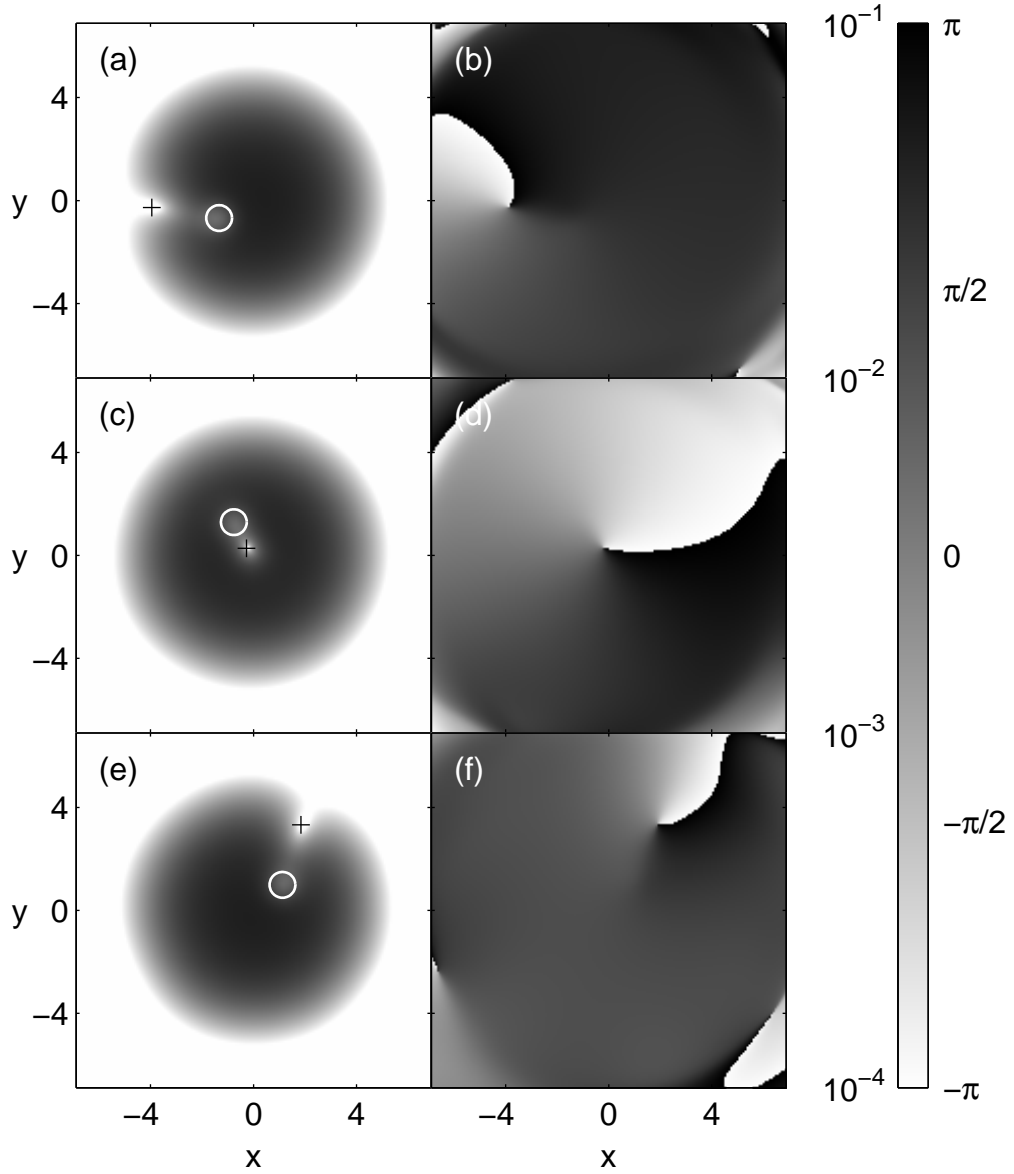


Figure 5.4: Sequence showing single vortex cycling in a rotationally stirred condensate, giving (a,c,e) probability density, and (b,d,f) phase. Times are (a,b)  $t = 8.80$ , (c,d)  $t = 18.35$ , and (e,f)  $t = 28.15$ . The circle denotes the stirrer. Parameters are as in Figure 5.1 except that  $r_s = 1.5$  and  $\omega_f = 0.5$ . See also Figure E.4.

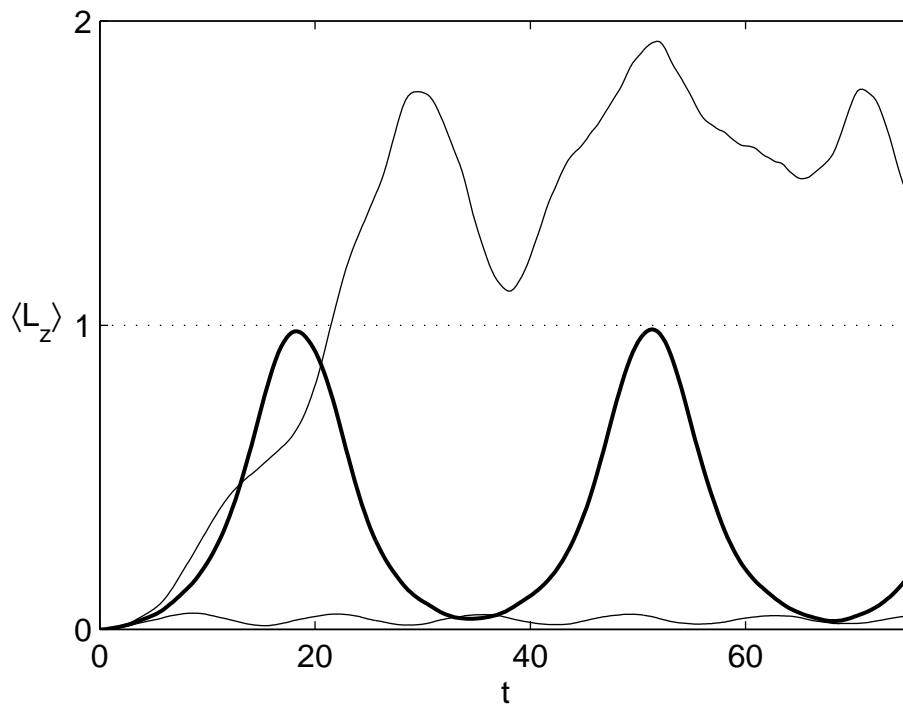


Figure 5.5: Angular momentum expectation values versus time for  $\omega_f = 0.5$  (thick line) which corresponds to Figure 5.4,  $\omega_f = 0.4$  (lower thin line), and  $\omega_f = 0.6$  (upper thin line). Other parameters as in Figure 5.4.

rotational stirring  $\omega_c$  decreases as the nonlinearity increases. Bounds on  $\omega_c$  found from extensive simulations of the GP equation give  $\omega_c$  in the range 0.6–0.8 for  $C = 30$ , in 0.5–0.6 for  $C = 88.13$ , and in 0.4–0.45 for  $C = 200$ . The  $C = 0$  case is an exception, in which we find no single vortex cycling regime. It is difficult to obtain accurate simulations at large values of  $C$  for numerical reasons, namely that the increased chemical potential requires a smaller time step size, while the decreased healing length requires a finer spatial grid, as we have discussed in Section 3.4.

In the  $C = 200$  case (for which  $W_0 = 10$ ,  $r_s = 1.5$ , and  $\omega_f = 0.4$ ), using a stirrer width  $w_s = 2$  causes single vortex cycling to occur. However, if the stirrer width is reduced to  $w_s = 1$ , approximately quartering the total stirrer beam power, then single vortex cycling does not occur. This indicates that a minimum stirrer size is required for single vortex cycling to occur. We have also studied effects of varying the radius  $r_s$  of the stirrer’s path, and we find that varying  $r_s$  (for a given angular frequency of stirring  $\omega_f$ ) changes the behaviour of the condensate. In the  $C = 88.13$  case with  $\omega_f = 0.5$  (other parameters as in Figure 5.1), for  $r_s = 3$  a single vortex only just enters the condensate. That is, the cycling is weak and incomplete. For  $r_s = 2$ , the cycling is much stronger, and for  $r_s = 1.5$  the vortex cycles right to the centre of the condensate (the case shown in Figure 5.4). In each of these cases, the stronger penetration of the single vortex into the condensate is reflected in a greater peak value of  $\langle L_z \rangle$ .

## 5.5 Speed of sound

A perturbation or object exceeding the speed of sound in a condensate has often been given as a criterion for the formation of vortices. For example, Jackson *et al.* [51] have investigated the effect of perturber moving through the centre of a condensate in a straight line with a constant speed (similar to our on-centre constant velocity perturber of Section 4.5.1), and found the formation of vortices in the wake of the stirrer. These results were analysed by them in terms of accumulated phase slip, and related to the local speed of sound.

By contrast, we have found that the single vortex cycling regime of a rotationally stirred condensate does not require the stirrer to exceed the speed of sound. Consider the case of a  $C = 88.13$  condensate stirred with  $\omega_f = 0.5$  (other parameters as in Figure 5.1): as  $r_s$  decreases, the linear speed of the stirrer decreases, while the density and thus the speed of sound [Equation (2.36)] ahead of the stirrer increase. While for  $r_s = 3$  the speed of the stirrer is close to the speed of sound ahead of the stirrer, as  $r_s$  decreases the stirrer speed becomes markedly subsonic, yet the vortex cycling behaviour becomes far stronger. This result emphasises that the single vortex cycling regime is not a speed of sound effect. Furthermore, because  $c_s$  increases and  $\omega_c$  decreases for increasing  $C$ , the speed of the stirrer required for single vortex cycling becomes much smaller than the speed of sound for large condensates.

What does the speed of sound tell us? When a stirrer moves through the condensate, it makes a depression in the density profile. If the speed of the stirrer exceeds the speed of sound, a depression (or wake) is left behind the stirrer, perhaps driving the condensate density to zero. Because the stirrer is moving too quickly, the condensate cannot fill in this hole, and also cannot move out of the way for the stirrer (which further pushes the condensate away from the hole). The low density region is a place where the density can easily be reduced to zero, facilitating the pair creation of vortices. However, this is only one mechanism for the formation of vortices. As we have shown, pairs of vortices may also be freely created in the distant, low density regions of the condensate, with one member of the pair being drawn into the condensate. We must conclude then that exceeding the speed of sound is perhaps a sufficient but certainly not a necessary condition for the creation of vortices in condensates. While the low density regions in the wake of the stirrer permit vortex pair formation, the low density regions outside the condensate are also suitable for this purpose; the effect of a rotating stirrer is to draw vortices from the outer regions deeper into the condensate.

## 5.6 Summary

Our simulations of a rotationally stirred condensate in two dimensions have demonstrated both prolific vortex formation, and most strikingly, a single vortex cycling regime. For stirring above a critical angular frequency, numerous vortices can enter the condensate, interact, and undergo pair creation and annihilation. If the condensate is rotationally stirred below the critical angular frequency  $\omega_c$ , a single vortex cycles in and out of the condensate. For this cycling to occur, however, the stirring potential must be both large enough and close enough to the centre of the condensate.



# Chapter 6

## Nonlinear two state model

### 6.1 Introduction

In this chapter, we introduce a simple nonlinear two state model which allows us to interpret and quantitatively reproduce the single vortex cycling regime of a rotationally stirred condensate. This model is motivated by the almost exactly complete cycling from the ground state to the central vortex state shown in Figure 5.4, and the distinct cycling behaviour of the angular momentum expectation value (the thick line of Figure 5.5). The two state model describes the single vortex cycling behaviour as a coherent process of the mean field, in which the wavefunction is decomposed into a symmetric component and a vortex component. The stirring potential transfers population between the symmetric and vortex component by a nonlinear form of Rabi cycling. The model predicts the critical angular frequency for rotational stirring  $\omega_c$ , below which single vortex cycling occurs, to be (in our dimensionless formalism) the difference in energy between the ground and central vortex eigenstates of the trap.

In the context of a two state atom in a light field, Rabi cycling is a well known behaviour, in which the atom undergoes a coherent cycling of population between the states, described by a system of three coupled ordinary differential equations [1]. These equations, known as the optical Bloch equations, are, in the case of a steady electric field amplitude, often referred to as the Rabi equations.

Our nonlinear two state model makes a number of quantitatively accurate predictions, including the critical angular frequency of rotational stirring  $\omega_c$ , and with some modification, accurately reproduces the cycling behaviour seen in the thick line of Figure 5.5. Although we at first use the two state model to explain the behaviour of the condensate in two dimensions, our derivation does not rely on this dimensionality and readily generalises to a three-dimensional condensate in an axially symmetric trap. In Chapter 7, we present compelling numerical evidence that the model also predicts the critical angular frequency of rotational stirring in three dimensions. In that chapter, we also use the model to explain the importance of stirrer symmetry. In Chapter 8, we show that the two state model is a valuable tool in understanding the stability of central vortex eigenstates and their response to a perturber.

## 6.2 Two state ansatz

The single vortex cycling behaviour can be understood quantitatively as nonlinear Rabi cycling between the ground and vortex states. The essential idea is that the stirring potential causes the condensate to cycle between the ground state and the first vortex state, analogous to the Rabi cycling of an atom in a light field. We decompose the condensate on a basis of a ground-state-like part (axially symmetric) and a vortex part (axially symmetric with an anticlockwise phase circulation). In the linear (i.e.  $C = 0$ ) limit the condensate would be represented as a superposition of the ground state and the first vortex state of the trap, but we find that in the general case, the nonlinearity of the GP equation prevents such a simple superposition from being a good representation of the system. In the nonlinear system, it is more accurate to decompose the system into collisionally coupled states, in which the radial form of each of the basis states is modified by its collisional interaction with the other. Many of the details of this decomposition can be found in Appendix D. We consider here only a stirrer rotating anticlockwise, and cycling between the ground and  $m = +1$  vortex eigenstates, but it is obvious that a similar result must hold for clockwise stirring and cycling between the ground and  $m = -1$  vortex eigenstates.



We represent the condensate mean-field wavefunction by the superposition of a symmetric component  $\phi_s(r, t)$  and a vortex component  $\phi_v(r, t)e^{i\theta}$ , where  $r$  and  $\theta$  are the usual polar representation of  $\mathbf{r}$ . Our ansatz is thus

$$\psi(\mathbf{r}, t) = a_s(t)\phi_s(r, n_v) + a_v(t)\phi_v(r, n_v)e^{i\theta}, \quad (6.1)$$

where  $a_s$  and  $a_v$  are the complex amplitudes of the symmetric and vortex components respectively. The vortex fraction is  $n_v = |a_v|^2$  and the symmetric fraction is  $n_s = |a_s|^2 = 1 - n_v$ , conserving total probability. The  $\phi_{s,v}$  are real nonnegative functions, and each of  $\phi_{s,v}$  is normalised to unity, that is

$$\int \phi_{s,v}^2 d\mathbf{r} = 1, \quad (6.2)$$

and  $\phi_s$  and  $\phi_v e^{i\theta}$  are orthogonal, as we show in Section D.1.1. The ansatz of Equation (6.1), along with the requirement that the components have real eigenvalues (in the absence of a stirrer), is the formal basis of our model. We will make an additional minor adjustment later (see Section 6.3) to improve the numerical agreement of the model with the full GP equation.

### 6.3 Coupled basis wavefunctions

In this and the following section, we present the framework for the analysis of the two state model. In order to make the logic of the derivations as clear as possible, we have chosen to consign a number of the mathematical details to Appendix D.

Eigenstates of the full time-independent GP equation [Equation (2.29)] are characterised by a single eigenvalue  $\mu$ . Of course, the ansatz wavefunction we employ is not an eigenstate of the full GP equation: we know that an off-centre vortex circles about the centre of the condensate [83]. We are guided in our choice of basis states by the requirement that in the absence of the stirrer, our ansatz should represent a vortex circling the origin at a constant radius and angular speed. This will be achieved if the coefficients  $a_s$  and  $a_v$  satisfy

$$\frac{da_s}{dt} = -i\mu_s a_s, \quad (6.3a)$$

$$\frac{da_v}{dt} = -i\mu_v a_v, \quad (6.3b)$$

where  $\mu_s(n_v)$  and  $\mu_v(n_v)$  are real, and so  $n_v$  is constant in the absence of the stirrer. This choice has the effect of allowing the phases of the two coefficients to evolve separately; the vortex circles the centre of the condensate with angular velocity  $\mu_v - \mu_s$ . We show in Section D.2 that if Equations (6.3) are satisfied then the basis wavefunctions  $\phi_s$  and  $\phi_v e^{i\theta}$  must satisfy the coupled equations

$$\mu_s \phi_s = \left[ -\frac{1}{r} \frac{d}{dr} \left( r \frac{d}{dr} \right) + \frac{r^2}{4} + C \left( n_s \phi_s^2 + 2F n_v \phi_v^2 \right) \right] \phi_s, \quad (6.4a)$$

$$\mu_v \phi_v = \left[ -\frac{1}{r} \frac{d}{dr} \left( r \frac{d}{dr} \right) + \frac{1}{r^2} + \frac{r^2}{4} + C \left( n_v \phi_v^2 + 2F n_s \phi_s^2 \right) \right] \phi_v, \quad (6.4b)$$

The derivation involves substituting the ansatz Equation (6.1) into the full GP equation [Equation (2.24)], and then projecting out separately the parts corresponding to  $\phi_s$  and  $\phi_v e^{i\theta}$ ; this procedure makes extensive use of the orthogonality of  $\phi_s$  and  $\phi_v e^{i\theta}$ . The factor  $F$  is in principle equal to one, but we have introduced it in order to improve numerical agreement with the full GP equation, as we discuss in below.

We obtain the lowest energy coupled basis wavefunctions  $\phi_s(r, n_v)$  and  $\phi_v(r, n_v) e^{i\theta}$  together with their eigenvalues  $\mu_s(n_v)$  and  $\mu_v(n_v)$  by solving Equations (6.4) for a given value of  $n_v$ . It is worth noting that for  $n_v = 0$ , Equation (6.4a) is uncoupled from Equations (6.4b) and  $\phi_s$  becomes simply the ground eigenstate of the full GP equation. Similarly, for  $n_v = 1$ , Equation (6.4b) is uncoupled from Equations (6.4a) and  $\phi_v e^{i\theta}$  is the  $m = +1$  central vortex eigenstate of the full GP equation. The end points of the cycling thus coincide with the eigenstates of the full time-independent GP equation.

In Equations (6.4), the inter-component repulsion terms (the terms with a factor  $F$ ) give rise to an energy barrier between the  $n_v = 0$  and  $n_v = 1$  states of the system (see Section 6.5.2), because the factor of two doubles the energy of inter-component repulsion compared to intra-component repulsion. The constraint on the system imposed by the ansatz of Equation (6.1) increases this energy barrier somewhat compared to the true (unconstrained GP simulation) case. We have introduced the factor  $F$  as an adjustable parameter, which allows us to heuristically correct for this exaggerated energy barrier.

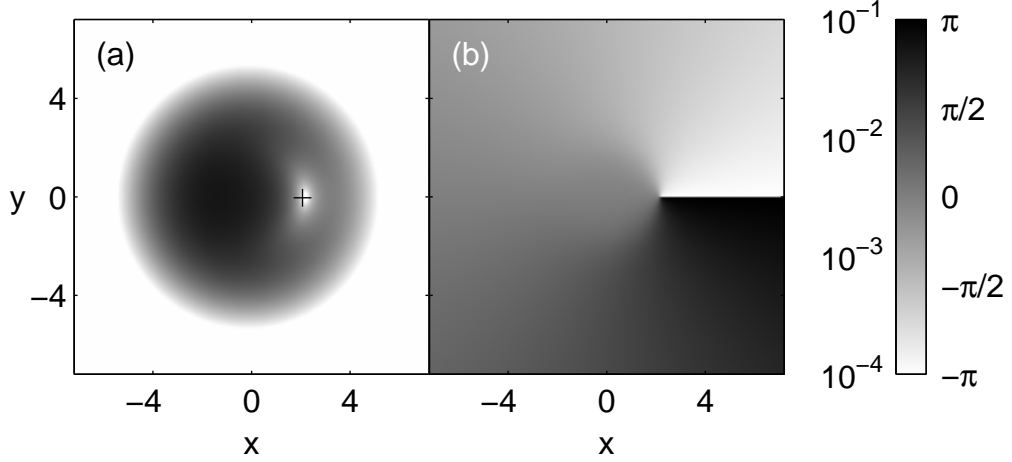


Figure 6.1: The condensate represented by the superposition wavefunction of Equation (6.1) for vortex fraction  $n_v = 0.5$ , showing (a) probability density and (b) phase. Parameters are  $C = 88.13$ ,  $F = 0.79$ , and  $\kappa_v = 10^{-3}$ .

For example, for  $C = 88.13$ , if we let  $F = 0.79$ , our two-state model produces behaviour which closely matches the results from the full GP equation (given in Section 6.4.3).

The superposition in Equation (6.1) produces a condensate with angular momentum expectation value  $\langle L \rangle = n_v$ , and a vortex whose distance from the centre of the trap decreases as  $n_v \rightarrow 1$ . We illustrate this in Figure 6.1 with the superposition state of Equation (6.1) for  $a_s = \sqrt{0.5}$  and  $a_v = -\sqrt{0.5}$ . Notice that when the phase difference of two components is  $\pi$ , the vortex lies on the  $x$  axis. In the absence of a stirrer, the vortex precesses about the centre of the condensate at a frequency  $\mu_v - \mu_s$ .

## 6.4 Nonlinear Rabi equations

Having specified the equations for the precise form of our basis wavefunctions [Equations (6.4)], we now find the time evolution of their coefficients  $a_s$  and  $a_v$  in the presence of the stirring potential. The details of this procedure are given in Section D.3. The essential idea is that we substitute Equation (6.1) into Equation (2.24), and project alternately onto the states  $\phi_s$  and  $\phi_v e^{i\theta}$ , to

obtain a pair of coupled equations for  $da_s/dt$  and  $da_v/dt$ . Noting that a stirring potential  $W(\mathbf{r}, t)$  constantly rotating with angular frequency  $\omega_f$  can be written [20]

$$W(\mathbf{r}, t) = e^{-i\omega_f t L_z} W'(\mathbf{r}) e^{+i\omega_f t L_z}, \quad (6.5)$$

where  $W'(\mathbf{r})$  does not depend on time, we collect the oscillating exponentials in time and transform to a frame which rotates with the stirring potential. We write our coefficients in this frame as

$$\tilde{a}_s = a_s e^{i\alpha_s}, \quad (6.6a)$$

$$\tilde{a}_v = a_v e^{i(\alpha_s + \omega_f t)}, \quad (6.6b)$$

where

$$\alpha_s = \int_0^t \mu_s(t') dt', \quad (6.7)$$

and we note that because the transformation affects only the phase of the coefficients,  $n_v = |\tilde{a}_v|^2$ . We thus obtain the nonlinear Rabi equations

$$\frac{d\tilde{a}_s}{dt} = -i\delta_s(n_v)\tilde{a}_s - \frac{i}{2}\Omega(n_v)\tilde{a}_v, \quad (6.8a)$$

$$\frac{d\tilde{a}_v}{dt} = -i[\Delta(n_v) + \delta_v(n_v)]\tilde{a}_v - \frac{i}{2}\Omega^*(n_v)\tilde{a}_s. \quad (6.8b)$$

Here

$$\Delta(n_v) = \mu_v(n_v) - \mu_s(n_v) - \omega_f, \quad (6.9)$$

and,

$$\delta_s(n_v) = \int \phi_s(n_v) W'(\mathbf{r}) \phi_s(n_v) d\mathbf{r}, \quad (6.10a)$$

$$\delta_v(n_v) = \int \phi_v(n_v) W'(\mathbf{r}) \phi_v(n_v) d\mathbf{r}, \quad (6.10b)$$

$$\Omega(n_v) = 2 \int \phi_s(n_v) W'(\mathbf{r}) \phi_v(n_v) e^{i\theta} d\mathbf{r}. \quad (6.10c)$$

In practice, we make  $\Omega$  real by having a  $W'(\mathbf{r})$  symmetric about the  $x$  axis. We note that in deriving Equations (6.10), we have made no assumptions about

the precise form of the rotating potential  $W$ , and so our model is also easily generalizable to an arbitrarily shaped stirring potential, including a rotating anisotropic potential.

Equations (6.8) formally resemble the usual linear Rabi equations [1], and hence we identify the  $\delta_\sigma$  as frequency shifts and  $\Omega$  as the bare Rabi frequency, but note that here these quantities are variable and depend on the value of  $n_v$ . Despite this nonlinear dependence, the concept of Rabi cycling provides a simple framework in which to understand the formation and dynamics of a single vortex: the stirring potential couples and causes cycling between the initial ground state and the  $m = +1$  central vortex state.

### 6.4.1 Linear Rabi cycling

If the condensate undergoes only weak single vortex cycling, then  $n_v$  varies only slightly and Equations (6.8) have behaviour similar to the usual linear Rabi equations [1]. Under these conditions, which occur for smaller stirring speeds or for a stirrer which is weak or far from the condensate centre, we can qualitatively understand behaviour such as the increased cycling frequency and decreased cycling amplitude. In the linear Rabi model (for which the detuning  $\Delta'$  and Rabi frequency  $\Omega$  are constant) the cycling frequency is given by the effective Rabi frequency  $\Omega' = (\Omega^2 + \Delta'^2)^{1/2}$ , and the maximum value of  $n_v$  is  $\Omega^2/\Omega'^2$ . We note that in our stirred condensate the linear Rabi detuning is given by  $\Delta' = \Delta + \delta_v - \delta_s$ . For example, in Figure 5.5 the condensate response to stirring for  $\omega_f = 0.4$  (lower thin curve) reveals an increase in oscillation frequency and decreased transfer to the pure vortex state, which are consistent with the linear Rabi predictions. A more quantitative treatment, essential in the case of significant cycling, requires the nonlinear character of Equations (6.8) to be taken into account, necessitating numerical solution.

### 6.4.2 Numerical method

In this section, we describe the method we use to solve the two state model. The numerical solution of Equations (6.8) to find trajectories in time of  $\tilde{a}_s(t)$  and  $\tilde{a}_v(t)$  requires the calculation of  $\mu_s(n_v)$ ,  $\mu_v(n_v)$ ,  $\delta_s(n_v)$ ,  $\delta_v(n_v)$ , and  $\Omega(n_v)$ ,

for all the values of  $n_v$  the system traverses. This requires solution of Equations (6.4), which is nontrivial, and thus to make this numerical solution of Equations (6.8) computationally feasible, we approximate these quantities using a lookup-table technique. We precalculate each of the quantities  $\mu_s$ ,  $\mu_v$ ,  $\delta_s$ ,  $\delta_v$ , and  $\Omega$ , for a fixed range of values of  $n_v$ , and then use cubic spline interpolation to find the quantities between the exact values of  $n_v$ . In the case we present, we have used 21 values of  $n_v$ , evenly spaced from  $n_v = 0$  to  $n_v = 1$ . We have verified that using a higher resolution lookup table does not significantly affect the results we present; we retain the lower resolution table for consistency with our earlier result [19].

We solve the coupled system given in Equations (6.4) for each of 21 values of  $n_v$  ranging from 0 to 1 in steps of 0.05. We use `fsolve` from the Matlab Optimization Toolbox [71] to find the solution using a Levenberg-Marquardt method. We solve the system for the points  $x > 0$  (we can reconstruct the  $x < 0$  points by symmetry) for  $\mu_s$ ,  $\mu_v$ ,  $\psi_s$ , and  $\psi_v$  simultaneously, together with the normalisation conditions on each of the wavefunctions. We represent the wavefunctions  $\psi_s$  and  $\psi_v e^{i\theta}$  each with 256 equally spaced points, over the range  $x \in [-20, 20]$  to give them suitable boundary conditions for Fourier decomposition (which we use to calculate the spatial derivatives, as detailed in Appendix C).

For  $n_v = 0$ , we seed the optimisation process with a Thomas-Fermi solution for  $\phi_s$ ,  $\mu_g$ , and  $\mu_v$ , and use  $r\phi_s$  as a crude, unnormalised guess<sup>1</sup> to seed  $\phi_v$ . We then solve the equations for other values of  $n_v$ , in order of increasing  $n_v$ , seeding each optimisation with the solution of the previous  $n_v$  as the best available guess, thereby reducing computational cost. We emphasise that the  $\psi_s$  found for  $n_v = 0$  and the  $\psi_v e^{i\theta}$  found for  $n_v = 1$  are the ground and vortex eigenstates respectively of the full time-independent GP equation; this gives the optimisation techniques described here application outside the evaluation of the two state model.

Once the values of  $\mu_{s,v}$ ,  $\delta_{s,v}$ , and  $\Omega$  have been precalculated, we integrate the system of ordinary differential equations [Equations (6.8)] using Matlab's `ode45`, an adaptive stepsize Runge-Kutta-Fehlberg method. We find values

---

<sup>1</sup>The sharp inner edge of the vortex Thomas-Fermi solution is unsuitable.

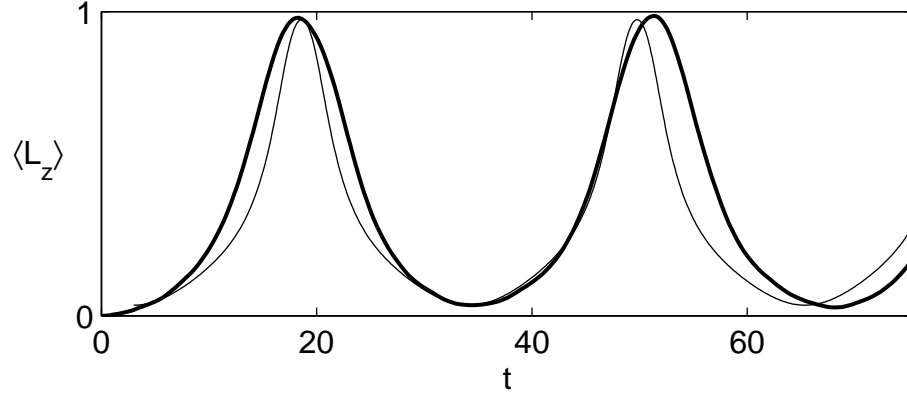


Figure 6.2: Single vortex cycling in a rotationally stirred condensate, showing the angular momentum expectation value for the full GP equation simulation (thick line) [same as the thick line in Figure 5.5], and the two state model (thin line). The two state model starts at  $t = 3$  with  $\tilde{a}_s = \sqrt{0.965}$  and  $\tilde{a}_v = -\sqrt{0.035}$ . Parameters as in Figure 5.4, and the two state model uses  $F = 0.79$ .

of  $\mu_{s,v}$ ,  $\delta_{s,v}$ , and  $\Omega$  from the lookup table by cubic spline interpolation (Matlab's `spline` function) which guarantees that the first two derivatives of the interpolated function are smooth.

### 6.4.3 Numerical solution

We now describe a particular case for which we have solved the two state model. We emphasise, however, that the greatest strength of the model is not that we can solve it quantitatively (as we demonstrate): more importantly, the model gives us physical insights into the dynamics of the rotationally stirred condensate. The importance of the numerical solution is that it verifies that the two state model can exhibit the same single vortex cycling dynamics that we have observed in the full time-dependent GP equation. For example, in Figure 6.2 we show that, if we take  $F = 0.79$ , we obtain excellent agreement between the two state model and the full GP equation, for the case shown in Figure 5.4.

We emphasise also that the coupled basis changes in the course of the cycling, as shown in Figure 6.3. In Figure 6.3(a) the system is in the ground state,

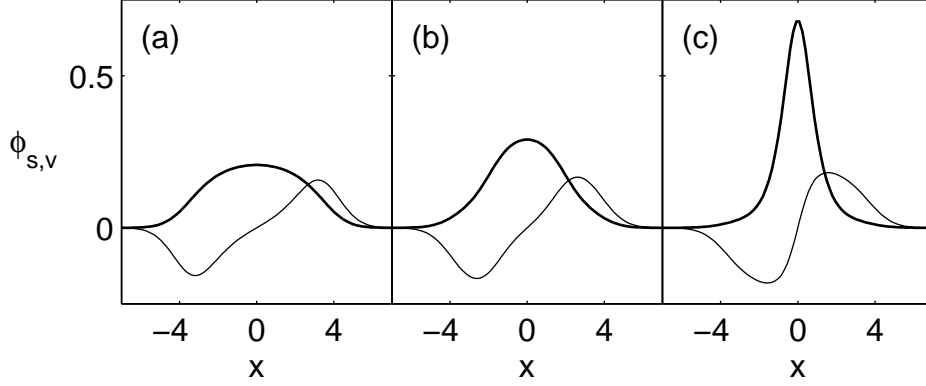


Figure 6.3: Coupled basis wavefunctions of the two state model  $\phi_s$  (thick line) and  $\phi_v e^{i\theta}$  (thin line). In (a)  $n_v = 0$  and  $\phi_s$  is the ground eigenstate, in (b)  $n_v = 0.5$  and the situation is the same as in Figure 6.1, and in (c)  $n_v = 1$  and  $\phi_v e^{i\theta}$  is the  $m = +1$  vortex eigenstate. Parameters are  $C = 88.13$  and  $F = 0.79$ .

and the symmetric component dominates and takes the unperturbed form of the ground state, forcing the corresponding vortex component outwards. For  $n_v = 0.5$  [Figure 6.3(b)], the two components apply an effective potential on each other and modify each other's shape. Once the system reaches the vortex state [Figure 6.3(c)], the vortex component is in the pure vortex eigenstate, and the corresponding symmetric component is squeezed into the centre.

In Figure 6.4 we present the various quantities of the two state model used in Figure 6.2. The eigenvalues are given in Figure 6.4(a), and show an avoided crossing close to  $n_v = 1$ . Because  $\mu_v > \mu_s$  for this case, in the absence of a stirrer, the vortex shown in Figure 6.1 always rotates in an anticlockwise direction. The corresponding energies  $\epsilon_s$  and  $\epsilon_v$  of the components [see Equations (6.13)] are given in Figure 6.4(b). For the same stirrer size and position as in Figure 5.4, the two state model energy shifts and Rabi frequency are given in Figure 6.4(c) and 6.4(d) respectively. All of the parameters used in the calculation of the two state model solution are the same as in the full GP equation.



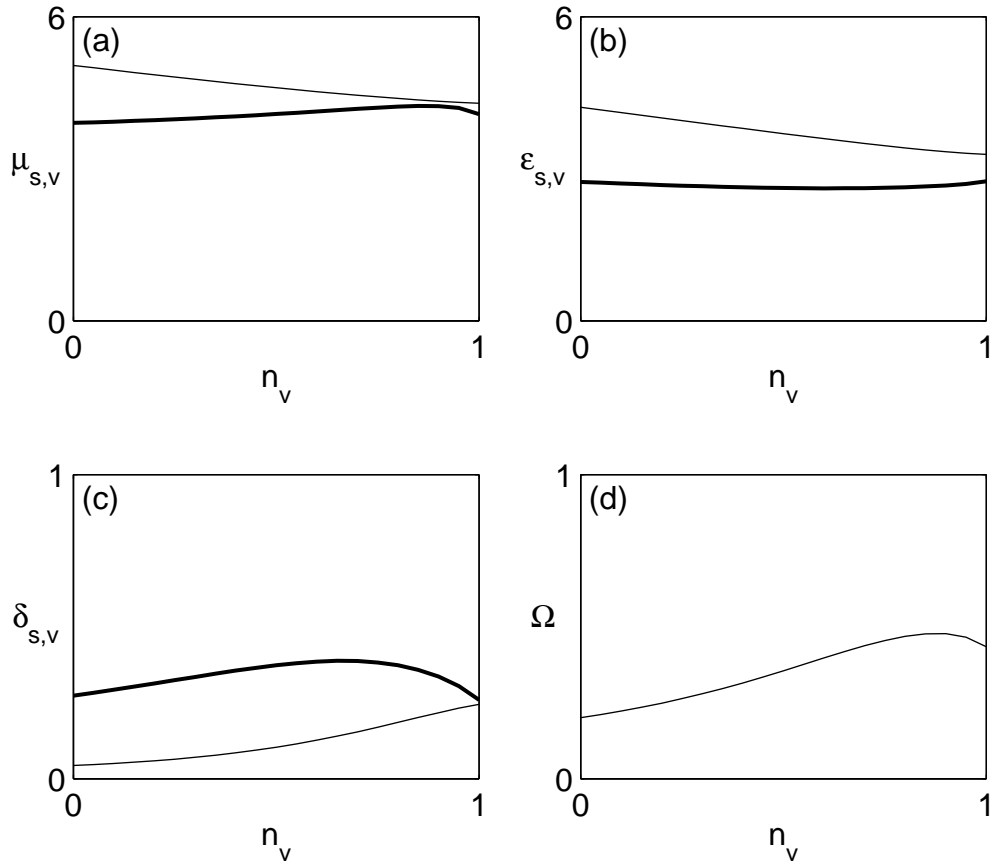


Figure 6.4: Quantities of the two state model corresponding to the two state solution of Figure 6.2, showing (a)  $\mu_s$  (thick line) and  $\mu_v$  (thin line), (b)  $\epsilon_s$  (thick line) and  $\epsilon_v$  (thin line), (c)  $\delta_s$  (thick line) and  $\delta_v$  (thin line), and (d) the Rabi frequency  $\Omega$ .

## 6.5 Energy in the rotating frame

The energy in the rotating frame is a valuable tool for understanding the dynamical behaviour of the nonlinear Rabi equations, and thus the conditions required for single vortex cycling to occur in the full GP equation. The energy  $E'$  in the frame rotating with the stirrer is [58, 57, 59]

$$E' = E - \omega_f \langle L_z \rangle. \quad (6.11)$$

In Section A.7, we show that  $E'$  is conserved by the GP equation, and so any cycling in the GP equation must follow a trajectory that conserves  $E'$ . For the two state model, we remind the reader that  $\langle L_z \rangle = n_v$ . The energy of the two state system  $E'_{two}$  (in the rotating frame) depends on the vortex fraction  $n_v$  and the phase angle  $\Theta = \text{Arg}(\tilde{a}_v^* \tilde{a}_s)$ , and is given explicitly by

$$\begin{aligned} E'_{two}(n_v, \Theta) = & (1 - n_v)(\epsilon_s + \delta_s) + n_v(\epsilon_v + \delta_v - \omega_f) \\ & + \sqrt{n_v(1 - n_v)} \Omega \cos \Theta. \end{aligned} \quad (6.12)$$

The energies of the components are given by

$$\begin{aligned} \epsilon_s = 2\pi \int r \phi_s \left[ -\frac{1}{r} \frac{d}{dr} \left( r \frac{d}{dr} \right) \right. \\ \left. + \frac{r^2}{4} + \frac{1}{2} C \left( n_s \phi_s^2 + 2F n_v \phi_v^2 \right) \right] \phi_s dr, \end{aligned} \quad (6.13a)$$

$$\begin{aligned} \epsilon_v = 2\pi \int r \phi_v \left[ -\frac{1}{r} \frac{d}{dr} \left( r \frac{d}{dr} \right) + \frac{1}{r^2} \right. \\ \left. + \frac{r^2}{4} + \frac{1}{2} C \left( n_v \phi_v^2 + 2F n_s \phi_s^2 \right) \right] \phi_v dr. \end{aligned} \quad (6.13b)$$

The nonlinear Rabi equations [Equations (6.8)] do not conserve  $E'_{two}$  exactly, although we know that the GP equation [Equation (2.24)] does conserve  $E'$ . This characteristic of the two state model is a consequence of the coupled basis [Equations (6.4)] in which  $\phi_{s,v}$  vary as  $n_v$  changes. In effect, our system is subject to a constraint [Equation (6.1)] which has the effect of a time-varying external potential, and unlike a fixed constraint, changes the energy of the system over time [43]. We find that in the case shown in Figure 6.2 above,  $E'_{two}$  varies by less than 4% over a cycle.

### 6.5.1 Critical angular frequency of rotational stirring

In this section we use the fact that the full GP equation conserves  $E'$  exactly to deduce the critical angular frequency of rotational stirring. We shall denote the lab frame energies of the ground eigenstate  $\phi_s(r, n_v = 0)$  and  $m = +1$  central vortex eigenstate  $\phi_v(r, n_v = 1)e^{i\theta}$   $E_g$  and  $E_v$  respectively. Complete cycling of the vortex to the centre of the condensate occurs when  $n_v$  reaches the value of 1, but as  $E'$  is conserved, this requires the energies in the rotating frame of the ground eigenstate (for which  $E' = E_g - \omega_f \times 0$ ) and the central vortex eigenstate (for which  $E' = E_v - \omega_f \times 1$ ) to be equal. Thus the critical angular frequency of rotational stirring  $\omega_c$  to permit single vortex cycling is given (for a small stirrer) by

$$\omega_c = E_v - E_g. \quad (6.14)$$

This is a readily calculable property of a condensate, and is particularly useful as it is independent of stirrer geometry. A finite stirrer shifts the energies of the ground and vortex eigenstates by  $\delta_s(n_v = 0)$  and  $\delta_v(n_v = 1)$  respectively, adjusting  $\omega_c$  by their difference. The effective critical angular frequency (which depends on the stirrer geometry) is

$$\omega'_c = [E_v + \delta_v(n_v = 1)] - [E_g + \delta_s(n_v = 0)]. \quad (6.15)$$

In general,  $\omega'_c$  is not shifted much from  $\omega_c$ , for example, in the  $C = 88.13$  case the finite stirrer size reduces  $\omega_c = 0.54$  to  $\omega'_c = 0.51$ . For very large stirrers, the energy shift prediction will become increasingly less accurate, as the distortion of the condensate will reduce the applicability of our ansatz Equation (6.1).

In Table 6.1 we list the critical angular speeds predicted by Equation (6.14) for a range of  $C$  values, along with the values of  $\omega_c$  found from our many numerical simulations of the full GP equation for  $C = 30$ ,  $C = 88.13$ , and  $C = 200$  cases. We cannot find  $\omega_c$  exactly from our simulations of the full GP equation, and so we report bounds for each value of  $C$ : the lower bound is the largest value of  $\omega_f$  for which we have observed single vortex cycling, while the upper bound is the smallest value of  $\omega_f$  for which we found multiple vortex behaviour. We also plot in Figure 6.5 the data given in Table 6.1.

$C$	$E_g$	$E_v$	$\omega_c$	simulation $\omega_c$
0	1	2	1	-
30	1.811	2.520	0.709	0.6–0.8
88.13	2.744	3.284	0.540	0.5–0.6
200	3.946	4.369	0.423	0.4–0.45
500	6.079	6.394	0.315	-
5000	18.860	19.000	0.140	-

Table 6.1: Critical angular frequency  $\omega_c$  for the two-dimensional condensate, as predicted by the two state model. The final column gives bounds on  $\omega_c$  found from extensive simulations of the full GP equation.

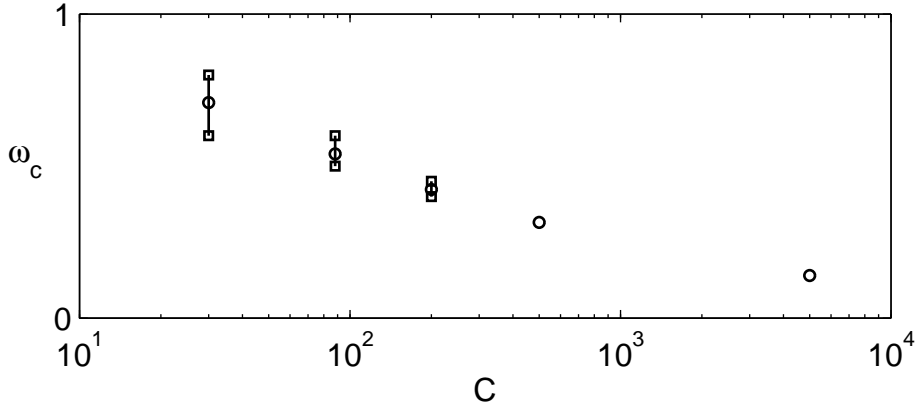


Figure 6.5: Critical angular frequency  $\omega_c$  predicted by the two state model (circles), and the bounds on  $\omega_c$  found from simulations of the full GP equation (squares). Values are from Table 6.1.

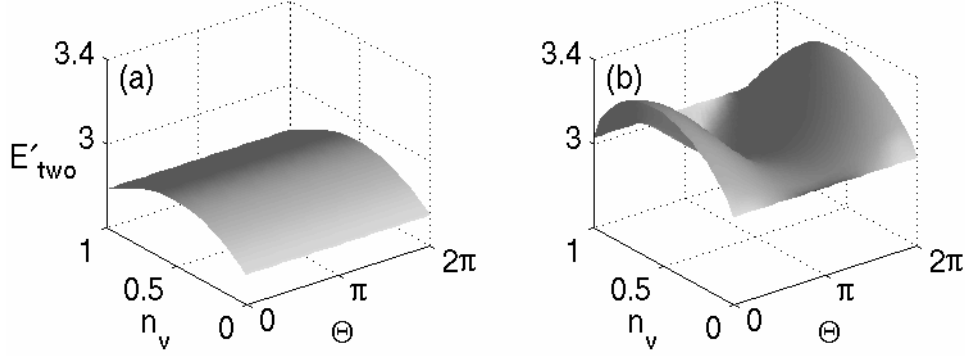


Figure 6.6: Energy in the rotating frame of the two state model, (a) in the absence of the stirrer, and (b) in the presence of the stirrer. Parameters as in Figure 6.2.

The agreement between the predictions from the two-state model and the full numerical simulation is excellent.

The critical angular frequency  $\omega_c$  for single vortex cycling, a dynamical process, is given by a criterion similar to that used to determine the thermodynamical stability of a central vortex in He II [57, 59, 94] or dilute alkali gas condensate [36]; the thermodynamical stability arguments consider the free energy of the system. These criteria differ in that the single vortex cycling regime is found for  $\omega_f$  *below*  $\omega_c$ , while the thermodynamical argument predicts stability for rotation *above* a critical angular frequency. We note that the form of Figure 6.5 is consistent with the heuristic result of Fetter [34] for thermodynamical stability of a vortex in a condensate.

### 6.5.2 Energy barrier

In Figure 6.6 we visualise  $E'_{two}$  as an energy surface, a function of  $n_v$  and  $\Theta$ , for the same parameters as in Figure 6.2. As shown in Figure 6.6(a), in the absence of a stirring potential, although the energies of the ground ( $n_v = 0$ ) and vortex ( $n_v = 1$ ) eigenstates are very close in energy, they are separated by a large energy barrier. The effect of introducing the stirring potential, as shown in Figure 6.6(b), is to deform the energy barrier and permit cycling from the ground to vortex state.

The energy barrier picture explains why the position and strength of the stirring potential are important in determining if single vortex cycling will occur. If the stirrer is far from the centre of the condensate, or is weak, then  $\Omega$  may be too small to distort the energy barrier sufficiently, and only incomplete cycling occurs even when  $\omega_f = \omega_c$ . This feature of the nonlinear system, which agrees with our  $r_s = 3$  simulations of the full GP equation, is in contrast to the ordinary Rabi case, where complete cycling occurs on resonance for any nonzero coupling field. For example, Figure 6.7(a) shows a case where  $\Omega$  (on average) decreases as  $r_s$  increases, and the corresponding single vortex cycling of the full GP simulation [Figure 6.7(b)] becomes weaker. The thick curves show the same situation as Figure 5.4, where full cycling occurs. As the distance of the stirrer from the centre increases, the Rabi frequency decreases (on average) and is less effective at distorting the energy barrier and permitting cycling between the ground and vortex states. This feature of the full GP simulations, correctly described by the two state model, is in marked contrast to on-resonance Rabi cycling in a linear two state system, in which a reduction in the Rabi frequency merely reduces the population transfer rate and cycling frequency yet full cycling still occurs. Our nonlinear two state model explains this difference.

We find that the width of the stirrer does not qualitatively change the dynamical behavior of the condensate; rather, the important issue is to generate a sufficiently large overlap (given by  $\Omega$ ) between the symmetric and vortex components, to cause single vortex cycling. We found in our full GP simulations of the  $C = 200$  case that a stirrer width of  $w_s = 1$  was insufficient to cause single vortex cycling, but a width of  $w_s = 2$  did induce cycling. The wider stirrer provided a Rabi frequency approximately four times that of the smaller stirrer, deforming the energy barrier and permitting cycling to occur, while the smaller stirrer could not. This behaviour in our simulations of the full GP equation is thus explained by the two state model.

### 6.5.3 Other characteristics

Although the two state model is strikingly successful in most respects, one remaining issue is that the position of the vortex in the condensate relative

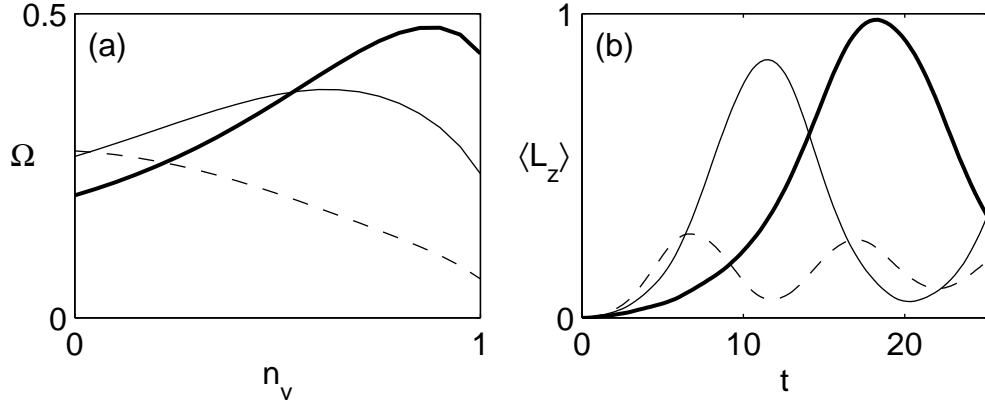


Figure 6.7: (a) The Rabi frequency of the two state model and (b) the angular momentum expectation value for the corresponding full GP simulations. The three lines correspond to  $r_s = 1.5$  (thick line),  $r_s = 2$  (thin line), and  $r_s = 3$  (dashed line). Parameters are otherwise as in Figure 6.4 [for (a)] and Figure 5.4 [for (b)].

to the position of the stirrer (given by  $\Theta$ ) deviates from that observed in the full GP simulations. Our ansatz [Equation (6.1)] permits the condensate density to heal about a vortex in the radial direction only; in the azimuthal direction the density has the form of an interference fringe and does not heal. A consequence of this is that the vortex is able to interact with the stirrer over a longer azimuthal distance than in the full GP representation, preventing a more representative evolution of  $\Theta$ .

## 6.6 Regime of validity

The nonlinear two state model describes a condensate rotationally stirred with  $\omega_f$  not more than the critical angular frequency  $\omega_c$ , and the validity of the two-state model breaks down when  $\omega_f$  exceeds  $\omega_c$ . In this regime higher energy vortex eigenstates are energetically accessible and mixed into the state of the system, as seen, for example, in Figure 5.1 and the upper thin curve of Figure 5.5. We can not expect the two state model to be relevant under these circumstances.

### 6.6.1 Linear regime

We noted in Chapter 5 that the  $C = 0$  condensate did not exhibit single vortex cycling. The two state model predicts  $\omega_c = 1$  for  $C = 0$ . Although no visible vortex cycling occurs below  $\omega_f = 0.25$ , a multiple vortex regime is entered at  $\omega_f = 0.8 < \omega_c$ . The formation of multiple vortices in the linear regime is a different type of behaviour to that which we have observed in the nonlinear system stirred just below  $\omega_c$ , in which we found single vortex cycling. The reason for this has been identified by Marzlin and Zhang [68], who modelled a vortex formation scheme which employs four counterpropagating lasers. They found, as we do in our stirring simulations, that in the linear regime multiple vortices would form, and pointed out that this was because in the linear regime all the vortex eigenstates of the system are equally spaced in energy. This gives rise to a “laddering” effect: viewed as multilevel system, if a process couples coherently from the ground to the  $m = +1$  central vortex eigenstate, then it may also couple from the  $m = +1$  to the  $m = +2$  central vortex eigenstate, and so forth, because the detuning for each transition is the same. The resulting superposition of higher  $m$  vortex eigenstates contains multiple vortices. The effect of the nonlinearity is to break the “laddering” effect by changing the energy spacing of the central vortex eigenstates, and so this effect does not occur in the nonlinear system. Our nonlinear two state model is not applicable for the  $C = 0$  case.



# Chapter 7

## Rotational stirring of three-dimensional condensates

### 7.1 Introduction

In this chapter, we extend our investigation of rotational stirring of a condensate, described in Chapter 5, into three dimensions. The numerical solution of the time-dependent Gross-Pitaevskii equation in three dimensions is a technically demanding task because of the large amount of computer memory required to store the computational grid. Furthermore, the processor time and memory bandwidth that must be used to operate on the large computational grid makes the efficiency of our method an important consideration, as we have discussed in Section 3.3.

Our Matlab implementation of the RK4IP algorithm in two dimensions is not sufficiently efficient for generalisation into three dimensions, partly because of the semantic constraints of the Matlab language [71]. We have completely reimplemented our numerical method in Python [84], as described in Section 3.3 and Appendix B, although we continue to use Matlab for analysis of the output data. We emphasise that our Python implementation of the RK4IP algorithm calculates full, general time-dependent solutions of the GP equation in three dimensions; our implementation is not reliant on cylindrical or any other symmetry. The implementation is sufficiently efficient to permit the simulation of experimentally interesting condensates on commodity PC

computer hardware.

We investigate the effect of rotationally stirring a condensate in traps with a range of geometries (oblate to prolate), and in each case we find that the single vortex cycling regime we discovered in two dimensions is also present in three dimensions. Because our full three-dimensional model can be directly related to current experimental configurations, we are able to give a detailed and specific experimental recipe to permit the investigation of this type of behaviour. We find that the parameter regime and timescales required are accessible to current experiments.

We also find that the nonlinear two state model that we presented in Chapter 6 accurately predicts the critical angular frequency of rotational stirring  $\omega_c$  for single vortex cycling in three dimensions. Furthermore, the model explains the importance of stirrer symmetry, predicting behaviour that we observe in simulations of the full time-dependent GP equation. We give the form of the two state model in three dimensions, and show that for three dimensions the same nonlinear Rabi equations are obtained as for two dimensions.

The line character of a vortex in three dimensions also gives rise to some qualitatively new behaviour that has no analogue in two dimensions. In a spherical trap, stirring of the condensate can produce two vortex lines which collide and exchange sections, a type of behaviour that hints at the richness of the dynamics of these structures. This was the first report of such dynamical phenomena in condensates [18, 17].

## 7.2 Three-dimensional model

The form of the theoretical model remains the same in three dimensions as it was in our two-dimensional treatment, except that the wavefunction  $\psi$  and potential  $V$  are now defined over three dimensions. In three dimensions, the Gaussian stirring potential is cylindrically symmetrical and parallel to the  $z$  axis. The total potential  $V = (x^2 + y^2 + \lambda^2 z^2)/4 + W$ , where

$$W(\mathbf{r}, t) = W_s(t) \exp \left[ - \left( \frac{|\boldsymbol{\rho} - \boldsymbol{\rho}_s(t)|}{w_s/2} \right)^2 \right], \quad (7.1)$$

and  $\boldsymbol{\rho}$  is the projection of  $\mathbf{r}$  onto the  $z = 0$  plane, and  $\boldsymbol{\rho}_s$  is the centre of the Gaussian in that plane.

In all our three-dimensional simulations, the initial state of the condensate is an eigenstate of the harmonic trap without the stirrer (typically the ground state). As a matter of practicality, it is much more convenient to begin our simulations from an eigenstate of the trap without the stirrer, because then one eigenstate can serve for many different stirrer positions and geometries.

### 7.3 Single vortex cycling

The condensate is stirred in a manner similar to that used in two dimensions (see Chapter 5). The stirrer moves in the anticlockwise sense in a circle of radius  $\rho_s$  with a constant angular velocity  $\omega_f$ , and we minimise transient effects by linearly increasing the stirrer amplitude from  $W_s = 0$  at  $t = 0$  to its final value  $W_s = W_0$  at  $t = \pi$ . With an appropriate choice of parameters, as in Figure 7.1, a single vortex line of positive sense (see Section 3.6.5) is drawn close to the centre of the condensate, and for continuous stirring cycles in and out. This is exactly the behaviour we found in two-dimensional condensates, and in fact the parameter choice for the single vortex cycling behaviour in three dimensions is guided by the same considerations outlined there, as we discuss below. In Figure 7.2 the evolution of the angular momentum expectation value is presented and confirms that for continuous stirring (thin line), the vortex cycles in and out of the condensate. We note that, as in the single vortex cycling regime in two dimensions, the stirrer moves well below the speed of sound. If we increase  $\omega_f$  so that  $\omega_f > \omega_c$ , we leave the single vortex cycling regime and multiple vortices penetrate the condensate, as in two dimensions.

#### 7.3.1 Generation of a central vortex state

In contrast to the two-dimensional case, the three-dimensional simulation can be unambiguously related to a realistic current experimental scenario. The  $C = 1000$  case shown in Figures 7.1–7.4 corresponds to  $N = 1.8 \times 10^4$  atoms of  $^{87}\text{Rb}$  in the  $|5S_{1/2}, F = 2, m_F = 2\rangle$  hyperfine state (for which we use an

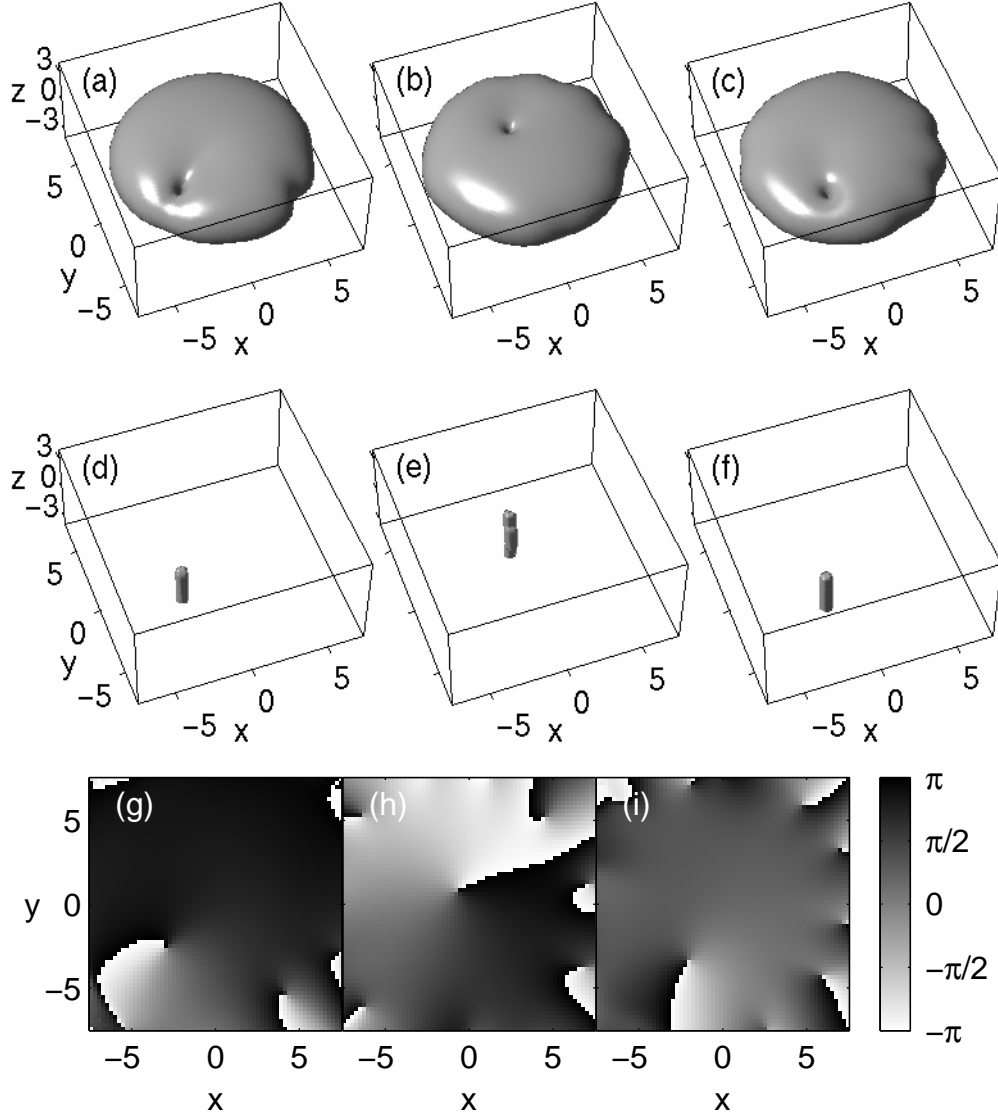


Figure 7.1: Sequence showing single vortex cycling in a rotationally stirred oblate condensate. The subfigures show (a–c) probability density isosurfaces (at  $|\psi|^2 = 10^{-4}$ ), (d–f) vortex lines ( $\kappa_v = 10^{-3}$ ), and (g–i) phase on the  $z = 0$  plane. The vortex lines detected are of positive sense. Times are (a,d,g)  $t = 13.70$ , (b,e,h)  $t = 25.76$ , and (c,f,i)  $t = 33.80$ . Parameters are  $C = 1000$ ,  $\lambda = \sqrt{8}$ ,  $W_0 = 4$ ,  $w_s = 4$ , and  $\rho_s = 2$ . The angular frequency of stirring  $\omega_f = 0.3$  is less than the critical angular frequency  $\omega'_c = 0.323$ . See also Figure E.5.

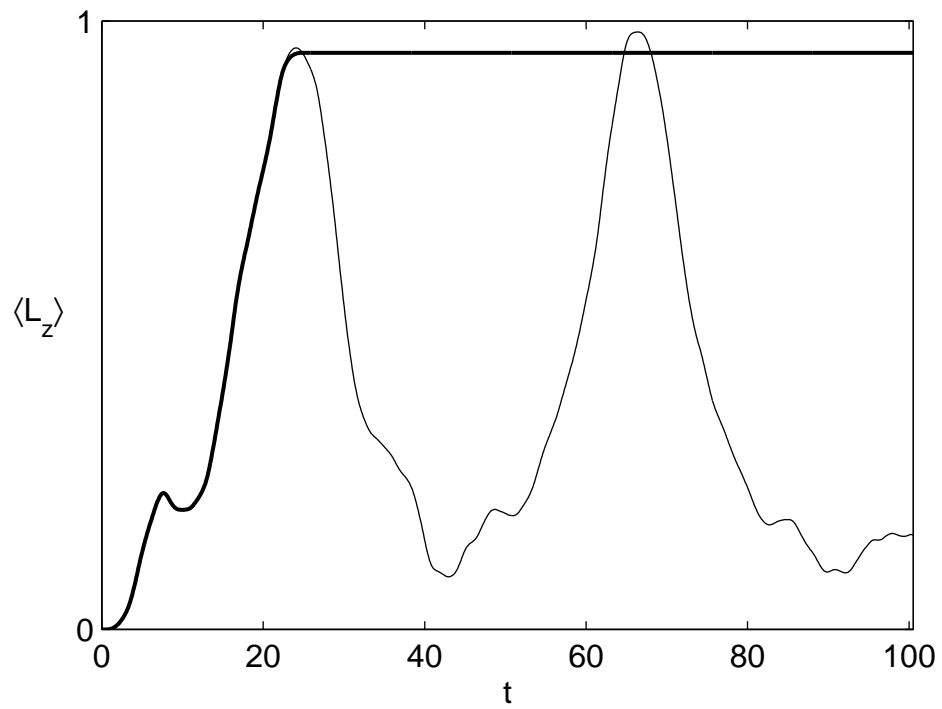


Figure 7.2: Condensate angular momentum expectation value for a rotationally stirred oblate condensate, for continuous stirring (thin line), or a stirrer linearly withdrawn between  $t = 7\pi$  and  $t = 8\pi$  (thick line). Parameters as in Figure 7.1.

s-wave scattering length  $a = 5.29$  nm [97]) in a time orbiting potential (TOP) trap with radial trap frequency  $\omega_r = 2\pi \times 15$  Hz and  $\lambda = \omega_z/\omega_r = \sqrt{8}$ .

We have chosen a somewhat small number of atoms and a shallow trap as these reduce  $C$  and consequently the computational difficulty of our simulations. For larger values of  $C$ , we would require a finer spatial grid (indicated by a reduced healing length) and also a smaller temporal step size (indicated by an increased chemical potential). However, we note that under the conditions of smaller number and a shallow trap, as has been pointed out by Lundh *et al.* [63], the larger effect of a vortex on the properties of the condensate aids experimental vortex detection.

For this example, our computational units of time and length [see Section 2.3] correspond to 10.6 ms and 1.97  $\mu\text{m}$  respectively, and the Thomas-Fermi diameter of the condensate in the radial direction of 11.7 corresponds to about 23  $\mu\text{m}$ . The stirrer Gaussian  $1/e$  diameter  $w_s = 4$  corresponds to a Gaussian  $1/e^2$  beam diameter of approximately 11  $\mu\text{m}$ . The required intensity of the stirring laser is detuning dependent, but can be easily calculated from the light shift potential, as we detail in Section 2.5. For example, if the laser beam is 50 nm blue-detuned from the 780 nm atomic transition ( $\sigma^+$  light on the fully stretched transition to the  $|5P_{3/2}, F = 3, m_F = 3\rangle$  hyperfine state), then the detuning is  $\Delta_L = 1.65 \times 10^{14} \text{ s}^{-1}$ , and a laser power of 300 nW is required for the 3 nK height stirrer we describe. The first angular momentum peak in Figure 7.2 occurs at 0.26 s, which is much less than the lifetime of such a condensate. The occurrence of the single vortex cycling behaviour in this experimentally accessible parameter regime suggests a method of preparing a central vortex state: stir the condensate as we have described, then remove the stirrer at the time when the angular momentum peak is expected. We illustrate the implementation of this method in Figure 7.2 with the thick curve, for which the stirrer is linearly withdrawn between  $t = 7\pi$  and  $t = 8\pi$ . Once the stirrer is removed,  $\langle L_z \rangle$  is constant and the vortex remains in the condensate, as shown in Figure 7.3, and circles about and close to the centre. Figure 7.4, where we plot the phase of the wavefunction, demonstrates that the central feature of Figure 7.3 is a vortex of positive circulation.

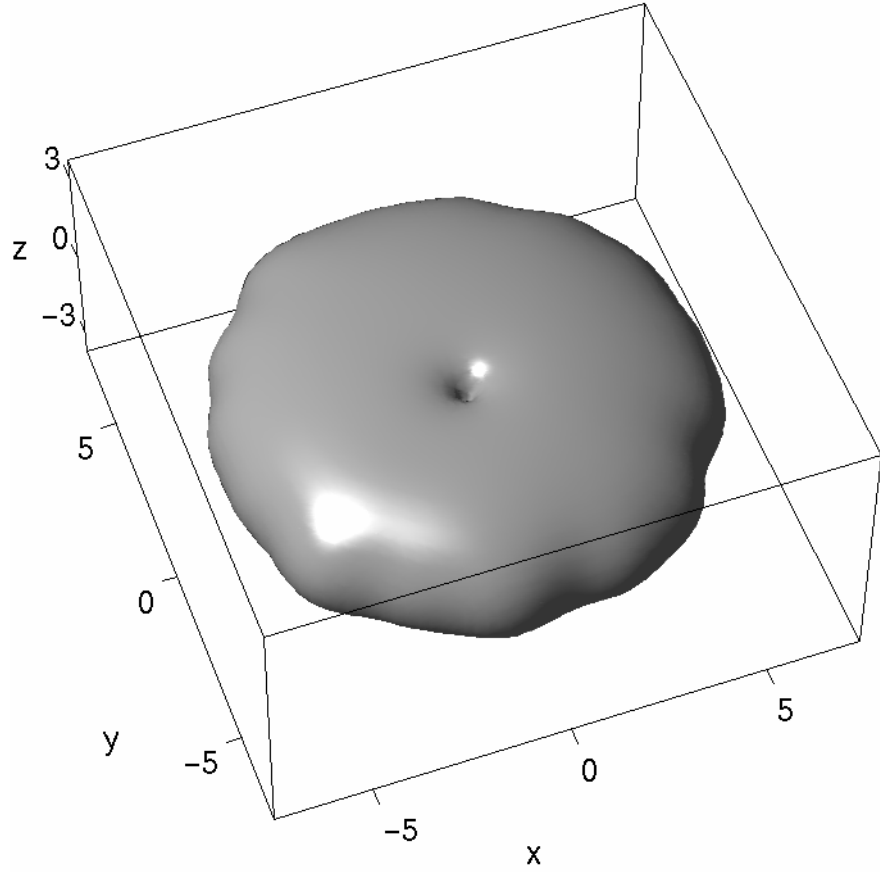


Figure 7.3: Probability density isosurface ( $|\psi|^2 = 10^{-4}$ ) for a rotationally stirred oblate condensate, where the stirrer has been linearly withdrawn between  $t = 7\pi$  and  $t = 8\pi$ . Here  $t = 94.12$ , and the hole near the centre of the condensate is a vortex that has been drawn in from the edge and remains close to the centre of the condensate. Parameters as in Figure 7.1. See also Figure E.6.

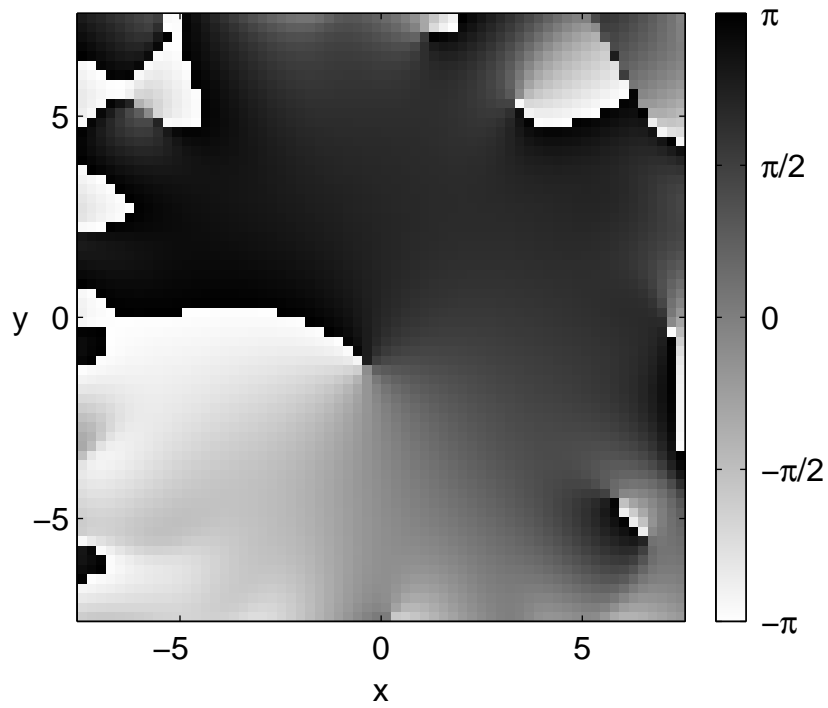


Figure 7.4: Phase in the  $z = 0$  plane for the condensate shown in Figure 7.3.



## 7.4 Two state model in three dimensions

The distinctive vortex cycling behaviour illustrated by the example in Figures 7.1–7.2 indicates that the two-state model described in Chapter 6 also has application in three-dimensions. We do not solve the two state model directly for the three-dimensional case, but we briefly outline the modifications required to extend the two-state model into three dimensions, showing that the resulting Rabi equations are of the same form. As in the two-dimensional case, we represent the condensate by an axisymmetric component  $\phi_s$ , and a vortexlike component  $\phi_v e^{i\theta}$  which has a circulation about the  $z$  axis, where  $\phi_s$  and  $\phi_v$  are real and nonnegative, so

$$\psi(\mathbf{r}, t) = a_s(t)\phi_s(\rho, z, n_v) + a_v(t)\phi_v(\rho, z, n_v)e^{i\theta}, \quad (7.2)$$

with  $\rho = \sqrt{x^2 + y^2}$ . This ansatz is the same as that made in two dimensions, except now the symmetric and vortex components are defined over  $z$  and  $\rho$  not just  $r$ . The derivation of the coupled equations is detailed in Appendix D. The basis wavefunctions  $\phi_s$  and  $\phi_v e^{i\theta}$  satisfy the following time-independent coupled equations,

$$\begin{aligned} \mu_s \phi_s = & \left[ -\frac{1}{\rho} \frac{d}{d\rho} \left( \rho \frac{d}{d\rho} \right) - \frac{d^2}{dz^2} \right. \\ & \left. + \frac{\rho^2 + \lambda^2 z^2}{4} + C (n_s \phi_s^2 + 2n_v \phi_v^2) \right] \phi_s, \end{aligned} \quad (7.3a)$$

$$\begin{aligned} \mu_v \phi_v = & \left[ -\frac{1}{\rho} \frac{d}{d\rho} \left( \rho \frac{d}{d\rho} \right) - \frac{d^2}{dz^2} + \frac{1}{\rho^2} \right. \\ & \left. + \frac{\rho^2 + \lambda^2 z^2}{4} + C (n_v \phi_v^2 + 2n_s \phi_s^2) \right] \phi_v. \end{aligned} \quad (7.3b)$$

As for Equations (6.4), the lowest energy eigenvalues  $\mu_s(n_v)$  and  $\mu_v(n_v)$  are found together with  $\phi_s$  and  $\phi_v$  by solving Equations (7.3) for a given choice of the vortex fraction  $n_v = |a_v|^2$  (where  $n_s = 1 - n_v$ ). As in the two-dimensional case, for  $n_v = 0$  or  $n_v = 1$ , Equations (7.3) reduce to time-independent GP equation for the ground or  $m = +1$  vortex eigenstate respectively. The resulting nonlinear Rabi equations for the two-state system (obtained by the same procedure given in Chapter 6 and Appendix D) are then identical in form to

Equations (6.8), but with the wavefunctions  $\phi_s$  and  $\phi_v$  now defined over  $\rho$  and  $z$  instead of  $r$ . All the other properties of the system hold.

The underlying assumption of our two-state model is that the ground state (or more generally,  $\phi_s$ ) is coupled primarily to the vortex state of lowest energy with axis parallel to the stirrer axis. In two dimensions, there are a limited number of excited condensate states in the appropriate energy range that can be coupled to the symmetric state by the stirring potential, and we have previously shown (in Chapter 6) that the two state model works well within a specified validity range. In three-dimensional cylindrically symmetric traps, many more condensate eigenstates exist, and although symmetry considerations limit the possible coupling from the symmetric state, a two state model places more constraint on the description of the system than in the two-dimensional case. We do not aim therefore to provide a detailed representation of the stirring behaviour with our two state model; instead, we use it primarily to provide conceptual understanding of the cycling behaviour. Nevertheless we also find it gives a quantitatively accurate prediction of the critical angular frequency of rotational stirring  $\omega_c$ , the frequency which causes a single vortex to cycle right to the centre of the condensate.

## 7.5 Role of trap geometry

We have examined the single vortex cycling behaviour using the full GP solution, for a variety of trap geometries including the oblate ( $\lambda = \sqrt{8}$ ), spherical ( $\lambda = 1$ ), and prolate ( $\lambda = 1/3$ ) cases, with a condensate of  $C = 1000$ , and a stirring potential of the same size and position as in Figure 7.1. We find that the critical rotational frequency for single vortex cycling is accurately predicted by the two state model as the difference in energy between the ground and vortex states of the condensate [modified by the finite size of the stirrer, as given in Equation (6.15)]. In table Table 7.1 and Figure 7.5, we give these predictions together with bounds found from our simulations of the full GP equation; agreement is excellent. As in the two-dimensional case (Chapter 5), a sufficiently large Rabi frequency is required to distort the energy barrier between ground and vortex state enough to permit cycling. When the critical

$\lambda$	$E_g$	$E_v$	$\omega_c$	$\omega'_c$	simulation $\omega_c$
$\sqrt{8}$	6.685	7.061	0.375	0.323	0.3–0.35
1	4.323	4.799	0.475	0.399	0.35–0.45
1/3	2.890	3.487	0.597	0.495	0.45–0.55

Table 7.1: Critical angular frequency of rotational stirring  $\omega_c$  for a three-dimensional condensate, and the effective critical angular frequency  $\omega'_c$  for stirrer geometry given by  $W_0 = 4$ ,  $w_s = 4$ , and  $\rho_s = 2$ . The final column gives bounds for  $\omega'_c$  found from our simulations of the full GP equation for this stirrer geometry.

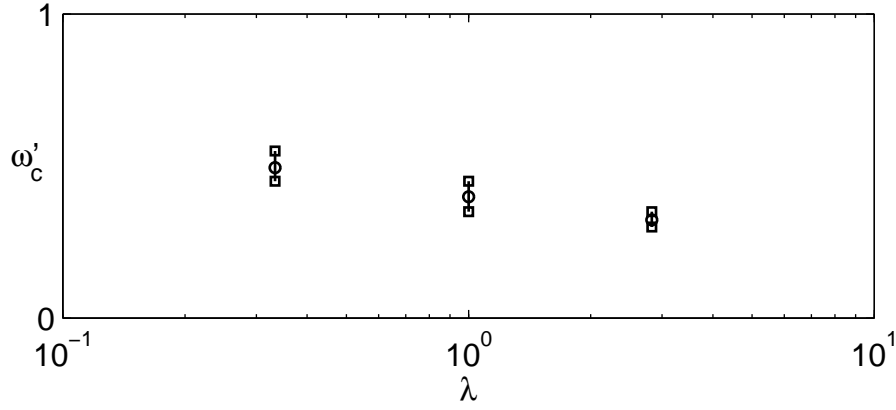


Figure 7.5: Effective critical angular frequency of rotational stirring  $\omega'_c$  (circles), and the bounds found from our simulations of the full GP equation (squares). Parameters and data as in Table 7.1.

frequency of rotation is exceeded, additional vortices penetrate the condensate.

It is worth noting that as the  $z$  component of the trapping potential becomes weaker (that is, as  $\lambda$  becomes smaller), then in addition to the vortex state, the stirring potential increasingly excites the dipole (centre of mass) oscillation of the condensate. This can be understood in terms of the Ehrenfest theorem (which we obtain in Section A.5): for our choice of parameters the mean force  $\langle -\nabla W \rangle$  of the stirrer increases as the condensate radial size decreases because the condensate is increasingly concentrated near the steepest part of the stirring potential. The centre of mass motion contributes angular

momentum  $\langle L_z \rangle_{COM}$  to the condensate angular momentum, where

$$\langle L_z \rangle_{COM} = \langle x \rangle \langle P_y \rangle - \langle y \rangle \langle P_x \rangle. \quad (7.4)$$

Thus, to characterise the angular momentum due to the presence of a vortex, we consider

$$\langle L_z \rangle_{vortex} = \langle L_z \rangle - \langle L_z \rangle_{COM}. \quad (7.5)$$

We find that  $\langle L_z \rangle_{COM}$  is negligible for the oblate ( $\lambda = \sqrt{8}$ ) case shown in Figure 7.2, and the peak of  $\langle L_z \rangle_{vortex}$  is only 0.03 less than the peak of  $\langle L_z \rangle$  shown in that figure; in that case the condensate is wider in the radial direction than for smaller values of  $\lambda$ , reducing the applied force and consequent dipole oscillation. For the spherical and prolate cases, the difference is significant, which can be seen by comparing Figure 7.6(a) with Figure 7.6(c) (spherical case), and comparing Figure 7.6(b) with Figure 7.6(d) (prolate case). We find that for all three trap geometries,  $\langle L_z \rangle_{vortex}$  cycles between 0 and 1 when  $\omega_f$  is less than  $\omega'_c$ ; this is the single vortex cycling regime, given by the thick lines in Figures 7.6(c,d). When  $\omega_f$  exceeds  $\omega'_c$ ,  $\langle L_z \rangle_{vortex}$  oscillates about 1 and multiple vortices penetrate the condensate; this is given by the thin lines in Figures 7.6(c,d).

The larger disturbance of the condensate by the stirrer for the  $\lambda = 1$  and  $\lambda = 1/3$  cases than for  $\lambda = \sqrt{8}$  alters the type of behaviour seen in the single vortex cycling regime. In the spherical ( $\lambda = 1$ ) case [Figures 7.7(a,b)], the stirring potential reduces the density at one edge of the condensate and permits the entry of a second vortex line at that edge, while in the prolate ( $\lambda = 1/3$ ) case [Figures 7.7(c,d)], the “cigar” shape of the condensate is deeply indented, and the vortex line is pressed up to the inside of the indentation. The deformation of each condensate increases with decreasing  $\lambda$ , because the height of the stirring potential is fixed ( $W_0 = 4$ ), while the chemical potential of the initial condensate state decreases with  $\lambda$ . In fact, for the  $\lambda = 1/3$  case,  $W_0$  exceeds the chemical potential of the ground eigenstate  $\mu = 3.84$ . By comparison, in the  $\lambda = \sqrt{8}$  case the chemical potential of the ground state is  $\mu = 8.95$ , more than twice the height of the stirring potential, the potential hardly disturbs the condensate, and the very pure single vortex cycling seen in Figures 7.1 and 7.2 is observed.

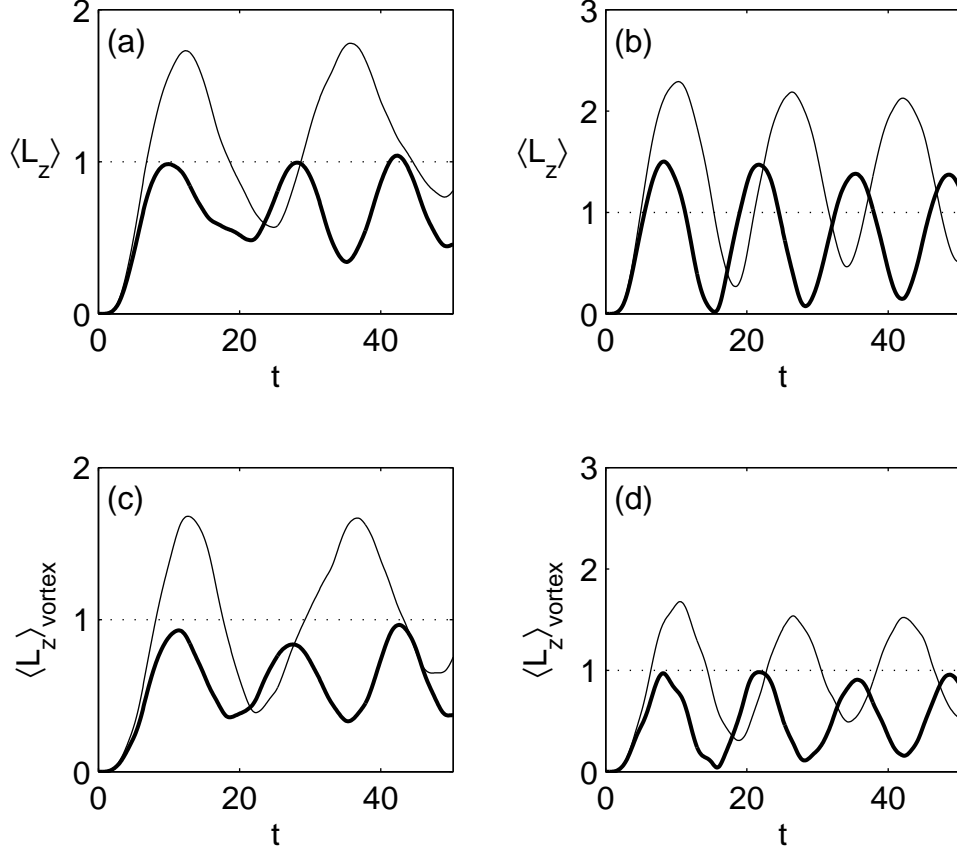


Figure 7.6: Angular momentum expectation values for rotationally stirred condensates, showing (a,b) the full angular momentum expectation value, and (b,c) the component of the angular momentum expectation value due to the presence of a vortex. In each case the single vortex cycling regime is shown as a thick line, and the multiple vortex regime as a thin line. For (a,c) the spherical case  $\lambda = 1$  and  $\omega'_c = 0.399$ ; we show results for  $\omega_f = 0.35 < \omega'_c$  (thick line) and  $\omega_f = 0.45 > \omega'_c$  (thin line). For (b,d) the prolate case  $\lambda = 1/3$  and  $\omega'_c = 0.495$ ; we show results  $\omega_f = 0.45 < \omega'_c$  (thick line) and  $\omega_f = 0.55 > \omega'_c$  (thin line). All other parameters as in Figure 7.1.

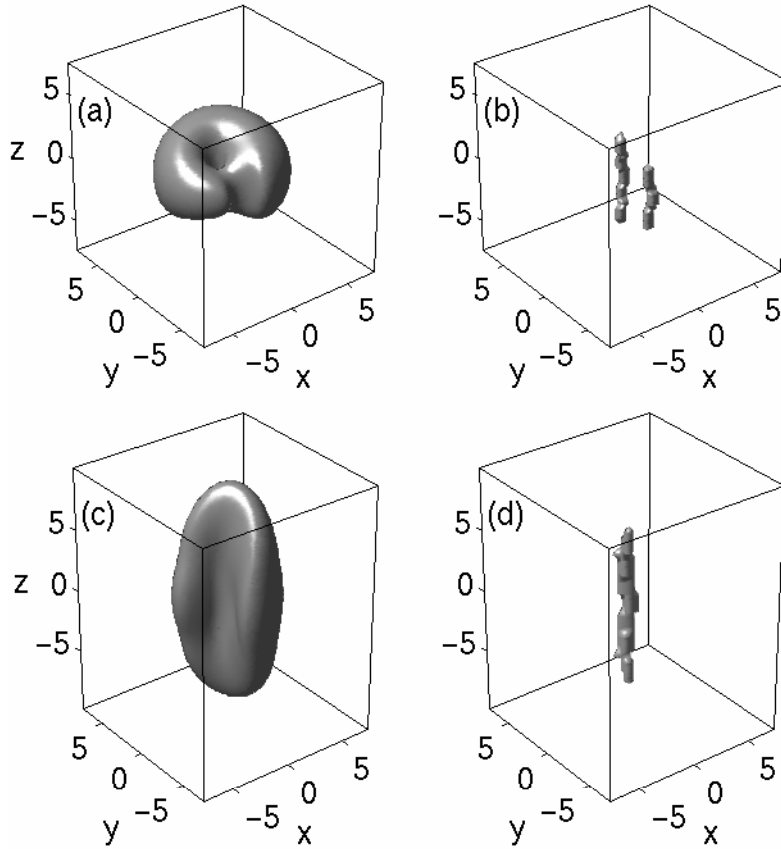


Figure 7.7: Rotationally stirred spherical and prolate condensates, showing (a,c) probability density isosurfaces (at  $|\psi|^2 = 10^{-3}$ ), and (b,d) vortex lines ( $\kappa_v = 10^{-3}$ ) for stirred condensates. The vortex lines detected are of positive sense. In (a,b) we show the spherical case ( $\lambda = 1$ ) for  $t = 11.31$ . In (c,d) we give the prolate case ( $\lambda = 1/3$ ) for  $t = 8.04$ . Other parameters are as in Figure 7.1.

We have retained the  $W_0 = 4$  stirrer in Figures 7.7 for consistency with the  $\lambda = \sqrt{8}$  results of Figures 7.1 and 7.2. We can obtain more distinct single vortex cycling behaviour in spherical ( $\lambda = 1$ ) case by using a weaker stirrer. For example, we have repeated the  $\lambda = 1$  case given in Figures 7.7(a,b) with a stirrer half the height ( $W_0 = 2$ ), with slightly increased stirring frequency  $\omega_f = 0.4 < \omega'_c$  (because  $\omega'_c = 0.437$  for this stirrer geometry), and with other parameters unchanged. With this weaker stirrer, we recover the distinctive single vortex cycling behaviour familiar from Figures 7.1 and 7.2, with negligible dipole oscillation. With such a weak stirrer, however, only one full cycle (peaking at  $t = 25.89$ ) is observed in a  $16\pi$  simulation.

## 7.6 Role of stirrer symmetry

We find that using a stirrer which does not have even symmetry is essential for single vortex cycling to occur. If the single stirrer used in Figure 7.1 is replaced by two half-height stirrers ( $W_0 = 2$ ) on opposite sides of the  $z$  axis, vortex cycling does *not* occur in the full GP model. Instead,  $\langle L_z \rangle$  exhibits only small oscillations and does not exceed 0.04. Likewise, if we stir the  $\lambda = 1/3$   $m = +1$  vortex eigenstate with two symmetrically placed stirrers just below  $\omega_c$ , no vortex cycling occurs and the vortex remains in the condensate. This is easily understood from our two state model, because the Rabi frequency  $\Omega$  [Equation (6.10c)] is zero for this stirrer configuration, as it is for any stirrer configuration of even symmetry. Simply put, an even coupling field cannot couple an even state to an odd state. In general, the Rabi frequency is zero for any  $W$  that is unchanged by a rotation of  $\pi$  about the  $z$  axis. For this reason, we expect any scheme which applies a constantly rotating symmetric distortion of the trapping potential (just below  $\omega_c$ ) to be ineffective at generating a single vortex in the condensate. It is interesting to note that Feder *et al.* [33] describe difficulties in generating vortices in time-dependent simulations of a rotating anisotropic trap, in the absence of high-frequency excitations. The trap used in that work is equivalent to a rotating distortion of even symmetry.

It is worth pointing out that our scenario of coherent cycling should be distinguished from vortex production by damping in a trap with a symmetric

rotating distortion, such as the recently reported experiment [64], or numerical damping schemes such as imaginary-time propagation used to find trap eigenstates [33]. In these situations, damping processes drive the system to the state with lowest energy in the rotating frame.

## 7.7 Vortex line collisions

In addition to confirming the basic features of the two state model of vortex cycling, our three-dimensional simulations also reveal striking new phenomena. The vortices produced in three dimensions by stirring are line vortices. In the  $\lambda = \sqrt{8}$  configuration, the lines are nearly straight and parallel to the stirrer axis, and when two lines of the same circulation form, we find they repel each other. For a spherical trap ( $\lambda = 1$ ) however, vortex lines along any direction are degenerate with the vortex eigenstate about the  $z$  axis (in the absence of the stirrer). Accordingly, the vortex lines can become more curved than in the oblate case, as we find in our simulations below the critical frequency, where the vortex that forms can have appreciable curvature. Above the critical frequency, when multiple vortices are drawn into the condensate, there is a striking consequence of this potential for vortex lines to deform: vortex lines can collide and exchange sections. In Figure 7.8, we show a collision sequence between two such curved vortex lines. The condensate is stirred somewhat above the critical frequency in a spherical trap, and by  $t = 6.79$  two vortex lines (both of positive sense [see Section 3.6.5]) have formed. The figure shows only the vortex lines (detected numerically), which have been shaded light and dark to distinguish one from the other. In Figure 7.8(a) the dark vortex line approaches the light vortex line from behind, and because of their mutual repulsion, the light line has developed a bulge. In Figure 7.8(b) the dark line is now close to the light line, causing the bulge to become recurved, with two small portions of the light line now nearly antiparallel to the dark line. In Figure 7.8(c) the two lines have completed a collision and exchanged their central sections. The key dynamical feature of this event is that, by curving, the lines become locally of opposite circulation at their point of contact, and so are attracted to each other and able to collide.



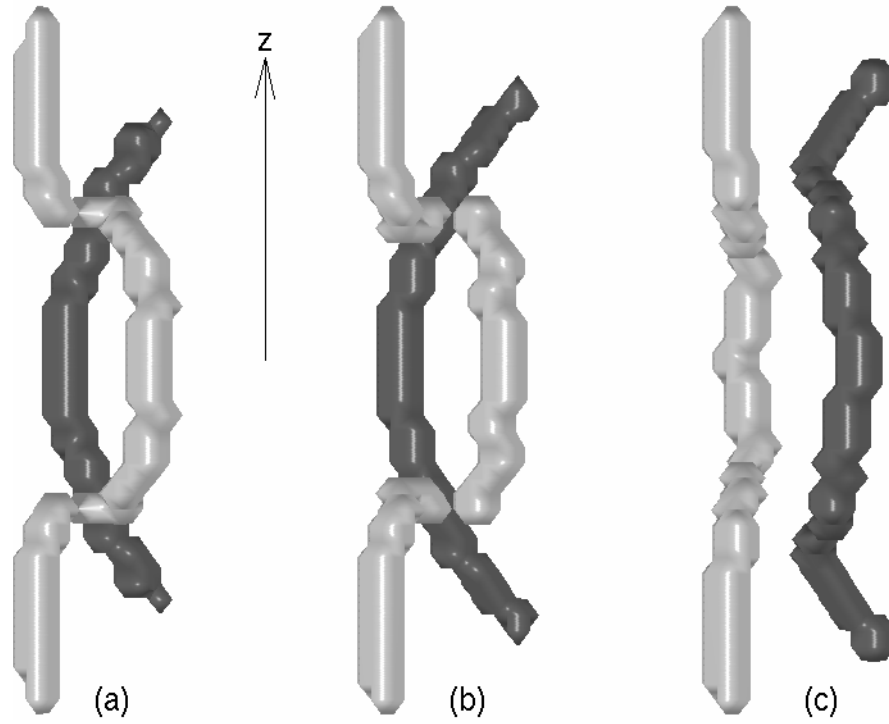


Figure 7.8: Sequence showing collision of vortex lines and exchange of sections in a rotationally stirred condensate. The view is from a position in the  $z = 0$  plane, looking almost down the  $y = -x$  line. In (a)  $t = 6.79$ , (b)  $t = 6.91$ , and (c)  $t = 7.04$ . The angular frequency of rotational stirring  $\omega_f = 0.45$  exceeds the effective critical angular frequency  $\omega'_c = 0.399$ . Other parameters are the same as in Figure 7.1, except that  $\lambda = 1$  and  $\kappa_v = 10^{-6}$ . See also Figure E.7.



# Chapter 8

## Vortex stability and persistent flow

### 8.1 Introduction

The stability of vortices in condensates has been a topic of some debate. Rokhsar [83] predicted that a singly quantised central vortex would be thermodynamically unstable and spiral out of a condensate. By contrast, Svidzinsky and Fetter [92] predicted, using a Thomas-Fermi approximation, that a singly quantised central vortex would be dynamically stable. Pu *et al.* [80] studied the effect of excitations on the stability of central vortices, and concluded that (for  $C > 0$ ) while a singly quantised central vortex would be stable, higher vortices could be unstable. Pu *et al.* [80] noted that their findings were consistent with our results in two dimensions (which we present in this chapter).

A point of confusion has been the distinction between thermodynamical and dynamical stability. A vortex is thermodynamically stable when its presence minimises the free energy of the system. This is the type of stability considered in studies of vortices in He II, in which a rotating container may allow a stable vortex to be present in the superfluid [57, 77, 59, 94]. On the other hand, dynamical stability of a vortex refers to the response of a vortex to a perturbation.

In this chapter, we are concerned with dynamical stability, and we have used two- and three-dimensional simulations to test the dynamical stability

(in the mean-field limit) of central vortex eigenstates by perturbing the condensate. We find that in the cases we consider, an  $m = +2$  central vortex is always unstable, in accord with previous findings, and we give a simple geometrical argument to explain this phenomenon. The  $m = +1$  vortex proves to be very stable, a feature which can be understood in terms of our nonlinear two state Rabi model. We also show that if the perturber is left in the  $m = +1$  eigenstate, the vortex remains in the condensate, a result which can be compared with persistent flow past an obstruction in He II.

In dilute alkali condensates, if the collision rate is low or the number of thermal atoms is small, the time required for a condensate to come into thermal equilibrium with its surrounding thermal cloud may be very long, and perhaps much longer than the condensate lifetime. It is in this regime that understanding the dynamical (as opposed to thermodynamical) stability of vortices becomes important. Experimental evidence is now available for the decay time of a vortex in a condensate [64], and indicates that in a high density condensate with a high energy vortex (along the long axis of the cigar-shaped condensate), the decay time of the vortex is still of the order of 1 s, which is much longer than the time scale for the experiment we propose in Section 7.3.1.

## 8.2 Vortex stability in two dimensions

In two dimensions, we perturb the condensate by inserting a Gaussian stirrer [given by Equation (5.1)] at a fixed position  $\mathbf{r}_s$ , with the stirrer height given by  $W_s(t) = W_0 \sin^2 2t$  between  $t = 0$  and  $t = \pi/2$ . After  $t = \pi/2$ , the perturber is removed. In Figure 8.1, we show with a sequence of figures the results of perturbing the  $m = +1$  eigenstate. The initial condition is given in Figures 8.1(a,b), and the stirrer is (nearly) fully inserted in Figures 8.1(c,d). The final figures in the sequence, Figures 8.1(e,f), show the condensate long after the perturber has been removed. We find that although the condensate wobbles vigorously, the vortex undergoes only a very stable small-amplitude oscillation about the trap centre. Our two state model of Chapter 6 provides a useful means of understanding this behaviour, since in the Rabi picture the perturbation constitutes stirring of very large effective detuning ( $\omega_f = 0$ ).

Consequently, there is a very small probability of transfer out of the initial vortex state.

The  $m = +2$  central vortex eigenstate contains a doubly-quantised vortex at its centre, and we perturb this eigenstate in precisely the same way as the  $m = +1$  eigenstate. As shown in Figure 8.2, upon perturbation the central vortex *immediately* dissociates into two unit vortices. These vortices remain near the centre of the condensate and circle around each other in a clockwise direction. This result is consistent with the well-known property of He II that vortices of the same sign repel [59].

### 8.3 Vortex stability in three dimensions

As we have shown in Chapter 7, three-dimensional condensates can exhibit dynamical behaviour which has no analogue in two dimensions, such as curving of vortex lines. As a consequence, it is not obvious *a priori* if the stability results which we have obtained in two dimensions are applicable in three dimensions. We have tested the dynamical stability of vortex eigenstates in three dimensions by a similar procedure to that we used in two dimensions. Beginning with a central vortex for  $C = 1000$  (an eigenstate of the time-independent GP equation), a perturbation was applied by linearly inserting (between  $t = 0$  and  $t = \pi/2$ ) and then withdrawing (between  $t = \pi/2$  and  $t = \pi$ ) a stirrer [given by Equation (7.1)] of the same size as in Figure 7.1 but at a fixed position  $\boldsymbol{\rho}_s$  in the laboratory frame. We find that for a range of trap geometries ( $\lambda = \sqrt{8}$ , 1, and  $1/3$ ), an  $m = +1$  central vortex line is dynamically stable, and remains near the centre of the condensate. As in the two-dimensional case, our two state model allows us to understand this result in terms of Rabi cycling. The stationary stirrer ( $\omega_f = 0$ ) provides a potential which is far-detuned from resonance ( $\omega_f = \omega_c$ ), and thus there is a low probability of transfer out of the initial (vortex) state. By contrast, in Figure 8.4 we show that for all of the trap geometries, the  $m = +2$  central vortex line is dynamically unstable and immediately dissociates into two unit vortex lines when perturbed. Again, we emphasise that these stability results refer to dynamical stability in the GP limit (that is,  $T = 0$ ), as opposed to thermodynamical stability [83, 35].

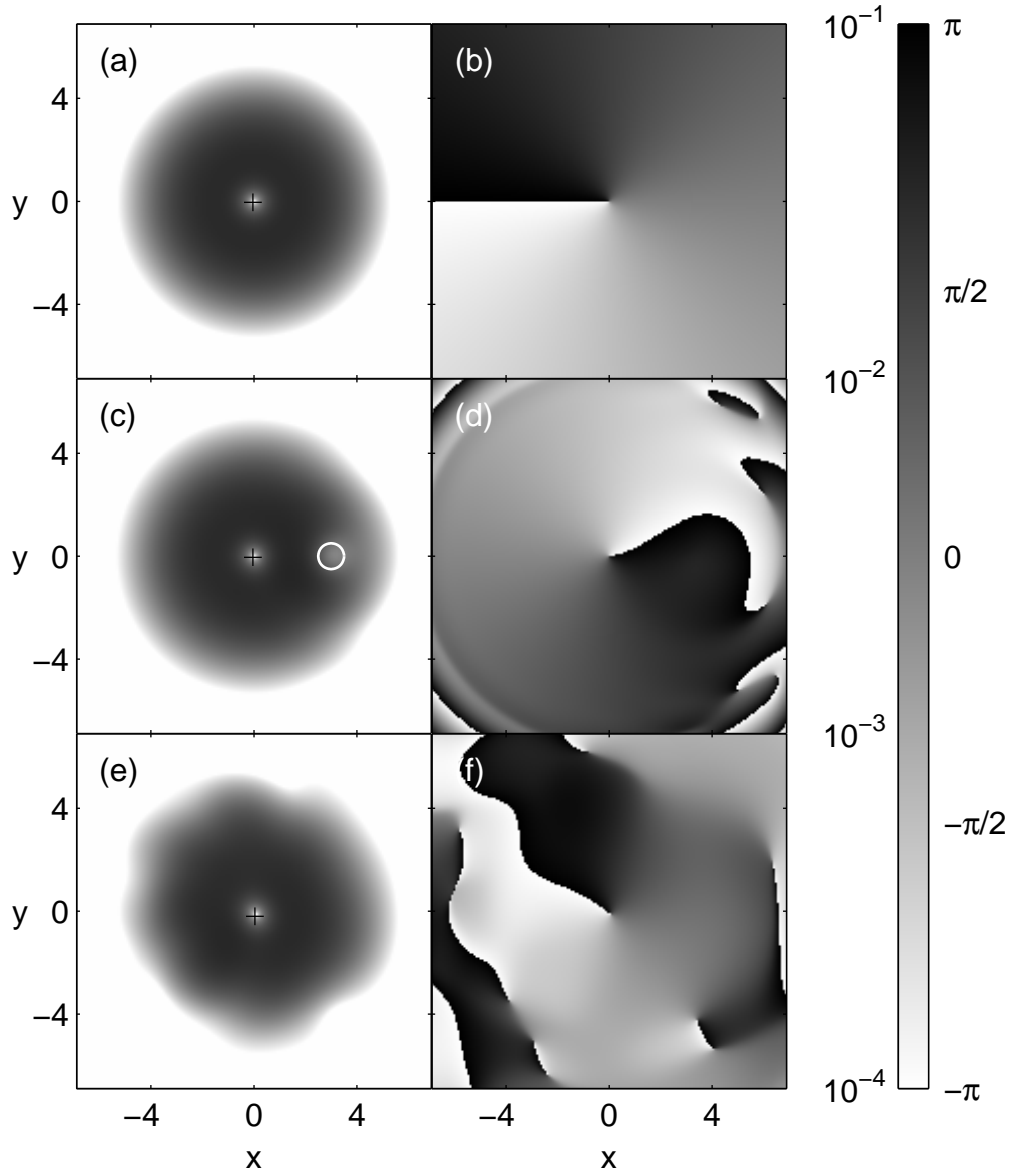


Figure 8.1: Sequence showing the perturbation of an  $m = +1$  central vortex eigenstate. We give (a,c,e) the probability density, and (b,d,f) the phase. Times are (a,b)  $t = 0$ , (c,d)  $t = 0.75$  (the circle marks the perturber), and (e,f)  $t = 4\pi$ . Parameters are  $C = 96.75$ ,  $W_0 = 10$ ,  $w_s = 1$ ,  $\mathbf{r}_s = (3, 0)$ , and  $\kappa_v = 10^{-3}$ .

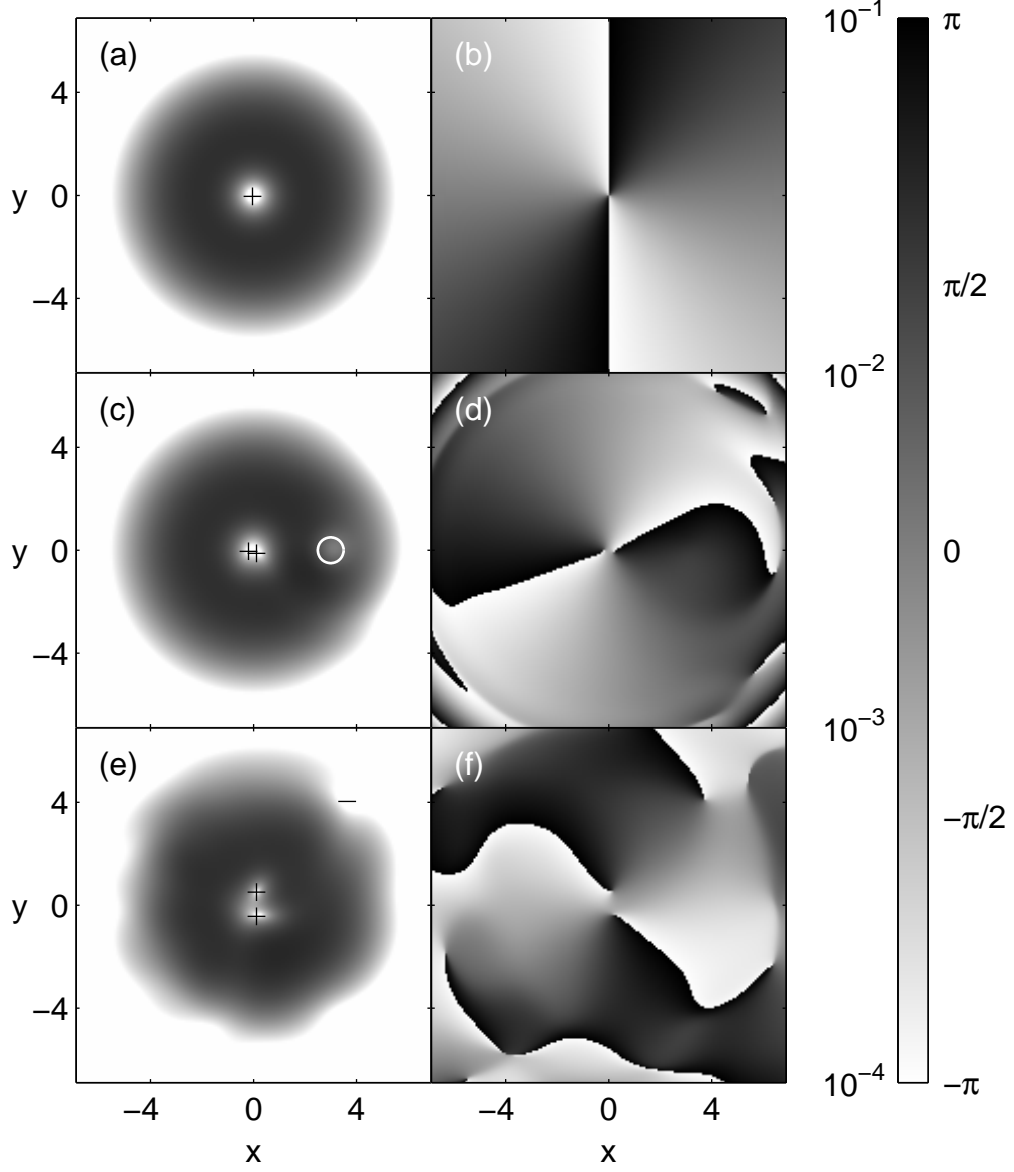


Figure 8.2: Sequence showing the perturbation of an  $m = +2$  central vortex eigenstate. We give (a,c,e) the probability density, and (b,d,f) the phase. Times and parameters are as in Figure 8.1 except that  $C = 97.97$ . We note that in (a) alone, the vortex detection algorithm makes two false positive detections near the origin. These elements of the vortex detection array  $\mathcal{V}$ , which are removed by hand, are due to the precise positioning and phase profile of this pure eigenstate causing  $\pi$  phase jumps between some grid points. See Section 3.6.

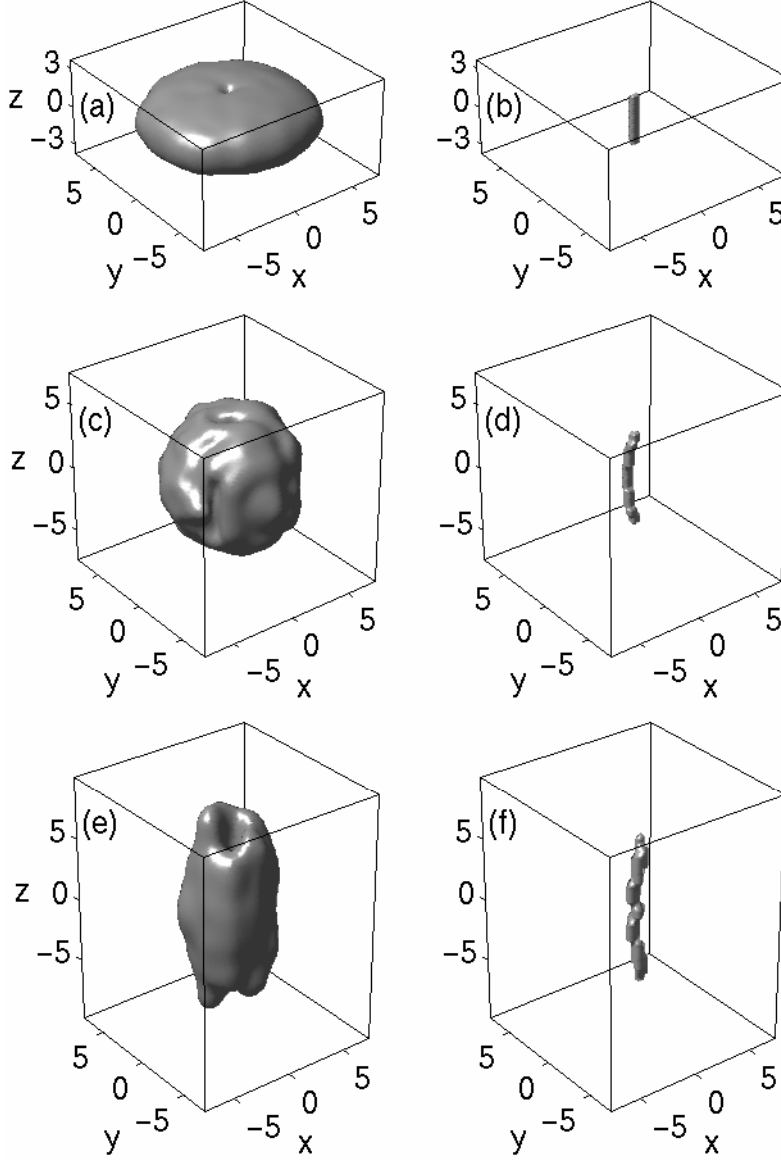


Figure 8.3: Central  $m = +1$  vortex eigenstate after perturbation, showing (a,c,e) probability density isosurfaces, and (b,d,f) vortex lines, at  $t = 16\pi$ . The vortex lines detected are of positive sense. The trap anisotropy is (a,b)  $\lambda = \sqrt{8}$ , (c,d)  $\lambda = 1$ , and (e,f)  $\lambda = 1/3$ . The isosurfaces are at (a,c)  $|\psi|^2 = 10^{-4}$ , and (e)  $|\psi|^2 = 10^{-3}$ . Parameters are  $C = 1000$ ,  $W_0 = 4$ ,  $w_s = 4$ ,  $\boldsymbol{\rho}_s = (2, 0)$ , and  $\kappa_v = 10^{-2}$ .



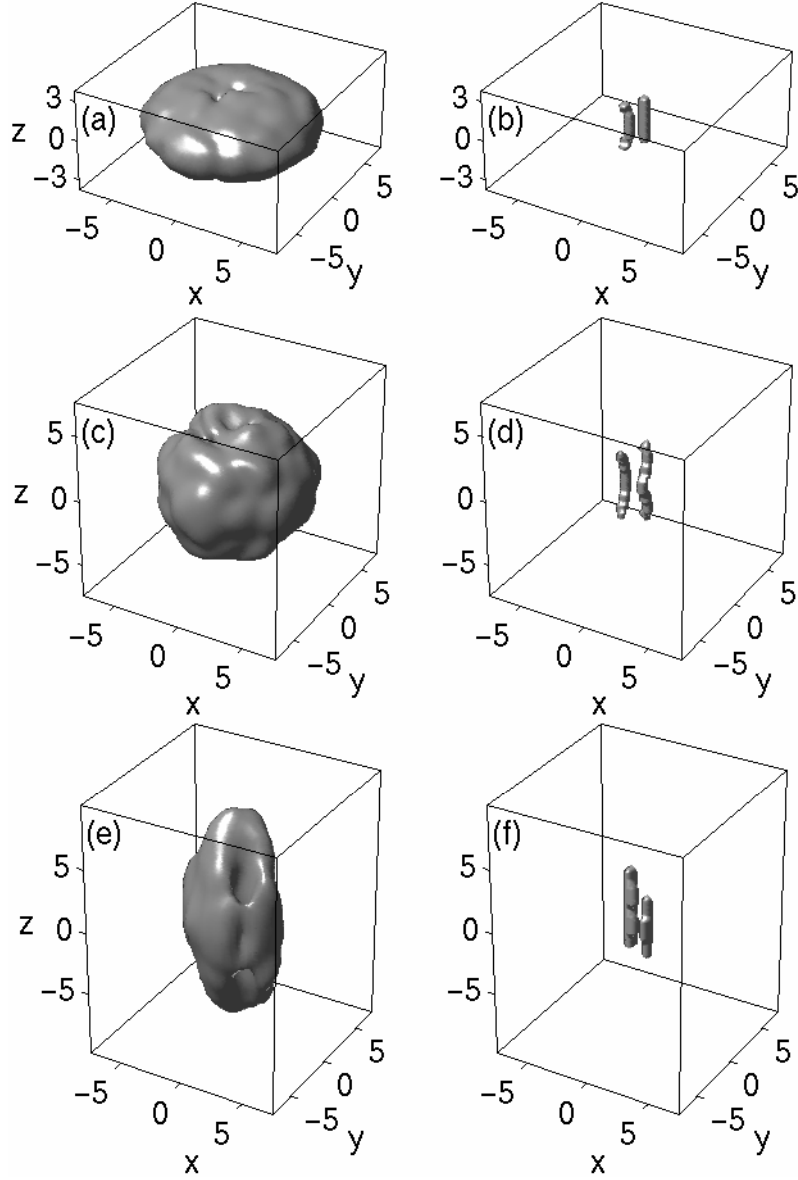


Figure 8.4: Central  $m = +2$  vortex eigenstate after perturbation, showing (a,c,e) probability density isosurfaces, and (b,d,f) vortex lines, at  $t = 16\pi$ . The vortex lines detected are of positive sense. All parameters are exactly as in Figure 8.3 (for corresponding subfigures), the only difference being the initial condition. We use a different viewpoint to show the separation between the vortex lines.

## 8.4 Persistent flow in a condensate

One of the fundamental and distinctive properties of superfluid He II is that it exhibits persistent rotation [77, 94]. If  $^4\text{He}$  in a rotating container is cooled below the “lambda” point (forming He II), then the superfluid continues to rotate even if the rotation of the container ceases [77], despite the roughness of the surface of the container. Even more dramatically, if a toroidal container packed with porous material and filled with  $^4\text{He}$  is similarly cooled and then stopped, the flow of the superfluid continues indefinitely (in excess of 12 hours) [94].

We investigate persistent flow in a trapped alkali condensate by modifying our perturbation of the three-dimensional  $\lambda = \sqrt{8}$   $m = +1$  central vortex eigenstate. The circulation of the central vortex is a superfluid flow, and we introduce an obstruction in the path of this flow. Instead of inserting and withdrawing the perturber as in the previous simulations, we linearly insert the perturber between  $t = 0$  and  $t = \pi$  and leave it in the condensate: the stationary perturber plays a role analogous to a porous obstruction in He II. We find in our simulation that the central vortex is displaced away from the perturber, but instead of falling out of the condensate as might have been expected, executes a small circle near the centre of the condensate. The fact that the vortex remains in the condensate is reflected by the angular momentum expectation value for this simulation, shown in Figure 8.5.

Our nonlinear two state model provided a significant insight into the issue of the dynamical stability of  $m = +1$  central vortex states, and precisely the same argument applies to the dynamical stability of persistent flow in condensates: a stationary perturber ( $\omega_f = 0$ ) corresponds to a very large detuning from resonance ( $\omega_f = \omega_c$ ) and so cycling between the vortex state and ground state does not occur, even over a long time. Despite the presence of an obstruction (the perturber), the superfluid (the condensate) exhibits persistent flow (the circulation of the vortex).

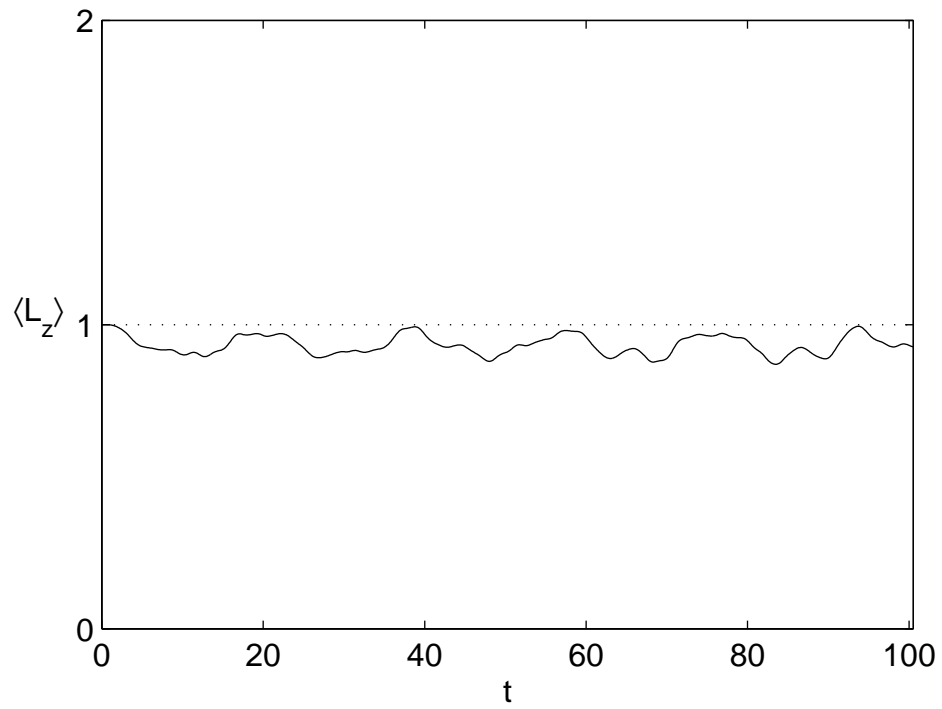


Figure 8.5: Angular momentum expectation value for a three-dimensional condensate, initially in the  $m = +1$  central vortex state, where a Gaussian perturber has been linearly inserted between  $t = 0$  and  $t = \pi$  and remains in the condensate. Parameters are the same as in Figures 8.3(a,b).

## 8.5 Effect of a uniform perturbation

We present here a simple geometrical analysis which allows us to understand qualitatively the difference in stability between the first and second quantised central vortex states: we consider a uniform perturbation, and study the local effect that this has on the central vortex. We shall study the system in two dimensions, and we note this analysis is also valid for any plane intersecting a vortex line in three dimensions. The  $m$ th quantised central vortex eigenstate (of lowest energy for that  $m$ ) is given in polar coordinates by

$$\psi_v(\mathbf{r}) = \phi(r)e^{im\theta}, \quad (8.1)$$

where the radial amplitude  $\phi$  is zero when  $r = 0$ , increases monotonically to  $\phi_{max}$  at  $r = r_{max}$ , and then decreases monotonically as  $r \rightarrow \infty$ . Following the circle  $r = r_{max}$ , we find a phase circulation of  $2\pi m$ . We consider a small uniform perturbation applied to the condensate. For brevity, we do not renormalise the wavefunction of the perturbed system, but we could for any uniform perturbation with a finite spatial extent. As we make only a local analysis, any long wavelength perturbation will have a similar effect to our uniform perturbation. The perturbed wavefunction is then

$$\psi_p(\mathbf{r}) = \phi(r)e^{im\theta} - \epsilon, \quad (8.2)$$

where the perturbation has amplitude  $\epsilon \ll \phi_{max}$ , and we have arbitrarily chosen its phase (without loss of generality). The phase circulation on the circle  $r = r_{max}$  is still  $2\pi m$ .

The effect of the perturbation is to split the density zero of  $\psi_v$  into  $|m|$  density zeros, each moved slightly from the origin, as we now analyse. For a small value of  $r$ , we can express  $\phi$  using a Taylor series expansion to first order about  $r = 0$  as

$$\phi(r) \approx r \frac{d\phi}{dr}. \quad (8.3)$$

The radial position  $r_v$  of the zeros of  $\psi_p$  are then given approximately by equating the two opposite amplitudes

$$r_v \frac{d\phi}{dr} = \epsilon, \quad (8.4)$$

to give

$$r_v = \frac{\epsilon}{d\phi/dr}, \quad (8.5)$$

while the azimuthal position of the zeros is given by  $\text{Arg } \psi_v = 0$ , so the zeros lie on angles

$$\theta_v = \frac{2\pi n}{|m|}, \quad (8.6)$$

where  $n \in \{0, 1, \dots, |m| - 1\}$ . Thus, the perturbing field separates the single central zero into  $|m|$  zeros. The lines where  $\theta = \theta_v + \pi/|m|$  are where the original wave was in phase with the perturbing wave, and so retain their original phase, dividing the new zeros into their own regions with circulating phase. We thus deduce, from the phase circulation of the system as a whole, that each one of the  $|m|$  zeros is a unit vortex with the same sign as  $m$ . The effect of the small perturbation is to split a central  $m$  vortex eigenstate into  $|m|$  unit vortices, which are distributed in a circle radius  $r_v$  about the origin. We illustrate in Figure 8.6 the effect of this splitting on  $m = +1$ ,  $m = +2$ , and  $m = +3$  vortices. Although in Figure 8.6 we show  $r_v$  to be the same for each case, in practice  $r_v$  will increase with increasing  $|m|$ ; this is because the centrifugal potential (the contribution to the Laplacian in Equation (2.29) due to the phase circulation) is proportional to  $m^2$ , and so  $d\phi/dr$  is smaller for larger  $|m|$ .

From this analysis, we see that the effect of a uniform perturbation on an  $m = +1$  central vortex is to merely shift the unit vortex, while in contrast, the effect on an  $m = +2$  central vortex is split the central vortex into two unit vortices which are shifted in opposite directions. Unlike a singly quantised vortex, which is made robust by the requirement that the phase circulation is preserved, nothing prevents the splitting of higher quantised vortices. This behaviour is consistent with our simulations of vortex perturbation in two and three dimensions.

We note that a different argument for the splitting of a doubly quantised vortex has been made by Rokhsar [83] in the context of thermodynamical stability, and that result is consistent with the scheme we present here.

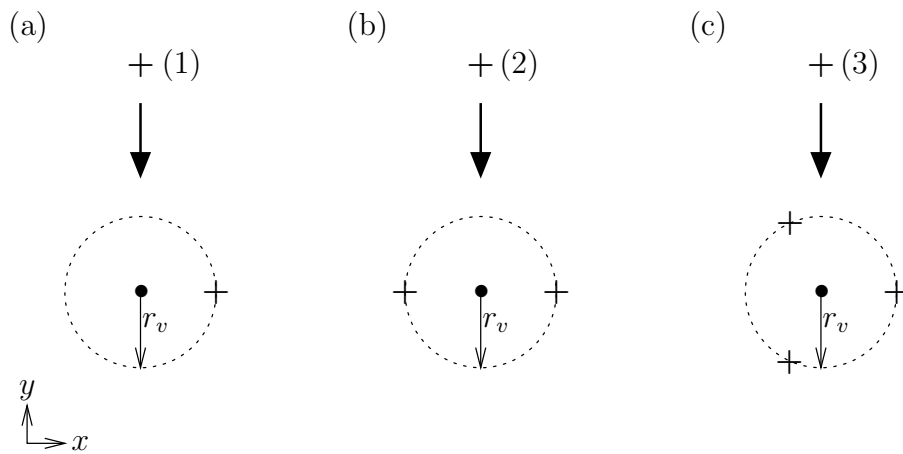


Figure 8.6: The effect of a uniform perturbation on a central vortex, for (a) a singly quantised ( $m = +1$ ) vortex, (b) a doubly quantised ( $m = +2$ ) vortex, and (c) a triply quantised ( $m = +3$ ) vortex.

# Chapter 9

## Conclusion

### 9.1 Vortex dynamics in condensates

In this work, we have conducted an extensive numerical and analytical investigation of the dynamics of vortices in dilute alkali gas Bose-Einstein condensates, in axially symmetric harmonic traps. Our work considers the condensate in the mean field limit, which is a low temperature limit well described by the Gross-Pitaevskii equation. The time-dependent Gross-Pitaevskii equation resists analytical treatment, and exploration of the dynamics of the condensate thus requires numerical solution, a very difficult computational undertaking. We have developed a highly efficient implementation of a numerical method to calculate the time evolution of the condensate. This implementation has allowed us to perform fully three-dimensional time-dependent simulations of condensates, calculations previously thought to require the use of supercomputers, using commodity PC computer hardware. We have also devised a robust and efficient numerical algorithm which automates the task of detecting vortices in the mean field.

Vortices are a characteristic feature of a superfluid; it is only their presence which permits circulation of the fluid, or allows two flows with different velocities to join. We have demonstrated with simulations in two dimensions that vortices are readily formed in condensates by a variety of means, including collisions between condensates or with an aperture, or by mechanical perturbation with a moving probe. We have shown that a rotationally stirred

condensate can exhibit, depending on the angular frequency of the stirrer, prolific formation of vortices, or a single vortex cycling behaviour.

Previously it had been thought that vortex formation was inherently related to perturbations exceeding the speed of sound, but we have shown that rotational stirring can form vortices even when the linear speed of the stirrer is much less than the local speed of sound. While the work of Jackson *et al.* [51] shows that exceeding the speed of sound may be sufficient for vortex formation, our results demonstrate that for rotational stirring this is not a necessary condition.

We have shown that the single vortex cycling induced by rotational stirring is a coherent phenomenon, and can be explained quantitatively using a nonlinear two state model. This model allows us to make a number of predictions, which are borne out by solutions of the full time-dependent GP equation. In particular, the model provides a quantitative prediction for the critical angular frequency of rotational stirring, at which a vortex cycles from the edge to the centre of the condensate. Although originally developed in two dimensions, we have shown how to extend the model into three dimensions, and have demonstrated by solution of the full GP equation that the predictions of the two state model also hold in three dimensions. The model enables us to understand that there is an energy barrier between the ground and vortex eigenstates of the condensate, and that stirring deforms the energy barrier and allows the vortex to penetrate the condensate.

We have related our simulations in three dimensions to current experimental configurations, and have demonstrated how the cycling behaviour could be used to generate a central vortex state. We have also given initial evidence of the rich dynamical behaviour of vortex lines: a collision between two vortex lines in which sections are exchanged.

Using time-dependent simulations in two and three dimensions, we have demonstrated that  $m = +1$  central vortex eigenstates are dynamically stable, and interpreted this stability in terms of our nonlinear two state model. This is an example of persistent flow past an obstruction, much like those demonstrated experimentally in He II. The  $m = +2$  central vortex eigenstates on the other hand are dynamically unstable, which we have explained with a simple



geometrical argument.

## 9.2 Directions for future work

The Matlab implementation of the RK4IP algorithm in two dimensions which we developed in this work has broad application in simulating Bose-Einstein condensates, and has already been adapted to condensates of two hyperfine components [31, 56]. The efficient Python implementation of the RK4IP algorithm can similarly be adapted to multi-component systems.

Vortices in condensates are attracting intense current interest, with recent experiments having obtained vortices in condensates [70, 64, 2], and early results showing that the line character of vortices is important [41]. Our efficient three-dimensional implementation of the numerical method can be used to further investigate the rich dynamics of these structures.

Marshall *et al.* [65] have shown (in two dimensions) that the GP equation can be used to simulate finite temperature effects. Our three-dimensional implementation of the numerical method can similarly be used to model cooling in three dimensions, or the influence of quasiparticle excitations on single vortex cycling and the dynamics of vortex lines.



# References

- [1] L. Allen and J. H. Eberly, *Optical Resonance and Two-Level Atoms* (Wiley, New York, 1975).
- [2] B. P. Anderson, P. C. Haljan, C. E. Wieman, and E. A. Cornell, “Vortex Precession in Bose-Einstein Condensates: Observations with Filled and Empty Cores,” *Physical Review Letters* **85**(14), 2857–2860 (2000).
- [3] M. H. Anderson, J. R. Ensher, M. R. Matthews, C. E. Wieman, and E. A. Cornell, “Observation of Bose-Einstein Condensation in a Dilute Atomic Vapor,” *Science* **269**(5221), 198–201 (1995).
- [4] M. R. Andrews, C. G. Townsend, H.-J. Miesner, D. S. Durfee, D. M. Kurn, and W. Ketterle, “Observation of Interference Between Two Bose Condensates,” *Science* **275**(5300), 637–641 (1997).
- [5] D. Ascher, P. F. Dubois, K. Hinsen, J. Hugunin, and T. Oliphant, *Numerical Python* (1999), see also <<http://numpy.sourceforge.net/>>.
- [6] V. Bagnato, D. E. Pritchard, and D. Kleppner, “Bose-Einstein condensation in an external potential,” *Physical Review A* **35**(10), 4354–4358 (1987).
- [7] R. J. Ballagh, “Partial Differential Equation Algorithm : Conceptual,” unpublished personal papers (1995).
- [8] R. J. Ballagh, K. Burnett, and T. F. Scott, “Theory of an Output Coupler for Bose-Einstein Condensed Atoms,” *Physical Review Letters* **78**(9), 1607–1611 (1997).

- 
- [9] R. J. Ballagh and B. M. Caradoc-Davies, “Coherent Vortex Dynamics in Two and Three Dimensional Bose-Einstein Condensates,” in *Directions in Quantum Optics*, edited by H. J. Carmichael, R. J. Glauber, and M. O. Scully, volume 531 of *Lecture Notes in Physics* (Springer, Berlin, 2000), in press.
  - [10] R. J. Ballagh, T. F. Scott, K. Burnett, and B. M. Caradoc-Davies, “Fundamental structures in Bose-Einstein Condensates : Formation of gray solitons and vortices by condensate collisions,” Poster presented at *Bose-Einstein Condensation in Atomic Vapors*, Castelvechio Pascoli, Italy, 12–17 July 1997.
  - [11] G. Baym and C. J. Pethick, “Ground-State Properties of Magnetically Trapped Bose-Condensed Rubidium Gas,” *Physical Review Letters* **76**(1), 6–9 (1996).
  - [12] J.-P. Blaizot and G. Ripka, *Quantum Theory of Finite Systems* (MIT Press, Cambridge, Massachusetts, 1986).
  - [13] P. B. Blakie, R. J. Ballagh, and C. Fox, in preparation.
  - [14] E. L. Bolda and D. F. Walls, “Detection of Vorticity in Bose-Einstein Condensed Gases by Matter-Wave Interference,” *Physical Review Letters* **81**(25), 5477–5480 (1998).
  - [15] B. H. Bransden and C. J. Joachain, *Introduction to quantum mechanics* (Longman, Harlow, Essex, 1989).
  - [16] D. A. Butts and D. S. Rokhsar, “Predicted signatures of rotating Bose-Einstein condensates,” *Nature* **397**(6717), 327–329 (1998).
  - [17] B. M. Caradoc-Davies, R. J. Ballagh, and P. B. Blakie, “Three-dimensional vortex dynamics in Bose-Einstein condensates,” *Physical Review A* **62**(1), 011602(R) (2000), see also Appendix F.
  - [18] B. M. Caradoc-Davies, R. J. Ballagh, and K. Burnett, “Coherent Vortex Dynamics in Bose-Einstein Condensates,” Poster presented at *Bose-*

- Einstein Condensation in Atomic Vapors*, San Feliu de Guixols, Spain, 11-16 September 1999.
- [19] B. M. Caradoc-Davies, R. J. Ballagh, and K. Burnett, “Coherent Dynamics of Vortex Formation in Trapped Bose-Einstein Condensates,” *Physical Review Letters* **83**(5), 895–898 (1999), see also Appendix F.
- [20] C. Cohen-Tannoudji, B. Diu, and F. Laloë, *Quantum Mechanics*, volume 1 (Wiley, New York, 1977).
- [21] C. Cohen-Tannoudji, J. Dupont-Roc, and G. Grynberg, *Atom-Photon Interactions : Basic Processes and Applications* (Wiley, New York, 1992).
- [22] F. Dalfovo, S. Giorgini, L. P. Pitaevskii, and S. Stringari, “Theory of Bose-Einstein condensation in trapped gases,” *Reviews of Modern Physics* **71**(3), 463–512 (1999).
- [23] F. Dalfovo, C. Minniti, and L. P. Pitaevskii, “Frequency shift and mode coupling in the nonlinear dynamics of a Bose-condensed gas,” *Physical Review A* **56**(6), 4855–4863 (1997).
- [24] F. Dalfovo and S. Stringari, “Bosons in anisotropic traps: Ground state and vortices,” *Physical Review A* **53**(4), 2477–2485 (1996).
- [25] K. B. Davis, M.-O. Mewes, M. R. Andrews, N. J. van Druten, D. S. Durfee, D. M. Kurn, and W. Ketterle, “Bose-Einstein Condensation in a Gas of Sodium Atoms,” *Physical Review Letters* **75**(22), 3969–3973 (1995).
- [26] R. J. Dodd, K. Burnett, M. Edwards, and C. W. Clark, “Excitation spectroscopy of vortex states in dilute Bose-Einstein condensed gases,” *Physical Review A* **56**(1), 587–590 (1997).
- [27] P. D. Drummond, “Central Partial Difference Propagation Algorithms,” *Computer Physics Communications* **29**, 211–225 (1983).

- 
- [28] R. Dum, J. I. Cirac, M. Lewenstein, and P. Zoller, “Creation of Dark Solitons and Vortices in Bose-Einstein Condensates,” *Physical Review Letters* **80**(14), 2972–2975 (1998).
- [29] M. Edwards and K. Burnett, “Numerical solution of the nonlinear Schrödinger equation for small samples of trapped neutral atoms,” *Physical Review A* **51**(2), 1383–1386 (1995).
- [30] M. Edwards, R. J. Dodd, C. W. Clark, P. A. Ruprecht, and K. Burnett, “Properties of a Bose-Einstein condensate in an anisotropic harmonic potential,” *Physical Review A* **53**(4), R1950–R1953 (1996).
- [31] A. Eschmann, R. J. Ballagh, and B. M. Caradoc-Davies, “Formation of Ramsey fringes in double Bose-Einstein condensates,” *Journal of Optics B: Quantum and Semiclassical Optics* **1**(4), 383–386 (1999).
- [32] D. L. Feder, C. W. Clark, and B. I. Schneider, “Vortex Stability of Interacting Bose-Einstein Condensates Confined in Anisotropic Harmonic Traps,” *Physical Review Letters* **82**(25), 4956–4959 (1999).
- [33] D. L. Feder, C. W. Clark, and B. I. Schneider, “Nucleation of vortex arrays in rotating anisotropic Bose-Einstein condensates,” *Physical Review A* **61**(1), 011601(R) (2000).
- [34] A. L. Fetter, “Dilute Bose-Einstein Condensate in a Trap: Characteristic Lengths and Critical Velocities,” in *Recent Progress in Many-Body Theories : Proceedings of the Ninth International Conference*, edited by D. Neilson and R. F. Bishop, 302–307 (World Scientific, Singapore, 1998).
- [35] A. L. Fetter, “Vortex Stability in a Trapped Bose Condensate,” *Journal of Low Temperature Physics* **113**(3), 189–194 (1998).
- [36] A. L. Fetter, “Theory of a dilute low temperature trapped Bose condensate,” in *Proceedings of the International School of Physics “Enrico Fermi” Course CXL : Bose-Einstein Condensation in Atomic Gases*,

- edited by M. Inguscio, S. Stringari, and C. E. Wieman, 201–263 (IOS Press, Amsterdam, 1999).
- [37] A. L. Fetter and J. D. Walecka, *Quantum Theory of Many-Particle Systems* (McGraw-Hill, San Francisco, 1971).
- [38] R. P. Feynman, *Statistical Mechanics : A Set of Lectures* (W. A. Benjamin, Reading, Massachusetts, 1972).
- [39] C. Fox, R. J. Ballagh, and A. Wall, in preparation.
- [40] M. Frigo and S. G. Johnson, *The Fastest Fourier Transform in the West (FFTW) 2.1* (1999), see also <http://www.fftw.org/>.
- [41] J. J. García-Ripoll and V. M. Pérez-García, “Nucleation of bended vortices in Bose-Einstein condensates in elongated traps,” [arXiv:cond-mat/0006368](https://arxiv.org/abs/cond-mat/0006368) (2000).
- [42] C. W. Gardiner, “Particle-number-conserving Bogoliubov method which demonstrates the validity of the time-dependent Gross-Pitaevskii equation for a highly condensed Bose gas,” *Physical Review A* **56**(2), 1414–1423 (1997).
- [43] H. Goldstein, *Classical Mechanics*, second edition (Addison-Wesley, Reading, Massachusetts, 1980).
- [44] A. Griffin, “Conserving and gapless approximations for an inhomogeneous Bose gas at finite temperatures,” *Physical Review B* **53**(14), 9341–9347 (1996).
- [45] A. Griffin, “A brief history of our understanding of BEC: From Bose to Beliaev,” in *Proceedings of the International School of Physics “Enrico Fermi” Course CXL : Bose-Einstein Condensation in Atomic Gases*, edited by M. Inguscio, S. Stringari, and C. E. Wieman, 1–13 (IOS Press, Amsterdam, 1999).
- [46] A. Griffin, D. W. Snoke, and S. Stringari, editors, *Bose-Einstein Condensation* (Cambridge University Press, 1995).

- 
- [47] J. L. Hall, M. Zhu, and P. Buch, “Prospects for using laser-prepared atomic fountains for optical frequency standards applications,” *Journal of the Optical Society of America B* **6**(11), 2194–2205 (1989).
- [48] D. A. W. Hutchinson, E. Zaremba, and A. Griffin, “Finite Temperature Excitations of a Trapped Bose Gas,” *Physical Review Letters* **78**(10), 1842–1845 (1997).
- [49] M. Inguscio, S. Stringari, and C. E. Wieman, editors, *Proceedings of the International School of Physics “Enrico Fermi” Course CXL : Bose-Einstein Condensation in Atomic Gases* (IOS Press, Amsterdam, 1999).
- [50] A. D. Jackson, G. M. Kavoulakis, and C. J. Pethick, “Solitary waves in clouds of Bose-Einstein condensed atoms,” *Physical Review A* **58**(3), 2417–2422 (1998).
- [51] B. Jackson, J. F. McCann, and C. S. Adams, “Vortex Formation in Dilute Inhomogeneous Bose-Einstein Condensates,” *Physical Review Letters* **80**(18), 3903–3906 (1998).
- [52] B. Jackson, J. F. McCann, and C. S. Adams, “Vortex rings and mutual drag in trapped Bose-Einstein condensates,” *Physical Review A* **60**(6), 4882–4885 (1999).
- [53] B. Jackson, J. F. McCann, and C. S. Adams, “Dissipation and vortex creation in Bose-Einstein condensed gases,” *Physical Review A* **61**(5), 051603(R) (2000).
- [54] G. M. Kavoulakis and C. J. Pethick, “Quasi-one-dimensional character of sound propagation in elongated Bose-Einstein condensed clouds,” *Physical Review A* **58**(2), 1563–1566 (1998).
- [55] M. Kozuma, L. Deng, E. W. Hagley, J. Wen, R. Lutwak, K. Helmerson, S. L. Rolston, and W. D. Phillips, “Coherent Splitting of Bose-Einstein Condensed Atoms with Optically Induced Bragg Diffraction,” *Physical Review Letters* **82**(5), 871–875 (1999).



- 
- [56] J. M. W. Krüger, *Dynamical Behaviour of Radio Frequency Output Couplers for a Bose-Einstein Condensate*, MSc thesis, University of Otago (2000).
  - [57] L. D. Landau and E. M. Lifshitz, *Statistical Physics*, second edition (Pergamon Press, Oxford, 1969).
  - [58] L. D. Landau and E. M. Lifshitz, *Mechanics*, third edition (Pergamon Press, Oxford, 1976).
  - [59] E. M. Lifshitz and L. P. Pitaevskii, *Statistical Physics : Part 2: The Condensed State* (Pergamon Press, Oxford, 1980).
  - [60] C. van Loan, *Computational Frameworks for the Fast Fourier Transform* (Society for Industrial and Applied Mathematics, Philadelphia, 1992).
  - [61] R. Loudon, *The Quantum Theory of Light*, second edition (Clarendon Press, Oxford, 1983).
  - [62] E. Lundh, C. J. Pethick, and H. Smith, “Zero-temperature properties of a trapped Bose-Condensed gas: Beyond the Thomas-Fermi approximation,” *Physical Review A* **55**(3), 2126–2131 (1997).
  - [63] E. Lundh, C. J. Pethick, and H. Smith, “Vortices in Bose-Einstein-condensed atomic fluids,” *Physical Review A* **58**(6), 4816–4823 (1998).
  - [64] K. W. Madison, F. Chevy, W. Wohlleben, and J. Dalibard, “Vortex Formation in a Stirred Bose-Einstein Condensate,” *Physical Review Letters* **84**(5), 806–809 (2000).
  - [65] R. J. Marshall, G. H. C. New, K. Burnett, and S. Choi, “Exciting, cooling, and vortex trapping in a Bose-condensed gas,” *Physical Review A* **59**(3), 2085–2093 (1999).
  - [66] J. L. Martin, *Magnetic Trapping and Cooling in Caesium*, DPhil thesis, Linacre College, University of Oxford (1997).
  - [67] K.-P. Marzlin and W. Zhang, “Laser-induced rotation of a trapped Bose-Einstein condensate,” *Physical Review A* **57**(5), 3801–3804 (1998).

- 
- [68] K.-P. Marzlin and W. Zhang, “Quantized circular motion of a trapped Bose-Einstein condensate: Coherent rotation and vortices,” *Physical Review A* **57**(6), 4761–4769 (1998).
- [69] K.-P. Marzlin, W. Zhang, and E. M. Wright, “Vortex Coupler for Atomic Bose-Einstein Condensates,” *Physical Review Letters* **79**(24), 4728–4731 (1997).
- [70] M. R. Matthews, B. P. Anderson, P. C. Haljan, D. S. Hall, C. E. Wieman, and E. A. Cornell, “Vortices in a Bose-Einstein Condensate,” *Physical Review Letters* **83**(13), 2498–2501 (1999).
- [71] C. Moler *et al.*, *MATLAB 5.3* (The MathWorks, Inc., 1999), see also <http://www.mathworks.com/>.
- [72] S. A. Morgan, *A Gapless Theory of Bose-Einstein Condensation in Dilute Gases at Finite Temperature*, DPhil thesis, St John’s College, University of Oxford (1999).
- [73] S. A. Morgan, R. J. Ballagh, and K. Burnett, “Solitary-wave solutions to nonlinear Schrödinger equations,” *Physical Review A* **55**(6), 4338–4345 (1997).
- [74] C. J. Myatt, *Bose-Einstein Condensation Experiments in a Dilute Vapor of Rubidium*, PhD thesis, University of Colorado (1998).
- [75] C. Nore, M. Abid, and M. E. Brachet, “Decaying Kolmogorov turbulence in a model of superflow,” *Physics of Fluids* **9**(9), 2644–2669 (1997).
- [76] C. Nore, M. Abid, and M. E. Brachet, “Kolmogorov Turbulence in Low-Temperature Superflows,” *Physical Review Letters* **78**(20), 3896–3899 (1997).
- [77] R. E. Packard and T. M. Sanders, Jr., “Observations on Single Vortex Lines in Rotating Superfluid Helium,” *Physical Review A* **6**(2), 799–807 (1972).

- 
- [78] W. H. Press, S. A. Teukolsky, W. T. Vetterling, and B. P. Flannery, *Numerical Recipes in C: The Art of Scientific Computing*, second edition (Cambridge University Press, 1992).
- [79] N.-P. Proukakis, *Microscopic Mean Field Theories of Trapped Bose-Einstein Condensates*, DPhil thesis, New College, University of Oxford (1997).
- [80] H. Pu, C. K. Law, J. H. Eberly, and N. P. Bigelow, “Coherent disintegration and stability of vortices in trapped Bose condensates,” *Physical Review A* **59**(2), 1533–1537 (1999).
- [81] C. Raman, M. Köhl, R. Onofrio, D. S. Durfee, C. E. Kuklewicz, Z. Hadzibabic, and W. Ketterle, “Evidence for a Critical Velocity in a Bose-Einstein Condensed Gas,” *Physical Review Letters* **83**(13), 2502–2505 (1999).
- [82] F. Reif, *Fundamentals of statistical and thermal physics* (McGraw-Hill, New York, 1965).
- [83] D. S. Rokhsar, “Vortex Stability and Persistent Currents in Trapped Bose Gases,” *Physical Review Letters* **79**(12), 2164–2167 (1997).
- [84] G. van Rossum, *Python 1.5.2* (Corporation for National Research Initiatives, 1999), see also <<http://www.python.org/>>.
- [85] P. A. Ruprecht, *Time-dependent Studies of Atomic Systems*, DPhil thesis, St John’s College, University of Oxford (1996).
- [86] P. A. Ruprecht, M. Edwards, K. Burnett, and C. W. Clark, “Probing the linear and nonlinear excitations of Bose-condensed neutral atoms in a trap,” *Physical Review A* **54**(5), 4178–4187 (1996).
- [87] P. A. Ruprecht, M. J. Holland, K. Burnett, and M. Edwards, “Time-dependent solution of the nonlinear Schrödinger equation for Bose-condensed trapped neutral atoms,” *Physical Review A* **51**(6), 4704–4711 (1995).

- 
- [88] A. I. Safonov, S. A. Vasilyev, I. S. Yasnikov, I. I. Lukashevich, and S. Jaakkola, “Observation of a Quasicondensate in Two-Dimensional Atomic Hydrogen,” *Physical Review Letters* **81**(21), 4545–4548 (1998).
- [89] T. F. Scott, R. J. Ballagh, and K. Burnett, “Formation of fundamental structures in Bose-Einstein condensates,” *Journal of Physics B: Atomic, Molecular, and Optical Physics* **31**(8), L329–L335 (1998).
- [90] L. A. Segel, *Mathematics Applied to Continuum Mechanics*, second edition (Dover Publications, New York, 1987).
- [91] S. Stringari, “Collective Excitations of a Trapped Bose-Condensed Gas,” *Physical Review Letters* **77**(12), 2360–2363 (1996).
- [92] A. A. Svidzinsky and A. L. Fetter, “Normal modes of a vortex in a trapped Bose-Einstein condensate,” *Physical Review A* **58**(4), 3168–3179 (1998).
- [93] J. Tempere and J. T. Devreese, “Fringe Pattern of Interfering Bose-Einstein Condensates with a Vortex,” *Solid State Communications* **108**(12), 993–996 (1998).
- [94] D. R. Tilley and J. Tilley, *Superfluidity and Superconductivity*, third edition (Institute of Physics Publishing, Bristol, 1990).
- [95] P. J. Ungar, D. S. Weiss, E. Riis, and S. Chu, “Optical molasses and multilevel atoms: theory,” *Journal of the Optical Society of America B* **6**(11), 2058–2071 (1989).
- [96] A. Wall, *Modulational Instability and Stimulated Raman Scattering in Optical Fibres*, MSc thesis, University of Otago (1996).
- [97] J. Weiner, V. S. Bagnato, S. Zilio, and P. S. Julienne, “Experiments and theory in cold and ultracold collisions,” *Reviews of Modern Physics* **71**(1), 1–85 (1999).
- [98] J. E. Williams and M. J. Holland, “Preparing topological states of a Bose-Einstein condensate,” *Nature* **401**(6753), 568–572 (1999).

- 
- [99] T. Winiecki, J. F. McCann, and C. S. Adams, “Pressure Drag in Linear and Nonlinear Quantum Fluids,” *Physical Review Letters* **82**(26), 5186–5189 (1999).
- [100] T. Winiecki, J. F. McCann, and C. S. Adams, “Vortex structures in dilute quantum fluids,” *Europhysics Letters* **48**(5), 475–481 (1999).



# Appendix A

## Properties of the Gross-Pitaevskii equation

### A.1 Outline

In this appendix, we prove some important properties of the time-dependent Gross-Pitaevskii equation [Equation (2.24)]. These properties provide valuable tests of the validity of our numerical methods, for if the quantities which are conserved by the GP equation are not approximately conserved by our methods, then they cannot reflect the true evolution of the system.

The conservation laws we prove in this appendix can be deduced with greater generality by considering the symmetry of the Lagrangian of the system. There is virtue, however, in a direct method of proof, and so we demonstrate here by explicit solution that the Gross-Pitaevskii equation contains all of the features expected by symmetry, and we also calculate the rates of change of those quantities which are not conserved. In particular we show that the Ehrenfest theorem [15] (and its analogue for angular momentum) hold for the GP equation (see also [73]).

### A.1.1 Time-dependent Gross-Pitaevskii equation

For the purposes of this appendix, it is most convenient to write the time-dependent GP equation with the time derivative alone on the left hand side,

$$\frac{\partial \psi(\mathbf{r}, t)}{\partial t} = -i [-\nabla^2 + V(\mathbf{r}, t) + C|\psi(\mathbf{r}, t)|^2] \psi(\mathbf{r}, t), \quad (\text{A.1})$$

because we will derive the conservation properties of the GP equation by differentiating the observables.

### A.1.2 Useful identities

If  $\psi(\mathbf{r})$  and  $\phi(\mathbf{r})$  are smooth scalar fields, then they satisfy Green's second identity,

$$\int_V (\phi \nabla^2 \psi - \psi \nabla^2 \phi) d\mathbf{r} = \int_S (\phi \nabla \psi - \psi \nabla \phi) \cdot d\mathbf{A}, \quad (\text{A.2})$$

where  $V$  is a volume bounded by  $S$ . The form of this identity most useful for our purposes occurs when the right hand side of Equation (A.2) is zero. We achieve this by taking  $V$  to be all space, and then for  $\psi(\mathbf{r})$  and  $\phi(\mathbf{r})$  and their derivatives vanishing as  $r \rightarrow \infty$ , Equation (A.2) becomes

$$\int \phi \nabla^2 \psi d\mathbf{r} = \int \psi \nabla^2 \phi d\mathbf{r}. \quad (\text{A.3})$$

Thus in an expression of this form, under integration over all space, the terms on either side of the Laplacian can be exchanged. This expression always holds for mean field (and its derivatives) representing the trapped condensates we consider. Other useful identities that we use in this appendix are

$$\nabla^2(x\psi) = x\nabla^2\psi + 2\frac{\partial\psi}{\partial x}, \quad (\text{A.4})$$

and

$$\begin{aligned} \nabla \times (f\mathbf{r}) &= f(\nabla \times \mathbf{r}) + (\nabla f) \times \mathbf{r} \\ &= -\mathbf{r} \times (\nabla f), \end{aligned} \quad (\text{A.5})$$

(since  $\nabla \times \mathbf{r} \equiv 0$ ).



## A.2 Probability

The mean field total probability is given by

$$p(t) = \int |\psi(\mathbf{r})|^2 d\mathbf{r} = \int \psi(\mathbf{r})^* \psi(\mathbf{r}) d\mathbf{r}, \quad (\text{A.6})$$

where we take  $p(0) = 1$  [Equation (2.25)]. Differentiating with respect to time,

$$\begin{aligned} \frac{dp}{dt} &= \int \left( \frac{\partial \psi^*}{\partial t} \psi + \psi^* \frac{\partial \psi}{\partial t} \right) d\mathbf{r}, \\ &\quad \text{and substituting Equation (A.1),} \\ &= \int \{ \psi [ +i(-\nabla^2 + V + C|\psi|^2) \psi^* ] \\ &\quad + \psi^* [ -i(-\nabla^2 + V + C|\psi|^2) \psi ] \} d\mathbf{r}, \\ &= i \int (\psi^* \nabla^2 \psi - \psi \nabla^2 \psi^*) d\mathbf{r}, \\ &\quad \text{and by Equation (A.3),} \\ &= 0, \end{aligned} \quad (\text{A.7})$$

and so  $p$  is a constant. That is, the GP equation conserves probability.

## A.3 Energy

The energy of the condensate is

$$E(t) = \int \left[ -\psi^* \nabla^2 \psi + \psi^* V \psi + \frac{1}{2} C |\psi|^4 \right] d\mathbf{r}, \quad (\text{A.8})$$

and its rate of change is given by

$$\begin{aligned} \frac{dE}{dt} &= \int \left[ -\frac{\partial \psi^*}{\partial t} \nabla^2 \psi - \psi^* \nabla^2 \frac{\partial \psi}{\partial t} \right. \\ &\quad + \frac{\partial \psi^*}{\partial t} V \psi + \psi^* \frac{\partial V}{\partial t} \psi + \psi^* V \frac{\partial \psi}{\partial t} \\ &\quad \left. + C \psi^* \psi^2 \frac{\partial \psi^*}{\partial t} + C \psi^{*2} \psi \frac{\partial \psi}{\partial t} \right] d\mathbf{r}. \end{aligned} \quad (\text{A.9})$$

Applying Equation (A.3) to the second term of Equation (A.9), then substituting Equation (A.1), we obtain

$$\begin{aligned}
\frac{dE}{dt} &= \int \psi^* \frac{\partial V}{\partial t} \psi d\mathbf{r} \\
&\quad + \int \left[ -i(-\nabla^2 \psi^* + V\psi^* + C|\psi|^2 \psi^*) \nabla^2 \psi \right. \\
&\quad \quad + i(-\nabla^2 \psi + V\psi + C|\psi|^2 \psi) \nabla^2 \psi^* \\
&\quad \quad + i(-\nabla^2 \psi^* + V\psi^* + C|\psi|^2 \psi^*) V\psi \\
&\quad \quad - i(-\nabla^2 \psi + V\psi + C|\psi|^2 \psi) V\psi^* \\
&\quad \quad + i(-\nabla^2 \psi^* + V\psi^* + C|\psi|^2 \psi^*) C|\psi|^2 \psi \\
&\quad \quad \left. - i(-\nabla^2 \psi + V\psi + C|\psi|^2 \psi) C|\psi|^2 \psi^* \right] d\mathbf{r}
\end{aligned}$$

and all the terms in the second integral cancel, giving

$$\begin{aligned}
&= \int \psi^* \frac{\partial V}{\partial t} \psi d\mathbf{r}, \\
&= \left\langle \frac{\partial V}{\partial t} \right\rangle.
\end{aligned} \tag{A.10}$$

Thus for a constant external potential  $V$ , the GP equation conserves energy.

## A.4 Position

The Ehrenfest theorem [15] relates the expectation values of the position, momentum, and force of the wavefunction of the Schrödinger equation, and shows that these values are connected by the same equations governing a classical particle: Newton's laws. Identical relations hold for the condensate; as we explicitly prove here, the nonlinearity does not change this result from the single particle case. The rate of change of the expectation value of the position is

$$\begin{aligned}
\frac{d\langle x \rangle}{dt} &= \int \left[ \frac{\partial \psi^*}{\partial t} x \psi + \psi^* x \frac{\partial \psi}{\partial t} \right] d\mathbf{r}, \\
&= +i \int \left[ (-\nabla^2 \psi^* + V\psi^* + C|\psi|^2 \psi^*) x \psi \right. \\
&\quad \left. - \psi^* x (-\nabla^2 \psi + V\psi + C|\psi|^2 \psi) \right] d\mathbf{r}, \\
&= +i \int \left[ -(x\psi) \nabla^2 \psi^* + \psi^* \nabla^2 (x\psi) - 2 \frac{\partial \psi}{\partial x} \right] d\mathbf{r},
\end{aligned} \tag{A.11}$$

and the first two terms of Equation (A.11) cancel by Equation (A.3), leaving the last term. Following a similar procedure for  $y$  and  $z$  yields

$$\frac{d\langle \mathbf{r} \rangle}{dt} = 2\langle \mathbf{P} \rangle, \quad (\text{A.12})$$

the first part of the Ehrenfest theorem. It is worth noting that the factor of two is an artifact of our choice of dimensionless quantities.

## A.5 Momentum

The rate of change of the expectation value of the momentum is

$$\begin{aligned} \frac{d\langle P_x \rangle}{dt} &= -i \int \left[ \frac{\partial \psi^*}{\partial t} \frac{\partial}{\partial x} \psi + \psi^* \frac{\partial}{\partial x} \frac{\partial \psi}{\partial t} \right] d\mathbf{r}, \\ &= \int \left[ (-\nabla^2 \psi^* + V \psi^* + C|\psi|^2 \psi^*) \frac{\partial \psi}{\partial x} \right. \\ &\quad \left. - \psi^* \frac{\partial}{\partial x} (-\nabla^2 \psi + V \psi + C|\psi|^2 \psi) \right] d\mathbf{r}, \\ &= \int \left[ -\frac{\partial \psi}{\partial x} \nabla^2 \psi^* + \psi^* \nabla^2 \frac{\partial \psi}{\partial x} + |\psi|^2 \frac{\partial V}{\partial x} \right. \\ &\quad \left. + C|\psi|^2 \left( \psi \frac{\partial \psi^*}{\partial x} + \psi^* \frac{\partial \psi}{\partial x} \right) \right] d\mathbf{r}. \end{aligned} \quad (\text{A.13})$$

The first two terms of Equation (A.13) cancel by Equation (A.3), while the last term

$$\frac{1}{2} C \int \frac{\partial}{\partial x} |\psi|^4 d\mathbf{r} = 0, \quad (\text{A.14})$$

by the fundamental theorem of calculus (integrating in the  $x$  direction) because  $|\psi|^4$  vanishes as  $x \rightarrow \pm\infty$ . Now only the third term of Equation (A.13) remains, and repeating for the  $y$  and  $z$  directions, we obtain

$$\frac{d}{dt} \langle \mathbf{P} \rangle = \langle -\nabla V \rangle, \quad (\text{A.15})$$

which is the second part of the Ehrenfest theorem. In the harmonic trap, with or without a stirrer, the momentum expectation value is in general, not conserved.

## A.6 Angular momentum

Angular momentum is of particular importance in our simulation of rotational stirring. We derive here the rate of change of the angular momentum expectation value  $\langle \mathbf{L} \rangle$ . For simplicity of derivation, we consider the rate of change of the parts of each component. We begin with

$$\begin{aligned}
 \frac{d\langle xP_y \rangle}{dt} &= -i \int \left[ \frac{\partial \psi^*}{\partial t} x \frac{\partial}{\partial y} \psi + \psi^* x \frac{\partial}{\partial y} \frac{\partial \psi}{\partial t} \right] d\mathbf{r}, \\
 &= \int \left[ (-\nabla^2 \psi^* + V \psi^* + C|\psi|^2 \psi^*) x \frac{\partial \psi}{\partial y} \right. \\
 &\quad \left. - \psi^* x \frac{\partial}{\partial y} (-\nabla^2 \psi + V \psi + C|\psi|^2 \psi) \right] d\mathbf{r}, \\
 &= \int \left[ - \left( x \frac{\partial \psi}{\partial y} \right) \nabla^2 \psi^* + \psi^* \nabla^2 \left( x \frac{\partial \psi}{\partial y} \right) \right. \\
 &\quad \left. - 2\psi^* \frac{\partial^2 \psi}{\partial x \partial y} - |\psi|^2 x \frac{\partial V}{\partial y} \right. \\
 &\quad \left. - C|\psi|^2 x \left( \psi \frac{\partial \psi^*}{\partial y} + \psi^* \frac{\partial \psi}{\partial y} \right) \right] d\mathbf{r}. \tag{A.16}
 \end{aligned}$$

As in the previous cases, the first two terms cancel by Equation (A.3). By considering its components, and using Equation (A.16) and the similar results for cyclic and anticyclic permutations of  $(x, y, z)$ , we can now write

$$\frac{d\langle \mathbf{L} \rangle}{dt} = \int \left[ -|\psi|^2 \mathbf{r} \times \nabla V - \frac{1}{2} C \mathbf{r} \times \nabla (|\psi|^4) \right] d\mathbf{r}, \tag{A.17}$$

noting that the third term in Equation (A.16) has cancelled in each component of Equation (A.17) because the order of differentiation can be exchanged. Using Equation (A.5), we see that the second term can be written as

$$\int \left[ \frac{1}{2} C \nabla \times (|\psi|^4) \right] d\mathbf{r} = 0, \tag{A.18}$$

by the application of Stokes' theorem to each component (because the density vanishes as  $r \rightarrow \infty$ ). This leaves only

$$\frac{d\langle \mathbf{L} \rangle}{dt} = \langle -\mathbf{r} \times \nabla V \rangle = \langle -i\mathbf{L}V \rangle, \tag{A.19}$$

which is an equation for torque analogous to the Ehrenfest theorem. We can conclude then that if  $V = V_0$  where

$$V_0 = \frac{x^2 + y^2 + \lambda^2 z^2}{4}, \quad (\text{A.20})$$

is the unperturbed axisymmetric (about the  $z$  axis) trapping potential, then

$$\mathbf{r} \times \nabla V_0 = \frac{yz}{2}(\lambda^2 - 1)\hat{\mathbf{x}} + \frac{xz}{2}(1 - \lambda^2)\hat{\mathbf{y}} + 0\hat{\mathbf{z}}, \quad (\text{A.21})$$

and so  $\langle L_z \rangle$  is conserved by the GP equation, but  $\langle L_x \rangle$  and  $\langle L_y \rangle$  are conserved only if  $\lambda = 1$  (spherically symmetric potential). In the presence of a stirring potential ( $V = V_0 + W$ ), these symmetries are broken,  $\langle \mathbf{L} \rangle$  is not conserved, and the stirrer can impart angular momentum to the condensate.

## A.7 Energy in the rotating frame

In Chapters 5 to 7, we study a condensate rotationally stirred with angular frequency  $\omega_f$ . The energy in a frame rotating about the  $z$  axis at a constant angular velocity  $\omega_f$  is given by [58, 57, 59]

$$E' = E - \omega_f \langle L_z \rangle, \quad (\text{A.22})$$

and so the rate of change of energy is

$$\frac{dE'}{dt} = \frac{dE}{dt} - \omega_f \frac{d\langle L_z \rangle}{dt}. \quad (\text{A.23})$$

We consider a stirring potential which is stationary in the rotating frame. The total external potential applied to the condensate is

$$V = V_0 + W, \quad (\text{A.24})$$

where  $V_0$  is the constant harmonic trapping potential, and we write the rotating stirring potential using rotation operators as [20]

$$W(\mathbf{r}, t) = e^{-i\omega_f t L_z} W'(\mathbf{r}) e^{+i\omega_f t L_z}, \quad (\text{A.25})$$

where  $W'(\mathbf{r})$  is time-independent. The stirrer thus rotates about the origin with angular velocity  $\omega_f$ . We note that we have made no restrictions on the

spatial form of  $W'$ . Differentiating Equation (A.24) with respect to time and then substituting into Equation (A.10) gives

$$\begin{aligned}
\frac{dE}{dt} &= -i\omega_f \int [\psi^* L_z(W\psi) - \psi^* W(L_z\psi)] d\mathbf{r}, \\
&\text{and expanding } L_z(W\psi) \text{ by the chain rule,} \\
&= -i\omega_f \int [\psi^*(L_z W)\psi + \psi^* W(L_z\psi) - \psi^* W(L_z\psi)] d\mathbf{r}, \\
&= -i\omega_f \int [\psi^*(L_z W)\psi] d\mathbf{r}, \\
&= -i\omega_f \langle (L_z W) \rangle.
\end{aligned} \tag{A.26}$$

To complete the evaluation of Equation (A.23), we need  $d\langle L_z \rangle/dt$ , which we obtain using Equation (A.19), and noting that  $\langle L_z V_0 \rangle = 0$  we have

$$\frac{d\langle L_z \rangle}{dt} = -i\langle (L_z W) \rangle, \tag{A.27}$$

and so

$$\begin{aligned}
\frac{dE'}{dt} &= \frac{dE}{dt} - \omega_f \frac{d\langle L_z \rangle}{dt}, \\
&= -i\omega_f \langle (L_z W) \rangle + i\omega_f \langle (L_z W) \rangle, \\
&= 0,
\end{aligned} \tag{A.28}$$

and  $E'$  is conserved.

# Appendix B

## Implementation of the RK4IP algorithm

This appendix details the Fourth-Order Runge-Kutta in the Interaction Picture (RK4IP) algorithm, which we use to solve the time-dependent GP equation [Equation (2.24)]. The basic algorithm has been described in other work (see for example [96]), but here we make significant improvements in the implementation and optimisations of the algorithm, and also describe a high performance implementation which minimises computer memory bandwidth.

### B.1 Fourth-order Runge-Kutta

In Section 3.3.2 we described how the time-dependent GP equation can be written in an interaction picture, and that Equation (3.4) is transformed into the form of a system of ordinary differential equations. The fourth-order Runge-Kutta method [78] advances a system of ordinary differential equations given by

$$\frac{d\mathbf{y}}{dt} = \mathbf{f}(\mathbf{y}, t), \quad (\text{B.1})$$

from  $\mathbf{y}_j$  at time  $t_j$  to  $\mathbf{y}_{j+1}$  at time  $t_{j+1} = t_j + \Delta t$  by the following method,

$$\mathbf{k}_1 = \Delta t \mathbf{f}(\mathbf{y}_j, t_j), \quad (\text{B.2a})$$

$$\mathbf{k}_2 = \Delta t \mathbf{f}(\mathbf{y}_j + \mathbf{k}_1/2, t_j + \Delta t/2), \quad (\text{B.2b})$$

$$\mathbf{k}_3 = \Delta t \mathbf{f}(\mathbf{y}_j + \mathbf{k}_2/2, t_j + \Delta t/2), \quad (\text{B.2c})$$

$$\mathbf{k}_4 = \Delta t \mathbf{f}(\mathbf{y}_j + \mathbf{k}_3, t_j + \Delta t), \quad (\text{B.2d})$$

$$\mathbf{y}_{j+1} = \mathbf{y}_j + [\mathbf{k}_1 + 2(\mathbf{k}_2 + \mathbf{k}_3) + \mathbf{k}_4]/6. \quad (\text{B.2e})$$

Note that the fourth-order Runge-Kutta makes four predictions, each refining the prediction of the previous; the first at the initial point  $t_j$ , the second and third at the mid point  $t_j + \Delta t/2$ , and the last at the final point  $t_j + \Delta t$ . The Runge-Kutta is a single step algorithm because it does not record values of  $\mathbf{y}$  prior to  $\mathbf{y}_j$ . This method has error terms  $O[(\Delta t)^5]$ , and thus is a fourth-order method. We apply this algorithm to Equation (3.4) and obtain the following method to advance the interaction picture wavefunction from  $\psi_j^I$  to  $\psi_{j+1}^I$  in a time step  $\Delta t$ ,

$$k_1 = -i\Delta t N_I(t_j)\psi_j^I, \quad (\text{B.3a})$$

$$k_2 = -i\Delta t N_I(t_j + \Delta t/2)(\psi_j^I + k_1/2), \quad (\text{B.3b})$$

$$k_3 = -i\Delta t N_I(t_j + \Delta t/2)(\psi_j^I + k_2/2), \quad (\text{B.3c})$$

$$k_4 = -i\Delta t N_I(t_j + \Delta t)(\psi_j^I + k_3), \quad (\text{B.3d})$$

$$\psi_{j+1}^I = \psi_j^I + [k_1 + 2(k_2 + k_3) + k_4]/6, \quad (\text{B.3e})$$

where we note that the  $k_i$  are now spatially dependent fields (like  $\psi$  and  $\psi_I$ ). To this point,  $t'$  is arbitrary [see Equation (3.5)], but if for a given step we choose  $t' = t_j + \Delta t/2$ , then the diffusion exponentials used to calculate  $N_I$  [see Equation (3.5)] in Equations B.3(b,c) become unity. As we have discussed in Section 3.3.3, the calculation of the diffusion exponential is computationally expensive, and so eliminating these terms is the first major optimisation we make; this efficient use of the midpoint positioning is one reason for our use of the the fourth-order Runge-Kutta method. The sequence of calculations to be carried out is then

$$k_1 = e^{-i(\Delta t/2)D}[-i\Delta t N(t_j)]e^{+i(\Delta t/2)D}\psi_j^I, \quad (\text{B.4a})$$

$$k_2 = -i\Delta t N(t_j + \Delta t/2)(\psi_j^I + k_1/2), \quad (\text{B.4b})$$

$$k_3 = -i\Delta t N(t_j + \Delta t/2)(\psi_j^I + k_2/2), \quad (\text{B.4c})$$

$$k_4 = e^{+i(\Delta t/2)D}[-i\Delta t N(t_j + \Delta t)]e^{-i(\Delta t/2)D}(\psi_j^I + k_3), \quad (\text{B.4d})$$

$$\psi_{j+1}^I = \psi_j^I + [k_1 + 2(k_2 + k_3) + k_4]/6. \quad (\text{B.4e})$$



From the definition of the interaction picture [Equation (3.3)], and with our choice of  $t'$ , the normal picture wavefunction at time  $t_j$  is

$$\psi_j = e^{+i(\Delta t/2)D} \psi_j^I, \quad (\text{B.5})$$

and we note that this term appears in Equation (B.4a). It is clear then that for each step, we must calculate the normal picture  $\psi_j$ . Nothing is lost, and clarity and ease of use are gained, by expressing the algorithm in terms of  $\psi_j$ , but we note that the algorithm still transforms into the interaction picture at each step. For a given step, the interaction picture is given by

$$\psi_j^I = e^{-i(\Delta t/2)D} \psi_j, \quad (\text{B.6})$$

and the wavefunction at time  $t_{j+1} = t_j + \Delta t$  is given by

$$\psi_{j+1} = e^{-i(\Delta t/2)D} \psi_{j+1}^I. \quad (\text{B.7})$$

We can now write the algorithm in the form of a single step which advances  $\psi_j$  to  $\psi_{j+1}$  in a time step  $\Delta t$ , as

$$\psi_I = e^{-i(\Delta t/2)D} \psi_j, \quad (\text{B.8a})$$

$$k_1 = e^{-i(\Delta t/2)D} [-i\Delta t N(t_j)] \psi_j, \quad (\text{B.8b})$$

$$k_2 = -i\Delta t N(t_j + \Delta t/2) (\psi_I + k_1/2), \quad (\text{B.8c})$$

$$k_3 = -i\Delta t N(t_j + \Delta t/2) (\psi_I + k_2/2), \quad (\text{B.8d})$$

$$k_4 = -i\Delta t N(t_j + \Delta t) e^{-i(\Delta t/2)D} (\psi_I + k_3), \quad (\text{B.8e})$$

$$\psi_{j+1} = e^{-i(\Delta t/2)D} \{ \psi_I + [k_1 + 2(k_2 + k_3)]/6 \} + k_4/6. \quad (\text{B.8f})$$

We have made another significant optimisation by cancelling the exponential terms in Equation (B.7) and Equation (B.4d), effectively taking  $k_4$  out of the interaction picture and putting it in the normal picture at time  $t_{j+1}$ . We note that every diffusion exponential operation has precisely the same arguments, with only the wave upon which the operator acts varying: this permits a simple, more efficient implementation of the diffusion exponential operation, as we discuss in Section B.3.

## B.2 Matlab implementation

To describe the implementation of our numerical method, we now adopt algorithmic notation, in which each  $\leftarrow$  denotes an assignment and the order of operations is significant. This notation allows us to express the further optimisations which we make in Section B.3. We emphasise that the implementation of the algorithm requires only two operators to be implemented (in addition to assignment [copying] and scalar multiplication), namely

$$\mathcal{D}(\alpha) = e^{-i(\Delta t/2)D}\alpha, \quad (\text{B.9a})$$

$$\mathcal{N}(\alpha, t) = -i \Delta t N(t)\alpha. \quad (\text{B.9b})$$

We begin with  $\psi$  given at time  $t$ , the beginning of the time interval. For a single step which updates  $\psi$  and  $t$  with their new values, the algorithm thus becomes

$$\psi_I \leftarrow \mathcal{D}(\psi), \quad (\text{B.10a})$$

$$k_1 \leftarrow \mathcal{D}[\mathcal{N}(\psi, t)], \quad (\text{B.10b})$$

$$t \leftarrow t + \Delta t/2, \quad (\text{time at the midpoint}) \quad (\text{B.10c})$$

$$k_2 \leftarrow \mathcal{N}(\psi_I + k_1/2, t), \quad (\text{B.10d})$$

$$k_3 \leftarrow \mathcal{N}(\psi_I + k_2/2, t), \quad (\text{B.10e})$$

$$t \leftarrow t + \Delta t/2, \quad (\text{time at the endpoint}) \quad (\text{B.10f})$$

$$k_4 \leftarrow \mathcal{N}[\mathcal{D}(\psi_I + k_3), t], \quad (\text{B.10g})$$

$$\psi \leftarrow \mathcal{D}\{\psi_I + [k_1 + 2(k_2 + k_3)]/6\} + k_4/6. \quad (\text{B.10h})$$

This form of the algorithm is precisely that which we have implemented in Matlab for simulating condensates in two dimensions.

## B.3 Efficient implementation in Python

In Section 3.3.4 we discussed the means by which we optimise the RK4IP algorithm, and we now detail the highly efficient form of the algorithm which we have implemented in Python and C. We can write the RK4IP algorithm in terms of exactly four types of operations on the large variables  $\psi$ ,  $\psi_I$ , and  $\psi_K$

(which are each the size of our computational grid), plus the advancement of time which we denote  $\mathbf{T}$ . The time  $t$  is a scalar variable, and  $\mathbf{T}$  is only included because its position in the order of the algorithm is significant. The four types of operations are

$$\alpha \leftarrow \beta, \quad \text{C (copying)} \quad (\text{B.11})$$

$$\alpha \leftarrow \mathcal{D}(\alpha), \quad \text{D (diffusion)} \quad (\text{B.12})$$

$$\alpha \leftarrow \mathcal{N}(\alpha, t), \quad \text{N (nondiffusion)} \quad (\text{B.13})$$

$$\alpha \leftarrow a\alpha + b\beta, \quad \text{S (weighted sum)} \quad (\text{B.14})$$

where  $a$  and  $b$  are real coefficients. Operation **D** is implemented in-place by first performing a forwards all-dimensional fast Fourier transform (FFT) in-place using FFTW [40], then using a **C** routine to multiply the coefficients in-place by the appropriate phase factors [Equation (C.12)] (including normalisation factors, as FFTW does not normalise its transforms), then performing the backwards all-dimensional FFT in-place using FFTW. Operation **N** is performed in-place; our implementation written in C requires negligible extra storage. Operation **C** is performed using Numerical Python's array constructor. Operation **S** is performed in-place (in  $\alpha$ ) in a C routine. The operation **S** performs a few unnecessary multiplications, because on seven occasions a coefficient of 1 is passed to the routine, but the performance of this routine is completely dominated by memory bandwidth saturation, and floating point multiplication is exceedingly cheap on the Pentium (and successors), taking only two clock cycles and being parallelisable with integer operations. We find that the cost of this design choice is totally insignificant, while it permits all the different types of sum operation to be performed with a single routine, simplifying code design and maintenance. The RK4IP algorithm which advances  $\psi$  and  $t$  over a time step of  $\Delta t$  then becomes

$$\psi_K \leftarrow \psi, \quad \text{C} \quad (\text{B.15a})$$

$$\psi \leftarrow \mathcal{D}(\psi), \quad \text{D} \quad (\text{B.15b})$$

$$\psi_I \leftarrow \psi, \quad \text{C} \quad (\text{B.15c})$$

$$\psi_K \leftarrow \mathcal{N}(\psi_K, t), \quad \text{N} \quad (\text{B.15d})$$

$$\psi_K \leftarrow \mathcal{D}(\psi_K), \quad \text{D} \quad (\text{B.15e})$$

$\psi \leftarrow \psi + \psi_K/6,$	S	(B.15f)
$\psi_K \leftarrow \psi_K/2 + \psi_I,$	S	(B.15g)
$t \leftarrow t + \Delta t/2,$	T	(B.15h)
$\psi_K \leftarrow \mathcal{N}(\psi_K, t),$	N	(B.15i)
$\psi \leftarrow \psi + \psi_K/3,$	S	(B.15j)
$\psi_K \leftarrow \psi_K/2 + \psi_I,$	S	(B.15k)
$\psi_K \leftarrow \mathcal{N}(\psi_K, t),$	N	(B.15l)
$\psi \leftarrow \psi + \psi_K/3,$	S	(B.15m)
$\psi_K \leftarrow \psi_K + \psi_I,$	S	(B.15n)
$\psi_K \leftarrow \mathcal{D}(\psi_K),$	D	(B.15o)
$\psi \leftarrow \mathcal{D}(\psi),$	D	(B.15p)
$t \leftarrow t + \Delta t/2,$	T	(B.15q)
$\psi_K \leftarrow \mathcal{N}(\psi_K, t),$	N	(B.15r)
$\psi \leftarrow \psi + \psi_K/6.$	S	(B.15s)

This form of the algorithm is exactly that implemented in Python [84] (and intended for two- and three-dimensional simulations). This implementation was used to perform all our simulations in three dimensions.

One final implementation note is that the phase factors  $e^{i(\Delta t/2)k^2}$ , which are used to calculate the diffusion operator in momentum space (detailed in Appendix C), are expensive to calculate, and can take one third of the computational time. Of great assistance is that  $\Delta t$  is fixed for any given simulation, and so we may precalculate the phase factors. In the Matlab implementation (for two dimensions), we optimise our algorithm by precalculating these phase factors, stored in an array the size of the computational grid. In the Python/C implementation, to save memory bandwidth and storage space, we precalculate the separated phase factors in each dimension, from which we can reconstruct the full phase factors by

$$e^{i(\Delta t/2)k^2} = e^{i(\Delta t/2)k_x^2} e^{i(\Delta t/2)k_y^2} e^{i(\Delta t/2)k_z^2}. \quad (\text{B.16})$$

The C code, which multiplies the momentum representation of  $\psi$  by the phase factors, efficiently performs this reconstruction.

# Appendix C

## Fourier techniques

Fourier techniques provide an efficient and accurate means of calculating the derivatives of the mean field wavefunction  $\psi$ , and in particular, for calculating the diffusion exponential used in the propagation of the GP equation. The exponential diffusion operator  $e^{-i\tau D}$  is readily calculated by spectral methods, because  $D$  is diagonal in momentum space.

### C.1 Fourier transform

The Fourier transform of  $\psi$  is given by

$$\phi(\mathbf{k}) = \int \psi(\mathbf{r}) e^{+i\mathbf{k}\cdot\mathbf{r}} d\mathbf{r}, \quad (\text{C.1})$$

where  $\mathbf{k}$  is the wavevector. Using the inverse relation, we can write  $\psi$  in terms of its Fourier components as

$$\psi(\mathbf{r}) = \left(\frac{1}{2\pi}\right)^M \int \phi(\mathbf{k}) e^{-i\mathbf{k}\cdot\mathbf{r}} d\mathbf{k}, \quad (\text{C.2})$$

where  $M$  is the dimensionality of the space over which  $\mathbf{r}$  is defined. Differentiating Equation (C.2) with respect to the components of  $\mathbf{r}$ , we obtain the gradient of  $\psi$ ,

$$\nabla\psi(\mathbf{r}) = \left(\frac{1}{2\pi}\right)^M \int (-i\mathbf{k})\phi(\mathbf{k}) e^{-i\mathbf{k}\cdot\mathbf{r}} d\mathbf{k}, \quad (\text{C.3})$$

and similarly the Laplacian,

$$\nabla^2 \psi(\mathbf{r}) = \left( \frac{1}{2\pi} \right)^M \int (-k^2) \phi(\mathbf{k}) e^{-i\mathbf{k} \cdot \mathbf{r}} d\mathbf{k}. \quad (\text{C.4})$$

Considering the series definition of the operator exponential [20], we see that we may write

$$e^{-i\tau D} \psi = \left( \frac{1}{2\pi} \right)^M \int e^{-i\tau k^2} \phi(\mathbf{k}) e^{-i\mathbf{k} \cdot \mathbf{r}} d\mathbf{k}, \quad (\text{C.5})$$

where  $D = -\nabla^2$  and  $\tau$  is some arbitrary time.

## C.2 Discrete Fourier transform

For our discrete representation, the Fourier transform becomes the discrete Fourier transform (using the conventions of Press *et al.* [78]), given by

$$\phi_{lmn} = \sum_{c=0}^{N_z-1} \sum_{b=0}^{N_y-1} \sum_{a=0}^{N_x-1} \psi_{abc} e^{+2\pi i a l / N_x} e^{+2\pi i b m / N_y} e^{+2\pi i c n / N_z}, \quad (\text{C.6})$$

which is efficiently calculated using the Fast Fourier Transform algorithm. As in the case of the continuous Fourier transform, we write our discretised wavefunction in terms of its Fourier components.

$$\psi_{abc} = \frac{1}{N_x N_y N_z} \sum_{n=0}^{N_z-1} \sum_{m=0}^{N_y-1} \sum_{l=0}^{N_x-1} \phi_{lmn} e^{-2\pi i a l / N_x} e^{-2\pi i b m / N_y} e^{-2\pi i c n / N_z}, \quad (\text{C.7})$$

The derivatives in the discrete Fourier representation can be found exactly as in the continuous representation, by differentiating Equation (C.7) with respect to  $a$  (as if  $a$  was a continuous variable) and then noting that  $dx/da = \Delta x$ , and similarly for the other dimensions. From the periodicity of the discrete Fourier transform, we can write the wavenumbers as given in Equation (C.10). The gradient of the wavefunction at each point is given by

$$(\nabla \psi)_{abc} = \frac{1}{N_x N_y N_z} \sum_{n=0}^{N_z-1} \sum_{m=0}^{N_y-1} \sum_{l=0}^{N_x-1} (-i\mathbf{k}_{lmn}) \phi_{lmn} e^{-2\pi i a l / N_x} e^{-2\pi i b m / N_y} e^{-2\pi i c n / N_z}. \quad (\text{C.8})$$

The wavevector is

$$\mathbf{k}_{lmn} = k_x(l)\hat{\mathbf{x}} + k_y(m)\hat{\mathbf{y}} + k_z(n)\hat{\mathbf{z}}, \quad (\text{C.9})$$

where the wavenumbers of the Fourier components are given by

$$k_x(l) = \begin{cases} \frac{2\pi l}{(\Delta x)N_x} & \text{if } l \leq N/2, \\ -\frac{2\pi(N-l)}{(\Delta x)N_x} & \text{if } l > N/2, \end{cases} \quad (\text{C.10})$$

and similarly for  $k_y(m)$  and  $k_z(n)$ . The Laplacian is given by

$$(\nabla^2 \psi)_{abc} = \frac{1}{N_x N_y N_z} \sum_{n=0}^{N_z-1} \sum_{m=0}^{N_y-1} \sum_{l=0}^{N_x-1} (-k_{lmn}^2) \phi_{lmn} e^{-2\pi i a l / N_x} e^{-2\pi i b m / N_y} e^{-2\pi i c n / N_z}. \quad (\text{C.11})$$

The exponential diffusion operator is calculated by

$$(e^{-i\tau D} \psi)_{abc} = \frac{1}{N_x N_y N_z} \sum_{n=0}^{N_z-1} \sum_{m=0}^{N_y-1} \sum_{l=0}^{N_x-1} e^{-i\tau k_{lmn}^2} \phi_{lmn} \times e^{-2\pi i a l / N_x} e^{-2\pi i b m / N_y} e^{-2\pi i c n / N_z}, \quad (\text{C.12})$$

where  $D = -\nabla^2$ , and although  $\tau$  is arbitrary, we always use  $\tau = \Delta t/2$  in the RK4IP algorithm.





# Appendix D

## Derivation of the nonlinear two state model

In this appendix, we give details of the derivation of the nonlinear two state model presented in Chapter 6. In this derivation, we avoid explicit reference to the dimensionality of the system, and so this treatment is valid for both the two-dimensional (Chapter 6) and three-dimensional (Chapter 7) cases.

### D.1 Preliminary results

Before deriving the equations for the coupled basis wavefunctions and the nonlinear Rabi equations, we first present some results which we will use to obtain those equations. The two-component ansatz is

$$\psi = a_s(t)\phi_s + a_v(t)\phi_v e^{i\theta}, \quad (\text{D.1})$$

where  $\phi_{s,v}$  are real, nonnegative functions, given in two dimensions by  $\phi_{s,v} = \phi_{s,v}(r, n_v)$  and in three dimensions by  $\phi_{s,v} = \phi_{s,v}(\rho, z, n_v)$ . The time derivative of  $\psi$  is

$$\frac{\partial \psi}{\partial t} = \frac{da_s}{dt}\phi_s + a_s \frac{\partial \phi_s}{\partial t} + \frac{da_v}{dt}\phi_v e^{i\theta} + a_v \frac{\partial \phi_v}{\partial t} e^{i\theta}. \quad (\text{D.2})$$

By differentiating the normalisation condition for  $\phi_{s,v}$  [Equation (6.2)] with respect to time, we find

$$\frac{d}{dt} \int \phi_{s,v}^2 d\mathbf{r} = 2 \int \phi_{s,v} \frac{\partial \phi_{s,v}}{\partial t} d\mathbf{r} = 0, \quad (\text{D.3})$$

and so we see that each  $\phi_{s,v}$  is orthogonal to its time derivative.

### D.1.1 Orthogonality by phase circulation

We now show that axially symmetric functions with different phase circulations are orthogonal. The integral

$$\int_0^{2\pi} e^{i\theta} d\theta = 0, \quad (\text{D.4})$$

because the contribution to the integral from each  $\theta' \in (0, \pi)$  is equal and opposite to the contribution from  $\theta' + \pi$ . A similar result holds for any  $e^{in\theta}$  (where  $n$  is a nonzero integer), which can be seen by substituting  $\bar{\theta} = n\theta$  to obtain

$$\int_0^{2\pi} e^{in\theta} d\theta = \frac{1}{n} \int_0^{2\pi n} e^{i\bar{\theta}} d\bar{\theta} = 0, \quad (\text{D.5})$$

by dividing the integration over  $\bar{\theta}$  into  $n$  regions of  $2\pi$  and applying Equation (D.4) to each region. Consequently, for any function  $\alpha$  which is independent of  $\theta$ ,

$$\int \alpha e^{in\theta} d\mathbf{r} = 0, \quad (\text{D.6})$$

where  $n$  is a nonzero integer, because we can perform the integration over  $\theta$  first. From Equation (D.6), we see immediately that  $\phi_s$  and  $\phi_v e^{i\theta}$  are orthogonal, that is

$$\int \phi_s \phi_v e^{i\theta} d\mathbf{r} = 0, \quad (\text{D.7})$$

because  $\phi_s \phi_v$  is independent of  $\theta$ .

### D.1.2 Expansion of the GP equation

In this derivation, we use notation which is independent of dimensionality. To maintain this generality, we write

$$\nabla^2(\phi_v e^{i\theta}) = e^{i\theta} \nabla^2 \phi_v - V_c \phi_v e^{i\theta}, \quad (\text{D.8})$$

where the centrifugal potential is given by  $V_c = 1/r^2$  in two dimensions and  $V_c = 1/\rho^2$  in three dimensions.  $V_c$  is the effective potential felt by the vortex component due to its circulation. Substituting our ansatz [Equation (D.1)] into the GP equation [Equation (2.24)] yields

$$\begin{aligned} \frac{\partial \psi}{\partial t} = -i & \left[ -a_s \nabla^2 \phi_s - a_v e^{i\theta} \nabla^2 \phi_v + a_v V_c \phi_v e^{i\theta} + a_s V \phi_s + a_v V \phi_v e^{i\theta} \right. \\ & + C a_s (n_s \phi_s^2 + 2n_v \phi_v^2) \phi_s + C a_v (n_v \phi_v^2 + 2n_s \phi_s^2) \phi_v e^{i\theta} \\ & \left. + C (a_v n_s \phi_s^2 \phi_v e^{-i\theta} + a_s n_v \phi_s \phi_v^2 e^{+2i\theta}) \right], \end{aligned} \quad (\text{D.9})$$

where we have written the terms with a coefficient of  $C$  in three parts: those with no dependence on  $\theta$ , those with a  $\theta$  dependence given by  $e^{i\theta}$ , and lastly those with a  $\theta$  dependence given by  $e^{in\theta}$  for some  $n \notin \{0, 1\}$ . The latter will always vanish under the integrations we perform.

## D.2 Coupled basis wavefunctions

We discussed in Section 6.3 the definition of our coupled basis wavefunctions, which have eigenvalues  $\mu_s$  and  $\mu_v$  given by Equations (6.3), in the absence of the stirrer ( $V = V_0$ ). Under those conditions, the vortex fraction is constant ( $dn_v/dt = 0$ ) and so  $\partial \phi_{s,v}/\partial t = 0$ , and integrating both sides of Equation (D.2) with respect to the  $\theta$ , and applying Equation (D.5), we obtain

$$\frac{da_s}{dt} \phi_s = \frac{1}{2\pi} \int_0^{2\pi} \frac{\partial \psi}{\partial t} d\theta, \quad (\text{D.10a})$$

$$\frac{da_v}{dt} \phi_v = \frac{1}{2\pi} \int_0^{2\pi} e^{-i\theta} \frac{\partial \psi}{\partial t} d\theta. \quad (\text{D.10b})$$

We then substitute Equations (6.3) in the left hand sides and Equation (D.9) in the right hand sides, and again apply Equation (D.5) to obtain

$$\mu_s \phi_s = [-\nabla^2 + V_0 + C(n_s \phi_s^2 + 2n_v \phi_v^2)] \phi_s, \quad (\text{D.11a})$$

$$\mu_v \phi_v = [-\nabla^2 + V_c + V_0 + C(n_v \phi_v^2 + 2n_s \phi_s^2)] \phi_v. \quad (\text{D.11b})$$

Note that this form is possible because in this case  $V = V_0$  does not depend on  $\theta$ . Writing the Laplacian in radial form and including  $V_c$  and  $V_0$  explicitly yields Equations (6.4) and Equations (7.3) for two and three dimensions respectively.

### D.3 Nonlinear Rabi equations

We now obtain the nonlinear Rabi equations by using the full potential  $V = V_0 + W$  in Equation (D.9) and projecting alternately onto the basis eigenfunctions. Using Equations (D.2), D.3, and D.6, we obtain

$$\frac{da_s}{dt} = \int \phi_s \frac{\partial \psi}{\partial t} d\mathbf{r}, \quad (\text{D.12a})$$

$$\frac{da_v}{dt} = \int \phi_v e^{-i\theta} \frac{\partial \psi}{\partial t} d\mathbf{r}. \quad (\text{D.12b})$$

Substituting Equation (D.9) into the right hand side, we obtain [again using Equation (D.6)]

$$\begin{aligned} \frac{da_s}{dt} = & -ia_s \int [-\phi_s \nabla^2 \phi_s + \phi_s V_0 \phi_s + C(a_s^2 \phi_s^2 + 2a_v^2 \phi_v^2) \phi_s] d\mathbf{r} \\ & - ia_s \int \phi_s W \phi_s d\mathbf{r} - ia_v \int \phi_s W e^{i\theta} \phi_v d\mathbf{r}, \end{aligned} \quad (\text{D.13a})$$

$$\begin{aligned} \frac{da_v}{dt} = & -ia_v \int [-\phi_v \nabla^2 \phi_v + \phi_v V_0 \phi_v + C(a_v^2 \phi_v^2 + 2a_s^2 \phi_s^2) \phi_v] d\mathbf{r} \\ & - ia_v \int \phi_v e^{-i\theta} W \phi_v e^{i\theta} d\mathbf{r} - ia_s \int \phi_v e^{-i\theta} W \phi_s d\mathbf{r}. \end{aligned} \quad (\text{D.13b})$$

Note that in the latter equations we cannot discard the terms containing  $e^{\pm i\theta}$ , because  $W$  is in general not independent of  $\theta$ . Equations (D.13) can be greatly simplified by noting that, from the normalisation condition [Equation (6.2)], we have

$$\mu_s = \int \phi_s \mu_s \phi_s d\mathbf{r}, \quad (\text{D.14a})$$

$$\mu_v = \int \phi_v \mu_v \phi_v d\mathbf{r}, \quad (\text{D.14b})$$

and so we can use Equations (D.11) to write Equations (D.13) as

$$\frac{da_s}{dt} = -i\mu_s a_s - ia_s \int \phi_s W \phi_s d\mathbf{r} - ia_v \int \phi_s W \phi_v e^{i\theta} d\mathbf{r}, \quad (\text{D.15a})$$

$$\frac{da_v}{dt} = -i\mu_v a_v - ia_v \int \phi_v e^{-i\theta} W \phi_v e^{i\theta} d\mathbf{r} - ia_s \left( \int \phi_s W \phi_v e^{i\theta} d\mathbf{r} \right)^*, \quad (\text{D.15b})$$

We identify the integral terms as containing the energy shift and Rabi frequency due to the presence of the stirrer.

### D.3.1 Effects of the stirrer

We write the stirrer potential  $W$  using the time-independent potential  $W'(\mathbf{r})$  and the rotation operators as [20]

$$\begin{aligned} W &= e^{-i\omega_f t L_z} W' e^{+i\omega_f t L_z}, \\ &= (e^{+i\omega_f t L_z})^\dagger W' e^{+i\omega_f t L_z}. \end{aligned} \quad (\text{D.16})$$

Noting that in polar form [20]

$$L_z = -i \frac{\partial}{\partial \theta}, \quad (\text{D.17})$$

(in our dimensionless units) we have

$$L_z \alpha e^{in\theta} = n \alpha e^{in\theta}, \quad (\text{D.18})$$

where  $\alpha$  is any function independent of  $\theta$ , and  $n$  is any integer. The effects of the stirrer can then be written

$$\int \phi_s W \phi_s d\mathbf{r} = \int \phi_s W' \phi_s d\mathbf{r}, \quad (\text{D.19a})$$

$$\int \phi_v e^{-i\theta} W \phi_v e^{i\theta} d\mathbf{r} = \int \phi_v W' \phi_v d\mathbf{r}, \quad (\text{D.19b})$$

$$\int \phi_s W \phi_v e^{i\theta} d\mathbf{r} = e^{+i\omega_f t} \int \phi_s W' \phi_v e^{i\theta} d\mathbf{r}. \quad (\text{D.19c})$$

We then make the definitions in Equations (6.10), and Equations (D.15) become

$$\frac{da_s}{dt} = -i[\mu_s + \delta_s]a_s - \frac{i}{2}e^{+i\omega_f t} \Omega a_v, \quad (\text{D.20a})$$

$$\frac{da_v}{dt} = -i[\mu_v + \delta_v]a_v - \frac{i}{2}e^{-i\omega_f t} \Omega^* a_s. \quad (\text{D.20b})$$

Note that in practice we can always choose our axes so that the stirrer is symmetrical about the  $x$  axis at  $t = 0$ . Under these circumstances,  $\Omega$  is strictly real and we can neglect the conjugation of  $\Omega$ .

### D.3.2 Rotating frame

The final steps in obtaining the nonlinear Rabi equations [Equations (6.8)] are to choose a new phase origin and transform to a rotating frame. In principle,

there is no limit on the size of  $\mu_s$  and  $\mu_v$ , and the phases of  $a_s$  and  $a_v$  may advance at any speed. We are not, however, interested in the absolute phase of these quantities; all the physically interesting information is contained in their phase difference. Furthermore, a rapid evolution of the phase makes the ordinary differential equations *stiff*, that is, the presence of high frequency components makes their numerical solution more difficult because a smaller step size is required. We thus write the phase of the coefficients relative to the angle  $\alpha_s$  [Equation (6.7)], the total phase accumulated by  $a_s$  due to  $\mu_s$ . We also eliminate the exponential terms in Equations (D.20) by moving into the rotating frame in which the stirrer is stationary. These transformations are given in Equations (6.6), where the exponential factor in Equation (6.6b) is the effect of transforming to the rotating frame [20]. Differentiating Equations (6.6) with respect to time and substituting Equations (D.20), Equation (6.9), and Equations (6.6), immediately yields the nonlinear Rabi equations [Equations (6.8)].

# Appendix E

## Colour plates

In this appendix, we present colour plates which are supplementary to the figures in the body of this work. These additional figures provide alternative representations of our results.





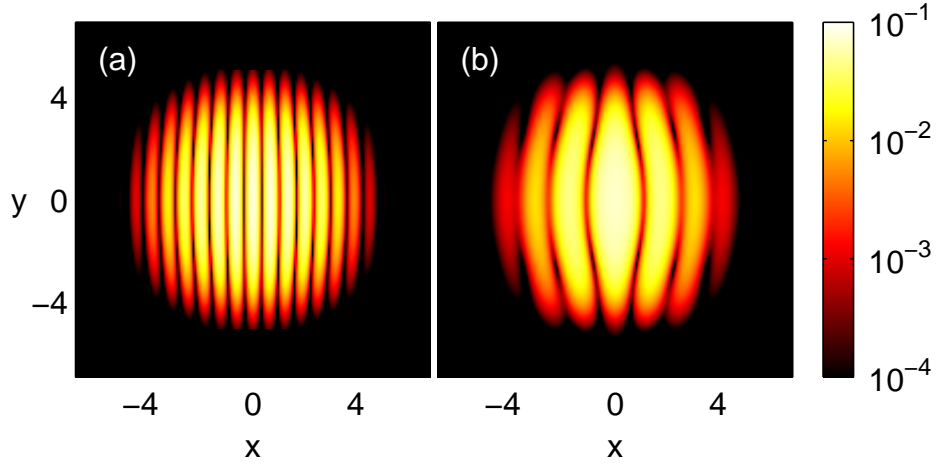


Figure E.1: Probability density of two condensates colliding (in two dimensions). The initial separation of the condensate centres was (a) 20.0, and (b) 10.0, and  $t = \pi/2$ . Vortex detection is not used for this figure. This is a colour version of Figure 4.1.

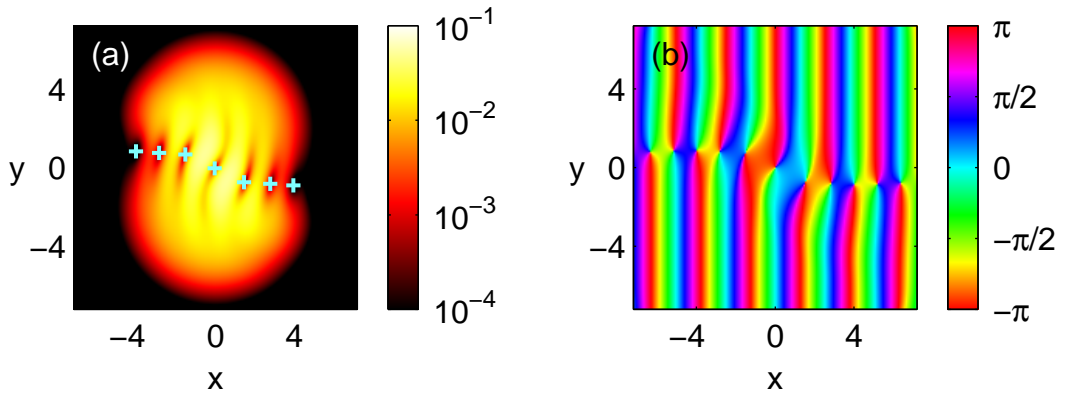


Figure E.2: Rotating collision of two condensates (in two dimensions), showing (a) probability density, and (b) phase, at  $t = \pi/2$ . This is a colour version of Figure 4.3.



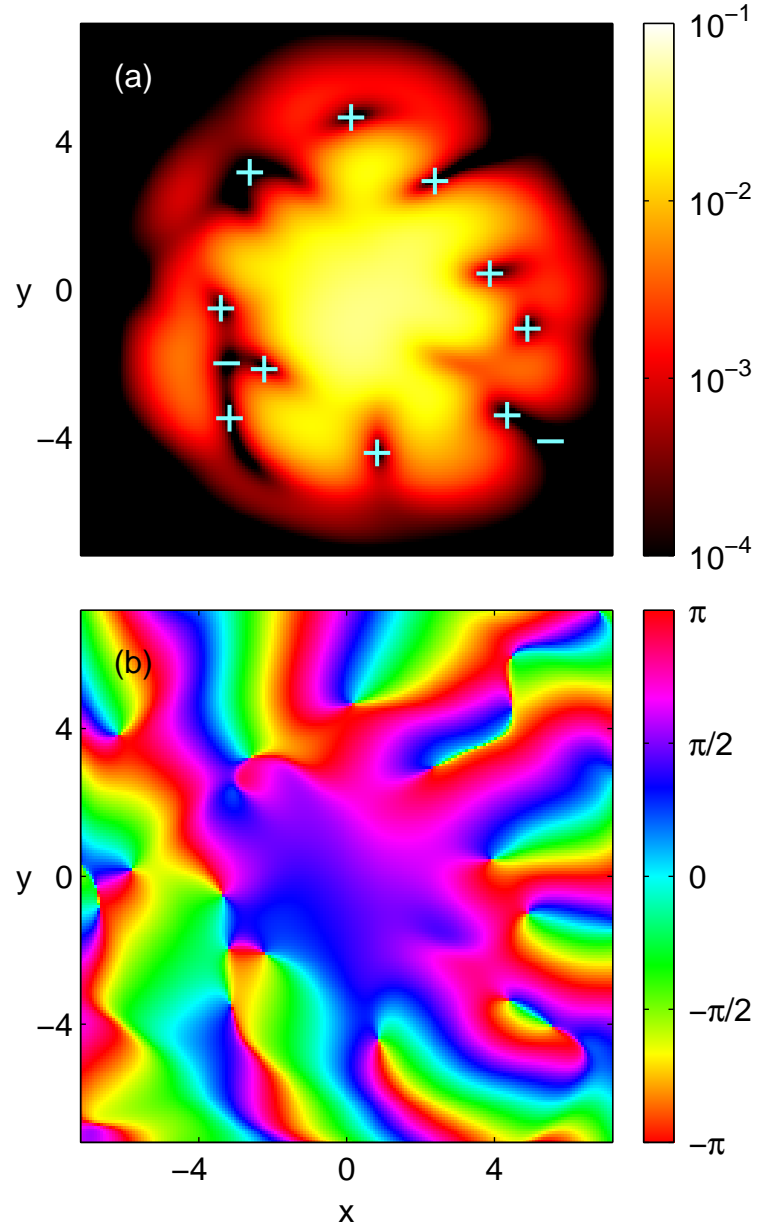


Figure E.3: Rotationally stirred two-dimensional condensate, showing (a) probability density, and (b) phase, at  $t = 12\pi$ . The stirrer was linearly withdrawn between  $t = 4\pi$  and  $t = 5\pi$ . This is a colour version of Figure 5.1.



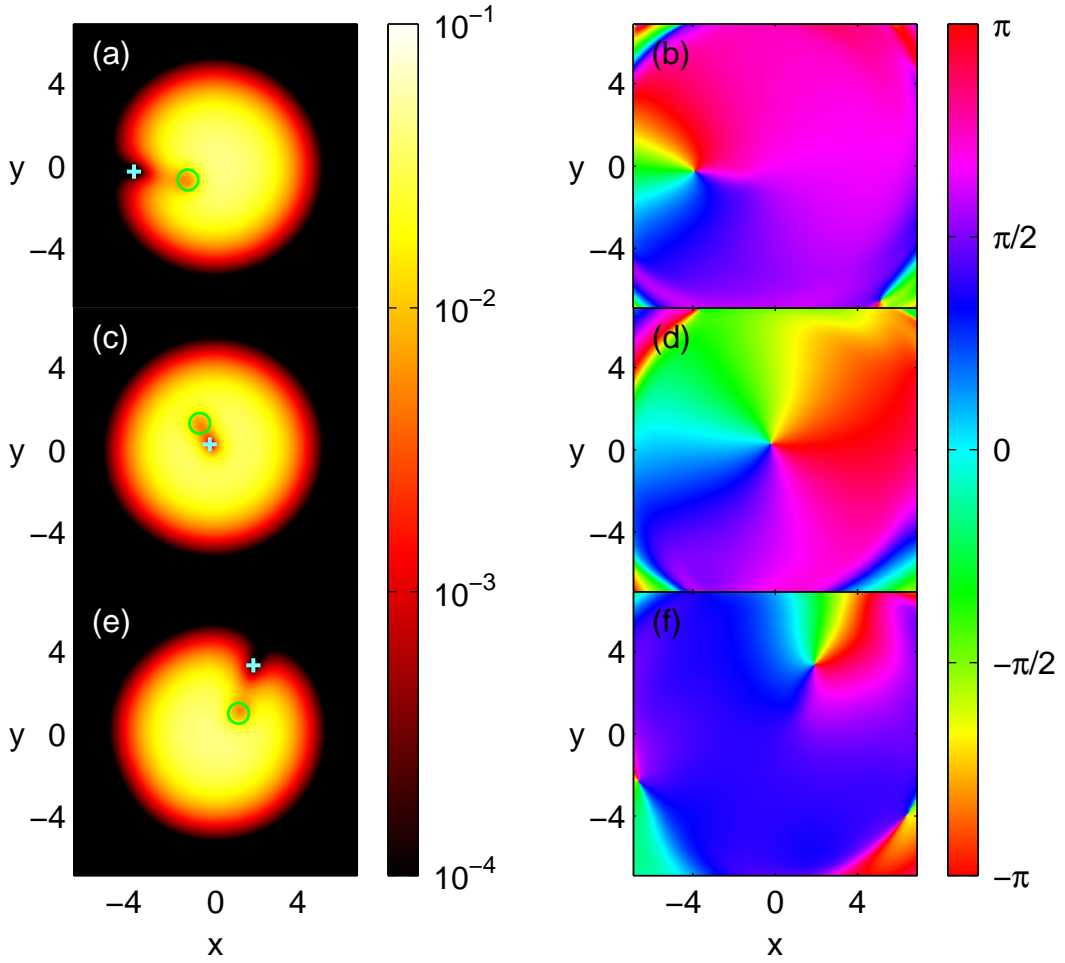


Figure E.4: Sequence showing single vortex cycling in a rotationally stirred two-dimensional condensate, giving (a,c,e) probability density, and (b,d,f) phase. Times are (a,b)  $t = 8.80$ , (c,d)  $t = 18.35$ , and (e,f)  $t = 28.15$ . The circle marks the stirrer. This is a colour version of Figure 5.4.



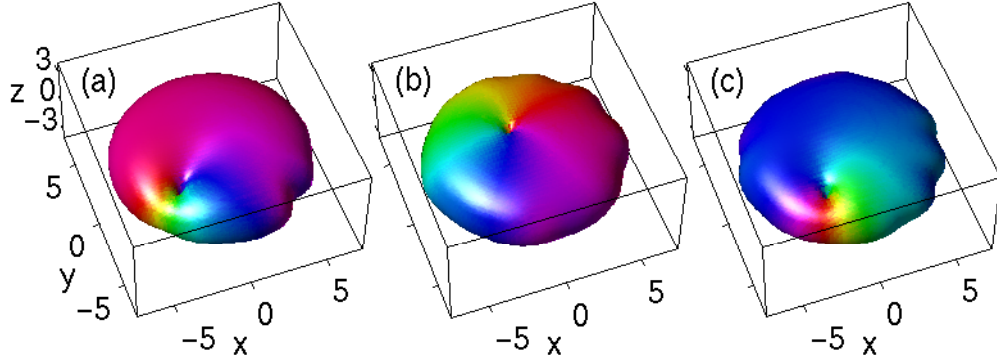


Figure E.5: Sequence showing single vortex cycling in a rotationally stirred oblate condensate, giving phase on a density isosurface ( $|\psi|^2 = 10^{-4}$ ), with the phase scale as in Figure E.6. Times are (a)  $t = 13.70$ , (b)  $t = 25.76$ , and (c)  $t = 33.80$ . This is the same sequence shown in Figure 7.1.

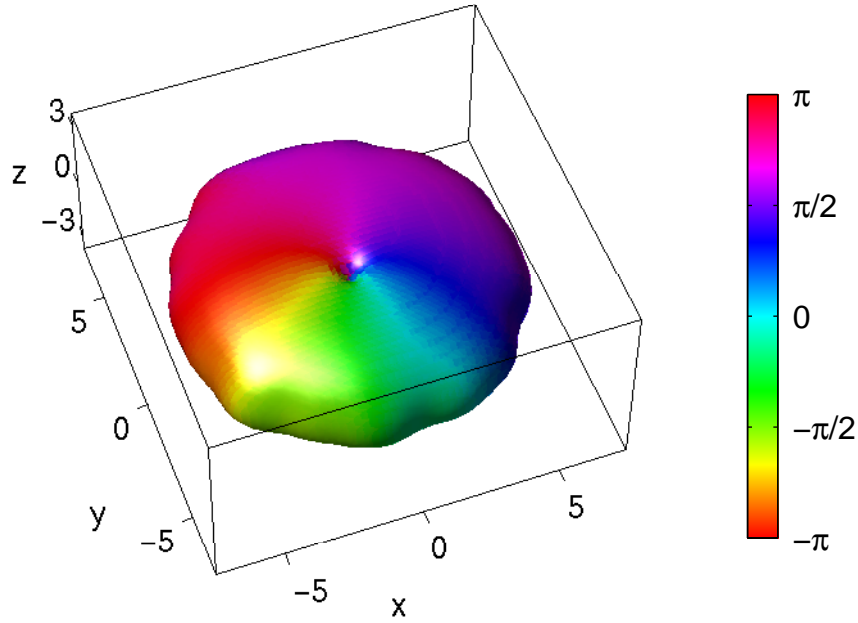


Figure E.6: Phase on a density isosurface ( $|\psi|^2 = 10^{-4}$ ) for an oblate condensate which has been rotationally stirred. Here  $t = 94.12$ . The stirrer was linearly withdrawn between  $t = 7\pi$  and  $t = 8\pi$ . This is the same situation shown in Figure 7.3.





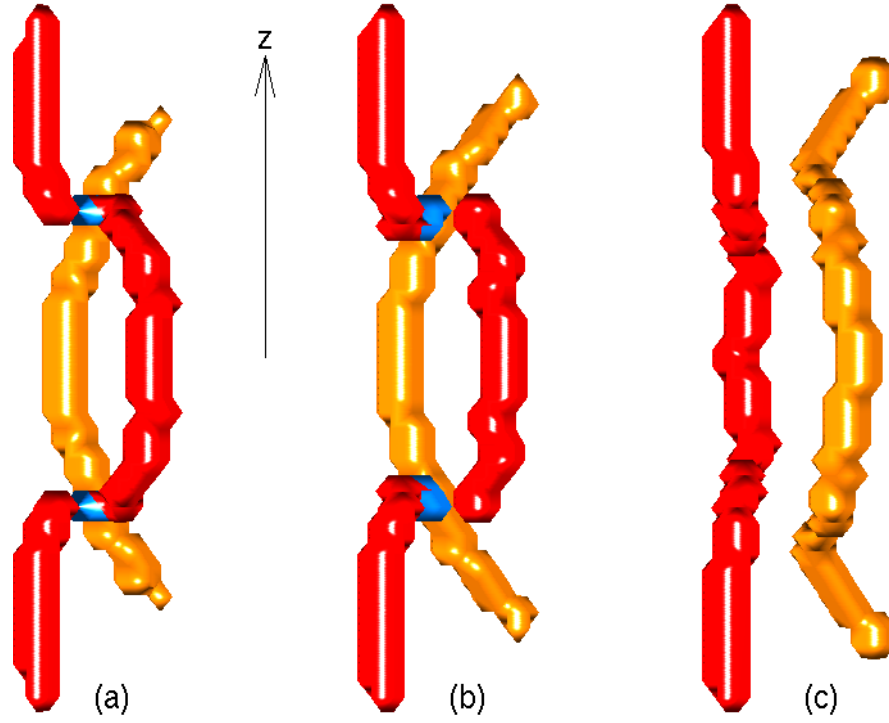


Figure E.7: Sequence showing collision of vortex lines and exchange of sections in a rotationally stirred spherical condensate. In (a)  $t = 6.79$ , (b)  $t = 6.91$ , and (c)  $t = 7.04$ . This is an alternative representation of Figure 7.8; here the two vortex lines are coloured to distinguish them and also to denote their sense of circulation. The first line is coloured red where the vortex detection array  $\mathcal{V} > 0$  (positive sense), and blue where  $\mathcal{V} < 0$  (negative sense). The second line is coloured orange, and  $\mathcal{V} > 0$  (positive sense) along the whole line. In (b), the blue sections of the first line become locally antiparallel to the second line, permitting the collision to occur.



# Appendix F

## Selected papers

In this appendix, we include verbatim copies of references [19] and [17], in which we have published many of the key results of this work.



### Coherent Dynamics of Vortex Formation in Trapped Bose-Einstein Condensates

B. M. Caradoc-Davies,<sup>1</sup> R. J. Ballagh,<sup>1</sup> and K. Burnett<sup>2</sup>

<sup>1</sup>Department of Physics, University of Otago, P.O. Box 56, Dunedin, New Zealand

<sup>2</sup>Clarendon Laboratory, Department of Physics, University of Oxford, Parks Road, Oxford OX1 3PU, United Kingdom  
(Received 5 February 1999)

Simulations of a rotationally stirred condensate show that a regime of simple behavior occurs in which a single vortex cycles in and out of the condensate. We present a simple quantitative model of this behavior, which accurately describes the full vortex dynamics, including a critical angular speed of stirring for vortex formation. A method for experimentally preparing a condensate in a central vortex state is suggested.

PACS numbers: 03.75.Fi, 47.32.Cc

The production of vortices has been a central issue in the study of superfluids. It has been demonstrated, for example, that attempts to produce bulk rotation in a cylinder of He II will lead to vortex production, a state which calculations show to be energetically favored. The currently realized [1,2] Bose-Einstein condensates (BEC) offer a new medium for studying vortices, and a number of theoretical studies have considered the properties of static vortices [3,4], their stability [5–8], excitation spectra [9,10], and phase sensitive detection techniques [11]. A variety of methods have been considered by which vortices could be formed in a BEC. Fetter [6] suggested that a rotating nonaxially symmetric trap could imitate the He II rotating cylinder, and obtained an approximate critical rotational speed for vortex production by a heuristic argument. Jackson *et al.* [12] showed that vortices may be generated by movement of a localized potential through a condensate, while Marzlin and Zhang [13] calculated vortex production using four laser beams in a ring configuration. Other numerical simulations, such as collisions of condensates [14,15], have shown in fact that vortex production appears to be a common consequence of mechanically disturbing a condensate.

In this paper, we consider a trapped BEC stirred rotationally by an external potential, and find and analyze a regime where only a single vortex forms. We present a simple quantitative model of this behavior, which accurately describes the full vortex dynamics in terms of a coherent process. The model gives the critical speed of rotation for vortex formation and explains a number of other features that are seen, including the stability of a central vortex (at  $T = 0$ ). Our investigation is based on the Gross-Pitaevskii (GP) equation for the condensate wave function  $\psi(\mathbf{r}, t)$ ,

$$i \frac{\partial \psi(\mathbf{r}, t)}{\partial t} = -\nabla^2 \psi(\mathbf{r}, t) + V(\mathbf{r}, t) \psi(\mathbf{r}, t) + C |\psi(\mathbf{r}, t)|^2 \psi(\mathbf{r}, t), \quad (1)$$

which is known to accurately describe condensates close to  $T = 0$ . In Eq. (1) we have used scaling and notation as in Ruprecht *et al.* [16];  $V(\mathbf{r}, t)$  is the external potential, and  $C$  is proportional to the number of atoms in the condensate

and the scattering length. We consider the GP equation in two dimensions only, and solve it numerically. We simulate the effect of stirring by adding to the stationary trap potential a narrow, moving Gaussian potential, representing, for example, a far-blue-detuned laser [17].  $V(\mathbf{r}, t)$  is given by  $r^2/4 + W(\mathbf{r}, t)$ , and the stirring potential

$$W(\mathbf{r}, t) = W_0 \exp \left[ -4 \left( \frac{|\mathbf{r} - \mathbf{r}_s(t)|}{w_s} \right)^2 \right], \quad (2)$$

is centered at  $\mathbf{r}_s(t)$ . The initial condensate state for our simulations is the lowest energy eigenstate of the time-independent GP equation [9] in which  $V$  includes the stationary stirrer. The stirrer moves anticlockwise on a circular path, accelerating constantly until  $t = \pi$ , when it reaches its final angular speed  $\omega_f$ . Figure 1, which shows the state of a condensate after it has been stirred for some time ( $t < 5\pi$ ) then left to freely evolve ( $t \geq 5\pi$ ), illustrates the complexity of behavior that can occur.

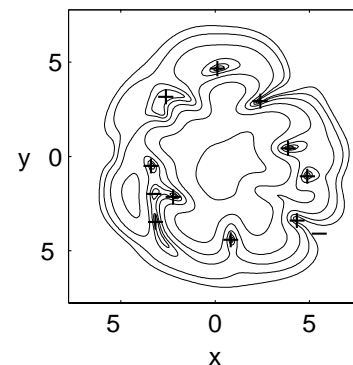


FIG. 1. Probability density at  $t = 12\pi$  of a condensate stirred, as described in the text, with the stirrer gradually withdrawn between  $t = 4\pi$  and  $5\pi$ . Contours are logarithmically spaced. Vortices are detected numerically by searching for their  $2\pi$  phase signature, and are marked near dense regions of the condensate by a + or - sign according to their sense.  $C = 88.13$ ,  $\omega_f = 1$ ,  $r_s = 3$ ,  $W_0 = 10$ , and  $w_s = 1$ .

Vortices of positive and negative circulation have formed and, as time progresses, move relative to each other, and annihilate when a positive and negative pair collide [18].

Amidst the complexity of possible behaviors, an important and simply characterized behavior emerges, namely the formation and dynamics of a single vortex. An example which illustrates the main features is given in Fig. 2, where sequential subfigures show the evolution of the condensate as the stirrer revolves. A single vortex enters at the edge of the visible region of the condensate, then cycles to the center of the condensate, and back to the edge. This cycle repeats regularly, as can be seen in Fig. 3 where the solid line shows the angular momentum  $\langle L \rangle$  plotted as a function of time for this case. At lower stirring speeds, similar vortex cycling occurs, but with progressively smaller amplitudes as  $\omega_f$  decreases, so that the vortex oscillates near the condensate edge. We have found that the condensate gains angular momentum even for very small values of  $\omega_f$ . The *critical angular speed*, which causes a single vortex to cycle right to the center of the condensate, we denote as  $\omega_c$ . In Table I we present results from our simulations that show that  $\omega_c$  decreases as  $C$  increases, in agreement with the heuristic result of Fetter [6].

The single-vortex behavior can be understood quantitatively in terms of a *nonlinear Rabi cycling* model. The essential idea is that the stirring potential causes the condensate to cycle between the ground state and the first vortex state, analogous to the Rabi cycling of an atom in a light field. We decompose the condensate on the basis

of a ground-state-like part (axially symmetric) and a vortex part (axially symmetric with an anticlockwise phase circulation). In the linear (i.e.,  $C = 0$ ) limit the condensate would be represented as a superposition of the ground state and the first vortex state of the trap. In the nonlinear system, it is more accurate to decompose the system into collisionally coupled states, in which the radial form of each of the basis states is modified by its collisional interaction with the other. Accordingly we assume that the condensate mean-field wave function can be represented approximately as

$$\psi(\mathbf{r}, t) = a_s(t)\phi_s(r, n_v) + a_v(t)\phi_v(r, n_v)e^{i\theta}, \quad (3)$$

where  $r$  and  $\theta$  are the cylindrical polar components of  $\mathbf{r}$ , and  $n_v = |a_v|^2$ . We obtain the lowest energy coupled eigenstates  $\phi_s(r, n_v)$  and  $\phi_v(r, n_v)e^{i\theta}$ , together with their eigenvalues  $\mu_s(n_v)$  and  $\mu_v(n_v)$ , by solving for a particular value of  $n_v$  the coupled time-independent radial GP equations,

$$\mu_\sigma \phi_\sigma = \left[ -\frac{1}{r} \frac{d}{dr} \left( r \frac{d}{dr} \right) + \frac{l_\sigma^2}{r^2} + \frac{r^2}{4} + C(n_\sigma \phi_\sigma^2 + 2n_\lambda \phi_\lambda^2) \right] \phi_\sigma. \quad (4)$$

Here  $\sigma$  and  $\lambda$  are either  $s$  or  $v$ ,  $l_s = 0$  and  $l_v = 1$  are the angular momenta of  $\phi_s$  and  $\phi_v e^{i\theta}$ , respectively,  $n_v$  is the fraction of the condensate in the vortex component, and  $n_s = 1 - n_v$  is the fraction in the symmetric component. The  $\phi_\sigma$  are real non-negative functions normalized as  $\int \phi_\sigma^2 d\mathbf{r} = 1$ , and  $\phi_s$  and  $\phi_v e^{i\theta}$  are of course orthogonal. The superposition in Eq. (3) produces a condensate with an angular momentum expectation value  $\langle L \rangle = n_v$ , and a vortex whose distance from the center of the trap decreases as  $n_v \rightarrow 1$ . In the absence of a stirrer, the vortex

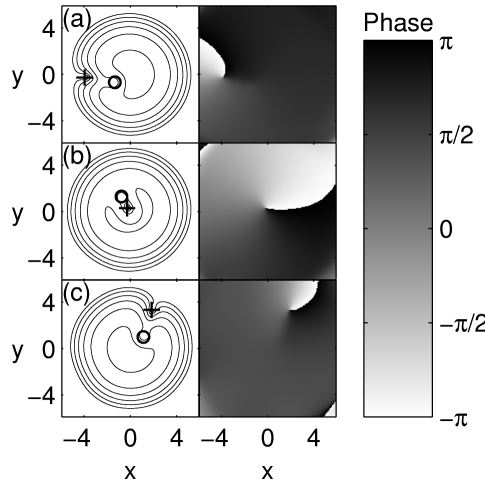


FIG. 2. Sequence of states for a condensate stirred from rest as described in the text. Probability density is shown in the left-hand column, and the phase of  $\psi$  in the right-hand column, for (a)  $t = 8.80$ , (b)  $t = 18.35$ , and (c)  $t = 28.15$ . The circle denotes the stirrer. Parameters are the same as in Fig. 1, except  $\omega_f = 0.5$  and  $r_s = 1.5$ .

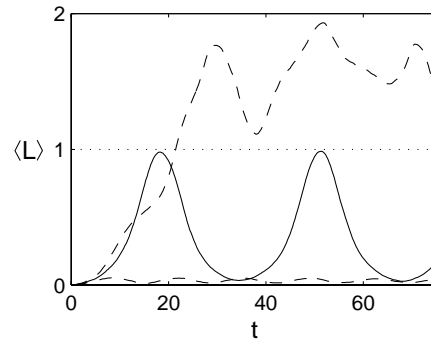


FIG. 3. Angular momentum expectation values versus time for  $\omega_f = 0.5$  (solid line),  $\omega_f = 0.4$  (lower dashed line), and  $\omega_f = 0.6$  (upper dashed line). Other parameters are the same as in Fig. 2.

TABLE I. Critical angular frequency  $\omega_c$  for the two-dimensional condensate. The final column gives bounds for  $\omega_c$  found from our simulations of the full GP equation.

$C$	$E_g$	$E_v$	$\omega_c$	Simulation $\omega_c$
0	1	2	1	...
30	1.811	2.520	0.709	0.6–0.8
88.13	2.744	3.284	0.540	0.5–0.6
500	6.079	6.394	0.315	...
5000	18.860	19.000	0.140	...

precesses about the center of the condensate at a frequency  $\mu_v - \mu_s$ . Substituting Eq. (3) into Eq. (1), and projecting alternately onto the states  $\phi_s$  and  $\phi_v e^{i\theta}$ , we obtain a pair of coupled equations for  $\tilde{a}_s$  and  $\tilde{a}_v$ . Noting that a constantly rotating stirring potential  $W(\mathbf{r}, t)$  can be written  $e^{-i\omega_f t L} W'(\mathbf{r}) e^{+i\omega_f t L}$ , and writing  $\tilde{a}_s = a_s e^{i\alpha_s}$ ,  $\tilde{a}_v = a_v e^{i(\alpha_s + \omega_f t)}$ , where  $\alpha_s(t) = \int_0^t \mu_s(t') dt'$ , we collect the oscillating exponential time dependences and transform to a frame which rotates with the stirring potential to obtain the following equations:

$$\frac{d\tilde{a}_s}{dt} = -i\delta_s(n_v)\tilde{a}_s - \frac{i}{2}\Omega(n_v)\tilde{a}_v, \quad (5a)$$

$$\frac{d\tilde{a}_v}{dt} = -i[\Delta(n_v) + \delta_v(n_v)]\tilde{a}_v - \frac{i}{2}\Omega^*(n_v)\tilde{a}_s. \quad (5b)$$

Here  $\Delta(n_v) = \mu_v(n_v) - \mu_s(n_v) - \omega_f$  and

$$\delta_\sigma(n_v) = \int \phi_\sigma(n_v) W'(\mathbf{r}) \phi_\sigma(n_v) d\mathbf{r}, \quad (6a)$$

$$\Omega(n_v) = 2 \int \phi_s(n_v) W'(\mathbf{r}) \phi_v(n_v) e^{i\theta} d\mathbf{r}. \quad (6b)$$

Equations (5) formally resemble the classic Rabi equations, and hence we identify the  $\delta_\sigma$  as frequency shifts and  $\Omega$  as the bare Rabi frequency, but note that here these quantities are variable and depend on the value of  $n_v$ . Despite this nonlinear dependence, the concept of Rabi cycling provides a simple framework in which to understand the formation and dynamics of a single vortex: the stirring potential couples and causes cycling between the initial ground state and the first excited vortex state. The energy  $E'$  in the frame rotating with the stirrer (obtained from the expectation value of  $H' = H - \omega_f L$ , where  $H$  is the lab frame Hamiltonian and  $L$  is the dimensionless angular momentum operator) is conserved, and thus in any solution to Eqs. (5),  $\tilde{a}_s$  and  $\tilde{a}_v$  must follow a trajectory that conserves  $E'$ . Complete cycling of the vortex to the center of the condensate occurs when  $n_v$  reaches the value of 1, but this requires the energies in the rotating frame of the ground state  $\phi_s(r, n_v = 0)$  and the first excited vortex state  $\phi_v(r, n_v = 1)e^{i\theta}$  to be equal. Thus the critical angular speed  $\omega_c$  is given by the relation

$$E_v - \omega_c = E_g, \quad (7)$$

where  $E_g$  and  $E_v$  are the lab frame energies of the ground state and first excited vortex state, respectively. A finite stirrer shifts these energies by  $\delta_s(n_v = 0)$  and  $\delta_v(n_v = 1)$ , respectively, adjusting  $\omega_c$  by their difference.

In Table I we list the critical angular speeds predicted by Eq. (7) for a range of  $C$  values, along with the values of  $\omega_c$  found from our numerical simulations of the full GP equation for  $C = 30$  and  $C = 88.13$  cases. The agreement between the predictions from the two-state model and the full numerical simulation is excellent.

It is difficult to obtain accurate simulations at large values of  $C$  for numerical reasons. The  $C = 0$  case is easily tractable, and although no visible vortex cycling occurs below  $\omega_f = 0.25$ , a multiple vortex regime is entered at  $\omega_f = 0.8 < \omega_c$ ; the reason being, as Marzlin and Zhang [13] have noted, that the trap levels are equally spaced for the linear case, so that mixing to higher vortex states readily occurs, and our two-state model is no longer valid. The success of the two-state model is dependent on the fact that, for  $C \neq 0$ , the spacing of the levels is nonuniform.

The Rabi model also allows us to explain other features of the behavior, such as the period of cycling, the response to smaller stirring speeds, and the effect of different values of stirring radius  $r_s$ . In Fig. 3 the condensate response to stirring just below the critical speed is shown, and reveals an increase in oscillation frequency and decreased transfer to the pure vortex state, compared to the critical case. In a simple Rabi model, where the detuning  $\Delta$  and Rabi frequency  $\Omega$  are constant, the cycling frequency is  $\Omega' = \sqrt{\Omega^2 + \Delta^2}$ , and the maximum value of  $n_v$  is  $(\Omega/\Omega')^2$ . By identifying the effective detuning for the two-state system to be  $\Delta + \delta_v - \delta_g$ , these expressions give a qualitative description of the subcritical stirring in Fig. 3. A more quantitative treatment requires the nonlinear character of Eqs. (5) to be taken into account, which is achieved by solving the coupled pair in Eq. (4) to find the eigenvectors and eigenvalues at each value of  $n_v$  and then using these to solve Eqs. (5). We note that in Eq. (4) the term  $2n_\lambda \phi_\lambda^2$  gives rise to an energy barrier between the  $n_v = 0$  and  $n_v = 1$  states of the system. The constraint on the system imposed by the ansatz of Eq. (3) increases this energy barrier slightly compared to the true (unconstrained) case, and the accuracy of our procedure can be improved by decreasing this factor of 2. For example, at  $C = 88.13$ , if we decrease the factor of 2  $\rightarrow 1.58$ , our two-state model produces behavior which closely matches the results from the full GP equation, as we show in Fig. 4. The energy barrier is deformed by the presence of the stirrer, allowing the system to cycle between the vortex and ground state. If the stirrer is far from the center of the condensate, or is weak, then  $\Omega$  may be too small to distort the energy barrier sufficiently, and only incomplete cycling occurs even when  $\omega_f = \omega_c$ . This feature of the nonlinear system, which agrees with our  $r_s = 3$  simulations of the full GP equation, is in contrast to the ordinary Rabi

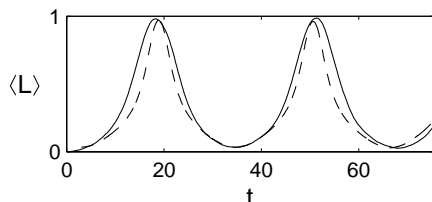


FIG. 4. Angular momentum versus time for the full GP equation simulation (solid line) and the two-state model (dashed line). The two-state model starts at  $t = 3$  with  $\bar{a}_s = \sqrt{0.965}$  and  $\bar{a}_v = -\sqrt{0.035}$ . Parameters are the same as in Fig. 2.

case, where complete cycling occurs on resonance for any nonzero coupling field.

The validity of the two-state model breaks down when  $\omega_f$  exceeds  $\omega_c$ , because then higher energy vortex eigenstates are energetically permitted and mixed into the state of the system, as seen, for example, in Fig. 1 and the upper dashed curve of Fig. 2.

The Rabi model provides some insight into the issue of the stability of a central vortex state [5,10]. We have tested this stability in the  $T = 0$  limit by simulation of the GP equation, taking the first excited  $l = 1$  vortex state and inserting and withdrawing a narrow stirrer at a fixed location in the laboratory frame. We find that, although the condensate then wobbles vigorously, the vortex undergoes only a very stable small-amplitude oscillation about the trap center [18]. We can interpret this as Rabi cycling of very large effective detuning (i.e.,  $\omega_f = 0$ ), and consequently very small transfer probability out of the initial vortex state.

The regular cyclic single-vortex behavior we have found also suggests an experimental technique for preparing a condensate in a central vortex state. By stirring a condensate for a half-cycle, a vortex will be drawn into a nearly central position.

In conclusion, we have given a simple, quantitative analysis of the single-vortex regime of a stirred condensate. Our two-state model captures the essential coherent dynamics, and accurately predicts the major features of this regime, but also provides a qualitative understanding in terms of the concepts of the well-known Rabi model. Our result for the critical angular frequency can be qualitatively related to that for a rotating cylinder of He II. However, in our case the condensate is inhomogeneous, and the trapping potential plays a central role, giving rise to well-separated condensate eigenstates, of which only the lowest two become significantly involved. It is worth remarking

that the speed of sound in the vicinity of the perturber has no relevance to the generation of vortices, in the scenarios we consider here. The model is also easily generalizable to an arbitrarily shaped stirring potential, including a rotating anisotropic potential. Our numerical calculations have been carried out in two spatial dimensions, but can be expected to apply to “pancake” condensates, where the dynamics in the axial direction are frozen out by very tight axial confinement. Qualitative features of our results may have even greater generality, since the two-state model has no direct dependence on dimensionality, and will apply in three dimensions if the system symmetry confines the stirrer to couple the ground state primarily to a single-vortex state.

We thank P. B. Blakie, C. W. Gardiner, and S. Morgan for valuable discussions. This work was supported by The Marsden Fund of New Zealand under Contract No. PVT603.

- [1] M. H. Anderson *et al.*, *Science* **269**, 198 (1995).
- [2] K. B. Davis *et al.*, *Phys. Rev. Lett.* **75**, 3969 (1995).
- [3] F. Dalfovo and S. Stringari, *Phys. Rev. A* **53**, 2477 (1996).
- [4] D. A. Butts and D. S. Rokhsar, *Nature (London)* **397**, 327 (1998).
- [5] D. S. Rokhsar, *Phys. Rev. Lett.* **79**, 2164 (1997).
- [6] A. L. Fetter, in *Recent Progress in Many-Body Theories*, edited by D. Neilson and R. F. Bishop (World Scientific, Singapore, 1998), pp. 302–307.
- [7] A. L. Fetter, *J. Low Temp. Phys.* **113**, 189 (1998).
- [8] A. A. Svidzinsky and A. L. Fetter, *Phys. Rev. A* **58**, 3168 (1998).
- [9] R. J. Dodd, K. Burnett, M. Edwards, and C. W. Clark, *Phys. Rev. A* **56**, 587 (1997).
- [10] A. A. Svidzinsky and A. L. Fetter, *cond-mat/9811348*.
- [11] E. L. Bolda and D. F. Walls, *Phys. Rev. Lett.* **81**, 5477 (1998).
- [12] B. Jackson, J. F. McCann, and C. S. Adams, *Phys. Rev. Lett.* **80**, 3903 (1998).
- [13] K.-P. Marzlin and W. Zhang, *Phys. Rev. A* **57**, 4761 (1998).
- [14] R. J. Ballagh, T. F. Scott, K. Burnett, and B. M. Caradoc-Davies, Poster presented at *Bose-Einstein Condensation in Atomic Vapors*, Castelvechio Pascoli, Italy, 1997.
- [15] B. Jackson, J. F. McCann, and C. S. Adams, *cond-mat/9901087*.
- [16] P. A. Ruprecht, M. J. Holland, K. Burnett, and M. Edwards, *Phys. Rev. A* **51**, 4704 (1995).
- [17] M. R. Andrews *et al.*, *Science* **275**, 637 (1997).
- [18] MPEG movies showing these results are available from (<http://www.physics.otago.ac.nz/research/bec>).



## Three-dimensional vortex dynamics in Bose-Einstein condensates

B. M. Caradoc-Davies, R. J. Ballagh, and P. B. Blakie

*Department of Physics, University of Otago, P. O. Box 56, Dunedin, New Zealand*

(Received 6 March 2000; published 15 June 2000)

We simulate in the mean-field limit the effects of rotationally stirring a three-dimensional trapped Bose-Einstein condensate with a Gaussian laser beam. A single vortex cycling regime is found for a range of trap geometries, and is well described as coherent cycling between the ground and the first excited vortex states. The critical angular speed of stirring for vortex formation is quantitatively predicted by a simple model. We report preliminary results for the collisions of vortex lines, in which sections may be exchanged.

PACS number(s): 03.75.Fi, 47.32.Cc

The formation and properties of vortices in Bose-Einstein condensates are attracting intense current interest. A number of schemes for producing vortices in trapped condensates have been proposed theoretically, and the first experimental creation of a topological vortex in a two-component condensate has been reported [1], in agreement with a numerical model [2]. Simulations of flow of a condensate past a spherical object have shown vortex ring solutions [3], and numerical studies of vortex formation in rotating traps have shown the formation of vortex arrays [4]. Very recently the first report has been made of the observation of vortices in a single-component condensate [5].

In an earlier paper [6], we showed that a rotationally stirred Bose-Einstein condensate, simulated in two dimensions, exhibits a simple single vortex cycling regime, a behavior we described as nonlinear Rabi cycling. In the present paper we demonstrate that the single vortex cycling regime is also found in full three-dimensional simulations of condensate stirring (as shown in Fig. 1), in a parameter regime accessible to current experiments. The single vortex regime is studied in a variety of trap geometries (oblate to prolate) as is the dynamical stability of central vortices. The line character of a vortex in three dimensions also gives rise to some qualitatively new behavior that has no analogue in two dimensions. We show that in a spherical trap, stirring of the condensate can produce two vortex lines that collide and exchange sections.

As in the earlier work, our treatment is based on the time-dependent Gross-Pitaevskii (GP) equation,

$$i \frac{\partial \psi(\mathbf{r}, t)}{\partial t} = [-\nabla^2 + V(\mathbf{r}, t) + C|\psi(\mathbf{r}, t)|^2] \psi(\mathbf{r}, t), \quad (1)$$

in dimensionless units [7]. The total external potential  $V(\mathbf{r}, t)$  is given by  $(x^2 + y^2 + \lambda^2 z^2)/4 + W(\mathbf{r}, t)$ , where the first term represents a cylindrically symmetric trap with trap anisotropy parameter  $\lambda$ . The second term  $W(\mathbf{r}, t)$  is the contribution of the stirrer, a far-blue detuned Gaussian laser beam cylindrically symmetric about a line parallel to the  $z$  axis,

$$W(\mathbf{r}, t) = W_s(t) \exp \left[ -\left( \frac{|\boldsymbol{\rho} - \boldsymbol{\rho}_s(t)|}{w_s/2} \right)^2 \right], \quad (2)$$

where  $\boldsymbol{\rho}$  is the projection of  $\mathbf{r}$  into the  $z=0$  plane, and  $\boldsymbol{\rho}_s$  is the center of the Gaussian stirrer in that plane.

The condensate is stirred in a manner similar to our earlier work [6], with the stirrer moving in a circle of radius  $\rho_s$  at a constant angular velocity  $\omega_f$ . Here, however, we begin with the ground state of the harmonic trap (with no stirrer present), and minimize transient effects by increasing the stirrer amplitude  $W_s$  linearly from zero to a final value of  $W_0$  between  $t=0$  and  $t=\pi$ . With an appropriate choice of parameters, as in Fig. 1, a single vortex with positive circulation is drawn close to the center of the condensate, and for continuous stirring cycles in and out. This is exactly the behavior found previously in a two-dimensional system [6], and in fact the parameter choice for the single vortex cycling behavior in three dimensions is guided by the same considerations outlined there, as we discuss below. Figure 2, where we plot the phase of the wave function, shows that the central feature of Fig. 1 is a vortex of positive circulation. In Fig. 3 the evolution of the angular-momentum expectation

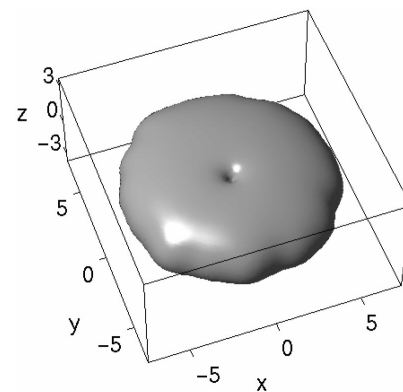
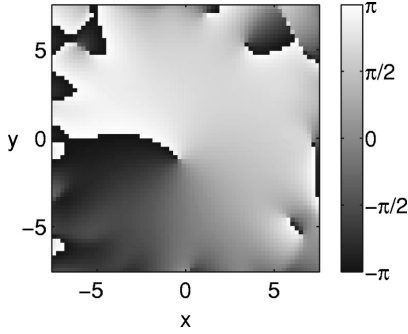


FIG. 1. Probability density isosurface ( $|\psi|^2 = 10^{-4}$ ) for a condensate stirred as described in the text, with the stirrer linearly withdrawn between  $t=7\pi$  and  $t=8\pi$ . Here  $t=94.12$ , and the hole near the center of the condensate is a vortex that has been drawn in from the edge and remains close to to the center of the condensate. Parameters are  $C=1000$ ,  $\lambda=\sqrt{8}$ ,  $W_0=4$ ,  $w_s=4$ , and  $\rho_s=2$ . The angular frequency of stirring  $\omega_f=0.3$  is less than the critical frequency  $\omega_c=0.323$ .

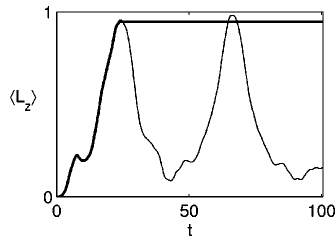
## RAPID COMMUNICATIONS

B. M. CARADOC-DAVIES, R. J. BALLAGH, AND P. B. BLAKIE

PHYSICAL REVIEW A **62** 011602(R)FIG. 2. Phase of  $\psi$  in the  $z=0$  plane for the condensate shown in Fig. 1.

value (which in our dimensionless units is 0 for the ground state and 1 for the central vortex state) is presented and confirms that for continuous stirring (thin line), the vortex cycles in and out of the condensate.

In contrast to the two-dimensional case, the three-dimensional simulation can be unambiguously related to a realistic current experimental scenario. The  $C=1000$  case shown in Figs. 1–3 corresponds to  $N=1.8 \times 10^4$  atoms of  $^{87}\text{Rb}$  in the  $|F=2, m_f=2\rangle$  hyperfine state (for which we use an  $s$ -wave scattering length  $a=5.29$  nm) in a time orbiting potential (TOP) trap with radial trap frequency  $\omega_r=2\pi \times 15$  Hz and  $\lambda=\omega_z/\omega_r=\sqrt{8}$ . For this example, our computational units of time and length [7] correspond to 10.6 ms and  $1.97 \mu\text{m}$ , respectively, and the Thomas-Fermi diameter of the condensate in the radial direction of 11.7 corresponds to about  $23 \mu\text{m}$ . The stirrer Gaussian  $1/e$  diameter  $w_s=4$  corresponds to a Gaussian  $1/e^2$  beam diameter of approximately  $11 \mu\text{m}$ . The required intensity of the stirring laser is detuning dependent, but can be easily calculated from the light shift potential  $\hbar\Omega^2/4\Delta$ , where  $\Omega$  and  $\Delta$  are the Rabi frequency and detuning, respectively, of the atom-laser interaction. For example, if the laser beam is 50 nm blue-detuned from the 780-nm atomic transition,  $\Delta=1.65 \times 10^{14} \text{ s}^{-1}$ , and a laser power of 300 nW is required for the 3-nK height stirrer we describe. The first angular-momentum peak in Fig. 3 occurs at 0.26 s, which is much less than the lifetime of the

FIG. 3. Condensate angular-momentum expectation value versus time, for the case of a constantly rotating stirrer (thin line) or stirrer linearly withdrawn between  $t=7\pi$  and  $t=8\pi$  (thick line). Parameters as in Fig. 1.

condensate. The occurrence of the single vortex cycling behavior in this experimentally accessible parameter regime suggests a method of preparing a central vortex state: stir the condensate as we have described, then remove the stirrer at the time when the angular-momentum peak is expected. We illustrate the implementation of this method in Fig. 3 with the thick curve, for which the stirrer is linearly withdrawn between  $t=7\pi$  and  $t=8\pi$ . Once the stirrer is removed, the vortex remains in the condensate, circling about and close to the center, and  $\langle L_z \rangle$  is constant.

The vortex cycling behavior illustrated by the example in Figs. 1–3 indicates that the two-state model described in our earlier work (for the two-dimensional case [6]) also has application in three-dimensions. Here we briefly outline the modifications required to extend the two-state model into three dimensions. We represent the condensate by an axisymmetric component  $\phi_s$  and a vortexlike component  $\phi_v e^{i\theta}$  that has a circulation about the  $z$  axis, where  $\phi_s$  and  $\phi_v$  are real and non-negative, so

$$\psi(\mathbf{r}, t) = a_s(t) \phi_s(\rho, z, n_v) + a_v(t) \phi_v(\rho, z, n_v) e^{i\theta}, \quad (3)$$

with  $\rho = \sqrt{x^2 + y^2}$ . We choose  $\phi_s$  and  $\phi_v$  to satisfy the following time-independent coupled equations:

$$\mu_s \phi_s = \left[ -\frac{1}{\rho} \frac{d}{d\rho} \left( \rho \frac{d}{d\rho} \right) - \frac{d^2}{dz^2} + \frac{\rho^2 + \lambda^2 z^2}{4} \right] \phi_s + C(n_s \phi_s^2 + 2n_v \phi_v^2) \phi_s, \quad (4a)$$

$$\mu_v \phi_v = \left[ -\frac{1}{\rho} \frac{d}{d\rho} \left( \rho \frac{d}{d\rho} \right) - \frac{d^2}{dz^2} + \frac{1}{\rho^2} + \frac{\rho^2 + \lambda^2 z^2}{4} \right] \phi_v + C(n_v \phi_v^2 + 2n_s \phi_s^2) \phi_v, \quad (4b)$$

where the eigenvalues  $\mu_s$  and  $\mu_v$  are found by solving Eqs. (4) for a given choice of the vortex fraction  $n_v = |a_v|^2$ . The quantity  $n_s = |a_s|^2 = 1 - n_v$ . We note that when  $n_v = 0$ , Eqs. (4) reduce to Eq. (4a), the time-independent GP equation for the ground state, while if  $n_v = 1$ , Eqs. (4) reduce to Eq. (4b), the time-independent GP equation for the first excited vortex. The resulting nonlinear Rabi equations for the two-state system [obtained by substituting Eq. (3) into Eq. (1)] are then identical in form to Eqs. (5)–(6) of [6], but with the wave functions  $\phi_s$  and  $\phi_v$  now defined over  $\rho$  and  $z$  instead of  $r$ .

The underlying assumption of our two-state model is that the ground state (or, more generally,  $\phi_s$ ) is coupled primarily to the vortex state of lowest energy with axis parallel to the stirrer axis. In two dimensions, there are a limited number of excited condensate states in the appropriate energy range that can be coupled to the symmetric state by the stirring potential, and we have previously shown [6] that the two-state model works well within a specified validity range. In three-dimensional cylindrically symmetric traps, many

more condensate eigenstates exist, and although symmetry considerations limit the possible coupling from the symmetric state, a two-state model places more constraints on the description of the system than in the two-dimensional case. We do not aim therefore to provide a detailed representation of the stirring behavior with our two-state model; instead, we use it primarily to provide a conceptual understanding of the cycling behavior. Nevertheless, we also find that it gives a quantitatively accurate prediction of the critical frequency of rotation  $\omega_c$ , the stirring frequency that causes a single vortex to cycle right to the center of the condensate. We have examined the single vortex cycling behavior using the full GP solution for a variety of trap geometries, including the oblate ( $\lambda = \sqrt{8}$ ), spherical ( $\lambda = 1$ ), and prolate ( $\lambda = 1/3$ ) cases, with a condensate of  $C = 1000$  and a stirring potential of the same size and position as in Fig. 1. We find that the critical rotational frequency for single vortex cycling is accurately predicted by the two-state model as the difference in energy between the ground and vortex states of the condensate [modified by the finite size of the stirrer; see Eq. (7) of [6]]. As in [6], a sufficiently large Rabi frequency is required to distort the energy barrier between ground and vortex state enough to permit cycling. When the critical frequency of rotation is exceeded, additional vortices penetrate the condensate.

It is worth noting that as the  $z$  component of the trapping potential becomes weaker (that is, as  $\lambda$  becomes smaller), then in addition to the vortex state, the stirring potential increasingly excites the dipole (center-of-mass) oscillation of the condensate. This can be understood in terms of the Ehrenfest theorem; for our choice of parameters the mean force  $\langle -\nabla W \rangle$  of the stirrer increases as the condensate radial size decreases because the condensate is increasingly concentrated near the steepest part of the stirring potential. The center-of-mass motion contributes angular momentum  $\langle L_z \rangle_{COM}$  to the condensate angular momentum, where

$$\langle L_z \rangle_{COM} = \langle x \rangle \langle P_y \rangle - \langle y \rangle \langle P_x \rangle. \quad (5)$$

We find that  $\langle L_z \rangle - \langle L_z \rangle_{COM}$  (which is a measure of the angular momentum caused by the presence of the vortex) for all three trap geometries cycles between 0 and 1 when  $\omega_f$  is slightly less than  $\omega_c$  (the single vortex cycling regime) and oscillates about 1 when  $\omega_f$  just exceeds  $\omega_c$  (and multiple vortices penetrate the condensate).  $\langle L_z \rangle_{COM}$  is small for the  $\lambda = \sqrt{8}$  case shown in Fig. 3.

If the single stirrer used in Fig. 1 is replaced by two stirrers of half the height but on opposite sides of the  $z$  axis, no vortex cycling occurs, and  $\langle L_z \rangle$  exhibits only small oscillations of amplitude less than 0.04. This is easily understood from our two-state model, because the Rabi frequency  $\Omega$  [see Eq. (6b) of [6]] is zero for this stirrer configuration, as it is for any stirrer configuration of even symmetry. It is worth pointing out that our scenario of coherent cycling should be distinguished from vortex production by damping in a trap with a symmetric rotating distortion, such as the recently reported experiment [5], or numerical damping schemes such as imaginary-time propagation [4].

Our three-dimensional simulations also allow us to test (in the mean-field limit) the stability of pure vortex eigenstates. Using as an initial state a central vortex (an eigenstate of the time-independent GP equation) for  $C = 1000$ , a perturbation was applied by linearly inserting and withdrawing (between  $t = 0$  and  $t = \pi$ ) a stirrer of the same size as in Fig. 1 but at a fixed position in the laboratory frame. We find that for a range of trap geometries ( $\lambda = \sqrt{8}$ , 1, or  $1/3$ ), the  $\langle L_z \rangle = 1$  vortex is dynamically stable, and remains near the center of the condensate. We can understand this result in terms of Rabi cycling. The stationary stirrer ( $\omega_f = 0$ ) provides a potential that is far-detuned from resonance ( $\omega_f \neq \omega_c$ ), and thus there is a low probability of transfer out of the initial (vortex) state. Indeed, if the stirrer remains fixed in the condensate after insertion and is not withdrawn, we find that the vortex still remains near the center of the condensate and follows a small closed path displaced slightly away from the stirrer. By contrast, for these geometries, the  $\langle L_z \rangle = 2$  central vortex eigenstate immediately dissociates into two unit vortices when perturbed. We note that these stability results refer to dynamical stability in the GP limit (that is,  $T = 0$ ), as opposed to thermodynamic stability [8,9].

In addition to confirming the basic features of the two-state model of vortex cycling, our three-dimensional simulations also reveal some new phenomena. The vortices produced in three dimensions by stirring are line vortices. In the  $\lambda = \sqrt{8}$  configuration, the lines are nearly straight and parallel to the stirrer axis, and when two lines of the same circulation form, we find they repel each other. For a spherical trap ( $\lambda = 1$ ), however, vortex lines along any direction are degenerate (in the absence of the stirrer) with the vortex eigenstate about the  $z$  axis. Accordingly, the vortex lines can become more curved than in the oblate case, as we find in our simulations below the critical frequency, where the vortex that forms can have appreciable curvature. Above the critical frequency, when multiple vortices are drawn into the condensate, there is a striking consequence of this potential

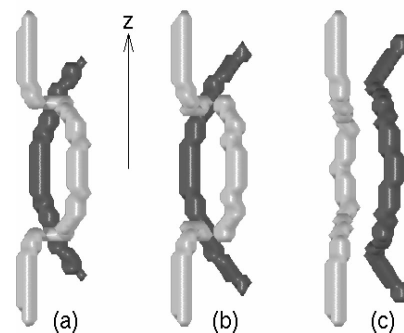


FIG. 4. Collision of vortex lines and exchange of sections in a stirred condensate. View is from a position in the  $z = 0$  plane, looking almost down the  $y = -x$  line. In (a)  $t = 6.79$ , (b)  $t = 6.91$ , and (c)  $t = 7.04$ . Parameters are the same as in Fig. 1 except that  $\lambda = 1$ . The angular frequency of stirring  $\omega_f = 0.45$  exceeds the critical frequency  $\omega_c = 0.399$ .

## RAPID COMMUNICATIONS

B. M. CARADOC-DAVIES, R. J. BALLAGH, AND P. B. BLAKIE

PHYSICAL REVIEW A **62** 011602(R)

for vortex lines to deform. In a collision between two such curved vortex lines, sections of the lines can be exchanged, as we show in the collision sequence in Fig. 4. The condensate is stirred somewhat above the critical frequency in a spherical trap, and by  $t=6.79$  two vortex lines (both of positive sense [10]) have formed. The figure shows only the vortex lines (detected numerically), which have been shaded light and dark to distinguish one from the other. In Fig. 4(a) the dark vortex line approaches the light vortex line from behind, and because of their mutual repulsion, the light line has developed a bulge. In Fig. 4(b) the dark line is now close to the light line, causing the bulge to become recurved, with two small portions now nearly antiparallel to the dark line. In

Fig. 4(c) the two lines have completed a collision and exchanged their central sections.

In conclusion, we have shown that the single vortex cycling regime we discovered previously in simulations of two-dimensional condensates is also present in three-dimensional condensates, for a range of trap geometries. We have related our simulations to current experimental configurations, and have demonstrated how the cycling behavior could be used to generate a central vortex state. We have investigated the dynamical stability of central vortex states, and have also given initial evidence of the rich dynamical behavior of vortex lines.

This work was supported by the Marsden Fund of New Zealand under Contract No. PVT902.

- 
- [1] M. R. Matthews *et al.*, Phys. Rev. Lett. **83**, 2498 (1999).
  - [2] J. E. Williams and M. J. Holland, Nature (London) **401**, 568 (1999).
  - [3] T. Winiecki, J. F. McCann, and C. S. Adams, Europhys. Lett. **48**, 475 (1999).
  - [4] D. L. Feder, C. W. Clark, and B. I. Schneider, Phys. Rev. A **61**, 011601(R) (2000).
  - [5] K. W. Madison, F. Chevy, W. Wohlleben, and J. Dalibard, Phys. Rev. Lett. **84**, 806 (2000).
  - [6] B. M. Caradoc-Davies, R. J. Ballagh, and K. Burnett, Phys. Rev. Lett. **83**, 895 (1999).
  - [7] Our units of time and length are  $\omega_r^{-1}$  and  $(\hbar/2m\omega_r)^{1/2}$ , respectively, where  $\omega_r$  is the trap frequency in the radial direction. The nonlinearity parameter  $C=8\pi aN(2m\omega_r/\hbar)^{1/2}$  and we normalize the wave function by  $\int |\psi(\mathbf{r},t)|^2 d\mathbf{r}=1$ .
  - [8] D. S. Rokhsar, Phys. Rev. Lett. **79**, 2164 (1997).
  - [9] A. L. Fetter, J. Low Temp. Phys. **113**, 189 (1998).
  - [10] Positive sense here means that following from the bottom to the top the direction of circulation is given by the right hand rule.